InSAR Applied to the Study of Active Volcanic and Seismic Areas in Africa

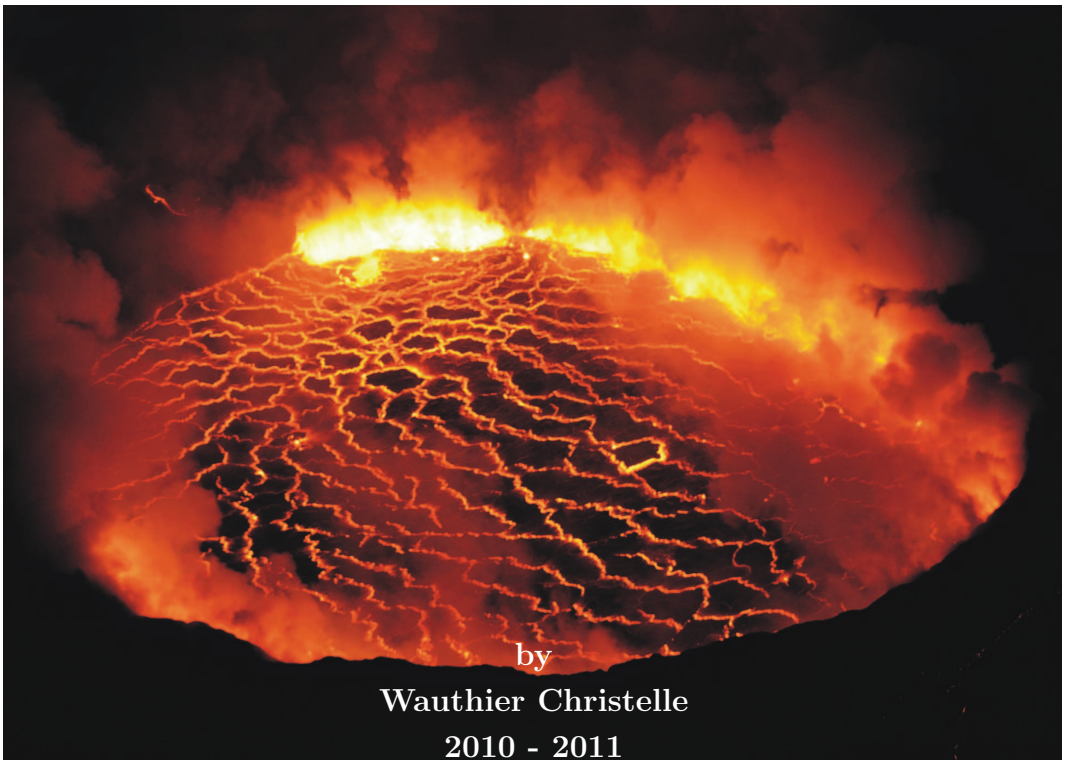

by
Wauthier Christelle
2010 - 2011

Thesis submitted in fulfilment of the requirements for the degree of Doctor in "'Architectural, Geological, and Civil"' Engineering Sciences

Promoter: Prof. Eric Pirard
Co-Promoter: Dr. François Kervyn

Abstract

Two active volcanic areas situated in immature portions of the East African Rift System (EARS): the Lake Kivu (Dem. Rep. of Congo) and Lake Natron (Tanzania) regions, which are located in the western and eastern branch, respectively, are still poorly known. Both areas indeed lack of ground-based networks, due to security problems or difficult field accessibility. The Lake Kivu area includes two volcanoes erupting frequently: the Nyamulagira and Nyiragongo volcanoes. The SAR database covering these volcanoes includes data from JERS, ERS-1&2, ENVISAT, ALOS, RADARSAT-1&2 satellites back from year 1996. SAR Interferometry (InSAR) is thus applied to study the ground deformations. MT-InSAR approaches, such as the "'StaMPS"' method, are used to give us new complementary information to better constrain the previous established eruption models, or gain new insights on eruptions missed by the conventional InSAR, as well as on magmatic and tectonic activity. When enough constrain are available, the ground displacements are modeled using a 3D-Mixed Boundary Elements Method combined with a neighborhood algorithm. Hence, the 1996, 2002, 2004 and 2010 eruptions of Nyamulagira are modeled. The modeling results, coupled with the StaMPS MT-InSAR results, bring new insights concerning the magma plumbing system of this poorly known volcano and its eruptive mechanisms. The collapse of the eastern flank of Nyamulagira, along the NNW-trend fractures network linking Nyamulagira and Nyiragongo volcanoes, can also be identified. InSAR also captures the ground displacements associated with the January 2002 Nyiragongo eruption. The modeling of this major event evidences a deep magma intrusion beneath the Lake Kivu. Such intrusions should be taken into account for hazard assessment. The magma could indeed finds its way to the Lake Kivu floor, as evidenced by the presence of several old phreato-magmatic cones, and causes a lake overturn. The low dikes overpressures found in the North Kivu and Lake Natron areas indicate that, although the rift is considered as immature, the rift extension is driven by the supply of magma from depth, rather than by the tectonics. A new criterion to identify the rifting stage is found to be the stress state. In the southern part of the rift, tectonic activity dominates, indicating that the tectonics is probably driving the rift opening there.

Résumé

Deux zones volcaniques actives situées dans des portions immatures du rift est-africain (EARS): les zones du lac Kivu (Rép. Dém. du Congo) et du Lac Natron (Tanzanie), localisées respectivement dans la branche ouest et est du rift, sont encore peu connues. Ces deux zones manquent en effet cruellement de réseaux de surveillance au sol, principalement à cause de problèmes d'insécurité ou d'accès. En ce qui concerne la zone du lac Kivu, la base de données SAR remonte à 1996 et comporte des données des satellites JERS, ERS-1&2, ENVISAT, ALOS, RADARSAT-1&2. L'interférométrie radar (InSAR) est donc utilisée afin d'étudier les déformations du sol. Des techniques de séries temporelles InSAR telles que la méthode "'StaMPS"' sont utilisées afin de nous apporter des contraintes supplémentaires sur les modèles éruptifs, ou nous donner de nouvelles informations sur des éruptions manquées par l'InSAR conventionnelle, ainsi que sur l'activité magmatique et tectonique. Lorsque suffisamment de contraintes sont disponibles, les déplacements du sol sont modélisés avec une méthode 3D mixte d'éléments frontières couplée à un algorithme de voisinage. Les éruptions de 1996, 2002, 2004 et 2010 du Nyamulagira ont ainsi été modélisées. Les résultats issus de ces modélisations, couplés aux résultats obtenus avec la méthode de séries temporelles StaMPS, permettent d'apporter de nouvelles contraintes sur le système d'alimentation magmatique du Nyamulagira ainsi que sur ses méchanismes éruptifs. L'effondrement du flanc est du volcan, le long de l'alignement NNW reliant le Nyamulagira au Nyiragongo, a aussi pu être mis en évidence. L'InSAR a également permis d'étudier l'éruption majeure de janvier 2002 du Nyiragongo. Les résultats de cette modélisation prouvent l'existence d'une intrusion profonde sous le lac Kivu. De telles intrusions devraient être intégrées à toute analyse d'aléas dans la région. Le magma pourrait en effet atteindre le fond du lac, comme en témoignent les nombreux anciens cônes phréatomagmatiques présents sur le fond du lac, et ainsi causer une déstabilisation du gaz contenu dans les couches profondes du lac. Les faibles surpressions obtenues pour les dikes au Natron et au Kivu indiquent que, bien que le rift soit encore jeune, l'extension est favorisée par la remontée de magma profond plutôt que par la tectonique. Un nouveau critère, l'état de contrainte, a ainsi pu être identifié afin de déterminer le stade d'un rift. Dans la partie sud du lac Kivu par contre, il semble que ce soit l'activité tectonique qui domine, ainsi, ce serait bien cette dernière qui favoriserait donc l'ouverture du rift à cet endroit.

Acknowledgements

I first would like to thank my promoter, Prof. Eric Pirard, for his continuous coaching during the thesis. All this adventure was made possible because he has always believed in me and in my vocation for the volcanology. He encouraged and guided me to succeed in that way (at least until now!). My warm acknowledgments also go to my co-promoter Dr. François Kervyn who gave me the opportunity to obtain this PhD grant, and offered me insightful research advices through all the thesis. The SAR images were acquired thanks to several projects he launched, and his knowledge of Africa was of great help to constrain my view on the remote-sensing data. I also wish to deeply thank Dr. Valérie Cayol from the Laboratoire Magmas and Volcans (LMV), Clermont-Ferrand, France. She trained me for the numerical modeling during my DEA in LMV, and from that moment, we closely collaborate. She has always helped me and guided me a lot during all the thesis with much patience. Her enthusiasm, positive advices and detailed comments, strongly helped me to make evolute my research in a right direction.

My work was supported by a Belgian Science Policy (Belspo) grant. The research was carried out at the Royal Museum for Central Africa (RMCA) in Tervuren. I wish thus to thank Director Guido Gryseels, Dr. Johan Lavreau, Prof. Luc André and Dr. Max Fernandez for their open mindedness as they gave me the opportunity to participate at numerous international congresses and to two amazing field missions.

I am deeply grateful to the General Director, Katcho Karume, the Scientific Director, Deogratias Kavotha, and all the scientists of the Goma Volcano Observatory for their precious help and availability during the January 2010 field mission in Kivu. Thanks also to Prof. Dario Tedesco from UNOPS (United Nations Office for Project Services). Thanks to Dr. Elifuraha Saria and Dr. Athanas S. Macheyeki for their help and pleasant company during the field mission in Tanzania.

I deeply thank Dr. Nicolas d'Oreye from the European Center for Geodynamics and Seismology (ECGS) and National Museum of Natural History of Walferdange in Luxembourg for many useful discussions and the access to SAR databases. Many many thanks to Benoît Smets, a friendly guy who almost began to work at RMCA at the same time as me. He helped me a lot by always sharing his discoveries and new interpretations on the Kivu area with enthusiasm. Warm thanks to Mike Poland (USGS) for the use of his amazing RADARSAT-1 database over Congo. A special acknowledgment to Dr. Damien Delvaux for his strong support during the Tanzania mission and his propensity to share interesting information on the EARS. I also thank Didier Van Aubel, Mr Fish Saumon Guy, for all the hilarious jokes and continuous emotional support during the hard moments. Thanks also to Sophie, Suzanne, Josyane, René, Anne-Catherine and all the other

friendly people met during these four exiting years at the Museum.

I thank Prof. Andy Hooper from TUDelft for his warm welcome, the great one-month training provided in InSAR time-series in Delft, and the useful discussion afterwards. From TUDelft, I also want to thank Prof. Ramon Hanssen and all the Radar Group people. Many thanks to Anneleen Oyen for her work on the modeling in Tanzania and moreover, for her nice company, the shared drinks and the Greek karaoke.

Thanks to Dr. Yo Fukushima and Prof. Jean-Luc Froger for the use of their codes and useful discussions about modeling and InSAR. Thanks also to Sergey for the processing of RADARSAT-2 data.

Sensei Pinard, who will easily recognize himself, was more than a Sensei and a source of inspiration, he is one of my best friends and I do not know what I would have done sometimes without his continuous support, great advices and friendship. Thanks a lot to my veryyyy patient parents who always have encouraged me to pursue my dreams. Thanks to my best friend Adeline, and also to Johana, Loulou, Arnaud, Massimo, the Bandidas,... Last but not least, I deeply thank Cédric who has curiously not run away from me, especially during the last very hard months of the thesis... I really love you.

Contents

List of Figures

List of Tables

Introduction

Study and monitoring of active volcanic areas in Africa can be problematic using ground-based methods, due to political tensions, security problems or difficult field accessibility. Remote-sensing techniques, particularly Synthetic Aperture Radar Interferometry (InSAR), are therefore very useful and provide robust observational tools for volcano monitoring and hazard assessment.

With the exception of the well-known and extensively studied Afar region (see, among others, studies by *Wright et al.* [2006]; *Hamling et al.* [2009]; *Keir et al.* [2011]; *Rowland et al.* [2007] and *Ayele et al.* [2009]), active areas of the East African Rift System (EARS), such as the Lake Kivu in the Democratic Republic of the Congo or Lake Natron in northern Tanzania, are poorly documented. Both areas suffer from the lack of ground-based geodetic measurements despite they are continuously affected by earthquakes and volcanic eruptions.

InSAR provides high spatial resolution low-cost measurements of ground displacements with a centimeter to sub-centimeter accuracy in favorable conditions [*Massonet and Feigl*, 1998] and over areas up to 100 km large. Nowadays InSAR is widely used to study a broad range of volcanic and seismic events (e.g. [*Bürgmann et al.*, 2000]; [*Lu et al.*, 2005]; [*Wright et al.*, 2006]; [*Yun et al.*, 2006]; [*Simons and Rosen*, 2007]; [*Fournier et al.*, 2010] and references therein).

C-band InSAR, using a radar wavelength of about 6 centimeters, can suffer from vegetation-induced temporal decorrelation [*Hanssen*, 2001], as commonly encountered in equatorial regions and in fertile volcanic areas. Yet, it is possible to overcome this issue by 1) using a large database of C-band data, with the highest temporal sampling possible, from different satellites such as ERS-1&2, ENVISAT and RADARSAT-1&2, and different viewing geometries (or beams) taken from ascending and descending orbits ; 2) using L-band sensors, characterized by a 23 centimeters wavelength, such as JERS or ALOS. A larger wavelength will indeed overcome most of the vegetation-induced temporal decorrelation, and 3) extending the capabilities of InSAR using for instance a Multi-Temporal (MT-InSAR) approach. These methods rely on large datasets to obtain high accuracy time-series deformation using pixels that are stable over long periods of time.

A large database of SAR images, from ERS and ENVISAT satellites, were acquired on the two EARS areas of interest in the framework of the SAMAAV (Study and Monitoring of Active African Volcanoes, Belgian Science Policy - Belspo - and the National Research Fund of Luxembourg Action-1 project and ESA Cat-1 project n 3224) and GORISK (funded by the Belgian Science Policy - Belspo - and the National Research Fund of Luxembourg, in the frame of the STEREO II program) projects. This rich database is complemented by several ALOS (ESA announcement of

opportunity AO3690), RADARSAT-2 (CSA SOAR project 5020) and RASARSAT-1 data (ASF and CSA project). The first aim of this thesis is to extract the most useful information with InSAR and related techniques from this large SAR database. A second purpose is to give new insights on the rift onset mechanisms and characteristics as the two areas of interest are both located in youthful and immature portions of the rift.

InSAR hence captured the displacements associated with the 2002 Nyiragongo eruption. On January 17, 2002, a system of fractures extending from the volcano to the city of Goma (15 km south of the volcano) opened. Two lava flows entered the town and forced 350,000 out of a total of 400,000 inhabitants to evacuate. About 15 % of the city was destroyed. The region around Nyiragongo area is threatened by various hazards. Firstly, the lava is known to be very fluid and able to produce rapid flows that can reach 100 km/h. These lavas were responsible for casualties during the 1977 eruption. Secondly, the eruptive fractures can reach the lake and produce phreatomagmatic eruptions. Moreover, Lake Kivu contains layers in which large amounts of dissolved carbon dioxide and methane occur. A magmatic eruption into the lake could disturb this stratification, release gas and cause a major regional disaster. The understanding of the processes involved in the eruption of the 2002 Nyiragongo eruption is therefore essential for an appropriate global hazard assessment. The hazard, combined with the vulnerability of the population, places the city of Goma and the surrounding region under very high natural risks.

InSAR captures as well ground displacements associated with several eruptions of its neighbor, the Nyamulagira volcano. This volcano, erupting on average every two to four years, is also a serious threat for the surrounding villages and the Virunga National Park. Displacements associated with two large magnitude seismic events were also measured.

To account for the complex ground deformation patterns captured by InSAR, a three-dimensional mixed boundary elements numerical modeling method (MBEM), which considers realistic topographies as well as any number of interacting pressure sources or faults, is combined with a near-neighborhood inversion method.

As we have a large database of ENVISAT and ERS-2 data from several beams and orbits configurations, we can go over a large period of ground displacements history to check if Multi-Temporal InSAR methods could give us complementary information to better constrain the previous established eruption models, or undetected eruptions or magmatic activity, as well as the rift dynamics. Furthermore, spanning long periods of time allows us to have a global view of the volcanoes dynamics rather than simply look at single eruption snapshot. Such time-series methods can indeed help to find common features between eruptions, study volcanoes endogenous growth or identify eruptive cycles for instance.

To better constrain the numerical models and check some deformation signals identified by InSAR on the ground, two field missions were done during this thesis. The first one took place in October 2007, just after a major seismic swarm which affected the Lake Natron area on the southern flank of the dormant Gelai volcano, neighbor of the famous Oldoinyo Lengai volcano. Interferograms covering the event shows an impressive graben structure a few kilometers wide and more than ten kilometers long. Field measurements were made along this structure and gathered during the field mission and subsequent interpretations permitted an accurate modeling of the available InSAR data which leads to several important publications, including one in Nature [*Calais et al.*, 2008]. The second one was made in January 2010 in the North Kivu

area. This second mission strongly helped to check hypothesis made for the Nyiragongo 2002 modeling and to confirm the presence of two main fractures trends in the city of Gisenyi, which were identified as being reactivated on an interferogram spanning the January 2002 Nyiragongo eruption. Finally, the Nyamulagira was erupting during the field mission, and major information were thus gathered mainly thanks to helicopter flights provided by MONUC (United Nations Organization Stabilization Mission in the Democratic Republic of the Congo) to help the modeling of the 2010 eruption.

The first chapter provides a review of the East African Rift Systems, the rifting mechanisms and presents the setting of the two areas studied, the Lake Kivu and Lake Natron areas. The main challenges of the study in the given context are also given in this chapter.

The radar remote-sensing and SAR interferometry basis are first explained in the Chapter 2. Two extensions of the conventional InSAR are then described, the Multi-Temporal InSAR with a special focus on the StaMPS package and the POLInSAR approach.

The third chapter explains the modeling and inversions methods in details. Uncertainties and parameter trade-offs are also used to investigate which dike parameters are better determined by inversions and how the determination is improved by combining data from several beams.

The InSAR results obtained for several eruptions and seismic events which occurred in the Lake Kivu area are after presented in Chapter 4. The seismic or volcanic events which were covered by sufficient data are also modeled with the 3D-MBEM approach.

Chapter 5 presents the results obtained again for the Lake Kivu area applying the StaMPS PS, SBAS or combined approach. In a first part, the ENVISAT data from seven different beams are used for characterizing the ground displacements which occurred during the December 2003 - April 2010 time period. In a second part, ERS-2 data are processed with the same tools to extend the time period back to June 1997.

The Tanzania field mission results are detailed and interpreted in Chapter 6 with the constrains on the subsequent modeling studies highlighted.

Finally, the Chapter 7 includes a broad discussion mainly focuses on the Lake Kivu area volcanic, magmatic and seismic activity. New hypothesis for the rift dynamics and its link with the volcanism in this area are further presented and compared with the Natron and other published studies.

Chapter 1

Geological Background

In this Chapter, the overall morphology of the East African Rift System (EARS) is presented. Then, models for its development are given, from tectonic and magmatic points of view. Two areas of the EARS rae described here. They are located in regions where the rift is youthful and immature: the Natron area (in northern Tanzania) and the Virunga area (in North Kivu, Dem. Rep. of Congo), situated in the western and the eastern branches of the rift, respectively. They will be studied in details in the next chapters with the aim to give new insights on the rift onset mechanisms and characteristics.

1.1 The East African Rift System (EARS)

1.1.1 Overall Morphology

The East African Rift System (EARS) is a volcanically and seismically active intra continental region undergoing the early stage of an ocean opening (Figure 1.1). This large scarp, lying above the East African Plateau, a broad intracontinental swell [*Ebinger*, 1989a], has two main branches: the eastern rift and the western rift branches (Figure 1.2). The EARS is formed at the surface by the alignment of several thousands kilometers of successive tectonic basins or rift valleys, limited by uplifted topographic features. Each basin is generally a subsiding, about one hundred kilometers long and a few tens kilometers wide, (half-)graben controlled by border and associated secondary normal faults, and filled by sediments and/or volcanic deposits. Strike slip faults sometimes accommodate transfer zones between two successive basins [*Ebinger and Furman*, 2002 - 2003] [*Chorowicz*, 2005]. The EARS is a depression bounded by high reliefs and mountainous areas on the two sides. Volcanoes can develop in and outside the rift, magma finding easily its way to rise through pre-existing weakness tectonic features. The EARS is characterized by a serie of complex tectonic settings with generally normal faults forming the (half-)grabens, but also sometimes with strike-slip faults in accommodation (transfer) zones between two successive basins [*Ebinger and Furman*, 2002 - 2003] [*Chorowicz*, 2005]. A given fault may record various type of movements depending of the stress regime.

Most of the great African lakes lie along the EARS, with the exception of the Lake Victoria which is located in the old stable rocks of the Tanzanian craton, between the two rift branches

(Figure 1.2). The eastern branch runs from the Afar triple junction to the north, through the Main Ethiopian Rift (MER), Turkana, Kenya (Gregory) rifts, the basins of the North Tanzanian divergence, and joins the western branch in the Rungwe region to the south. The western branch runs from the Lake Albert to the north, through the Lake Edward, Kivu, Tanganika, Rukwa, the Rungwe region to ends in the Lake Malawi area to the south [*Chorowicz*, 2005] [*Ruppel*, 1995].

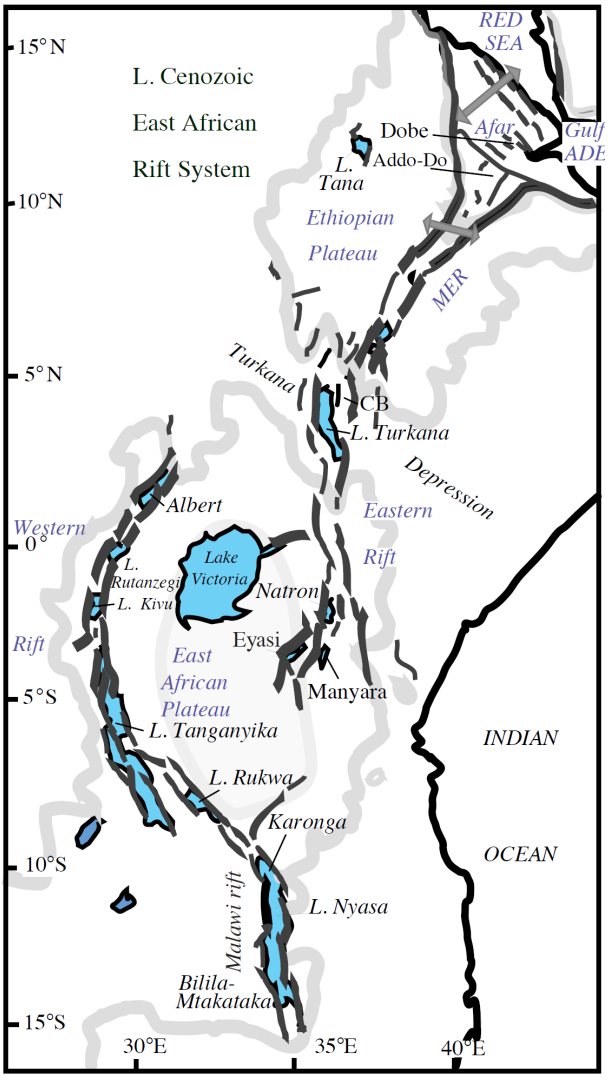

Figure 1.1: The East African Rift System. Plateau standing above 1000 meters are entoured by bold shaded lines. Grey arrows show extension direction in the Afar and Main Ethiopian rifts (MER). CB is Chew Bahir Basin. After [*Ebinger et al.*, 1999]

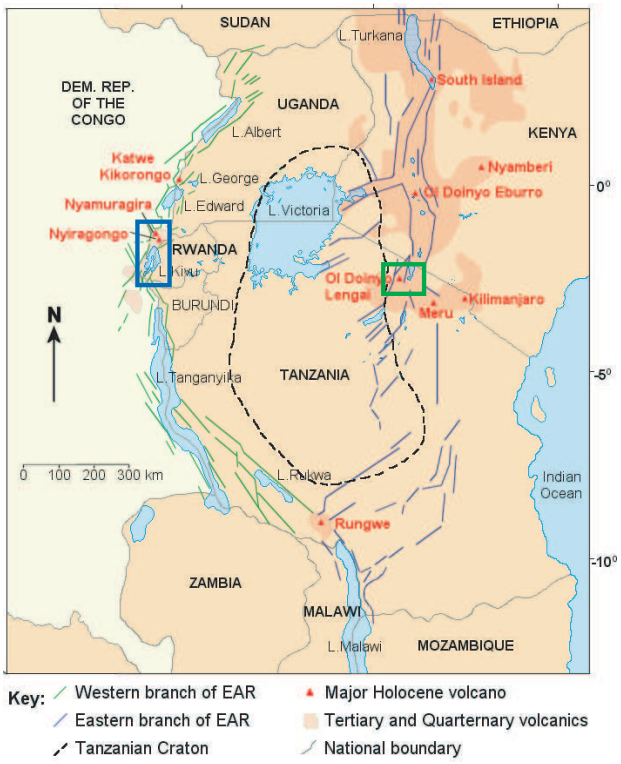

Figure 1.2: The two branches of the EARS and main Holocene volcanoes, modified after [*Colclough*, 2005]. The Natron area (Figure 1.5) is green-squared, while the Kivu area (Figure 1.6) is blue-squared

1.1.2 Rifting Models

As evidenced by theorical and numerical modeling studies, interactions of the lithosphere with a dynamic astenosphere, inducing intrusive heating or stretching, lead to a mechanical weakening of the lithosphere and to a subsequent continental break-up. During the early rifting stages, the thermal and mechanical properties of the lithosphere mainly impose the strain distribution [*Bassi*, 1995] [*Buck*, 2004]. The yield strength of the lithosphere determines the along-axis segmentation [*Ebinger*, 2005], i.e. the size of the successive kinematically linked rift basins, the length and depth of the faults and the relief of the rift shoulders [*Hayward and Ebinger*, 1996].

Two classes of continental break-up models are distinguished (Figure 1.3): tectonic-driven models involve a pure mechanical stretching of the lithosphere [*McKenzie*, 1978] [*Dunbar and Sawyer*, 1989], while the magma-driven models include a magmatic component in an astenosphere-lithospheric coupled model [*Buck*, 2004]. The strain extension is localized differently in the two models as the rifting progresses to seafloor spreading. In tectonic-driven models, the strain is accommodated by large offset faults in brittle layers and ductile deformation in other layers. On the opposite, in magma-driven models, the faults, have small offsets, and are located above areas of magma supply which accommodates the strain. Magma penetrates the bottom of lithosphere, which is more ductile, and feeds dikes that intrude the stronger upper part of lithosphere. The plate strength is reduced (heat transfered by magma) as the rifting progresses, and new upper areas behave now more in a ductile way, allowing thus the magma to intrude at shallower levels than previously. Magma supply promotes rifting at lower plate-driving stresses than faulting as melt in buoyant. Therefore, break-up is easier when magmatism is involved (magma-driven rift). In active rifts, hybrid models between tectonic-driven and magma-driven rift models could likely

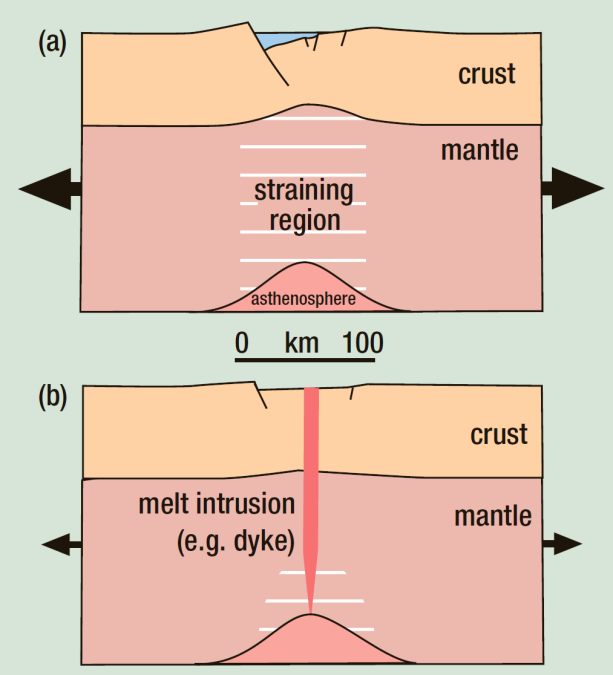

Figure 1.3: Conceptual models for an extensive rheologically layered continental lithosphere: a) fault-controlled or tectonic-driven and b) magma-driven lithosphere stretching. After [*Ebinger*, 2005]

be closer to reality [*Ebinger*, 2005].

Four characteristics help to define the vertical and horizontal crustal movements evolution and break-up: 1) the lithospheric strength which can be deduced from rock mechanic experiments, 2) the volume of magma added to the plate, obtained through seismic, geodetic, geochemical, gravity and magnetotelluric studies, 3) the degree and distribution of mechanical stretching estimated from the geometrical analysis of the faults and comparison between stretched and adjacent unstretched lithosphere, and 4) the recent strain rate which can be derived from geodetic data such as GPS, study and modeling of earthquakes and fault-slip. Older strain rates could be much more speculative to infer [*Ebinger*, 2005].

1.1.3 The EARS Development

The EARS architecture can be defined from its structural and magmatic components [*Ebinger and Furman*, 2002 - 2003]. The EARS lies above two main plateaus: the ≈ 1000 m high East African plateau, and the ≈ 2500 m high Ethiopia-Yemen plateau (Figure 1.1). The latter has indeed accumulated 2 km of volcanic material erupted over the plateau region between 45 and 25 Ma, with the largest volume (trapps) extruded simultaneously with the opening of the Red Sea and Gulf of Aden [*Wolfenden et al.*, 2005]. These two plateaus could be actually part of a larger uplift area extending from southern Africa to the Red Sea, as evidenced by the Turkana depression (Figure 1.1) which is a failed Mesozoic rift system [*Nyblade and Robinson*, 1994].

Above the hot astenosphere, uplifts and volcanic extrusions developed, as evidenced by the last decade geophysical and geochemical data. However, the location, depth extent and continuity of the hot astenosphere are not well constrained because of data gaps and limited resolution of tomographic models [*Montelli et al.*, 2004]. The large African plate is moving slowly towards

NNW with respect to the lower mantle velocity anomaly located presently below southern Africa. Along the western and eastern branches of the EARS, the volcanism and rift extension propagate from the north towards the south because of the NNW motion of the African plate. However, the uplift timing of the plateaus is not well constrained [*Ebinger*, 2005]. Thermochronology studies indicate that the uplift of the Ethiopian plateau is likely to have occurred at 30 - 35 Ma, as well as the eastern part of the East Africa plateau [*Pik et al.*, 2003]; [*Noble et al.*, 1997].

Of all the major plate boundaries, the EARS kinematics are the least well constrained. *Stamps et al.* [2008] propose a kinematic model including three subplates between Nubia and Somalia. An 3.2 Ma-average spreading rate and transform fault offsets along the southwest Indian Ridge are inferred from GPS data and earthquake slip vectors. The directions of extension are roughly EW varying spatially along the rift, depending of the plate involved. Strain in the EARS could be localized along narrow rift structures which isolate large lithospheric blocks. The angular plate velocities found by *Stamps et al.* [2008] predict an opening at a rate of 1 to $4mm/yr$ across the western and eastern branches, increasing from north to south for the former, and from south to north for the latter. As the eastern branch propagates into the Tanzanian craton, the extension rate along the Eastern branch decreases towards south, and is consistent with a progressive disappearance of prominent active faults. These calculations correlate with the age of the rifting onset, which is from $12 - 15$ Ma to 8 Ma from the north to the south along the western branch, and 5 Ma to the present for the eastern branch [*Ebinger*, 1989a].

Figure 1.4 illustrates the three typical different stages of the rift development described in *Ebinger* [2005]. Each part of the EARS can be categorized in one of these three rifting stages to trace the distribution of strain and magmatism as rifting progresses to seafloor spreading.

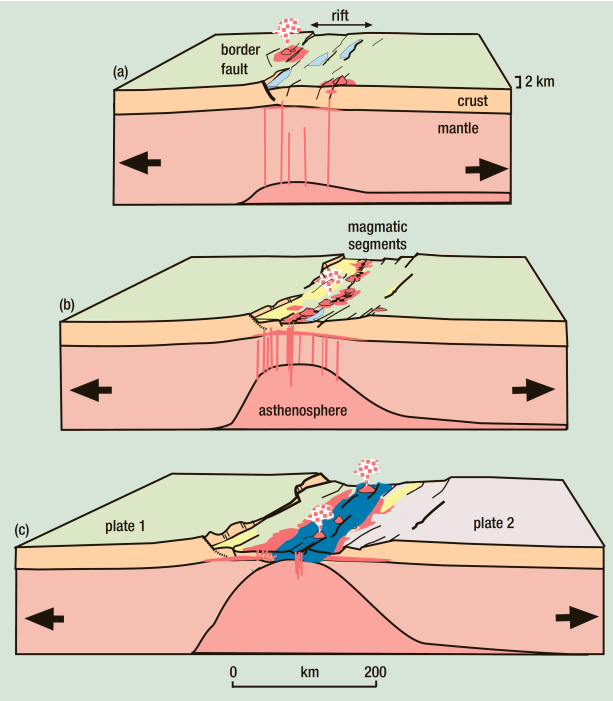

Figure 1.4: Three-stage model for continental break-up, after [*Ebinger*, 2005]

Stage a): 0-5 Ma

The layered lithosphere begins to thin through brittle and ductile deformation ≈ 0 to 5 Ma after the rifting onset. A decompression melting occurs because the thinning lithosphere is replaced by astenospheric buoyant plumes, leading thus to a heat transfer. Magma is accreted at a boundary between the crust and the mantle, but a small volume is able to rise up to crustal level, building volcanoes. At the bottom of the plate, magmatic fluids can modify and melt rocks. In the brittle crust, deformation is accommodated by slip along border or detachment faults, while the opposite side of the tectonic basin accommodates such movements by bending. The asymmetry of the basin is enhanced by the lithostatic rebound and changes in layers thickness. The onset of rifting (Figure 1.4a) occurs in cold and again strong continental lithosphere.

In the EARS, this sequence can be observed in the western branch, in the Lake Kivu area for instance (Figure 1.6), but also in the southern part of the eastern branch in the Lake Natron area, Tanzania (Figure 1.5), this latter area is indeed less than 5 Ma old. Extensional cracks and faults can develop at the surface as the plate-driving forces induce a pull on the thick plate. Pre-existing weakness areas, such as the boundary between the oldest 3 Ga Tanzanian craton and the thinner 0.5 Ga old lithosphere to the east [*Foster et al.*, 1997], could guide the faults location, but new faulting trends can also be created. The fact that the EARS divide itself in the two branches could be explained by the presence of the stable, strong, cold and thick Tanzanian craton. It is indeed easier, mechanically-speaking, to bypass it than to break it. [*Ebinger*, 2005]

Stage b): 10-15 Ma

The lithosphere thins with time, accommodating increasing strain by faulting and ductile deformation. More and more melting occurs as the astenosphere rises to shallower crustal levels. Magma rises up to the surface forming fault-parallel cracks. A magmatic segment forms where the intrusions occurred. The detachment faults are inactive as the magma supply accommodates strain at lower tectonic stresses that faulting.

This stage of rifting (Figure 1.4b) can be observed in the Main Ethiopian Rift (MER), in the northern part of the EARS (Figure 1.1). Voluminous volcanic eruptions (Ethiopian traps) deeply modified the plate beneath the uplifted plateau. Rifting in the MER began at 11 Ma, with a narrowing of the deformation area and the onset of slip on border faults often associated with volcanic centers. The MER magmatic segments are roughly 60 km long, 20 km wide, marked by aligned volcanoes, fissures and short faults in the central basin. The magmatism and faulting are more localized since 1.8 Ma [*Ebinger and Casey*, 2001]. Presently, strain is accommodated by repeated intrusions which are mainly aseismic. In the 10 kilometers of the seismogenic crust above the intrusions, small offset faults and dikes accommodate the strain [*Keir et al.*, 2006]. If the magma supply and/or the strain rate increase again, a new oceanic lithosphere will be created in the magmatic segments, and the underlying mantle lithosphere and thick crust will begin to subside below sea level; the rift entering in stage c) (Figure 1.4c) [*Ebinger*, 2005].

Stage c): Seafloor spreading

When the thinned lithosphere breaks-up, a new oceanic crust is created, and the passive margin subsides below sea level as the heat is transferred from the astenosphere. Rifting is entered in

stage c), the seafloor spreading, in parts of the Red Sea rift, and along the length of the Gulf of Aden rift [*Ebinger*, 2005].

1.2 Focus on the Eastern Branch: the Lake Natron Area

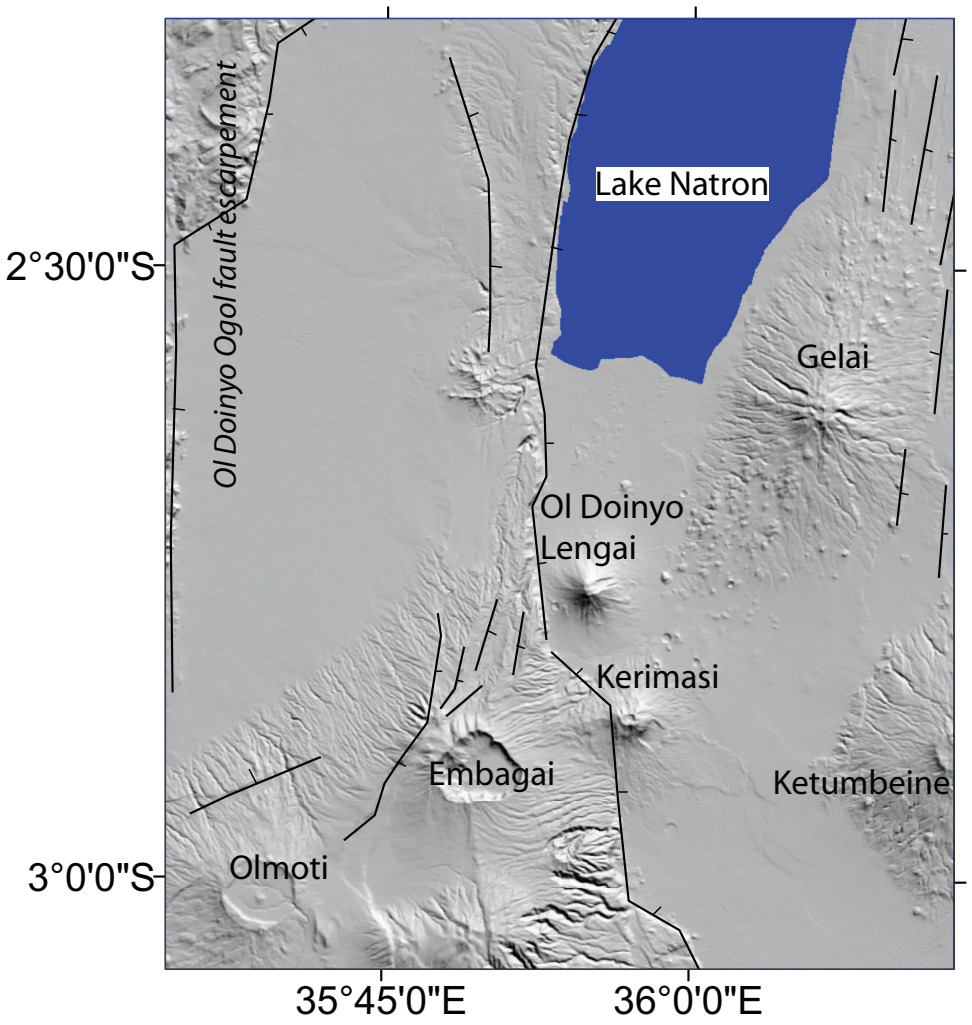

Figure 1.5: The Lake Natron area. Black lines are normal faults after [*Foster et al.*, 1997] [*Dawson*, 1992] [*Wiedenmann*, 2003]

On the opposite to the western branch, the eastern branch of the EARS is characterized by a moderate seismicity and the presence of many volcanoes. The eastern branch is ≈ 50-80 km wide to the north and 200 km wide to the south. With current far-field extension rates of the order of 3 to 4 mm/yr [*Stamps et al.*, 2008], the eastern branch has experienced only a few kilometers of crustal thinning [*Birt et al.*, 1997], with a lithospheric thickness of 90 km close to the 125-km-thick lithosphere outside the rift [*Green et al.*, 1991] [*Nyblade et al.*, 2000].

The 5 Ma old Natron basin lies near the southern termination of the eastern branch, the divergent boundary between the Somalian and Nubian plates. Alkaline and basaltic volcanism coexisted with initial faulting [*Ebinger et al.*, 1997]. The Natron basin is an asymmetrical facing-

East half graben [*Foster et al.*, 1997]. The 120 km long western border steep escarpment of the rift in this region is the Ol Doinyo Ogol escarpment (Figure 1.5). Closer to the lake, a second system of major normal faults creates a second escarpment [*Foster et al.*, 1997] [*Dawson*, 1992].

Figure 1.5 shows that the area includes several volcanoes. The Ol Doinyo Lengai is the youngest active volcano in North Tanzania and is the only active volcano on Earth emitting natrocarbonatite lavas. It is a 2962 m high active strato-volcano characterized by a dominant effusive activity from small cones on the crater floor producing low ($\approx 510°$) temperature, very fluid lavas [*Dawson et al.*, 1990]. It actually started growing after a major faulting period which formed the Natron basin approximately 1 Ma ago [*Foster et al.*, 1997] [*Dawson*, 1992]. Gelai shield volcano, 2942 m high, is considered as a dormant volcano, as there have been no eruptions for at least 10,000 years. The flanks of this volcano are covered by dense vegetation. They are very rough and less steep than those of the Lengai volcano.

1.3 Focus on the Western Branch: the Lake Kivu Area

The western branch of the EARS is characterized by an en echelon[1] succession of 40-70 km-wide grabens and half-graben basins in 100 km-long segments, often filled by water to form lakes [*Ebinger*, 1989b] [*Ebinger et al.*, 1991] [*Ebinger and Furman*, 2002 - 2003]. It is indeed here that the deep and anoxic[2] African Great Lakes are nested [*d'Oreye et al.*, 2010]. The rift is bordered by high-angle normal fault systems, dipping at angles between 40° and 60° [*Zana and Hamagushi*, 1978] [*Shudofsky*, 1985], bounding one side of spoon-shaped basins. Planar border faults along one side of the rift basins probably penetrate the crust, as suggested by the depth-to-detachment estimation of 20-30 km, the rollover geometry of the asymmetric basins, and an active seismicity in a 0-30 km depth range [*Ebinger*, 1989a].

Successive basins are linked by accommodation zones, which are areas characterized by oblique-slip transfer faults. Volcanism began at $\approx$ 12 Ma in the north and at $\approx$ 7 Ma in the south before, or simultaneously with, the development of western branch sedimentary basins. The progressive hanging-wall collapse and uplift of the rift flanks during Pleistocene time have narrowed the asymmetric basins [*Ebinger*, 1989a]. This rift development is close to the more magmatically active Kenya rift, where the volcanism began 11 Ma (before the initial volcanism in the western branch). Initially isolated basins are now linked through the north to south propagation of western branch border-fault segments. The segmentation of the western branch is promoted by this along-axis propagation [*Ebinger*, 1989a].

In contrast to the widespread volcanism observed in the Eastern, or Gregory (Kenyan) Rift System, volcanic provinces in the Western Rift are volumetrically small, hence a large majority of the western branch lacks magmatism. Four volcanic regions comprise the Western Rift; from north to south these are the Toro-Ankole area in western Uganda, the Virunga and South-Kivu provinces along the borders of the Democratic Republic of the Congo, Rwanda, Burundi and southern Uganda, and the Rungwe area in southwestern Tanzania (Figure 1.2). All of these four provinces are characterized by silica-undersaturated mafic volcanism and the local development

[1] en echelon features (fissures, faults,...) are features that are parallel in trend to each other, but offset to either the left or right

[2] Anoxic waters are areas of sea water or fresh water that are depleted of dissolved oxygen

of evolved products from centralized volcanic edifices. Volcanic products are locally hyper-sodic and ultra-potassic, and also include diverse products such as tholeiites (Kivu) and carbonatites (Toro-Ankole) [*Ebinger and Furman*, 2002 - 2003].

1.3.1 The Kivu Basin

The Kivu basin is constituted of two half-graben basins linked across the rift valley by a horst that serves as a hinge for subsidence in both basins. The Idjiwi horst, $\approx$ 700 m a.s.l, probably extends north of Idjiwi Island (Figure 1.6) to the northern end of the Lake Kivu, as suggested by seismic reflection data from Lake Kivu [*Wong and Herzen*, 1974]. The western side of the Lake Kivu is bounded by a steep border fault escapement larger than 1500 m high, limiting a basin filled with up to 500 m of sediments and of basalts derived from the Virunga Volcanic Province (VVP, Figure 1.6) to the north [*Wong and Herzen*, 1974].

The eastern rift escarpment is less marked [*Ebinger*, 1989b]. Field observations indicate that the western border fault served as the master fault for crustal extension during Quaternary time [*Ebinger*, 1989b]. A second volcanic province, the South Kivu Volcanic Province (SKVP, Figure 1.6) lies in a transfer accommodation zone between the Kivu Basin and the Rusizi basin to the south [*Ebinger*, 1989b].

1.3.2 The Virunga Volcanic Province

High-angle (50° - 70°) east-dipping faults border the western margin to the north of Kivu basin (Figure 1.6 and 1.7) [*Pouclet*, 1977]. The Virunga Volcanic Province lies within an accommodation zone where northwest-striking fissures, marked by active shield volcanoes, crosscut the rift valley [*Ebinger*, 1989a]. The spatial distribution of basalt flows within the Virunga Volcanic Province suggests that initial volcanism at 12.6 Ma preceded or was simultaneous with initial faulting and basin subsidence [*Bellon and Pouclet*, 1980].

The Virunga Volcanic Province, which has approximately 50 km of total extension and lies within the Virunga National Park covering an area of 7900 km^2, including eight large volcanoes, which are from the east to the west (Figure 1.6): the stratovolcanoes Muhavura (4,127 m), Gahunga (2,474 m), Sabinyo (3,647 m), Visoke (3,711 m), Karisimbi (4,507 m), Mikeno (4,437 m) and Nyiragongo (3,470 m), and finally the shield volcano Nyamulagira (3,058 m).

Of these volcanoes only Nyamulagira and Nyiragongo have recently erupted. Brief eruptions of Visoke occurred in 1957, and Mihaga (a cone of Nyamulagira) in 1954 [*Guern*, 1987]. Nyamulagira and Nyiragongo are characterized by effusive activities, i.e. Strombolian and Hawaiian activities. Both aa and pahoehoe lava flows can be generated during their eruptions. Lavas have K-rich basaltic compositions, i.e. a low silica content [*Rogers et al.*, 1998], and thus low viscosities. Thus, the lava flows are very thin and often flow tens of kilometers from the source vent. *Kasahara et al.* [1991] assumed a mean thickness of 3 m for the historical lava flows of Nyamulagira; while the steeper slopes of Nyiragongo induce in thinner flows.

The Nyamulagira Volcano

Nyamulagira (or Nyamuragira in Kiniarwanda) is Africa's most active volcano, with one eruption every 2-4 years [*Smets et al.*, 2010c]. Nyamulagira is a shield volcano (Figure 1.8).

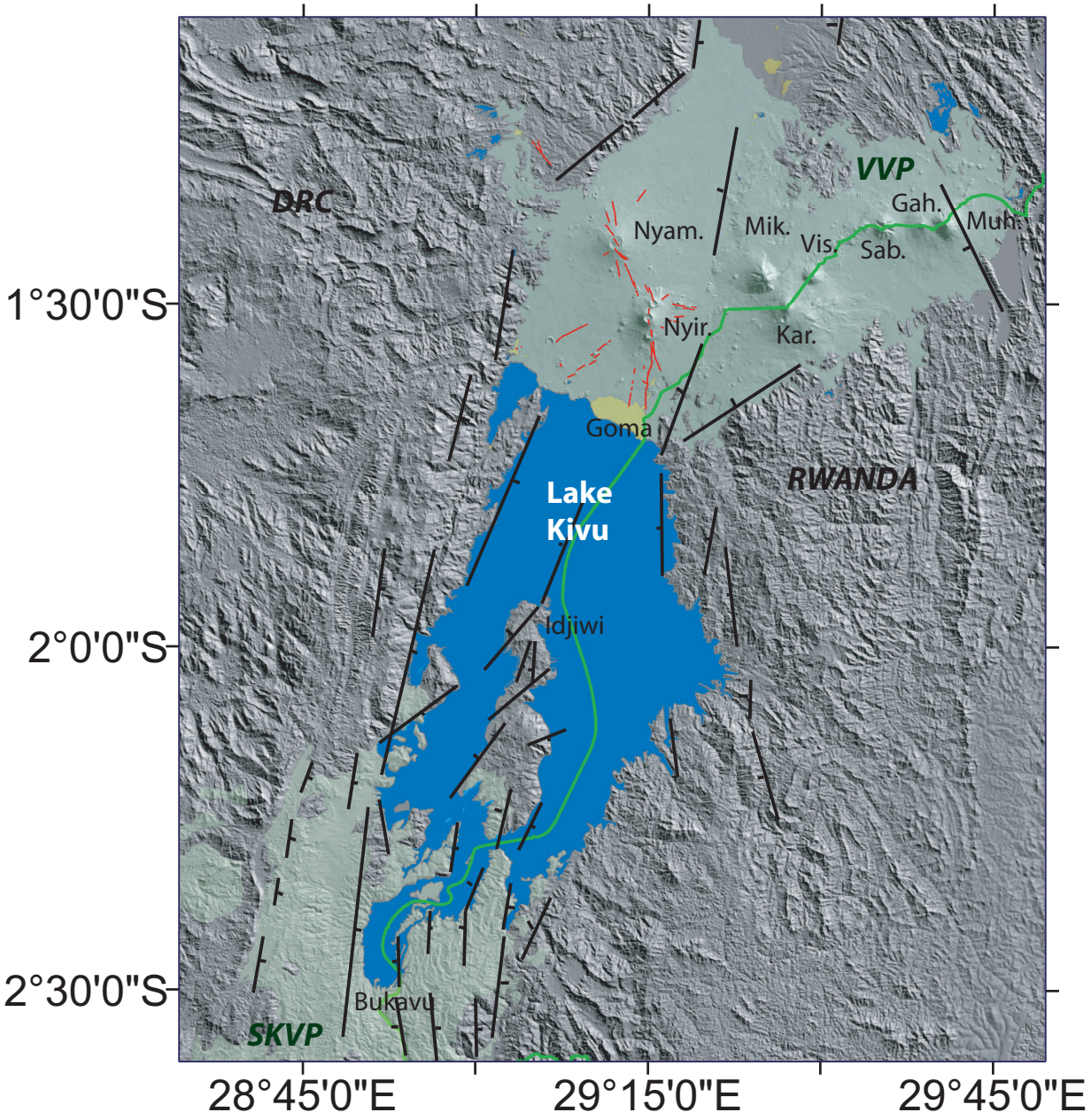

Figure 1.6: The Lake Kivu area. Black lines are normal faults after [*Villeneuve*, 1980] [*d'Oreye et al.*, 2010]. Red lines are volcanic features in the Nyamulagira-Nyiragongo volcanic fields. Nyam. = Nyamulagira, Nyir. = Nyiragongo, Mik. = Mikeno, Vis. = Visoke, Kar. = Karisimbi, Sab. = Sabinyo, Gah. = Gahunga, and Muh. = Muhavura. VVP = Virunga Volcanic Province and SKVP = South Kivu Volcanic Province.

Cone and eruptive fissure distributions at Nyamulagira and Nyiragongo follow the NE trend, but also a NNW-trending fracture network, which may be due to the stress field generated by the interplay between the magmatic systems of both volcanoes [*Gudmundsson and Andrew*, 2007] or to the reactivation of Precambrian basement faults (Figure 1.9) [*Smets et al.*, 2010a]. The main edifices of Nyamulagira and Nyiragongo are located at the intersection between the two trends, and the main volcanic seismic events recorded in the area occur along this trend [*Kasahara et al.*, 1992]. An aseismic area from 3.5 to 7 km beneath the Nyamulagira edifice is interpreted by *Hamaguchi and Zana* [1983] as a magmatic reservoir.

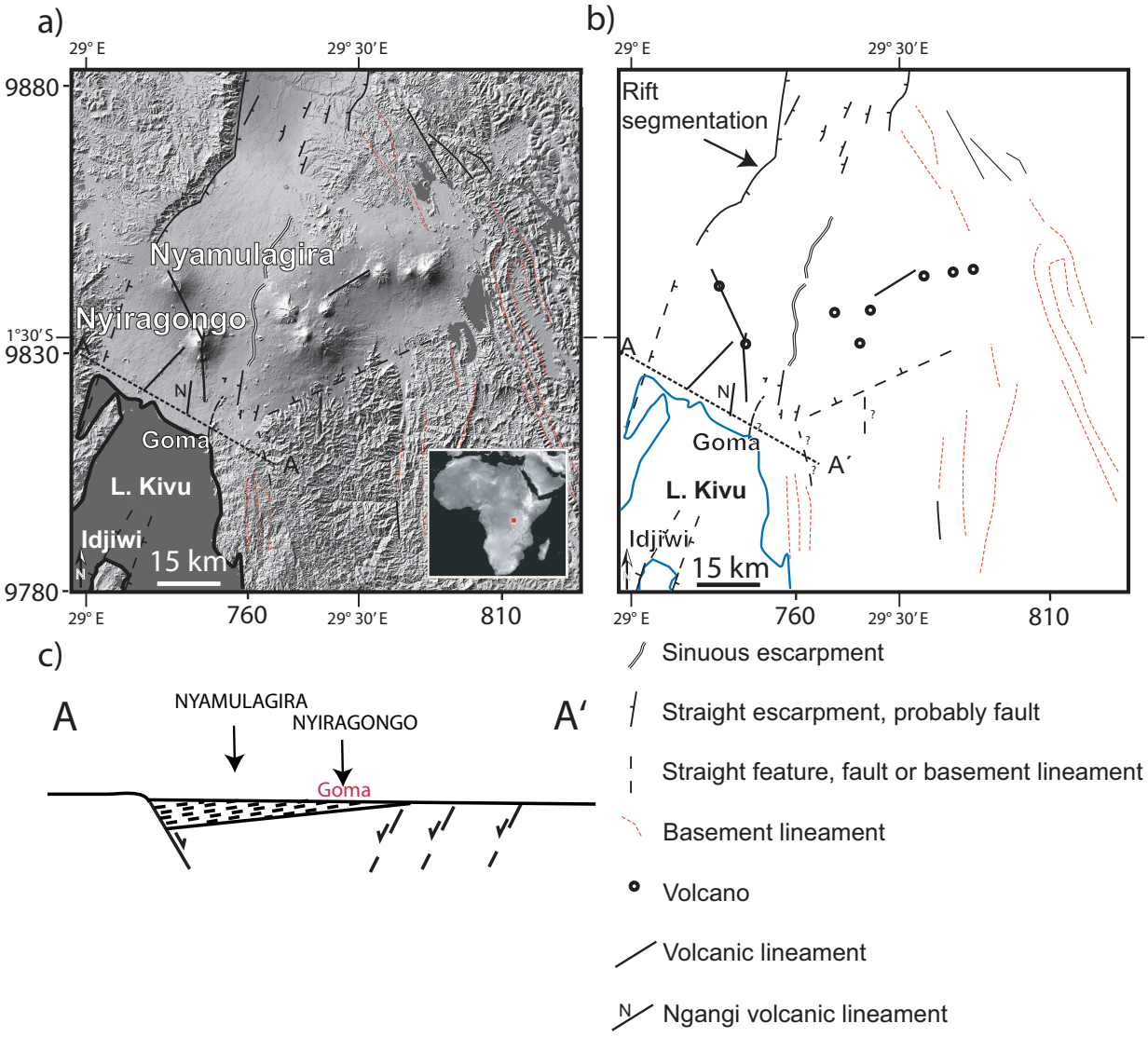

Figure 1.7: Tectonic setting of the Nyiragongo area. a) Shaded relief topographic map of north Kivu indicating the locations of the Nyiragongo and the Nyamulagira volcanoes. b) Main tectonic and volcanological features of the area. c) Schematic AA' profile: the rift is most likely a half-graben with a marked normal fault on the western side and no clear normal bounding fault on the eastern side.

The Nyamulagira summit is characterized by a $\approx$ 2 km radius summit caldera that has walls up to about 100 meters high (Figure 1.10) crossed by numerous fractures, with a 440 m wide pit crater, about 90 meters deep, in its NE part and large depression in its SW half part, about 60 meters deep (Figure 1.11), resulting from a collapse during the eruption of 1938-40. Concentric fissures are visible on the upper eastern flank of the caldera (Figure 1.12), and probable thus indicate an on-going eastern flank collapse.

The NNW-trend fracture network linking the Nyamulagira's and Nyiragongo's volcanoes starts actually from inside the caldera as showed by the Figure 1.13 (up) where this trend is clearly visible, with a clear western scarp prolongating inside the caldera. Furthermore, on the upper southeastern flank (Figure 1.13 (down)), the fractures network is actually a graben structure, with a highest western escarpment. This graben feature could be the surface expression of the tensile stresses induced above the deep dike as it has been observed worldwide [*Rubin and*

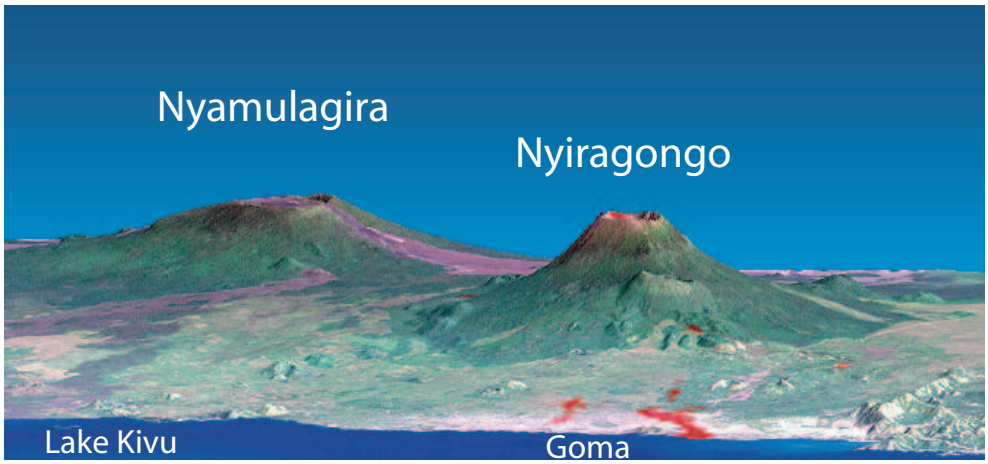

Figure 1.8: Image combining a Landsat satellite image and a digital elevation model from the Shuttle Radar Topography Mission (SRTM). The shield volcano Nyamulagira is in the background on the left and the steep stratovolcano Nyiragongo on the right. Lake Kivu is in the foreground, and the city of Goma has a light pink speckled appearance along the shoreline. Nyiragongo peaks at about 3,470 meters elevation and stands 2,000 meters above Lake Kivu. Topographic expression has been exaggerated vertically by a factor of 1.5 for this visualization (image credit: NASA/JPL/NIMA).

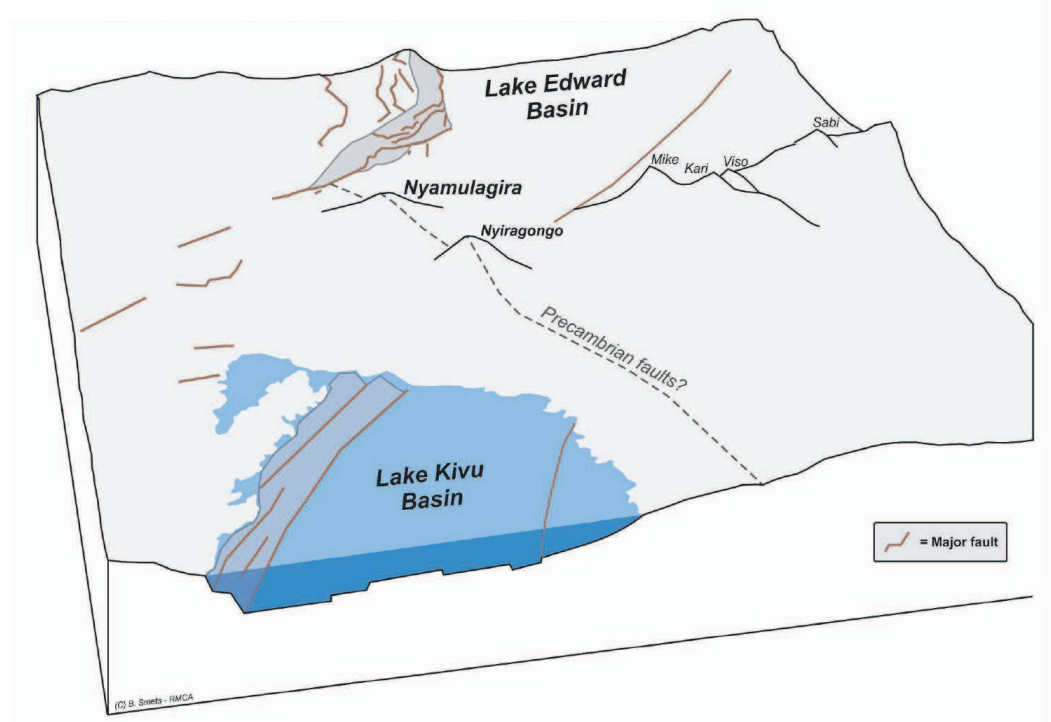

Figure 1.9: 3D-view of the transition zone between Lake Edward and Lake Kivu basins. Nyamulagira and Nyiragongo volcanoes are located in the transition zone, along a NNW-SSE fracture network which seems to correspond to an inherited Precambrian basement structure, after [*Smets et al.*, 2010a].

Pollard, 1988]; [*Rubin*, 1992].

After the voluminous and long 1938-1940 eruption, volcanic activity of Nyamulagira was dominated by lower flank eruptions, whereas the following eruptions are mainly concentrated

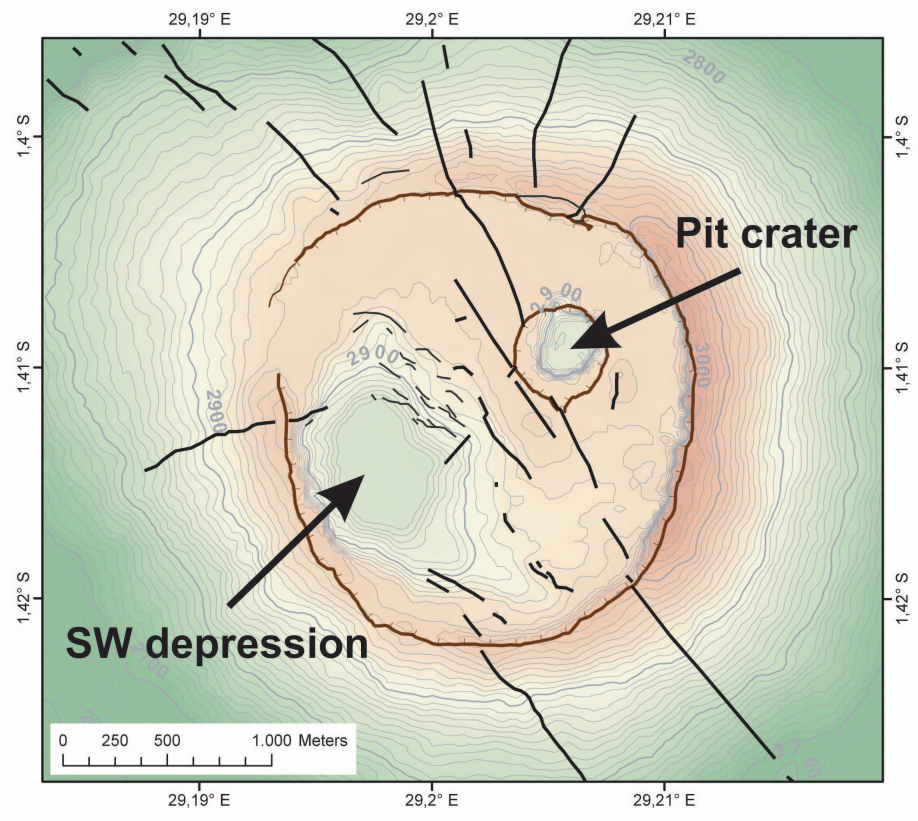

Figure 1.10: The summit caldera of the Nyamulagira with its NE pit crater (depth ≈ 90 m), and the SW depression (depth ≈ 60 m) probably created by a roof shallow reservoir collapse during the major 1940-48 eruptions. Each isoline represents 10 meters of elevation change. After *[Smets et al., in prep.]*

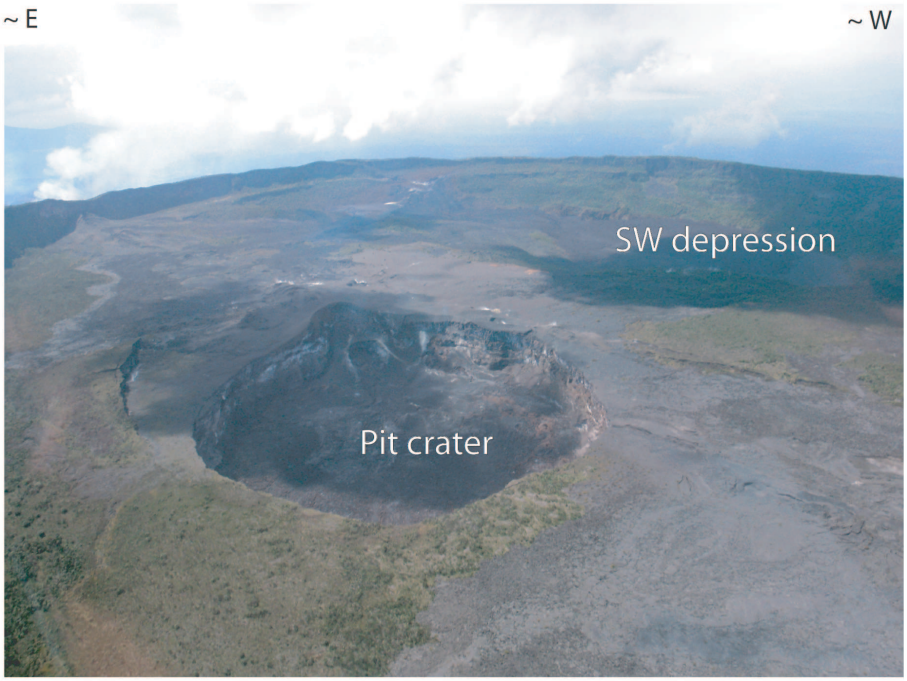

Figure 1.11: The summit caldera of the Nyamulagira viewed from the north, picture taken on January 17, 2010.

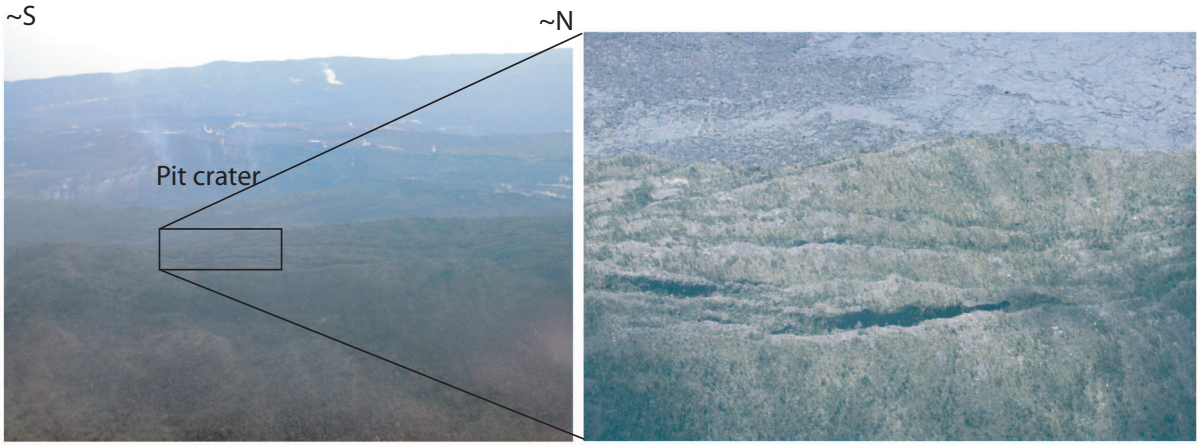

Figure 1.12: Eastern upper flank of the Nyamulagira viewed from the east (pictures taken on January 17, 2010, and right picture is courtesy of Benoît Smets).

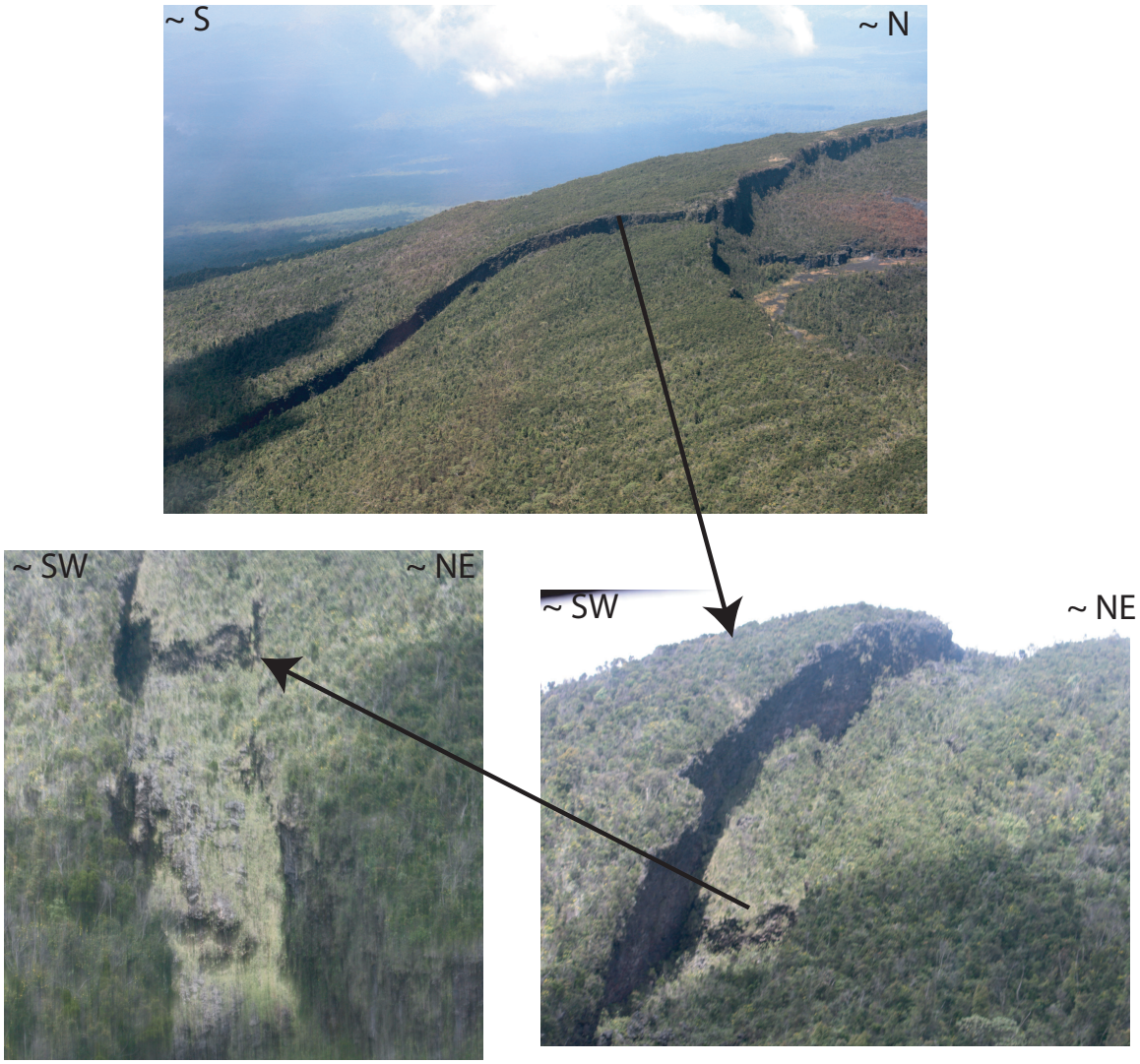

Figure 1.13: Southeastern upper flank of the Nyamulagira (pictures taken on January 25 and courtesy of Benoît Smets).

along the NNW-SSE fracture network, in the upper flanks and in the caldera [*Smets et al.*, 2010a] (Table 1.1). Nyamulagira eruptions generally induced localized ground deformation on its flanks, with less than 5 km^2 of total extension from the eruptive fissures and vents [*Colclough*, 2005] [*Wauthier et al.*, 2009] [*Wauthier et al.*, 2010], with the exception of the 2006 eruption, which occurred further on the low southern flank, had no summit activity [*Tedesco et al.*, 2007b], and generated a 20 km^2 ground deformation area [*d'Oreye et al.*, 2008] [*Cayol et al.*, 2010] extending toward the neighboring Nyiragongo volcano.

Lava flows from eruptions in 1938-2010 were mapped with both optic and radar satellite imagery and compiled into a GIS database together with data from other sources, such as maps, geo-databases, publications, unpublished notes and field data. The Figure 1.14 shows the new map of Nyamulagira combining data from the two remote sensing techniques, optical and radar, and from the literature.

Nyamulagira's lava field covers over 1100 km^2 and contains more than 100 flank cones. Lavas are basic, SiO_2-undersaturated and K-rich [*Kampunzu et al.*, 1982] [*Aoki and Yoshida*, 1983] [*Aoki et al.*, 1985]. Such a composition results in very low viscosity lavas able thus to flow for tens of kilometers. Nyamulagira's eruptions can pose a non-negligible hazard for local populations and their environment. Coupled with deforestation, political and social unrest as well as important demographic and urban growth, the potential risk/impact from Nyamulagira's volcanic hazards increases accordingly. Villages, roads and the protected forest of the Virunga National Park (VNP) are under the threat of volcanic eruptions.

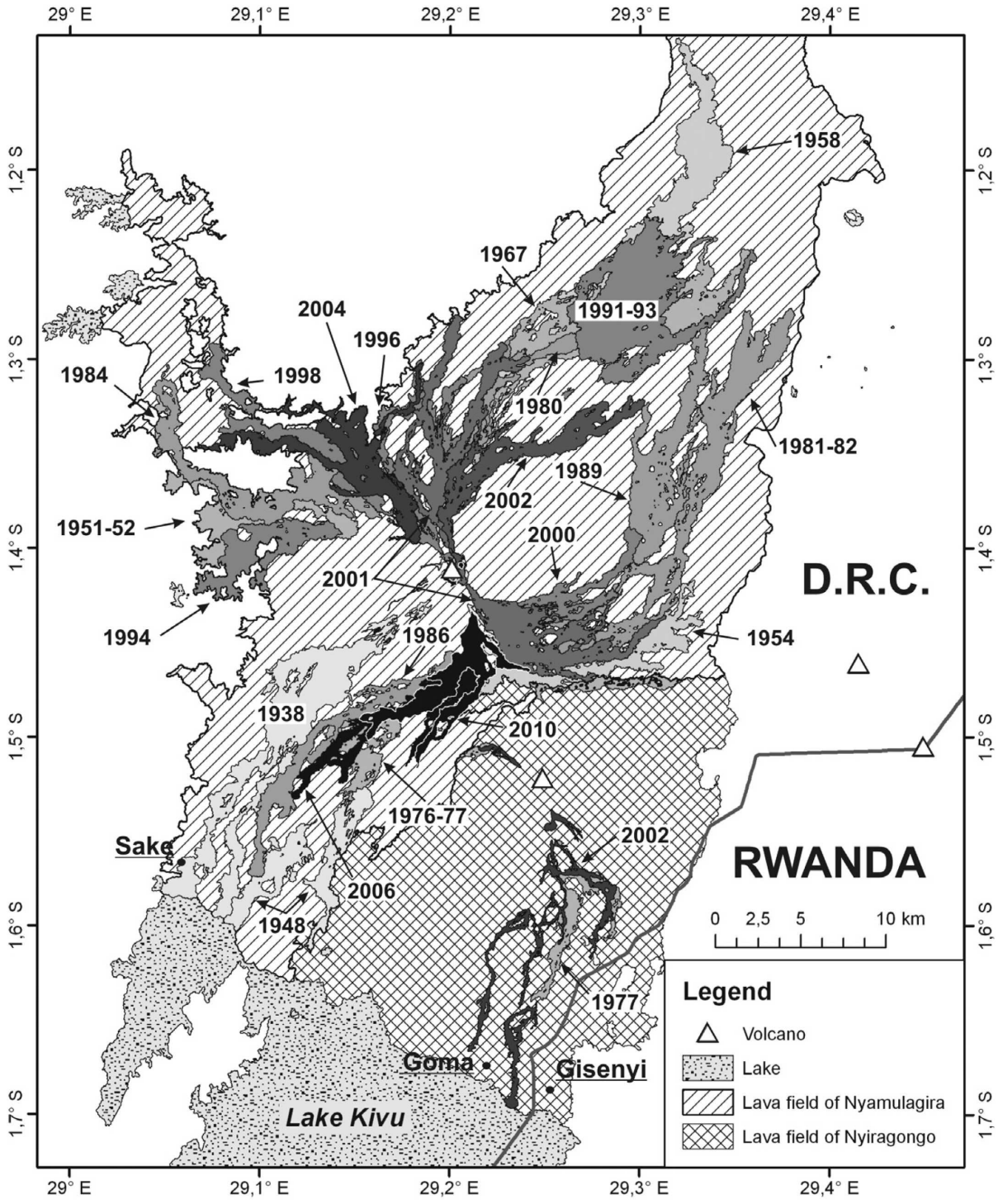

Figure 1.14: The Nyamulagira volcanological map, after [*Smets et al.*, 2010c]

StartDate	*StopDate*	*Location*
01/28/1938	06/25/1940 or after	Summit, SE and SW flanks
03/01/1948	07/15/1948 or after	SW flank
11/16/1951	01/16/1952	NNW fissure zone
02/21/1954	05/28/1954	SSE fissure zone
11/17/1956	11/18/1956	Summit caldera
12/28/1957	12/29/1957	Summit caldera and SSE fissure zone
08/07/1958	11/21/1958	N flank
04/23/1967	05/03/1967	N flank
03/24/1971	04/28/1971 or after	WNW flank
12/23/1976	April 1977	SSW flank
01/30/1980	02/23/1980	N flank
12/25/1981	01/14/1982	SE flank
02/23/1984	03/14/1984	NW flank
07/16/1986	08/20/1986	south flank
12/30/1987	01/04/1988	N flank
04/23/1989	After 08/04/1989	Summit, SE and E flanks
09/20/1991	02/08/1993	NE flank
07/04/1994	07/24/1994	W flank
12/01/1996	12/16/1996 or after	N flank
10/17/1998	10/29/1998 Summit	NW flank
01/27/2000	02/11/2000 or after	SE flank
02/06/2001	04/05/2001 or after	N and SSE flanks
07/25/2002	Between 08/09 and 09/27/2002	Summit caldera, N and S flanks
05/08/2004	05/28/2004 or after	Summit and NNW flank
11/27/2006	12/05/2006 or after	south flank
01/02/2010	01/27/2010	SE flank

Table 1.1: Eruptive history of recent Nyamulagira eruptions [*Smets et al.*, 2010c]

The Nyiragongo Volcano

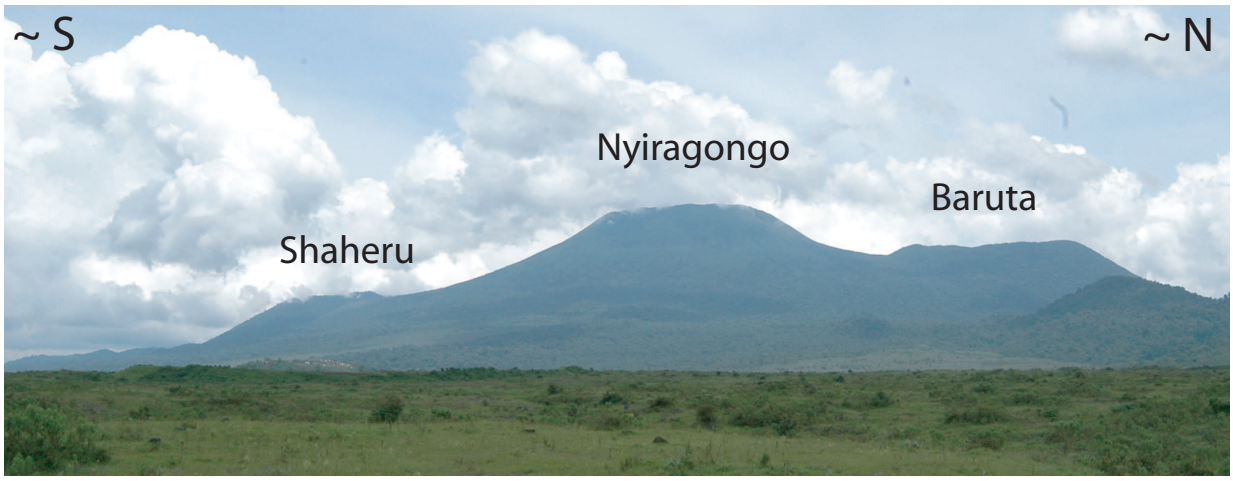

Figure 1.15: The Nyiragongo volcanic complex (photo credit: Benoît Smets)

Nyiragongo is one of the few volcanoes on Earth to host an active lava lake. It is located 15 km north of the city of Goma, and the adjacent Rwandan city of Gisenyi, both situated on the shore of Lake Kivu. Nyiragongo has not been much studied, in great part due to to persistent political tensions in the country. This volcanic complex is actually formed by the superposition of three stratovolcanoes (Figure 1.15), from North to South: the oldest Baruta edifice (3,148 m), the active Nyiragongo vent (3,470 m), characterized by very steep slopes (20° - 50°), a summit caldera of ≈ 1.2 x 1.3 km [*Tazieff*, 1949] [*Tazieff*, 1977b] [*Richard*, 1957] and an associated lava lake (Figure 1.16), and finally the Shaheru (2,600 m).

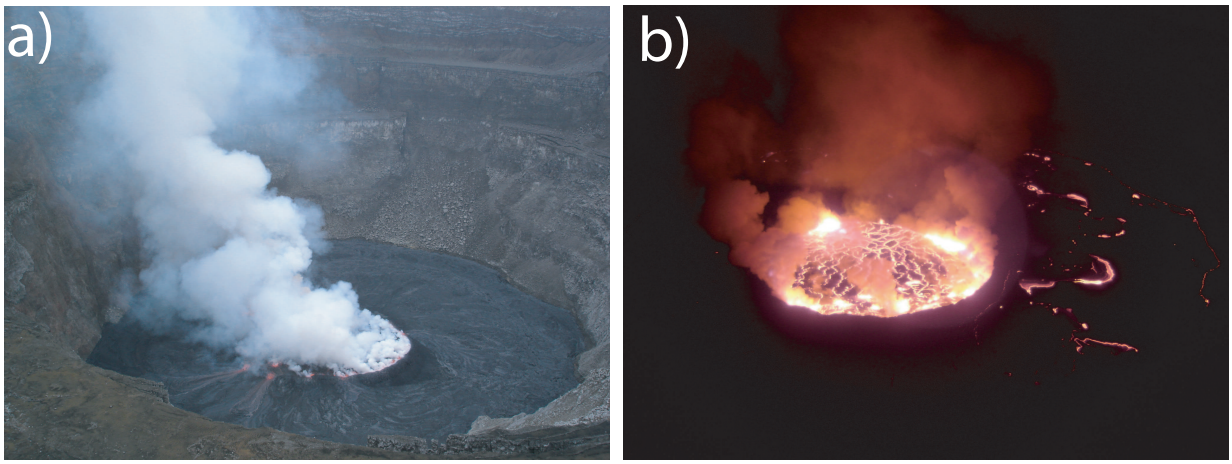

Figure 1.16: The Nyiragongo summit lava lake during the day (a) and the nighttime (b) (photos credit: Benoît Smets)

More than 100 spatter and cinder cones are identified on the Nyiragongo flanks where parasitic vents opened [*Platz et al.*, 2004]. These cones formed preferentially along fractures striking generally NS or NE-SW. Some phreatomagmatic cones - resulting from magma and water interaction - are also identified, such as the Mount Goma in the city of Goma on the lake Kivu floor.

An aseismic area from 10 to 14 km below the Nyiragongo edifice was interpreted by *Tanaka* [1983] as the main magmatic reservoir. However, another aseismic area was identified between 0 and 14 km beneath the edifice when the lava lake was active thus it has been interpreted by *Demant et al.* [1994] as a permanent connection between the lava lake and a shallow magmatic reservoir.

The Nyiragongo magma is known for lavas with very low viscosities. The Nyiragongo lava compositions differ strongly from the Nyamulagira lava or other Virunga volcanoes lava. *Platz et al.* [2004] present the following petrogenetic model from petrological and geochemical data for the Nyiragongo: small degree partial melts are generated at the lithosphere-astenosphere boundary. Due to the extensional context, these silicate melts are able to rise through the lithosphere. The fractionation of olivine and melilite from the parental magma occurred in shallow reservoirs $\approx$ 10 to 14 km depth [*Demant et al.*, 1994], leading to the formation of a residual pyroxene-rich nephelinitic melt. As evidenced by the presence of leucite in the volcanic products, small magma batches can after rise through the volcanic edifice and form other shallower magmatic reservoirs ($<$ 4 km depth). Lava and pyroclastic deposits from successive low-viscosity shallow magma eruptions form the alternated layers of the stratovolcano. The present summit crater shape could be explained by the draining-induced-collapse of several shallow reservoirs during a major eruption. The refilling of these shallow reservoirs during continuous Hawaiian and Strombolian activities could have created the semi-persistent lava lake.

The last two eruptions (Table 1.2) which occurred in 1977 and 2002, were fissural eruptions. They induced the draining of the lava lake. Lava that propagated with high velocities towards Goma with individual flows entering the Lake Kivu in 2002. The average thickness for the 1977 Nyiragongo lava flows has been estimated at 1 meter, although flows only a few mm thick formed on the steep upper slopes [*Tazieff*, 1977a]. From year 1984, Nyiragongo activity is limited to the lava lake.

StartDate	*StopDate*	*Location*
01/10/1977	01/10/1977 or after	N, NW and S flanks
01/17/2002	01/18/2002 or after	NW and S flanks

Table 1.2: Eruptive history of recent Nyiragongo eruptions

Ground-based Monitoring Networks

Following the 2002 Nyiragongo eruption, several ground-based stations were installed and maintained by the Goma Observatory (OVG) (Figure 1.17), thanks to several international projects such as the GORISK project (co-led by the Royal Museum for Central Africa, Belgium, and the National Museum of Natural History, Luxembourg), the NOVAC project (USA) and also thanks to the INGV support. The network includes presently 7 GPS stations, 4 tiltmeters, 4 DOAS stations and 7 seismometers.

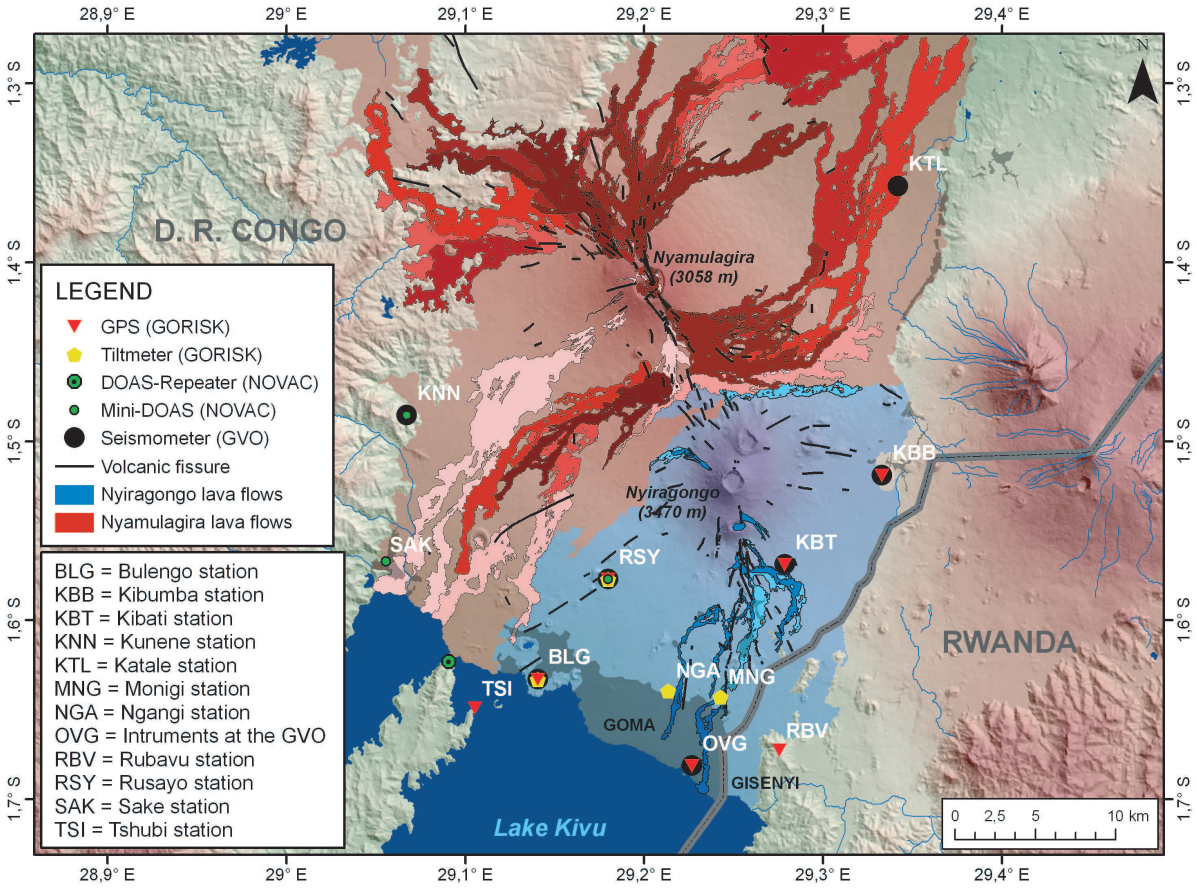

Figure 1.17: Ground-based monitoring networks, after *[Smets et al., in prep.]*

InSAR Monitoring

The North Kivu area is monitored by InSAR since the launch of the JERS satellite in 1996 (Table 2.1). Since then, a total of 8 eruptions occurred at Nyamulagira volcano, an eruption occurred at the Nyiragongo volcano and two earthquakes with magnitude larger than 5.9 also took place in the area (Figure 1.18).

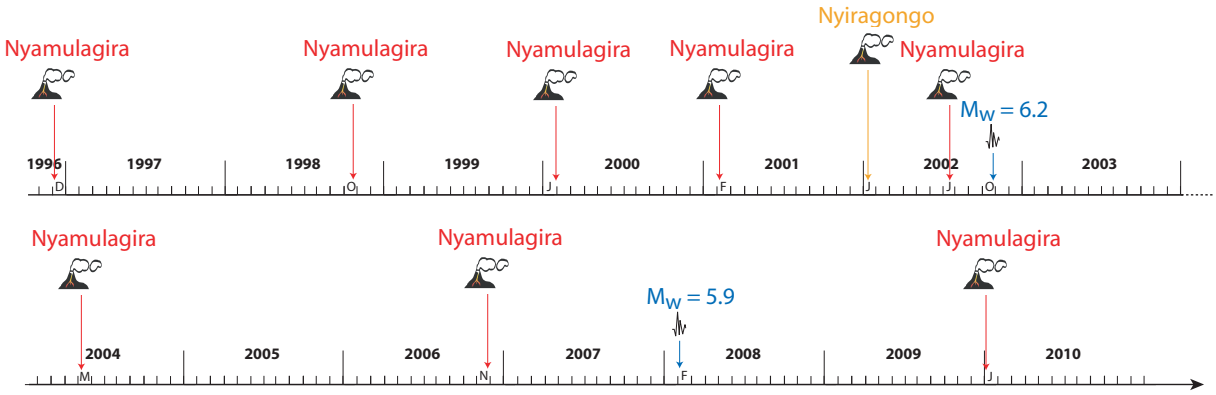

Figure 1.18: Time-line with all the volcanic and the two strongest seismic events which occurred in the Kivu area, DRC, from the year 1996 till present

1.4 Interest and Challenges of the Study

As ground based monitoring networks were only installed after the January 2002 Nyiragongo eruption, this major eruption and the previous seismic or volcanic events in the area were only captured by InSAR geodetic measurements. Furthermore, most of the ground-based stations are installed close to the city of Goma, due to security, maintenance and access reasons. This implies that the Nyamulagira activity remains poorly monitored with ground-based methods. The stations are often damaged or looted and many data gaps exist, degrading their quality and making them hard to use. Finally, the depth accuracy for the OVG seismic data is low (probably larger than 10 km). Thus, the modeled intrusions shapes could not be constrained with the local seismic data.

The Lake Natron area, located in northern Tanzania, also lacks of ground-based stations. New GPS stations are now being installed, but the InSAR data are the only geodetic data to cover efficiently the past deformation events.

The use of remote-sensing techniques, and particularly InSAR-based approaches, is therefore necessary to monitor and study these poorly known areas of the EARS. Building SAR archive database has been among the major inputs of the SAMAAV project (Study and Monitoring of Active African Volcanoes, Belgian Science Policy - Belspo - and the National Research Fund of Luxembourg Action-1 project and ESA Cat-1 project n° 3224) and the key of success for all subsequent InSAR analysis over these two targets. InSAR-related techniques used will be explained in the following Chapter 2. When a ground deformation signal from seismic and/or volcanic origin is satisfactorily captured by InSAR, we can constrain the sources responsible of the deformation signal by using a combined forward numerical modeling and inversion approach. This method is described in Chapter 3 and the modeling results are given in Chapter 4. The contribution of the Multi-Temporal InSAR approach to the understanding of recent volcanic eruptions and associated rifting processes in the North Kivu area are then detailed in Chapter 5.

Chapter 2

Radar Remote-Sensing Methods

The different radar remote-sensing methods used in this study are presented. Firstly, the synthetic aperture radar interferometry (InSAR) technique, which aims to generate ground displacements maps, is described. Secondly, the time series applications of InSAR are presented, with a focus on the StaMPS method. Lastly, the polarimetric InSAR (POLInSAR) approach, which takes the benefit of several polarization modes, is explained. The applicability of this method is moreover preliminarily investigated.

2.1 Radar Interferometry (InSAR)

2.1.1 Radar Remote Sensing

The following definition of remote-sensing (RS) can be used: Remote sensing is the science of acquiring information about the Earth's surface without actually being in contact with it. This is done by sensing and recording reflected or emitted energy, and processing and analyzing that information. In many remote sensing techniques, the process involves an interaction between the incident radiation and the targets of interest.

The microwaves - or radar - wavelengths range from about 1 mm to 1 m (Figure 2.1) [*CCR*, 2011]. Radar RS techniques include both active and passive sensors. The longer wavelengths have similar characteristics as the wavelengths used for radio broadcasts, while the shorter wavelengths approach the thermal infrared region properties. The microwaves, having longer wavelengths than the visible and infrared waves, are not sensitive to atmospheric scattering so that they can penetrate the cloud cover, dust, smog and rainfalls. Radar data can therefore be collected at any time and under almost all weather conditions. The passive radar RS is roughly similar to the thermal RS in the sense that sensors record the energy naturally transmitted by the Earth surface. In this study, the focus is on the active form of radar RS, with radar sensors providing their own source of illumination.

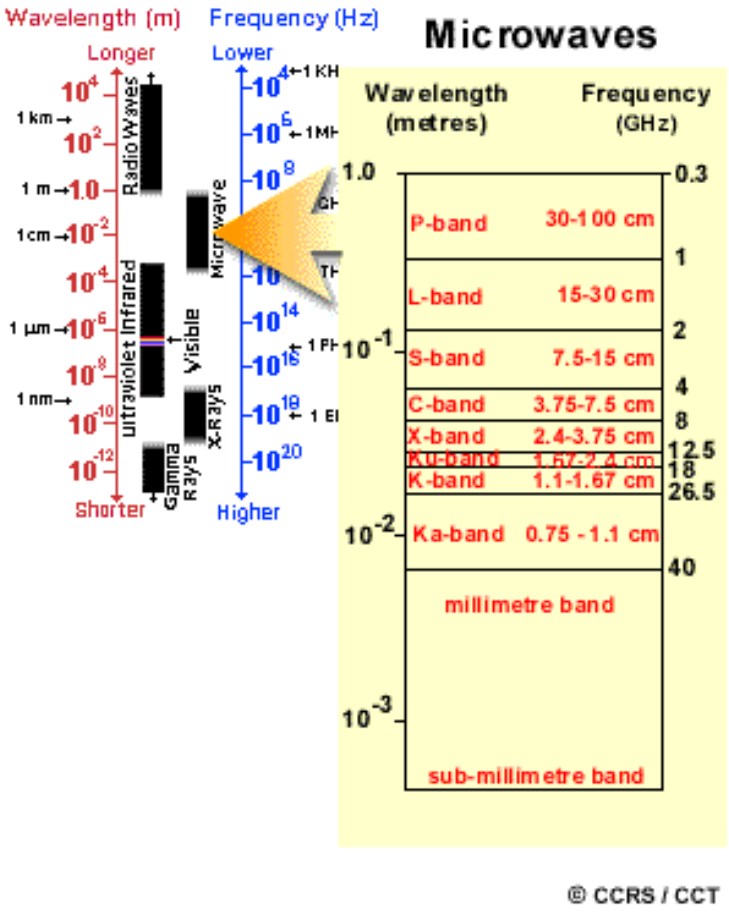

Figure 2.1: The Electromagnetic spectrum, with the microwave (radar) region highlighted, after [*CCR*, 2011]

2.1.2 The Radar Concept

RADAR is the acronym for Radio Detection And Ranging. The primary aim of a radar system is to measure the distance - or range - to a given target. The radar device is mainly composed of a transmitter, a receiver, an antenna and an electronic system to process the data. Successive short bursts - or pulses of microwaves - are transmitted by the transmitter at regular intervals, and the antenna focuses these pluses into a beam. The radar illuminates the target obliquely, in a perpendicular plane with respect to the platform motion direction (Figures 2.3 and 2.4). Indeed, as shown in Figure 2.2, the side-looking view allows to remove the ambiguity between targets (symmetry effects).

The surface, constituted of a multitude of objects, will reflect - or backscatter part - of the transmitted energy back to the radar antenna. The distance and location of the targets, with respect to the radar position, can be calculated by measuring the time delay (phase) of the backscattered echo signal, due to the almost pure sinusoidal nature of the signal (Figure 2.3). A two-dimensional image is then created by the recording and processing of the backscattered signals as the platform moves forward [*CCR*, 2011].

Like all electromagnetic signals, a radar echo carries an amplitude (A in Figure 2.3) and a phase (φ in Figure 2.3). Thus, the data are complex numbers and the resulting high-resolution image is also complex.

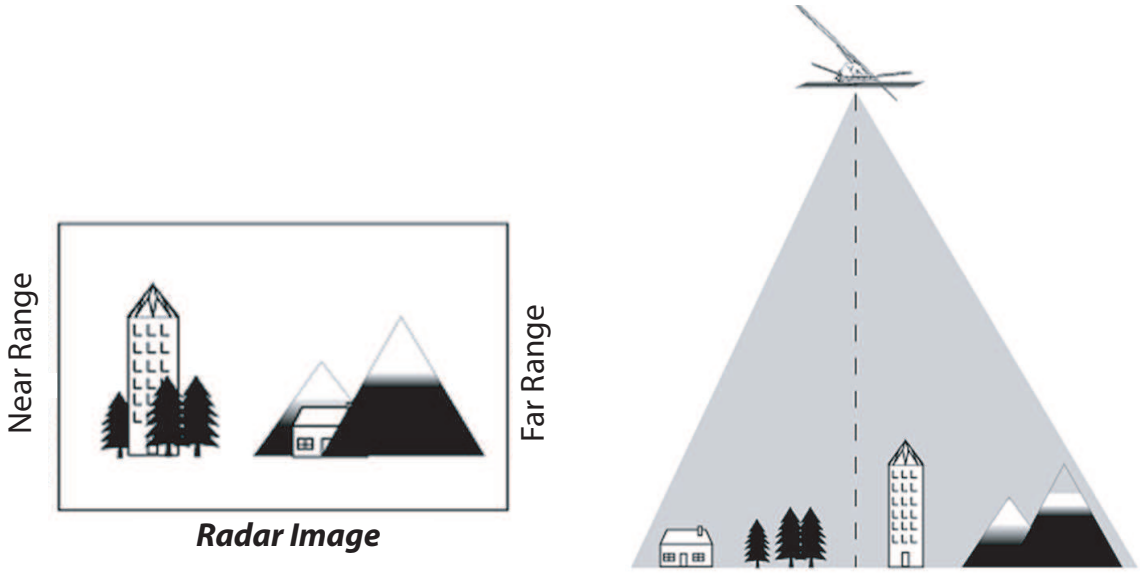

Figure 2.2: If the angle of view was vertical rather than oblique, the resulting image would be an unusable mix of targets located right and left of the satellite flight path, after [*Froger*, 2003]

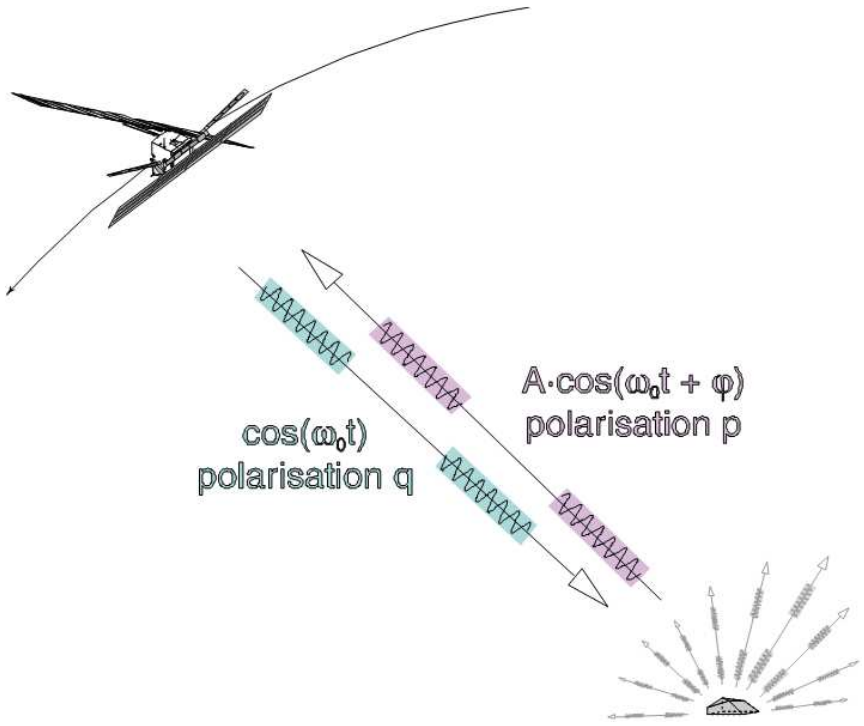

Figure 2.3: Functions of a radar system: Transmission of a radar signal (microwave radiation), reception of the echo signal backscattered by the target object, and recording of the amplitude A and the phase φ of the echo signal, after [*Froger*, 2003]

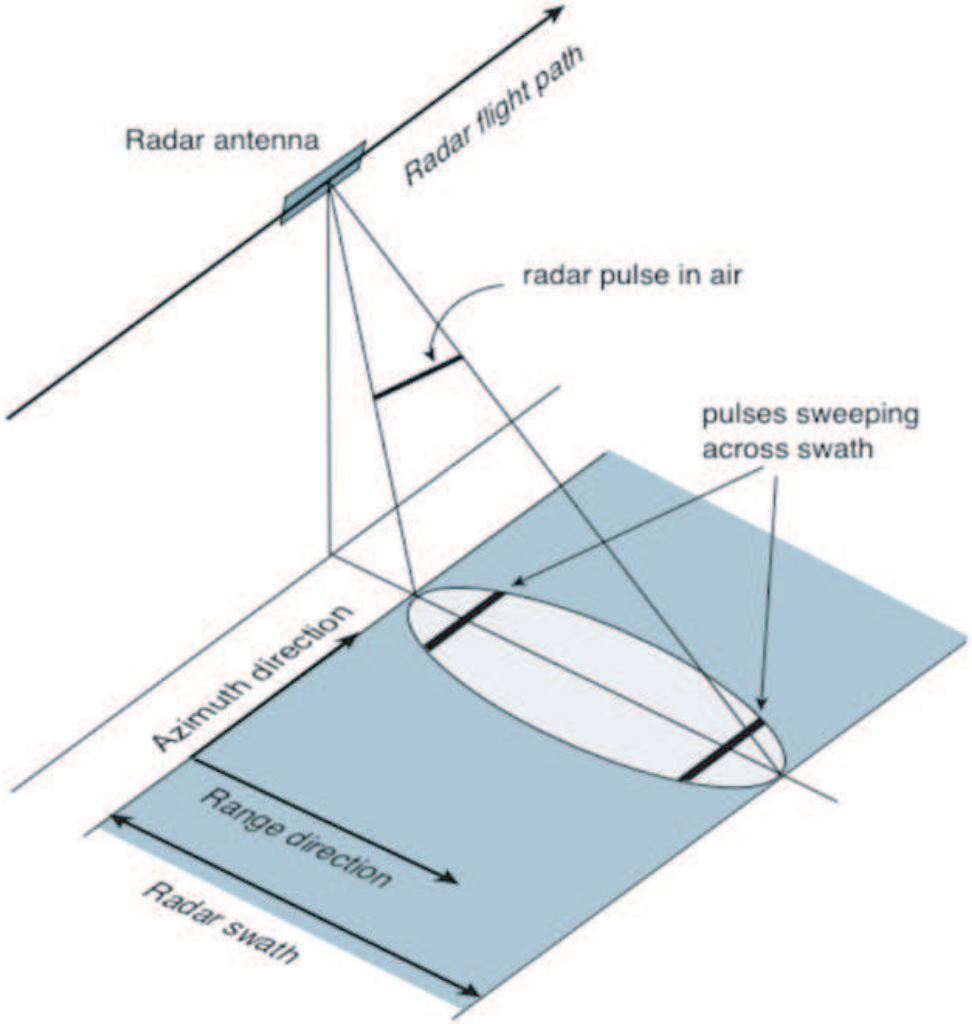

Figure 2.4: Geometry of a radar on a moving platform. Azimuth direction is also called along-track, while the range direction is also known as ground range. The slant range is the oblique distance of a particular point on the ground from the SAR sensor, after [*Rosen*, 2002]

The SAR orbit geometry is near-circular, polar, sun-synchronous. When the satellite travels from the south to the north he follows an ascending orbit, and from the north to the south, a descending one. Satellites have generally an altitude of about 760 km, and a typical repeat cycle of a few tens of days.

2.1.3 Synthetic Aperture Radar (SAR)

Early missions have demonstrated that SAR is able to reliably map the Earth's surface and characterize its physical properties, such as the topography, morphology, roughness and dielectrical properties of the target. SEASAT, launched in 1978, was the first NASA SAR satellite dedicated to Earth observation [*Bamler and Hartl*, 1998].

The azimuth direction, also called along-track, is the direction parallel to the SAR platform trajectory, while the range direction, also known as ground range, is the direction perpendicular

to the SAR trajectory. The slant range is the oblique distance of a particular point on the ground from the SAR sensor (Figure 2.4).

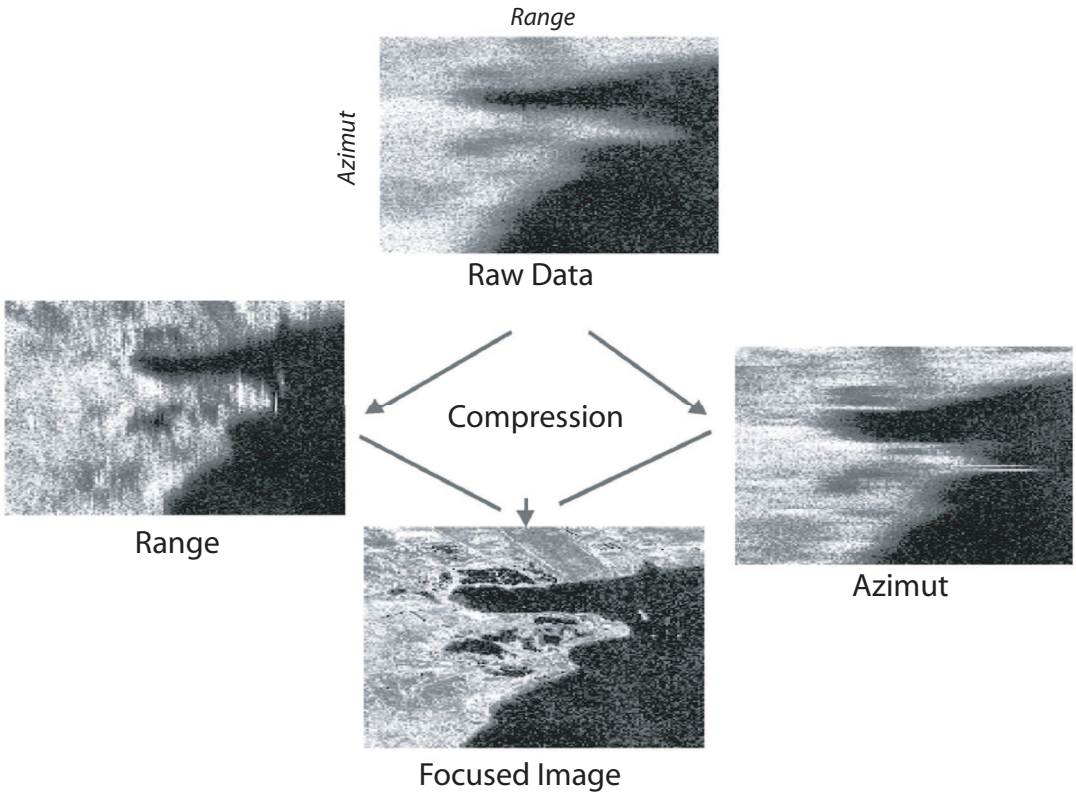

Figure 2.5: Focusing: a high resolution focused image, which is called a Single Look Complex (SLC) is obtained from a low resolution, blurred raw image, after [*Froger*, 2003]

While the sensor is moving along its flight path, it transmits microwave pulses into the antenna's illumination footprint at the rate of the Pulse Repetition Frequency (PRF) and receives the echoes of each pulse scattered back from the ground. The SAR receiver detects the amount of echoes coherently and separates it into individual echoes, each corresponding to a transmitted pulse. Typical pulse carrier wavelengths used are approximately 3 cm (X-band), 6 cm (C-band), 9 cm (S-band), and 24 cm (L-band) (Table 2.1). Frequencies are in the range of 1-10 kHz [*Bamler and Hartl*, 1998].

The raw data acquired by the radar have to be processed to lead to an useful single-look complex image (SLC). The different operations leading to this SLC image formation are called $focusing$ (Figure 2.5). The transmitted pulses sweep across the swath (Figure 2.4) at the speed of light c, while simultaneously, the scene is scanned in the along-track direction at the velocity of the antenna footprint. These two scanning mechanisms, which have different timescales, can be treated independently. Arranging the echoes side-by-side allows us to create a raw data matrix, which is a coarse image of the scattering target (Figure 2.5). The radar coordinates are (Figure 2.4): *range* and *azimuth*, which are the distance of the scatterer from the SAR (measured perpendicularly from the flight path), and its position along the flight path, respectively.

Sensor	*Mission Period*	*Wavelength (cm)*	*Orbital Cycle (days)*	*Mean Inc. Angle (°)*	*Remarks*
JERS-1	1992-1998	23.5 (L-band)	44	35	low S/N ratio due to hardware pb
ERS-1/ERS-2	1992-2003	5.67 (C-band)	35	23	1 day revisit cycle during TANDEM mission
RADARSAT-1	1995-2007	5.77 (C-band)	24	20 - 50	multi-incidence angle, multiresolution, ScanSAR option
ENVISAT	2003-2011	5.6 (C-band)	35	15 - 45	multi-incidence angle, ScanSAR option, very accurate orbit, several polarization modes
ALOS	2006-2011	23.5 (L-band)	46	21.5 - 41.5	multi-incidence angle, multiresolution, ScanSAR option, experimental full polarization mode
TERRASAR-X	2007-present	3 (X-band)	11	15 - 60	multi-incidence angle, multiresolution, ScanSAR and Spotlight options, experimental full polarization mode
RADARSAT-2	2007-present	5.77 (C-band)	24	10 - 60	multi-incidence angle, multiresolution, ScanSAR option, full polarization mode, left and right-looking modes

Table 2.1: Recent spaceborne SAR systems suitable for repeat-pass interferometry and covering our targets in the EARS

In the range direction, the image properties are governed by the radar principle. Thus, the range resolution is given by the duration of the transmitted pulse (or the inverse of the bandwidth): short pulse lengths (high bandwidths) allow a finest range resolution (Figure 2.6a). The SAR processing or focusing applies a deconvolution in the range direction thanks to a range or chirp modulation and compression (interested reader can find the technical details in, among others, [*Elachi*, 1988] or [*Hanssen*, 2001]).

The raw data azimuth resolution is limited to the antenna footprint size (equation 2.1). Indeed, the azimuth resolution r is proportional to the ratio of wavelength λ to the length of the antena in the azimuth direction L

$$r = \frac{R\lambda}{L} \tag{2.1}$$

and R is the range. Considering an antenna size $L = 10$ m, a wavelength of $\lambda = 5.6.10^2$ m, and a range $R = 1000$ km, the natural orbital resolution of an orbiting instrument is 5600 m. As the antenna size cannot reasonably be increased to several tens of km to get similar resolutions as optical sensors, a way to overcome this strong limitation has to be found. The solution comes from the synthetic aperture radar (SAR) processing or focusing which simulates a large size antenna. Indeed, the phase history of every scatterer as it traverses the antenna beam is registered, therefore, the phase history carries all the information about the azimuth position of the scatterer (Figure 2.6b). The SAR focusing,also applies a deconvolution in the azimuth direction to resolve different scatterers within the aperture. It can focus the raw data to an azimuth resolution of about half the physical antenna length, independently of the range, wavelength and sensor velocity [*Bamler and Hartl*, 1998].

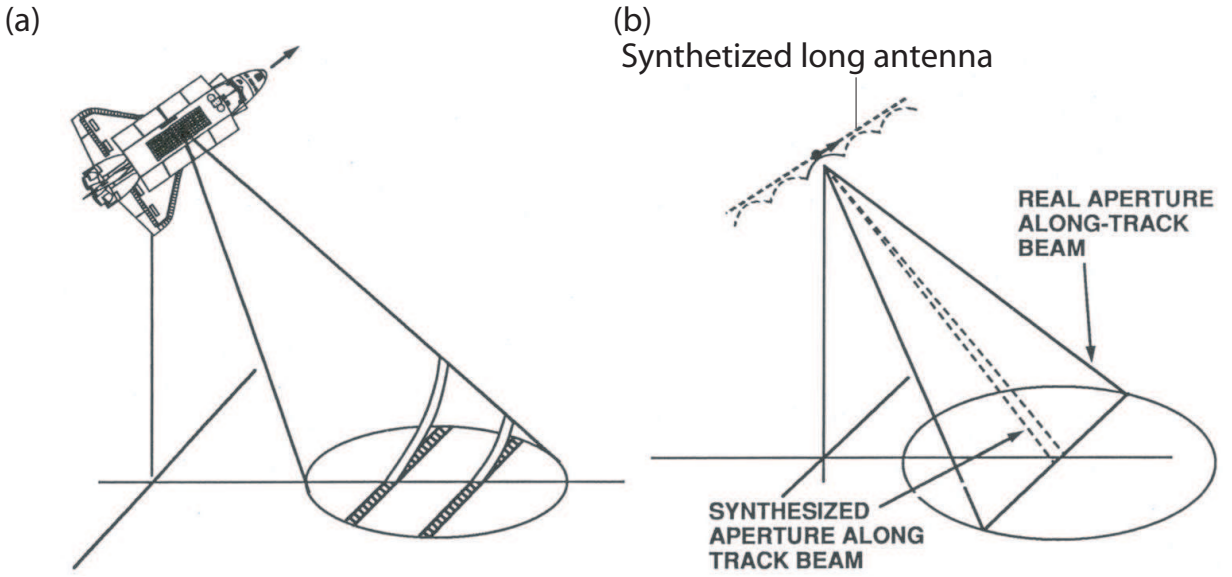

Figure 2.6: (a) The range resolution is achieved by short pulse length (high bandwidth). (b) The azimuth resolution is achieved by coherently combining echoes from multiple pulses along-track (synthesize a long antenna), after [*Rosen*, 2002]

The SAR processing filters are generally designed to focus the response of the scatterer at its zero-Doppler coordinates - or deskewed geometry. The zero doppler coordinate is the range and azimuth where the radar and the scatterer are closest from each other (zero-Doppler line in Figure 2.7). The zero-Doppler term is inherited from the classical radar theory employing the concept of Doppler frequency shift [*Bamler and Hartl*, 1998]. However, it is worth noting that other configuration for focusing exist such as the Doppler centroid - or skewed geometry [*Hanssen*, 2001].

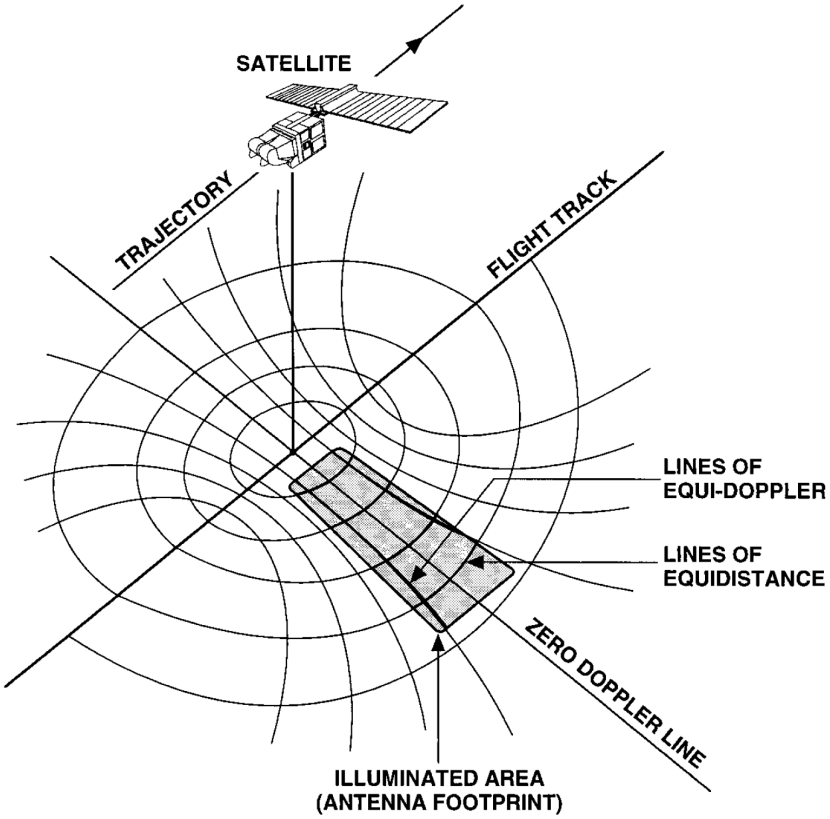

Figure 2.7: Two different principles help to improve the resolution in a SAR image. First, the samples of the returning signal are sorted according to their round trip flight time. Second, the Doppler frequency shift is then used to sort the samples along the direction of the flight i.e the azimuth direction. After [*Massonet and Feigl*, 1998]

2.1.4 SAR Images Properties

The Speckle Effect

As depicted in Figure 2.8, the echo of an individual resolution cell is the result of the echoes vector combination of the many elementary scatterers inside the pixel. The echoes are not necessarily in phase and the result is highly random for each resolution cell and gives a noisy appearance to the image (Figure 2.9A), which is called speckle. Two procedures can be used to attenuate the speckle effect: 1) a spatial filtering which decreases the spatial resolution to increase the radiometric one, 2) a multilook filtering, obtained by staking several amplitude images (Figure 2.9B). The multilook increases the radiometric resolution without degrading the spatial one (Figure 2.9).

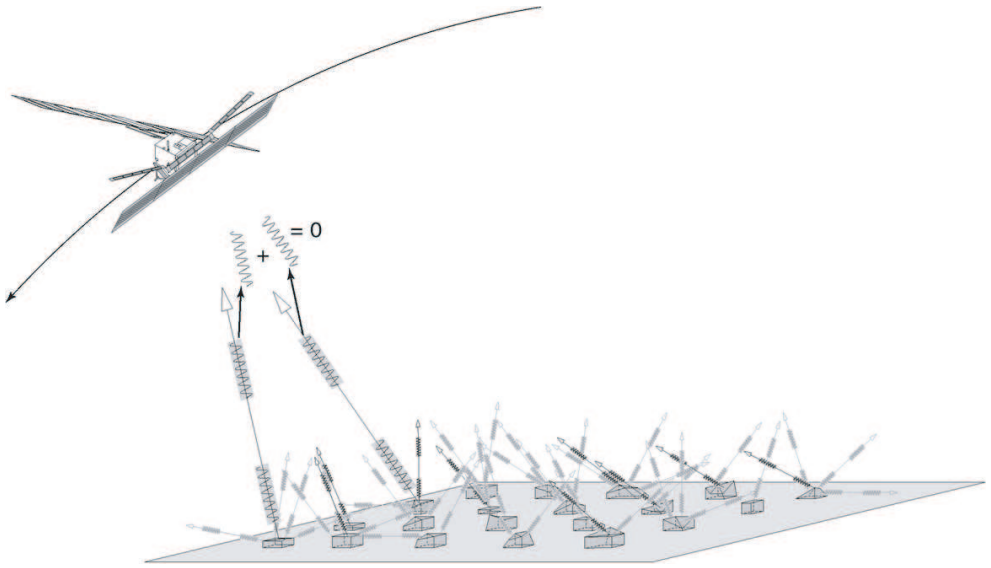

Figure 2.8: The speckle effect due to the random distribution of phase of each scatterer, which can be additive or destructive, after [*Froger*, 2003]

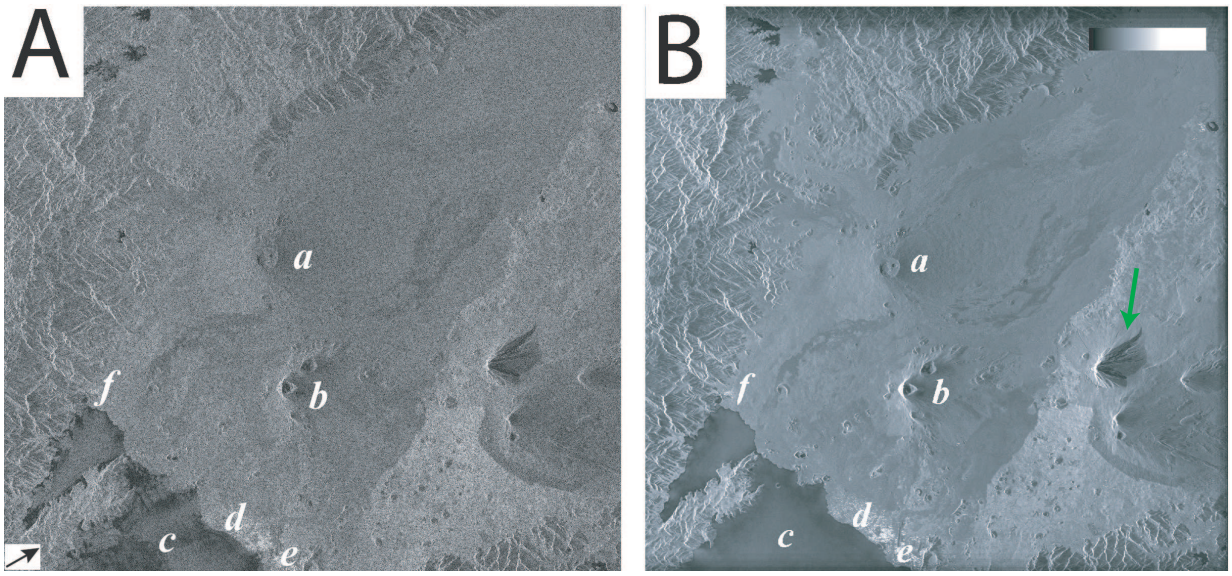

Figure 2.9: A) Amplitude radar image over the North Kivu area acquired from an Envisat ascending orbit. B) The multilook procedure, stacking several (here 28) SAR amplitude images, can strongly reduce the speckle effect. See text for a, b, c, d, e and f explanation. Geometric distortions called foreshortening and shadowing (green arrow) are visible for the high volcanoes reliefs

Geometric Distortions

Another drawback of the radar imagery comes from the oblique geometry used to sort the echoes by their distance from the antenna. In mountainous areas, several points in a pulse line may share the same distance to the instrument and therefore will mix their contributions in the same range pixel. This phenomenon, called layover (Figure 2.10), which is actually the extreme limit of the foreshortening effect (Figure 2.10 and Figure 2.9), occurs where the average topographic slope between two points exceeds the incidence angle of the radar (23 for ERS for instance, as shown in Table 2.1). A last distortion, called shadowing, appears when ground areas have slopes

unseen by the radars (Figure 2.11 and indicated by a green arrow in Figure 2.9B).

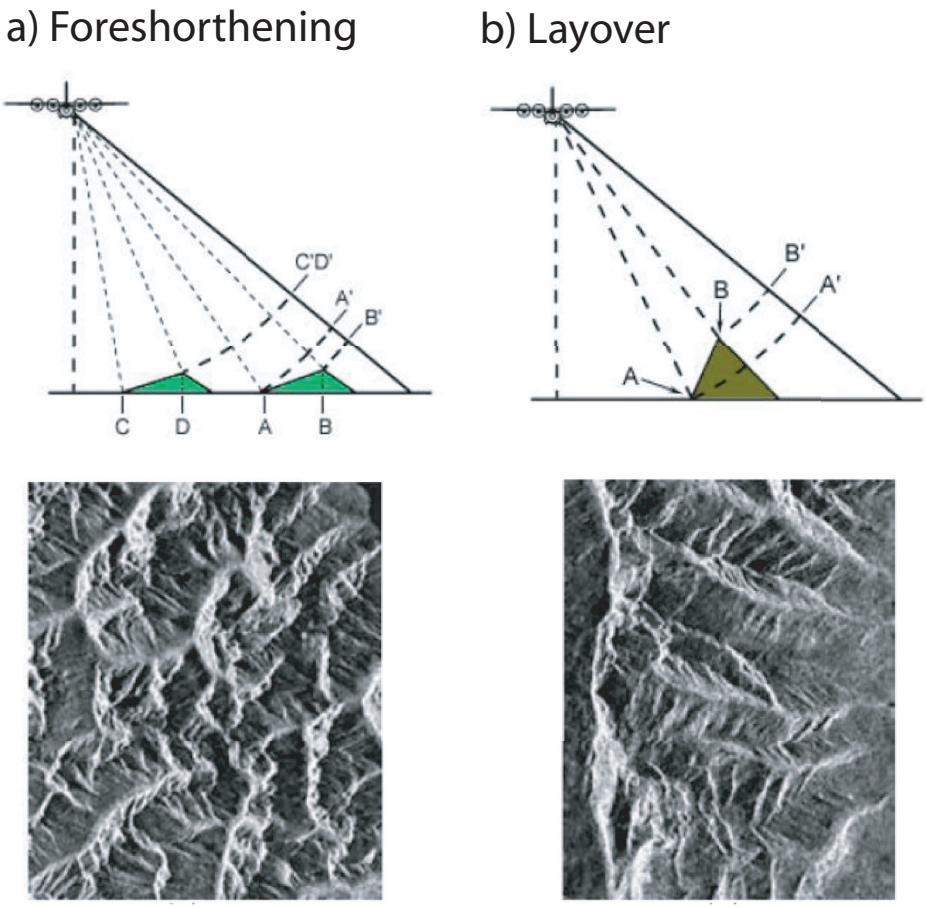

Figure 2.10: The foreshortening effect affects ground areas sloping towards the Radar, and the extreme effect for steep slopes is the layover, after [*CCR*, 2011]

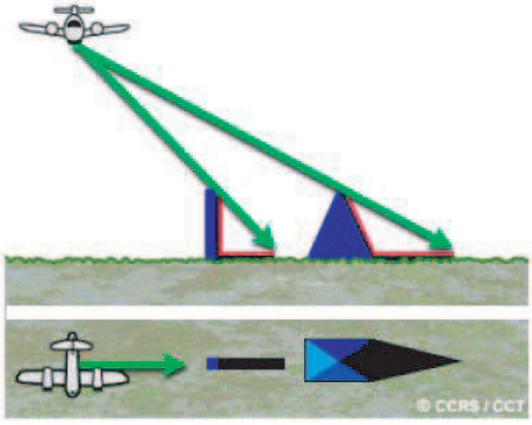

Figure 2.11: The shadowing effect, after [*CCR*, 2011]

Amplitude

The amplitude of the radar image represents the reflectivity, which represents the variability of the terrain to send the energy back to the sensor. Typically, smooth surfaces, such as the calm Lake Kivu (c) in Figure 2.9, appear dark in a radar image because the surface acts as a perfect reflector (the reflection is said to be specular), sending almost all of the radar signal away from the satellite. If the surface of the water is ruffled because of the wind for instance, reflective facets comparable in size to the wavelength are not directional and transmit part of the energy back to the sensor. Most natural reflectors are diffuse reflectors, sending a greater or a lesser part of the signal back to the radar. In Figure 2.9, one can see that the vegetated flanks of the Nyamulagira volcano (a) and the lava flows reflect differently the energy back to the sensor, leading to a noisy aspect for the vegetation, and a more smooth and bright aspect for the lava flows. Corner reflectors are corner-like structures such as sidewalk curbs, windows, and roofs, as well as fault scarps or ground fissures, can create very bright returns, [*Zebker and Goldstein*, 1986] (see for instance the cities of Goma (d), Sake(f) and Gisenyi (e), or the Nyiragongo left steep slope at the summit (b) in Figure 2.9). Radar waves can penetrate dry materials with low conductivity, such as soil in arid deserts, snow on very cold ice fields, or sparse vegetation [*Blom and Elachi*, 1981]. Longer wavelengths (for instance L-band) penetrate a relatively thin tree canopy more deeply that shorter ones (for instance X-band) [*Hagberg et al.*, 1995] [*Rignot*, 1996].

Phase

The phase (modulo 2π) is a two way measurement of the number of phase cycles between the earth and satellite distance with an added random component coming from the properties of the different scatterers constituting a pixel. As a consequence, phase images appear noisy with pixel values uniformly distributed between 0° and 360° as depicted in Figure 2.12.

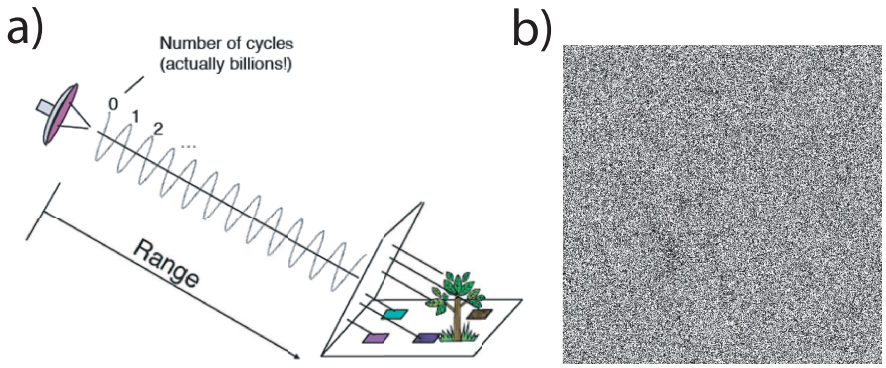

Figure 2.12: The phase is a measure of the range and ground properties. (a) The phase of the radar signal is the number of cycles of oscillation that the wave executes between the radar and the surface and back again. The total phase is two-way range measured in wave cycles plus a random component from the surface. The collection of random path lengths jumbles the phase of the echo and makes one radar image phase useless (b), modified after [*Rosen*, 2002]

2.1.5 SAR Interferometry (InSAR)

SAR images are generally acquired from slightly different orbits also referred to as imaging geometries. Lets consider two SAR images composed of complex values, y_1 and y_2, which can be decomposed in an amplitude and a phase component using:

$$y_1 = |y_1| \, exp\,(j\varphi_1) \tag{2.2}$$

$$y_2 = |y_2| \, exp\,(j\varphi_2) \tag{2.3}$$

The second SLC y_2 grid must be precisely aligned, coregistered and resampled to the geometry of the first SLC y_1 grid [*Zebker and Goldstein*, 1986] [*Hanssen*, 2001]. The complex multiplication yields the complex interferogram:

$$y_1 y_2* = |y_1| \, |y_2| \, exp\,(j(\varphi_1 - \varphi_2)) \tag{2.4}$$

The observed phase values φ_1 and φ_2 in the two images for resolution cell P are:

$$\varphi_1 = \frac{-2\pi 2R_1}{\lambda} + \varphi_{scat,1} \tag{2.5}$$

$$\varphi_2 = \frac{-2\pi 2R_2}{\lambda} + \varphi_{scat,2} \tag{2.6}$$

where R_1 and R_2 (Figure 2.13) are the geometric distances (ranges), and $\varphi_{scat,1}$ and $\varphi_{scat,2}$ are the contributions of the scattering phases in both images. Ignoring any signal propagation delays, and assuming that the scattering characteristics remain the same for both acquisitions ($\varphi_{scat,1}$ = $\varphi_{scat,2}$), the estimated interferometric phase (ϕ_{int}) can be directly related to the difference in path length to a target from the imaging platform in the line of sight (LOS) direction (Figure 2.13):

$$\phi_{int} = \frac{-4\pi}{\lambda} \, \Delta R \tag{2.7}$$

The interferometric phase, determined modulo 2π, is called an interferogram. It is coded with fringes ($0 - 2\pi$ radians), with an arbitrary colorscale. Examples of ascending ENVISAT interferograms superimposed on the amplitude are shown in Figure 2.14. The interferometric phase can be decomposed into the following components:

$$\phi_{int} = \phi_{base} + \phi_{topo} + \phi_{defo} + \phi_{atmo} + \phi_{noise} \tag{2.8}$$

where ϕ_{base} is the phase difference due to baseline changes between the positions (see B in Figure 2.13) of the satellite corresponding to the two acquisitions, ϕ_{topo} is due to the topography, ϕ_{defo} is due to the ground displacements which occurred between the two SAR acquisitions, ϕ_{atmo} is generated by the atmospheric delay, and ϕ_{noise} is due to other terms including the acquisition system noise

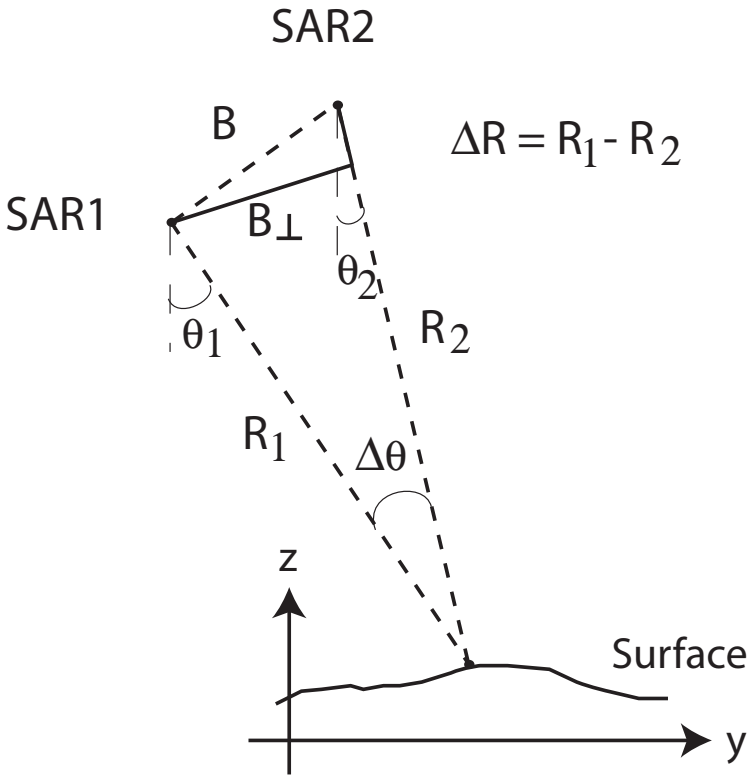

Figure 2.13: SAR interferogram imaging geometry in the plane normal to the flight direction. R_1 and R_2 are the geometric distances (ranges), B is the baseline (distance between the two SAR positions), and θ_1, θ_2 are the look angles.

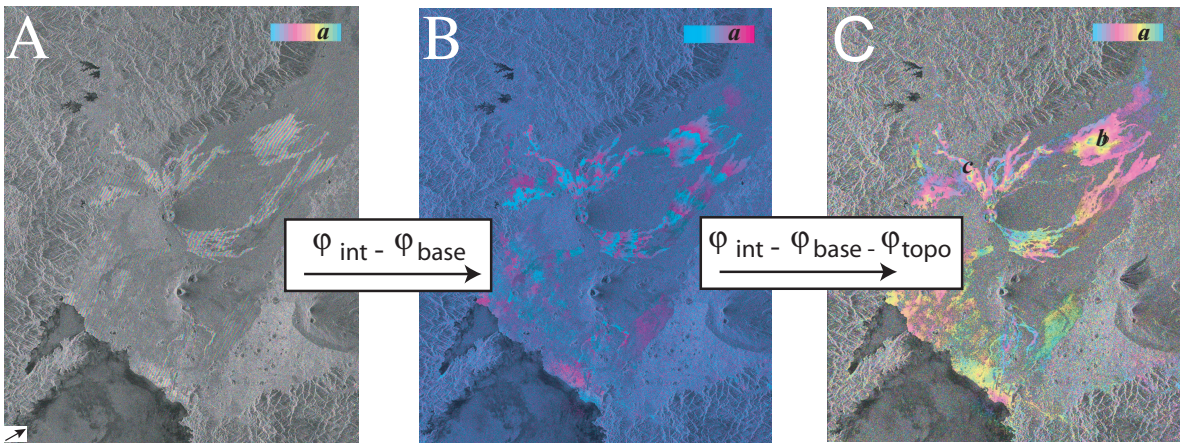

Figure 2.14: ENVISAT ascending interferograms of the North Kivu Virunga area, RDC, superimposed on the amplitude radar image. A) Uncorrected interferometric phase, the high-frequency parallel orbital fringes are clearly visible. B) Interferometric phase corrected for the baseline contribution. Topographic fringes are clearly visible surrounding the reliefs. C) Interferometric phase corrected for the baseline contribution and the topography. This interferogram is often called a deformation interferogram. Lava flow compactions (for instance in *b* and *c*) are visible. For instance in *b*, a phase increase of about 1 fringe (equals to 1 full color cycle here in the sense *blue-red-yellow*) towards the center of deformation and lava flow field is observed, which corresponds to a range increase (of 2.8 cm), meaning that the ground is moving *away* from the satellite (LOS subsidence).

Contribution of the baseline between the orbital trajectories (ϕ_{base})

Most of the observed path difference corresponds to the difference in viewpoint caused by the shift in orbital trajectory between the two image acquisitions (Figure 2.14A). The convergence or divergence, even if less than 1 meter, of the orbital trajectories can also create along-track fringes over the length of the image. Once all the apriori knowledge of the orbits has been used to eliminate this type of contribution, there may be residual fringes, which can be eliminated by an orbital tuning [*Massonet and Feigl*, 1998], or by removing a linear trend, assumed to be the residual orbital phase signal.

Contribution of the topography (ϕ_{topo})

Eliminating the orbital contribution reveals an underlying stereoscopic effect, as the radar observes the relief from two slightly different points of view. This topographic contribution corresponds to the phase difference induced by the difference in the distance target-sensor, resulting in fringes which follow the reliefs, similarly as topographic contour lines (Figure 2.14B). To quantify these topographic fringes, the notion of height (or altitude) of ambiguity, h_{amb}, which is the shift in altitude needed to produce one topographic fringe, is defined [*Hanssen*, 2001]:

$$h_{amb} = \left| \frac{\lambda R_1 sin\theta}{2B_\perp} \right| \tag{2.9}$$

where $B_\perp$ is the perpendicular baseline, depicted in Figure 2.13.

This sensitivity to the topographic relief can be used to generate a digital elevation model (DEM). To obtain a continuous interferometric phase map, the differential phase between all neighboring pixels has to be integrated, which is called the phase unwrapping process, and the unwrapped phase can then be converted to topography. InSAR was first developed to map the Earth's topography [*Zebker and Goldstein*, 1986] and was the technology on board of the Shuttle Radar Topography Mission (SRTM) [*Farr et al.*, 2007]. However, in this study, we are interested in ground displacements, thus the topographic contribution will be removed thanks to an external DEM (SRTM $\approx$ 30 m posting for the Kivu area, and $\approx$ 90 m posting for the Natron area). This DEM is used to generate a synthetic interferogram which is then be substracted from the original interferogram, removing fringes associated to ground elevation, and leaving fringes that represent surface displacements. Possible residual topographic fringes will be considered as noise in the resulting interferogram. This technique called Differential InSAR or D-InSAR, was first successfully applied to study the Landers earthquake [*Massonnet et al.*, 1993] [*Zebker et al.*, 1994a].

Contribution of the ground displacements (ϕ_{defo})

Ground displacements along the line of sight (LOS) between the radar and the target can be determined by removing the orbital and topographic contributions. Any ground displacement appears directly as a phase shift with respect to the rest of the scene. The radar measures thus the scalar change $\Delta\rho$ of the satellite-to-ground distance, which equals the component of the displacement vector $\mathbf{u}$ projected in the direction of the radar axis:

$$\Delta\rho = -\mathbf{u} \,.\, \mathbf{s} \tag{2.10}$$

where **s** is the unit vector pointing from the ground point toward the satellite [*Massonet and Feigl*, 1998]. A group of pixels moving by 1 cm along the radar axis between the two image acquisitions changes the round trip distance by 2 cm. Moving along the Line Of Sight (LOS) by half the wavelength will thus create one deformation fringe (see for instance b or c in Figure 2.14C).

Contribution of the atmosphere (ϕ_{atmo})

As two images are acquired at different moments, the atmospheric characteristics are not identical. Differences in the troposphere or the ionosphere properties between the two acquisition times will affect the apparent path length between the radar and the surface. Over small spatial scales, the phase delay is mainly due to the spatial variation of water vapor content in the troposphere, which results from turbulent and vertical stratification contributions [*Hanssen*, 2001]. The vertical stratification of the atmosphere results in atmospheric phase delay that are correlated with the ground elevation [*Delacourt et al.*, 1998] [*Beauducel et al.*, 2000]. Several methods exploit the correlation between phase and topography to correct for the atmospheric effects [*Chaabane et al.*, 2007] [*Lopez-Quiroz et al.*, 2009]. Using more than two SAR images can allow us to identify which SAR image is affected by an atmospheric phase delay. The different interferometric combinations of images enables the unambiguous identification of the image containing anomalies, and correlation between interferograms having a common image can be used to correct for local turbulent effects [*Chaabane et al.*, 2007]. The ionospheric effects are due to variation of the Total Electron Content [*Hanssen*, 2001]. Longer wavelength, such as L-band, are more sensitive to ionospheric effects.

Other Contributions (ϕ_{noise})

Other phenomena include instrumental noise such as the oscillator instability. Changes in the backscattering properties of the ground can also modify the phase of an interferogram [*Gabriel et al.*, 1989] [*Massonet and Feigl*, 1998].

Phase Unwrapping

For interferometric applications, the principal observation is the relative wrapped phase signal ϕ_{int}^{w} of the absolute phase signal ϕ_{int}, which is unknown:

$$\phi_{int}^{w} \;=\; mod\{\phi \,+\, \pi, 2\pi\} \,-\, \pi, \quad with \tag{2.11}$$

$$\phi^{int} \;=\; \frac{-4\pi}{\lambda}\,\Delta R \,+\, \phi_N \;=\; 2\pi k \,+\, \phi_N \tag{2.12}$$

where $\phi_N \;\in\; [-\pi,\, \pi]$ expresses phase noise, and k is the integer ambiguity number [*Hanssen*, 2001]. Without any assumption, it is not possible to solve the integer ambiguity number. The forward problem which consists of wrapping the absolute phase to the $[-\pi,\, \pi]$ is straightforward. But unwrapping the relative phase is a non-unique and non-linear, and therefore a non trivial inverse problem. Variable phase noise, as well as geometric distortions (foreshortening, layover...) are the main problem origins. Several classes of algorithms exist such as the Residue-cut, the

Least-Squares and minimal cost or network flow methods. In this study, the Snaphu phase unwrapping algorithm, which is a statistical-cost network-flow algorithm [*Chen and Zebker*, 2001], is used. The algorithm considers the unwrapping problem as a global minimization problem with integer variables [*Hanssen*, 2001].

Coherence

The complex coherence, or complex correlation coefficient γ, is defined as [*Hanssen*, 2001]:

$$\gamma \;=\; \frac{E\left\{y_1\, y_2^*\right\}}{\sqrt{E\left\{|y_1|^2\right\} E\left\{|y_2|^2\right\}}} \qquad \text{with} \qquad 0 \le \gamma \le 1. \tag{2.13}$$

A coherence value corresponds to each pixel in the interferogram. The coherence can be used as a measure for the accuracy of the interferometric phase, or as a tool for image classification.

In practical situations, the accuracy of phase observations of an uniform region is assumed to be stationary. Under the assumption of ergodicity, the ensemble averages can be replaced by spatial averages, obtained over a limited area surrounding the pixel of interest. We can therefore define the maximum likelihood estimator of the coherence magnitude over an estimation window of N pixels [*Seymour and Cumming*, 1994]:

$$\gamma \;=\; \frac{\left|\sum_{n=1}^{N} y_1^{(n)}\; y_2^{*(n)}\right|}{\sqrt{\sum_{n=1}^{N}\left|y_1^{(n)}\right|^2\;\sum_{n=1}^{N}\left|y_2^{(n)}\right|^2}} \tag{2.14}$$

The absolute value of the coherence, which ranges between 0 and 1, is equivalently described as a function of the phase signal to noise ratio (SNR) [*Foster and Guinzy*, 1967] [*Prati and Rocca*, 1992] [*Zebker and Villasenor*, 1992] [*Bamler and Just*, 1993]:

$$|\gamma| \;=\; \frac{SNR}{SNR \;+\; 1} \tag{2.15}$$

An example of an ENVISAT coherence image for the North Kivu Virunga area, with the minimal time span for ENVISAT (35 days), is given in Figure 2.15A. Lava flows clearly appear as coherent areas. Urban areas such as the city of Goma are also high coherent areas, while the vegetated flanks of the volcanoes are decorrelated, even with short temporal and perpendicular baselines. It can be seen that the coherence decreases with increasing time span B_t (Figure 2.15A and 2.15B) and with increasing perpendicular baselines B_p (Figure 2.15A and 2.15C).

2.1.6 Sources of Decorrelation

The main limitation of InSAR comes from the decorrelation of the phase signal. The total decorrelation is the product of several decorrelation terms, corresponding to different decorrelation sources [*Hanssen*, 2001],

$$\gamma_{tot} \;=\; \gamma_{geom} \;\times\; \gamma_{DC} \;\times\; \gamma_{vol} \;\times\; \gamma_{temporal} \;\times\; \gamma_{thermal} \;\times\; \gamma_{processing} \tag{2.16}$$

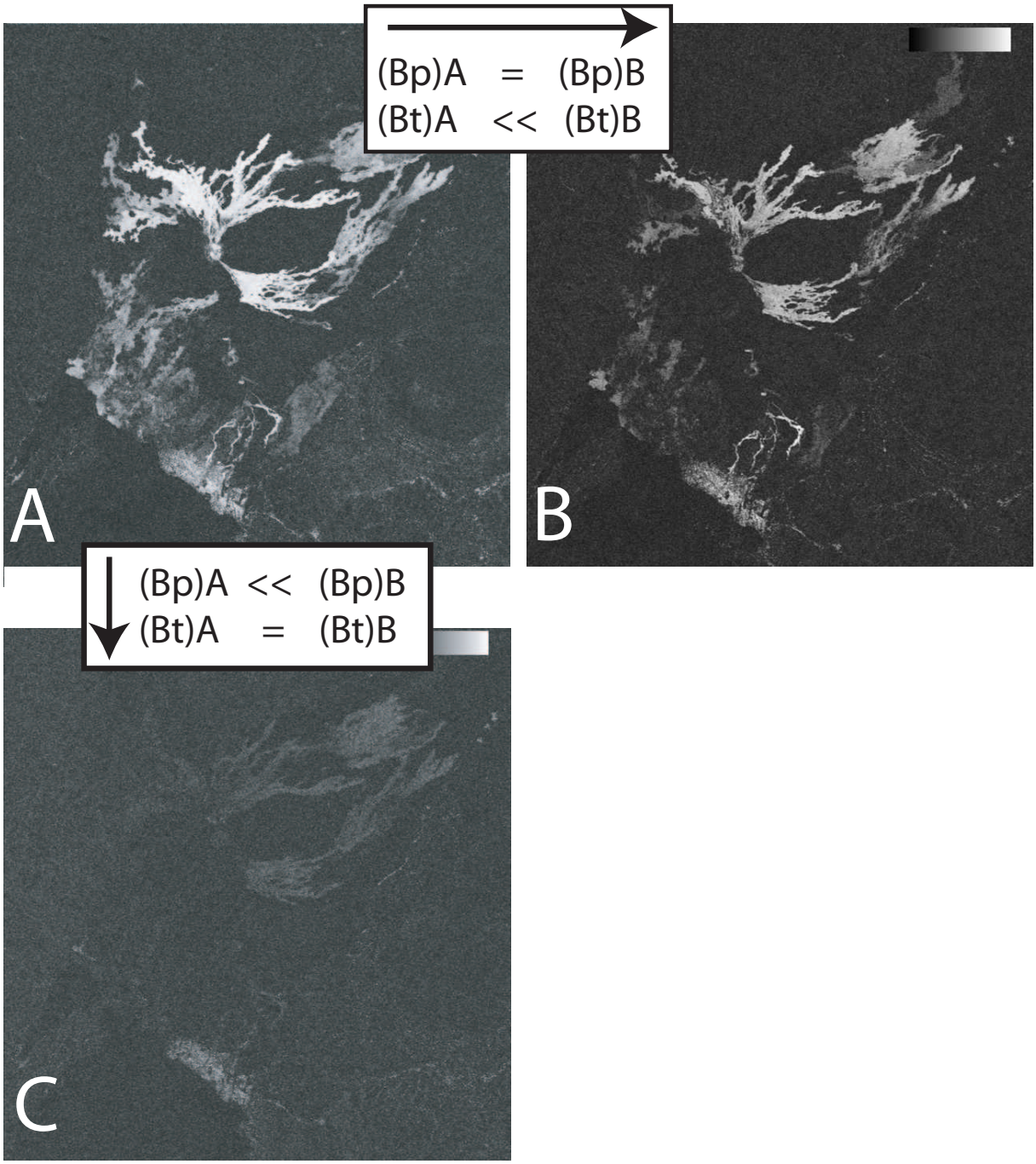

Figure 2.15: Coherence images from ENVISAT ascending interferograms of the North Kivu Virunga area, RDC. The time spans (B_t) for the A, B and C coherence images are 35, 315 and 35 days respectively. The perpendicular baselines (B_p) for the A, B and C coherence images are 77, 75 and 826 meters respectively

Geometric decorrelation (γ_{geom})

The baseline or geometric decorrelation (γ_{geom}) is caused by the two different local incidence angles. The amount of decorrelation increases linearly with the amount of spectral shift between the two SAR acquisitions. Spectral shift can be due to topography, atmosphere or deformation. The fundamental condition for interferometry, expresses that a pixel must not stretch or shrink by more than a fraction of the wavelength from one image to another [*Massonet and Feigl*, 1998]:

$$2l\ (sin\,\theta_1\ - sin\,\theta_2)\ <\ \lambda \tag{2.17}$$

where l is the length perpendicular to the trajectory of a pixel on the ground ($\approx$ 20 m for ERS), λ is the wavelength (6cm), and θ_1 and θ_2 are the local incidence angles.

For the topography, the baseline decorrelation depends on the critical baseline $B_{\perp,crit}$, which is the baseline causing a spectral shift equal to the bandwidth BR. It is a function of the wavelength λ, the incidence angle θ_{inc}, and the topographic slope ς, and is defined positively away from the satellite [*Hanssen*, 2001]:

$$B_{\perp,crit}\ =\ \lambda\frac{B_R}{c}R_1 tan(\theta_{inc}-\varsigma) \tag{2.18}$$

The geometric decorrelation due to topography can thus be defined as [*Hanssen*, 2001]:

$$|\gamma_{geom,topo}|\ =\ \begin{matrix}\frac{B_{\perp,crit}-B_\perp}{B_{\perp,crit}} & |B_\perp|\le B_{\perp,crit}\\ 0 & |B_\perp|> B_{\perp,crit}\end{matrix} \tag{2.19}$$

For a flat horizontal terrain, the ERS critical baseline is approximately 1.1 km. However, in practical cases, as depicted in Figure 2.15, the phase correlation is already low with a perpendicular baseline (B_p) larger than 600 meters. C-band interferograms with baselines (B_p) larger than 600 meters will therefore be considered as too noisy for an analysis. However, as shown in Figure 2.16, the critical baseline increases with the wavelength, and L-band interferograms such as JERS or ALOS will have a larger critical baseline (until about 6 and 13 km, respectively) and higher overall phase correlations.

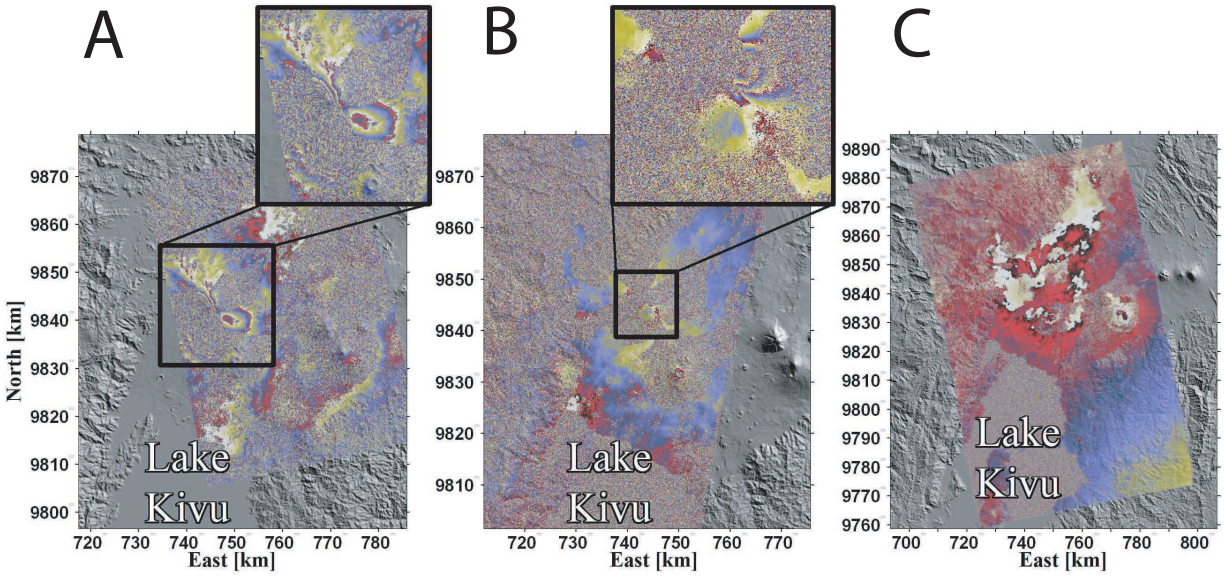

Figure 2.16: Comparison of three interferograms covering the Nyamulagira-Nyiragongo area. From left to right: A) ENVISAT C-band ascending interferogram spanning the 2006 eruption, Bp = 197 m, inc. ang. = 44°, Bt = 35 days. The inset shows the displacement field on the slopes of the Nyamulagira volcano. B) JERS L-band descending interferogram spanning 1996 eruption, Bp = 152 m, inc. ang. 34°, Bt = 132 days. The inset shows the displacement field on the northern flank of the Nyamulagira volcano. C) ALOS L-band ascending interferogram spanning no particular event. No clear deformation is visible. Bp = 400 m, inc. ang. = 34°, Bt = 92 days. Correlation of the ALOS interferogram is clearly better than for the other interferograms over the whole area.

The maximum detectable ground deformation gradient is one fringe per pixel, or the dimensionless ratio of the wavelength to the pixel size [*Hanssen*, 2001]; this value depends thus on the radar sensor. The maximum detectable deformation gradient is 3×10^{-3} for ERS and 13×10^{-3} for JERS. For instance, the coseismic deformation during the Gelai crisis in North Tanzania locally exceeds this threshold in C-band ENVISAT interferograms, creating decorrelated pixels (Figure 2.17C). For gradual movements, we must choose time spans between images such that the displacement gradients remain below this threshold.

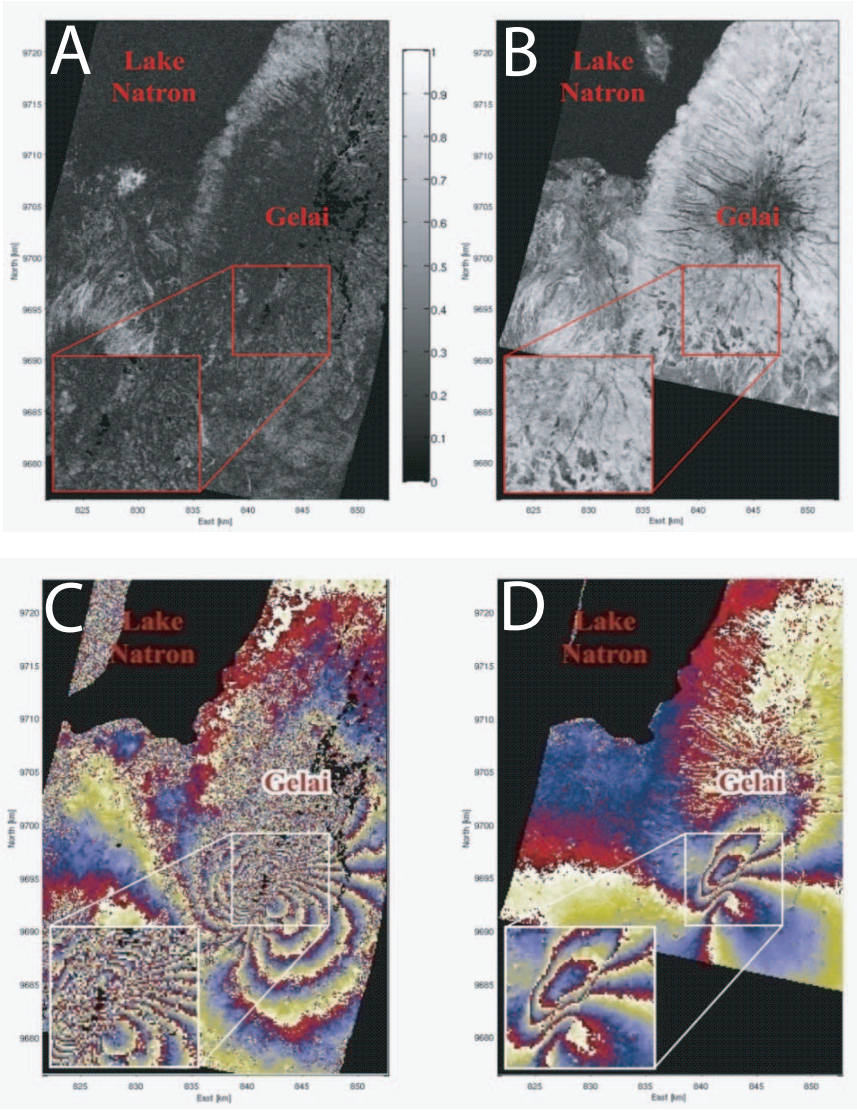

Figure 2.17: Comparison of two coherence images (A and B) and interferograms (C and D) covering the Lake Natron area. From left to right: A) ENVISAT C-band ascending interferogram spanning the 2007 rifting crisis, Bp = -28.5 m, inc. ang. = 23°, Bt = 175 days. B) ALOS L-band ascending interferogram spanning the event, Bp = -544 m, inc. ang. = 34°, Bt = 46 days. Coherence of the ALOS interferogram is clearly better than for the other interferogram over the whole area. Some surface ruptures are visible on the inset of the ALOS coherence (B). Some areas of *C* are affected by incoherence induced by too large gradients of deformation. Insets show the southern Gelai flank which was the most affected by the magmato-seismic crisis and surface ruptures. Modified after [*Oyen et al.*, 2008]

Doppler Centroid Decorrelation (γ_{DC})

The Doppler centroid decorrelation (γ_{DC}) is caused by the differences in the Doppler centroids between the two acquisitions. This problem explains for instance why all ERS-2 data over our targets in Africa during year 2001 are unusable. From 7 February 2000, an error in two out of three gyroscopes of ERS-2 reduced its Doppler steering capabilities [*Hanssen*, 2001]. This effect can also be significant with RADARSAT-1 data.

Volume (γ_{vol}) and Temporal Terrain Decorrelations ($\gamma_{temporal}$)

The volume decorrelation (γ_{vol}) is caused by the penetration of the radar signal in the scattering medium (Figure 2.15), while the temporal terrain decorrelation ($\gamma_{temporal}$) is caused by physical changes in the imaged terrain, affecting thus the scattering characteristics of the surface (Figure 2.17B). The scattering component of the phase (φ_{scat} in Equation 2.6) is a function of the distribution of scatterers and the viewing direction of the radar [*Hanssen*, 2001]. Useful correlated interferometric phase observations are only possible whenever the scattering components φ_{scat,t_i} are more or less the same during each of the two acquisitions, expressed by the temporal coherence $\gamma_{temporal}$. High temporal coherence values are obtained for areas without or with a very sparse vegetation such as arid or polar areas. It is better to use longer wavelengths radar data, for instance L-band over C or X-band data, in vegetated areas, since these instruments are less sensitive to small changes in the scattering characteristics (Figures 2.17 and 2.16).

The Thermal ($\gamma_{thermal}$) and Processing Decorrelations ($\gamma_{processing}$)

The thermal decorrelation ($\gamma_{thermal}$) is caused by changing characteristics of the system, including gain factors and antenna characteristics. It can be estimated theoretically by determining the signal-to-noise ratio of a specific system [*Zebker et al.*, 1994b] [*Zebker*, 1996]. Finally, the processing induced decorrelation ($\gamma_{processing}$) results from the chosen algorithms, for coregistration and interpolation for instance [*Hanssen*, 2001]. As depicted in Figure 2.16, the JERS interferograms are for instance affected by much more instrumental noise than the ALOS data, thus even with a smaller perpendicular baseline, the JERS interferogram is of worse quality than a similar ALOS one

2.1.7 InSAR Softwares

In this study, free softwares such as Doris [*Kampes et al.*, 2003] or ROI-PAC [*Rosen et al.*, 2004] are used. With the exception of the RADARSAT-2 data processing which is made with the commercial Gamma software. All the algorithms and procedures implemented in this package are described in various documentation of the software such as [*Buckley*, 2000]. Generally, for the study of a particular deformation event, ROI-PAC will be used following the steps depicted in Figure 2.18, while for the time-series analysis with StaMPS, Doris will be used to process the interferograms.

For ENVISAT and ERS, the orbits used will be those provided by ESA. For RADARSAT, ALOS and JERS, the orbits information used are in the image header file. Note that when starting from raw data, the ROI-PAC focusing is an actual Doppler algorithm. However, when starting

from the SLC data, the focusing (made by ESA) is a Zero-Doppler focusing approach. Data are then filtered with an adaptative filter that takes the coherence into account. If necessary, a linear orbital trend is removed from the wrapped filtered data and the result is unwrapped again with the Snaphu algorithm. The multilooking factor for the interferogram is adapted on a case-by-case basis.

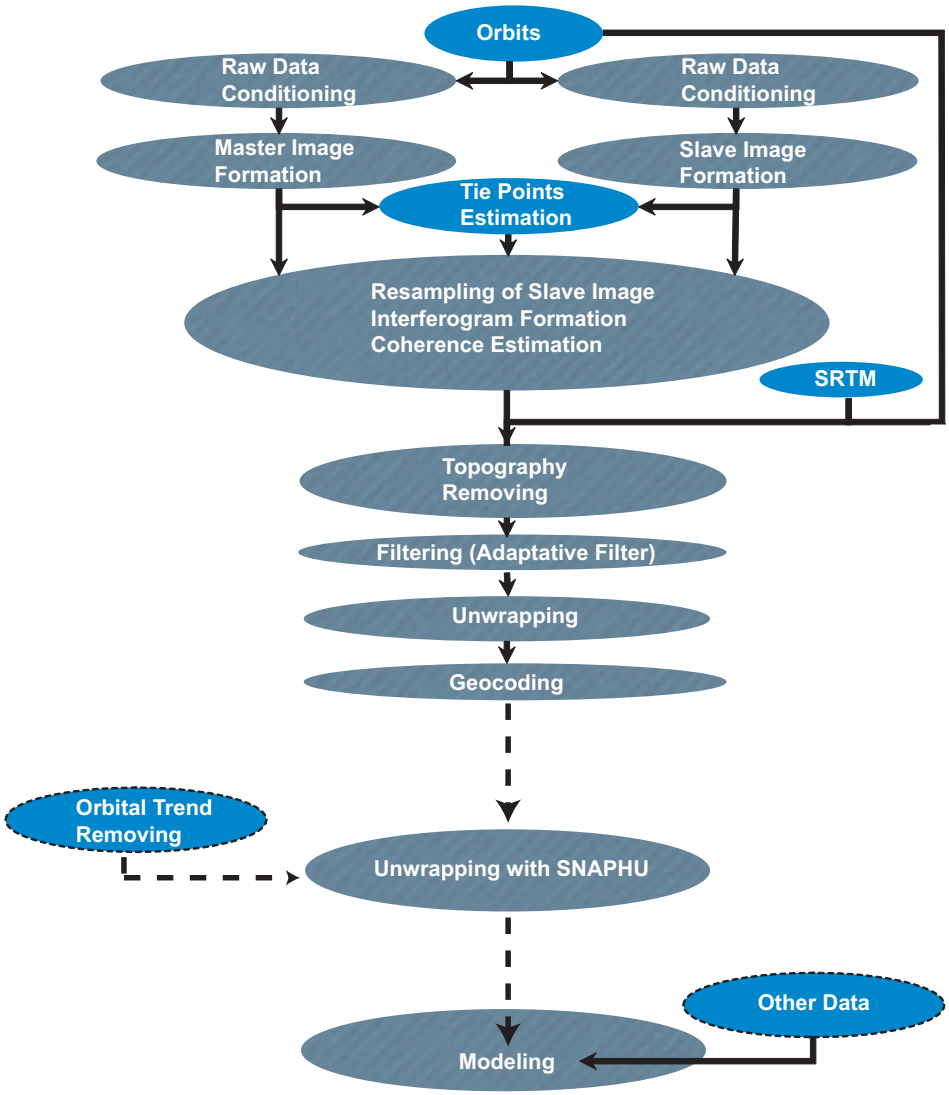

Figure 2.18: The ROI-PAC simplified two-pass processing flowchart as used in this study, modified after [*Fielding*, 2010]

2.2 Multi-Temporal InSAR

Interesting extensions of conventional InSAR are the multi-temporal InSAR techniques (MT-InSAR). Their goal is to address some of the conventional InSAR limitations such as the phase errors induced by decorrelation, topographic errors and atmospheric delays. MT-InSAR techniques involve the processing of multiple SAR acquisitions over the same area, allowing for the correction of uncorrelated phase noise terms, and reducing errors associated with the ground deformation measurements. Two classes of MT-InSAR algorithms are defined: the persistent

scatterers (PS) and small baseline (SBAS) methods. Each of these set of methods is designed for a specific type of scattering mechanism [*Hooper*, 2008].

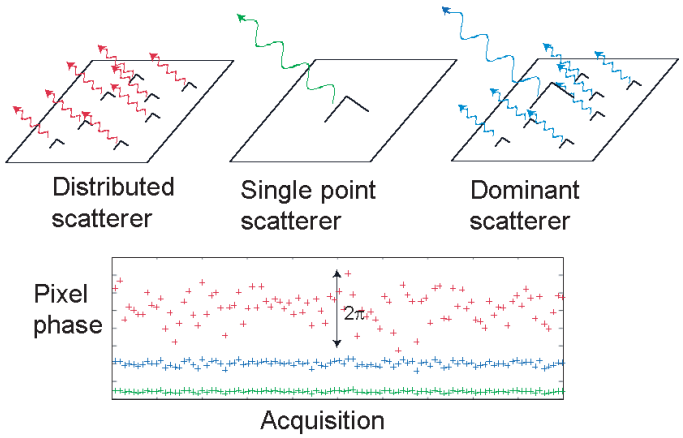

Figure 2.19: Scattering mechanism models for a SAR resolution cell: distributed scatterers (red), ideal single point scatterer (green) and persistent scatterer (blue). The persistent scatterer has a much smaller phase variation than the distributed scatterer. After [*Shanker*, 2010].

In PS methods, the pixels can be identified from their phase variation in time [*Ferretti et al.*, 2001] [*Kampes*, 2010] or in space [*Hooper et al.*, 2004] [*van der Kooij et al.*, 2006] [*Hooper*, 2008]. As we saw previously, the pixel value in a SAR image is the sum of the contribution of all the scatterers present within this resolution cell (Figure 2.19). A PS pixel is a pixel in which a single scatterer dominates, while the other scatterers contributions are negligible. The received signal is stable as the phase contribution of decorrelation will be almost constant in time.

When a pixel contains several scatterers with similar strength (distributed scatterer in Figure 2.19), the phase variation due to decorrelation in time will mask the signal of interest, with a random, and thus useless, interferometric phase. This kind of pixels are actually a large part of the pixels in natural vegetated terrains. A way to overcome this issue, with minimizing the decorrelation, is to form interferograms only with short temporal (B_t) and spatial perpendicular baselines (B_p). A spectral filter in range and in azimuth can also be used to decrease the decorrelation [*Hooper*, 2008]. Hence, these SBAS pixels will have a phase which decorrelates little over short time periods. Simple stack of interferograms [*Sandwell and Price*, 1998] is actually the simplest form of SBAS approaches, with the calculation of an average velocity model, and allows the mitigation of atmospheric effects, by averaging several interferograms.

2.2.1 The StaMPS Software Package

The Stanford Method for PS (*StaMPS*) was initially developed for PS applications in natural terrain [*Hooper et al.*, 2004] [*Hooper et al.*, 2007] and since, has been extended to include also a small baseline approach [*Hooper*, 2008]. Presently, we can combine both approaches, to extract the deformation signal at more points (Figure 2.20) and with a higher overall signal-to-noise ratio than can either approach do alone [*Hooper*, 2008].

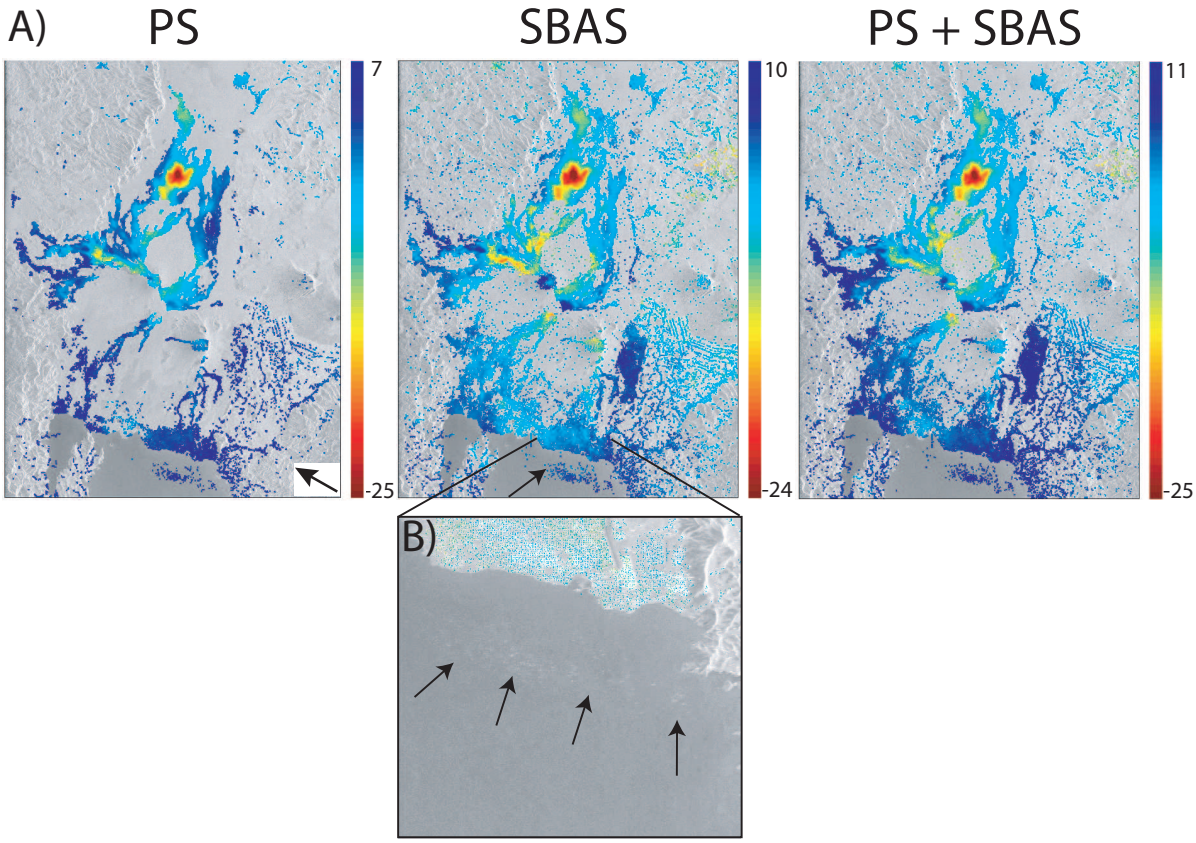

Figure 2.20: Comparison of selected pixels by the PS (left), SBAS (middle) and the combined approach (PS + SBAS, right), showed with the mean LOS velocity map, corrected for the topographic error, obtained fur the all ENVISAT descending scene (time span: 2003/01/16 - 2010/03/25) using the StaMPS package. The number of pixels selected before merging are 194,140, 2,202,033 and 2,205,000, respectively. The SBAS and the combined approach (PS + SBAS) allow us thus to select more than 11 times pixels than the PS approach alone. After merging, mainly to have numerical manageable number of pixels and to facilitate the unwrapping, with a resample size of 200 m, these numbers decrease to 26,767, 26,951 and 49,434, respectively.

As we are interested in studying ground deformation, the interferometric phase of deformation interferograms is studied. However, added to the useful deformation information remain several phase components which can contaminate the signal of interest [*Hooper et al.*, 2004] [*Shanker*, 2010]:

$$\phi_{int,x,i} = \phi_{defo,x,i} + \Delta\phi_{\epsilon,x,i} + \phi_{atmo,x,i} + \Delta\phi_{orb,x,i} + \phi_{noise,x,i} \tag{2.20}$$

where $\phi_{defo,x,i}$ represents the phase due to deformation, $\Delta\phi_{\epsilon,x,i}$ refers to the error introduced by using imprecise topographic information, $\Delta\phi_{orb,x,i}$ refers to the error introduced due to the use of inaccurate orbit trajectories, $\phi_{atmo,x,i}$ corresponds to the atmospheric delay between the two acquisition used to form the interferogram and $\phi_{noise,x,i}$ represents the phase noise due to the scattering background and other uncorrelated noise terms. x represents the spatial index of the considered pixel in interferogram i.

PS pixels are the pixels with very little variation in the scatterer noise term ($\phi_{noise,x,i}$ negligible). A set of spatial and temporal filtering routines are included in the StaMPS package. They allow the estimation of each phase contributions of Equation 2.20 by assuming their spectral

behavior. Table 2.2 presents the assumed spectral properties for each contribution. The low pass contribution from Table 2.2 are estimated using a combination of a low pass filter and an adaptive phase filter [*Hooper et al.*, 2007] to preserve the wrapped interferometric fringes.

	Origin	*Spatial Component*	*Temporal Component*
$\phi_{defo,x,i}$	Deformation	Low freq	Low freq
$\phi_{atmo,x,i}$	Atmosphere	Low freq	High freq
$\Delta\phi_{orb,x,i}$	Orbital errors	Low freq	High freq
$\phi_{noise,x,i}$	Scatterer noise	High freq	High freq
$\Delta\phi_{\epsilon,x,i}$	DEM Error	High freq	Correlated with baseline

Table 2.2: Spectral characteristics for various phase components of the observed interferometric phase for a PS pixel, after [*Hooper*, 2006]

Table 2.2 shows that the deformation signal, the atmospheric phase delay, and orbital errors are spatially correlated and can be thus estimated simultaneously as a combined term for each interferogram. The DEM error term can be estimated on a pixel-by-pixel basis. The various steps involved in the estimation of the spatially correlated phase terms are shown in Figure 2.21.

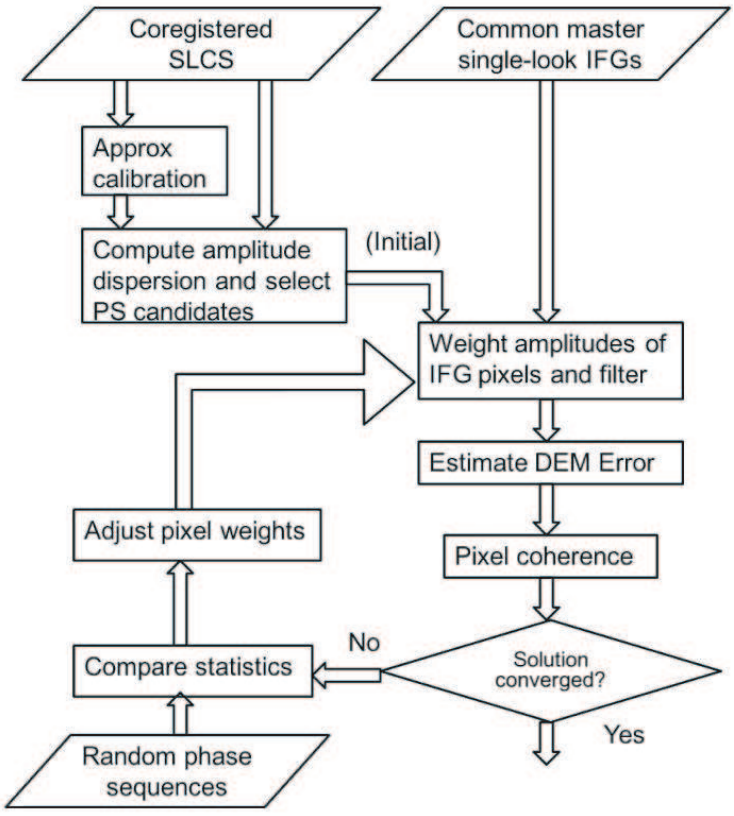

Figure 2.21: The StaMPS package workflow for estimating spatially correlated phase terms for every PS candidate in each interferogram. The outputs of this processing step include estimates of spatially correlated terms, geometric errors and pixel coherences. After [*Shanker*, 2010]

2.3 POLarimetric InSAR (POLInSAR)

POLInSAR differs from conventional InSAR in that it allows generation of interferograms for arbitrary transmit/receive polarization pairs. The polarization of a radar wave being a function of the geometrical and electronical properties of the ground target, it can be used to characterize and classify natural and artificial surfaces. The phase of an interferogram changes with the choice of polarization, and consequently, important bio and geophysical parameters can be extracted by interpreting this change in the right way. POLInSAR allows us to overcome limitations of InSAR and polarimetry techniques when taken alone [*Cloude*, 2007].

2.3.1 Polarization

As we saw in the first section of this chapter, an electromagnetic wave is characterized by an amplitude, a phase, and also by a give polarization (Figure 2.3). The polarization of an electromagnetic (EM) wave describes the orientation of the electric field in a plane perpendicular to the propagation direction. For a plane electromagnetic wave, the length of the electric field vector represents the amplitude of the wave. The rotation rate of this vector is the frequency of the wave, while the polarization is the orientation and shape of the pattern traced by the end of the vector [*CCR*, 2011].

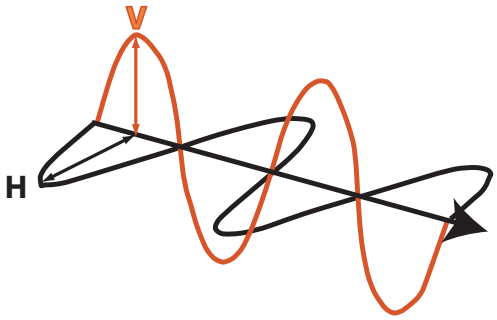

Figure 2.22: Examples of horizontal (black) and vertical (red) polarizations of a plane electromagnetic wave

The waveform of the electric field of an EM wave can be predictable - the wave is either polarized - or random - or the wave is unpolarized - or a combination of both. As depicted in Figure 2.22, an example of a fully polarized wave would be a monochromatic sine wave, with a single, constant frequency and stable amplitude.

Many radars are designed to transmit microwave radiation that is either horizontally polarized (H) or vertically polarized (V). A transmitted wave of either polarization can generate a backscattered wave with a variety of polarizations. It is the analysis of these transmitted and received polarization combinations that constitutes the science of radar polarimetry. Any polarization on either transmission or reception can be synthesized by using H and V components with a well-defined relationship between them. For this reason, systems that transmit and receive both of these linear polarizations are commonly used. With these radars, there can be four combinations of transmitted and received polarizations: HH (horizontally transmitted and horizontally received), VV (vertically transmitted and vertically received), HV (horizontally transmitted and vertically received), and VH (for vertically transmitted and horizontally received). Radar systems

can be single polarized, dual polarized or fully polarimetric such as RADARSAT-2 for instance (Table 2.1).

As wavelength, the polarization affects how a radar system sees the elements in the scene. Therefore, radar imagery collected using different polarization and wavelength combinations may provide different and complementary information. Furthermore, when three polarizations are combined in a color composite, the information is presented in a way that an image interpreter can get information on the surface characteristics. These are the principles behind the polarimetry technique which has successful applications in agriculture, forestry, geology... essentially for mapping purposes. [*CCR*, 2011]

2.3.2 The POLInSAR Approach

POLInSAR algorithms use signal coherence (or phase and local phase variance) rather than backscattered power. Full polarimetric sensors provide three independent polarimetric measurements of the radar signal backscattered by the terrain: HH, VV, HV and VH. In the case of backscattering, HV and VH channels are equal, leading thus to three independent measurements.

Full polarimetric sensors measure the complex scattering matrix for each resolution cell of the observed scene for the two SAR acquisitions, leading to the following two scattering matrices S_1 and S_2 [*Lopez-Martinez et al.*, 2005], each corresponding to a SAR scene:

$$S_1 = \begin{pmatrix} S^1_{HH} & S^1_{HV} \\ S^1_{VH} & S^1_{VV} \end{pmatrix} \qquad and \qquad S_2 = \begin{pmatrix} S^2_{HH} & S^2_{HV} \\ S^2_{VH} & S^2_{VV} \end{pmatrix} \tag{2.21}$$

Assuming reciprocal scattering, the corresponding three-dimensional Pauli-scattering vectors k_1 and k_2 are [*Cloude and Papathanassiou*, 1997]:

$$k_1 = \frac{1}{\sqrt{2}} \left[S^1_{HH} + S^1_{VV} \; S^1_{HH} - S^1_{VV} \; 2S^1_{HV}\right]^T \quad and \quad k_2 = \frac{1}{\sqrt{2}} \left[S^2_{HH} + S^2_{VV} \; S^2_{HH} - S^2_{VV} \; 2S^2_{HV}\right]^T \tag{2.22}$$

The complete information measured by the SAR sensor can be represented in form of three 3×3 complex matrices T_{11}, T_{22} and Ω_{12}:

$$T_{11} = k_1^*.k_1 \qquad T_{22} = k_2^*.k_2 \qquad \Omega_{12} = k_1^*.k_2 \tag{2.23}$$

where k_1^* and k_2^* are the conjugate of the complex vectors k_1 and k_2.T_{11} and T_{22} are the conventional Hermitian polarimetric coherency matrices [1], which describe the polarimetric properties of each individual image, while Ω_{12} is a non-Hermitian complex matrix which contains the polarimetric and interferometric information [*Lopez-Martinez et al.*, 2005].

w_1 and w_2 are the two normalized target vectors which correspond to the two scattering mechanisms optimizing the coherence and $w_1^\dagger$ and $w_2^\dagger$ are their complex conjugates $\mu_1 = w_1^\dagger.k_1$ and $\mu_2 = w_2^\dagger.k_2$ are the backscattering coefficients. By analogy with scalar interferometry (Equation 2.13), we can express the coherence as [*Deraw*, 2007]:

[1] A hermitian matrix $A^\dagger$ is a square matrix with complex entries equal to its own conjugate transpose, such that the element of the i-th row and j-th column equals the complex conjugate of the element of the j-th row and i-th column $a_{i,j} = a^*_{j,i}$

$$\gamma \;=\; \frac{|\langle \mu_1\, \mu_2^* \rangle|}{\sqrt{\langle \mu_1 \mu_1^* \rangle\, \langle \mu_2 \mu_2^* \rangle}} \;=\; \frac{\left|\left\langle w_1^\dagger \Omega_{12} w_2^\dagger \right\rangle\right|}{\sqrt{\left\langle w_1^\dagger T_{11} w_1 \right\rangle \left\langle w_2^\dagger T_{22} w_2 \right\rangle}} \tag{2.24}$$

The coherence (2.24) can be optimized using the maximization of the Lagrangian function [*Deraw*, 2007]:

$$L \;=\; |w_1^\dagger\, \Omega_{12}\, w_2^\dagger| + \lambda_1 (w_1^\dagger\, T_{11}\, w_1 \;-\; C_1) \;+\; \lambda_2 (w_2^\dagger\, T_{22}\, w_2 \;-\; C_2) \tag{2.25}$$

which gives the following eigenvalue problem:

$$\nu\, w_2 \;=\; T_{22}^{-1}\, \Omega_{12}^\dagger\, T_{11}^{-1}\, \Omega_{12}\, w_2 \qquad \textit{and} \qquad \nu\, w_1 \;=\; T_{11}^{-1}\, \Omega_{12}\, T_{22}^{-1}\, \Omega_{12}^\dagger\, w_1 \tag{2.26}$$

Resolving this system will lead to the optimum coherence given as the maximum eigenvalue [*Deraw*, 2007]:

$$\gamma_{max} \;=\; \sqrt{\nu_{max}} \tag{2.27}$$

The eigenvectors w_1 and w_2 associated with the maximum eigenvalue correspond therefore to the scattering mechanism in each acquisition which optimizes the coherence and allows to generate the *best optimized* interferogram [*Deraw*, 2007]:

$$\mu_{1,opt}\, \mu_{1,opt}^* \;=\; w_{1,opt}^\dagger\, \Omega_{12}\, w_{2,opt} \tag{2.28}$$

Finally, the coherence optimization leads to three optimized coherences. Each corresponds to an independent scattering mechanism and to three interferograms indicating the mean location of the mechanism center [*Deraw*, 2007].

The Polarimetric SAR Data Processing and Educational Tool (PolSARpro) aims to facilitate the accessibility and exploitation of multi-polarised SAR datasets including those from ESA Third Party Missions (ALOS PALSAR), Envisat ASAR Alternating Polarisation mode products, RADARSAT-2 and TerraSAR-X. PolSARpro is developed under contract to ESA by a consortium comprising IETR at the University of Rennes 1, The Microwaves and Radar Institute (HR) of DLR and AEL Consultants, together with Dr Mark Williams. All elements of the PolSARpro project are distributed by ESA free of charge, including the source code. The results presented in the following case-study are obtained using PolSARpro software.

Case-Study: La Palma Island, Canary Islands

La Palma in the Canary Islands (Spain) is an active volcanic area (Figure 2.23). This area is monitored by C-band InSAR satellites such as ERS and ENVISAT *[P. Gonzalez and J. Fernandez, pers. com., 2009]*. Several areas in La Palma Island are covered by dense vegetation, leading to rapid decorrelations. After two to three acquisition cycles (i.e. 2-3 months), even for interferograms with small perpendicular baselines, coherence is only maintained in areas covered by recent lava flows [*Perlock and et al.*, 2008]. The ALOS/PALSAR sensor can therefore bring information missing with C-band monitoring. The new L-band ALOS interferograms calculated for this island show very good coherence on the whole island for perpendicular baselines inferior

to about 700 meters, even for larger time spans up to one year. For comparison with the ALOS data, we have used a couple of full polarimetric Quad-Pol images covering the southern part of the island. This couple was studied by means of the POLInSAR technique.

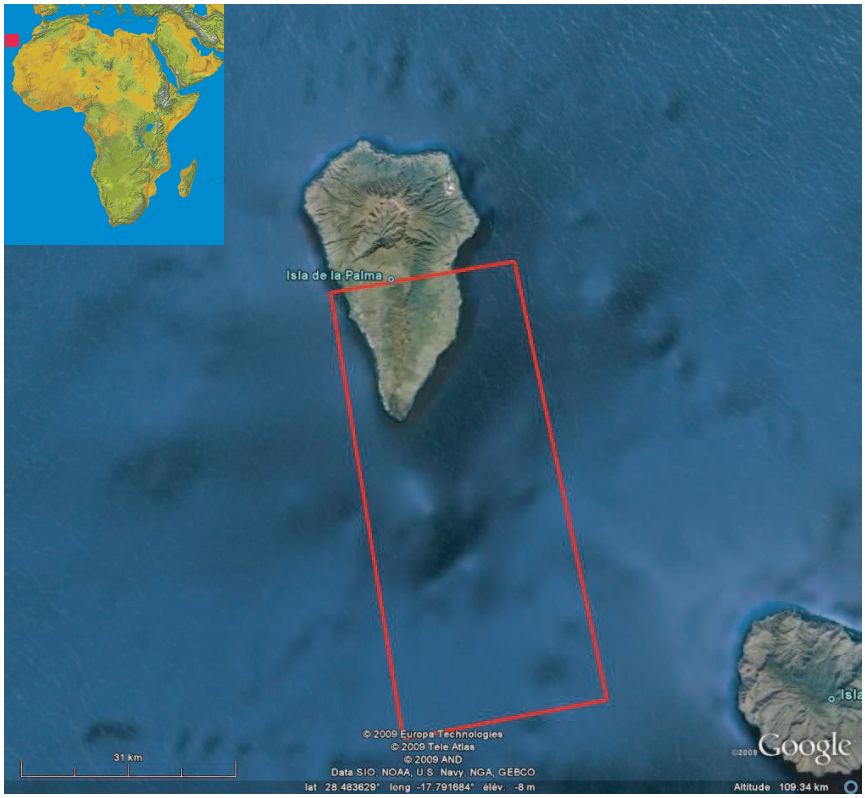

Figure 2.23: Location of La Palma island. The red rectangle shows the ALOS Quad-Pol image swath area

Coherences obtained for the HH, VV and HV polarization modes (the classic mode used in interferometry is HH) and the optimized coherences [*Cloude and Papathanassiou*, 1998] are shown in Figure 2.24A. The optimized coherence histogram on the island is clearly narrowed by the optimization procedure and the distribution peak shifted towards higher coherence values (from ≈ 0.2 to 0.5), especially for the optimized coherence derived from the first eigenvalue (Coherence opt1 in Figure 2.24B). The corresponding optimized phase signal is therefore improved. However, this gain is of limited interest regarding volcano monitoring applications in this area. First, HH L-band ALOS InSAR already offers fully satisfactory coherent interferograms with higher resolution. Initial results, obtained from Quad-Pol data and the POLInSAR technique, are potentially interesting in order to improve phase signal quality as shown for La Palma Island. The Quad-POL data have a worse spatial resolution than the other PALSAR products ($\approx$ 20 m for the full polarimetric mode against $\approx$ 10 m in the fine beam standard more) and the gain is not really a surplus value in our applications. Second, PALSAR full polarimetric mode is an experimental mode, the available number of Quad-POL images is therefore limited, especially for African areas. Therefore, the monitoring of these area by means of Quad-Pol POLInSAR on a regular basis is currently not feasible.

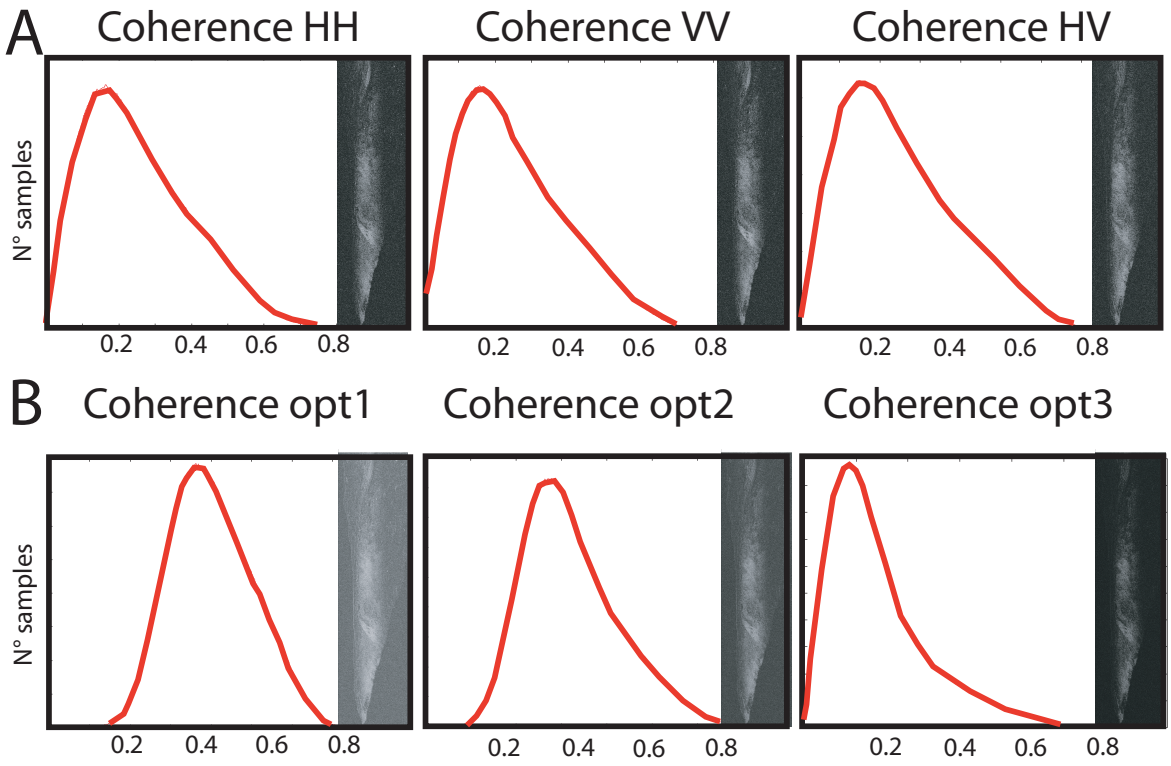

Figure 2.24: Coherence distributions and images for South of La Palma Island: A: a) HH classic polarization mode, b) VV polarization, c) HV polarization. B: a) Optimized coherence 1, b) Optimized coherence 2, and c) Optimized coherence 3.

Chapter 3

Modeling and Inversions

In this chapter the modeling and inversion of the used InSAR ground displacements methods is described. Sensitivity of the model to the topographic and sources meshes is also studied. Finally synthetic tests considering a dike connected to the ground are described to evaluate which dike parameters can effectively be resolved and how the resolution is improved when using several viewing geometries. This study is of general interest as, with the increased number of SAR data available, studying fault and volcano deformations with multiple viewing geometries is becoming more widespread.

3.1 Modeling

To determine the sources of the observed InSAR displacements, a method that combines a 3D numerical modeling method and a Monte Carlo inversion method is used [*Fukushima et al.*, 2005].

3.1.1 3D Boundary Element Modeling

The numerical modeling method is a mixed boundary element method (MBEM) [*Cayol and Cornet*, 1997], based on the combination of two boundary element methods: the direct [*Rizzo*, 1967] and displacement discontinuity methods [*Crouch*, 1976]. The direct method allows accurate and fast modeling of structures such as topography, cavities or reservoirs, whereas the displacement discontinuity method is suitable for fractures. With this method, mechanical interactions between sources are taken into account.

The edifice is assumed to be linearly elastic, homogeneous and isotropic. Except if explicitly mentioned in the Chapter 4,the Young's modulus and Poisson's ratio are fixed to values of 5 GPa and 0.25 respectively, a value deducted from a seismic velocity profile of the Virunga area [*Mavonga*, 2010] and corrected by a factor of 0.25 to account for the difference between static and dynamic modulus at sea level [*Cheng and Johnston*, 1981b]. Indeed, preliminary models of the Nyiragongo 2002 and Nyamulagira eruptive dikes showed that this dike was emplaced around that depth. For a detailed discussion on the elastic parameters in the case of the Nyiragongo 2002 modeling see Section 4.1.4 in Chapter 4.

When dikes are connected to the ground surface, they are assumed to be roughly quadrangles, with their top part corresponding to the eruptive fissure, and their bottom part corresponding

to a straight line defined by 6 parameters (Figure 3.1) chosen in order to be able to restrict the model search to mechanically plausible models [*Fukushima et al.*, 2005]. Three parameters *Dip* (dip angle), *Shear* (angle between the dip direction and the line connecting the top and bottom line midpoints) and *Botelv* (elevation of the bottom line midpoint with reference to sea level) define the location of the bottom line midpoint. Three other parameters *Botlen* (length of the bottom side scaled to that of the top side), *Twist* (horizontal angle between the top and bottom sides) and *Botang* (vertical angle of the bottom side) determine the position of the two end points of the bottom line. The top line location of the main quadrangular part can also be inverted if needed by adding until four extra parameters (*northern* and *southern ends* coordinates in Figure 3.2).

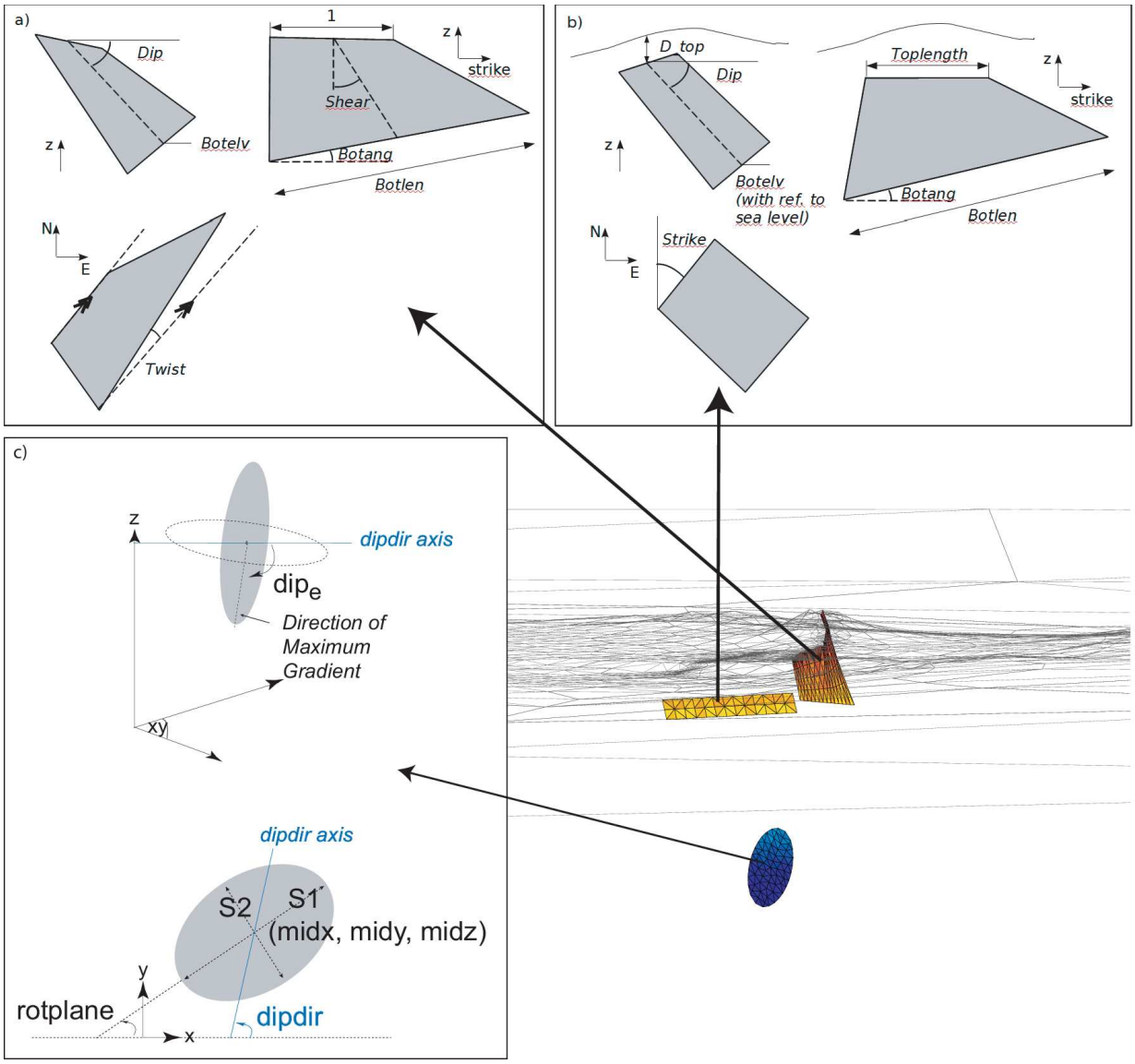

Figure 3.1: For the modeling, the sources and the topography are meshed. Three types of source are studied using the following geometrical parameters: (a) a dike reaching and (b) a dike - or a fault - not reaching the ground surface. (c) A deflating reservoir. See text for the parameters explanation.

If the dike is connected to several fissures at the surface, more sophisticated parameters can be added to define the geometry of this connection, see [*Fukushima et al.*, 2005] and Figure 3.2

for a detailed explanation. In Chapter 4, the inverted parameters will systematically be given on a case-by-case basis.

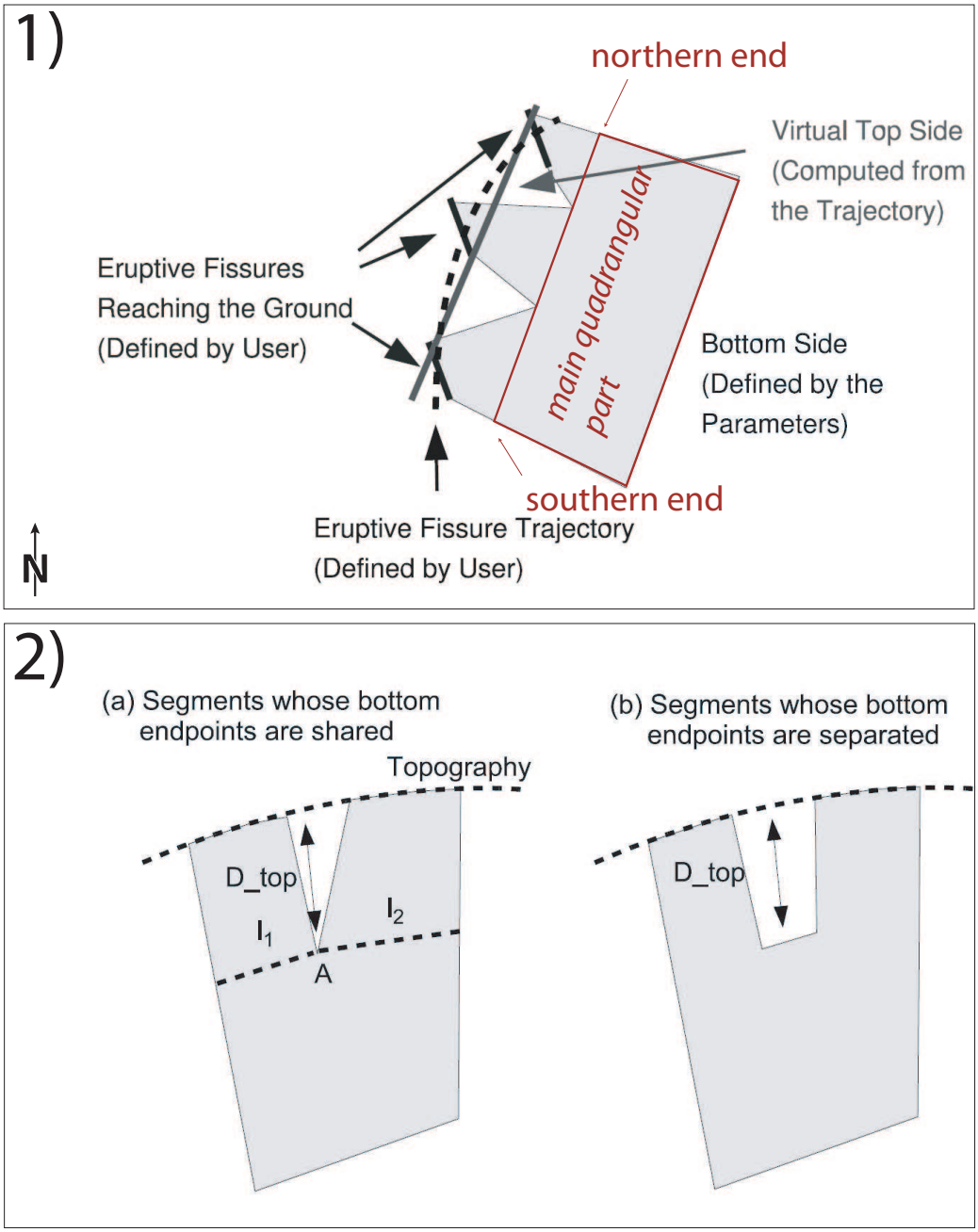

Figure 3.2: 1) Virtual top side is used as a reference to determine the geometry of the bottom side, it is defined from the eruptive fissure trajectory in such a way that it parallels the line connecting the endpoints of the trajectory and its midpoint coincides the mean of the trajectory. The topside location (*northern* and *southern ends*) of the main quadrangular part can also be defined by the user. 2) Schematic figure explaining the parameterization of the segmented part. D_{top} is the along-dip length of the segmented parts. (a) Two segments share an endpoint. *Segmentgeom* defines the ratio of the bottom lengths of two segments. D_{top} and *Segmentgeom* (l_1, l_2) define the position of the joint point A on the curved dike surface. (b) Two segments can also be apart from each other. Modified after [*Fukushima et al.*, 2005].

To keep the number of parameters reasonably low for an efficient inversion, dikes - or faults - not connected to the ground surface are assumed to have a simpler quadrangular shape, with

straight top and bottom sides (Figure 3.1). The top side, assumed to be horizontal, is defined by three parameters, $Toplength$ (length), D_{top} (average depth below the ground surface), and Strike (angle with respect to the north direction). The bottom side is defined by three other parameters, Dip (dip angle), $Botelv$ (elevation of the bottom line midpoint above sea level), $Botlen$ (length of the bottom side scaled to that of the top side) and $Botang$ (vertical angle of the bottom side).

Magmatic reservoirs are represented by elliptic sources defined by eight geometrical parameters (Figure 3.1). $(midx, midy, midz)$ define the position of the ellipse center, S_1 and S_2 define the lengths of the two axes (with $S_1 > S_2$), the ellipse is rotated in the xy plane (anticlockwise from x-axis) of a $Rotplane$ angle, dipped in the direction defined by $Dipdir$ (anticlockwise from x-axis) of a Dip_e angle (measured from horizontal, an horizontal ellipse will thus have a $Dip_e = 0$). [*Fukushima et al.*, 2005]

The prescribed boundary conditions are tractions which are assumed to be perturbations of an initial state of stress. Tractions are zero at the ground surface, and are equal to overpressures on dikes or reservoirs, or to shear stress drops along faults [*Cayol and Cornet*, 1997]. In this study, constant dike overpressures are assumed, as a previous study showed, that pressure gradients could not be constrained [*Fukushima et al.*, 2005]. The dike and fault geometries are inverted simultaneously as the tractions, leading to a minimum of seven parameters per structure.

Topographic Mesh

Topographic boundary is meshed by planar triangular elements. In order for the limited extension of the mesh to have a negligible influence on computed displacements (less than 2%), the size of topographic meshes is ten times larger than the maximum horizontal dimension of the deformation source [*Cayol*, 1996]. The density of topographic mesh will be case-dependent and compromises have to be found between the model accuracy and the calculation time. The topographic mesh is dense close to the deformation sources where displacement gradients are the largest and becomes coarser further away. A previous study [*Wauthier*, 2007] showed that the nodes density close to the eruptive fissure(s) is the most critical parameter for the model accuracy (Figure 3.3). For the Nyiragongo 2002 eruption, it was determined that the topographic mesh adjoining the eruptive fissures should have elements with at least 200 meters interval in order to obtain a realistic opening distribution (Figure 3.3). We determine that, far from the deformation sources, a $\leq$ 1500 meters interval leads to a $\approx$ 3% absolute error on estimated ground displacements for a calculation time gain of a factor 3 with respect to a denser mesh with a 500 meters interval. In areas of large deformation gradients, smaller nodes intervals are used, i.e $\leq$ 500 meters.

An example of topographic mesh for the Virunga area used in the 2002 Nyiragongo January eruption modeling (Chapter 4, Section 4.1) is given in Figure 3.4. This topographic mesh is constructed from the DEM used for the InSAR processing and further includes a rough bathymetry [*Capart*, 1955] [*Schmid et al.*, 2010]. The mesh has a radius of 200 km. It is constituted of 3408 elements and 1706 nodes.

For the modeling of Nyamulagira eruptions (Chapter 4, Section 4.2), as the deformation signals extensions are much smaller than for the 2002 Nyiragongo eruption, the nodes density for the topographic mesh will be increased, considering an interval of 50 meters between the nodes adjoining the eruptive fissures.

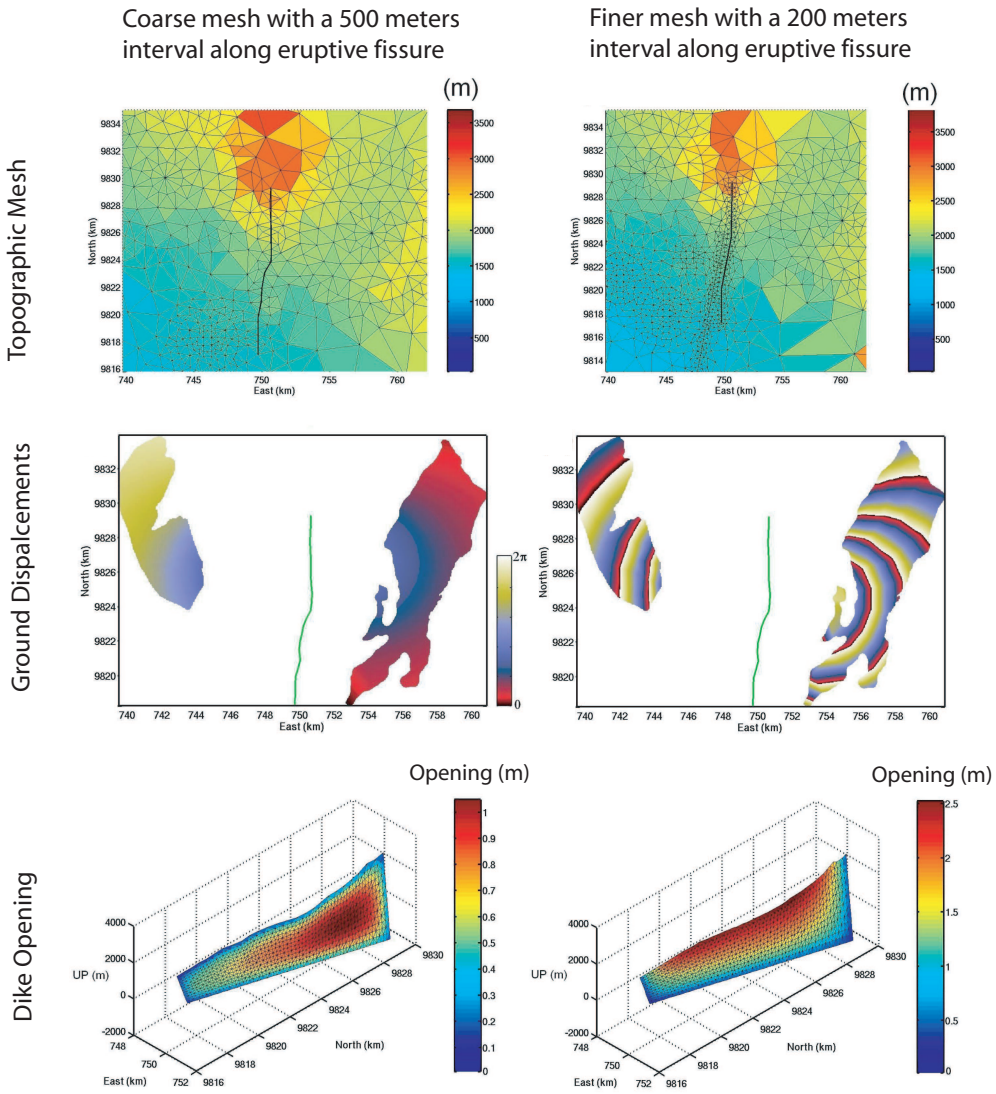

Figure 3.3: Nodes density close to the eruptive fissure(s) is the most critical parameter for the model accuracy. For the Nyiragongo 2002 eruption, it was determined that the topographic mesh adjoining the eruptive fissures should have elements with at least a 200 meters interval in order to obtain a realistic opening distribution [*Wauthier*, 2007].

Structure Mesh

Source boundaries are also meshed by planar triangular elements. *Cayol and Cornet* [1997] showed that coarse meshing of the sources mainly induces an overestimation of the amplitude of surface deformations, leading to an underestimation of source overpressures [*Fukushima et al.*, 2005]. To find the best compromise between calculation time and model accuracy, a comparison of coarse meshes with denser meshes is done. For the Nyiragongo 2002 eruption, it was determined that a 400 meters mesh interval leads to an absolute error of $\approx$ 1.6 % and decreases the calculation time of a factor 2 with respect to a 200 meters mesh interval, and is thus considered as a good compromise. However, when several sources are modeled, it is needed to make the inversion time manageable. Using a 800 meters mesh interval for a second buried source leads to an absolute error of $\approx$ 4.5 % (200 meters), which is still reasonable.

For the Nyamulagira eruptions (Chapter 4, Section 4.2), as the sources extensions are also

smaller than for the 2002 Nyiragongo eruption, the nodes density for the structures meshes will be increased up to a 100 or 200 meters interval between the nodes.

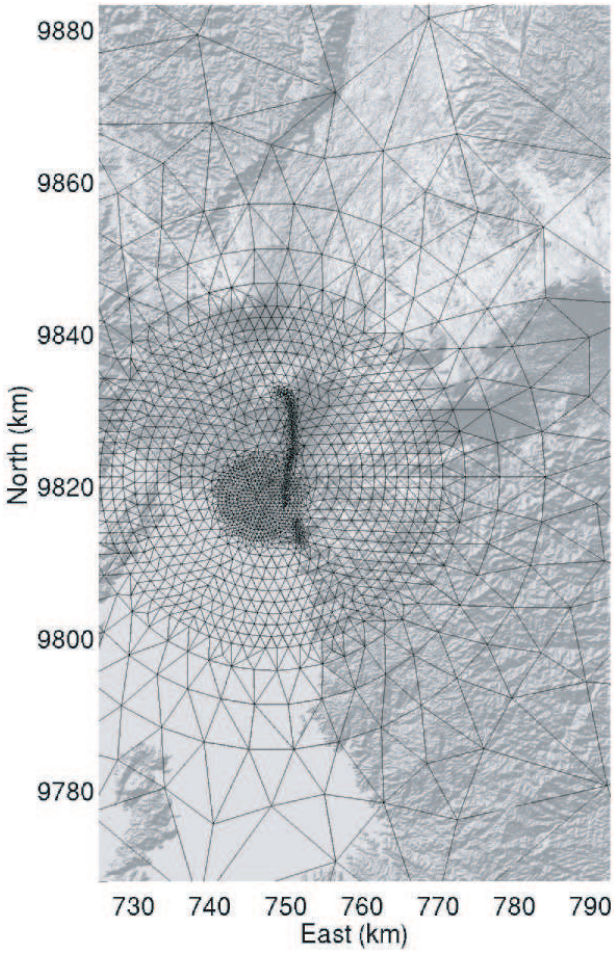

Figure 3.4: Topographic mesh on the shaded DEM used for the modeling of the Nyiragongo 2002 eruption

3.1.2 Near Neighborhood Inversions

A near neighborhood inversion algorithm, which consists of two stages: *search* [*Sambridge*, 1999a] and *appraisal* [*Sambridge*, 1999b], is used. In the search stage, good data fitting regions of the model space are explored. A misfit function is defined which quantifies the discrepancy between observed and modeled displacements [*Fukushima et al.*, 2005]. It is written as:

$$\chi^2 = (u_0 - u_c)^T C_d^{-1} (u_0 - u_c) \tag{3.1}$$

where u_0 and u_c are vectors of observed and modeled line-of-sight (LOS) displacements, respectively, formed by concatenating data from the different viewing geometries, and C_d is the data covariance matrix.

To make the misfit computation numerically manageable, vectors of observed and modeled displacements u_0 and u_c are constructed by subsampling the observed and modeled LOS displacements at the same points. Data are subsampled at circular gridded points in such a way that

the number of subsampled points is denser close to the deformation sources and coarser further away. The choice of a subsampling circular grid method was guided by the results of *Fukushima et al.* [2005], who showed that, for dikes, the sub-sampling method does not significantly affect the inversion result. Pixels with a coherence threshold of less than 0.15 are rejected from the subsampling process. For instance, after subsampling, the 5.6 million points of an original RADARSAT-1 descending data covering the 2002 Nyiragongo event were reduced to 1286 points as depicted in Figure 3.5.

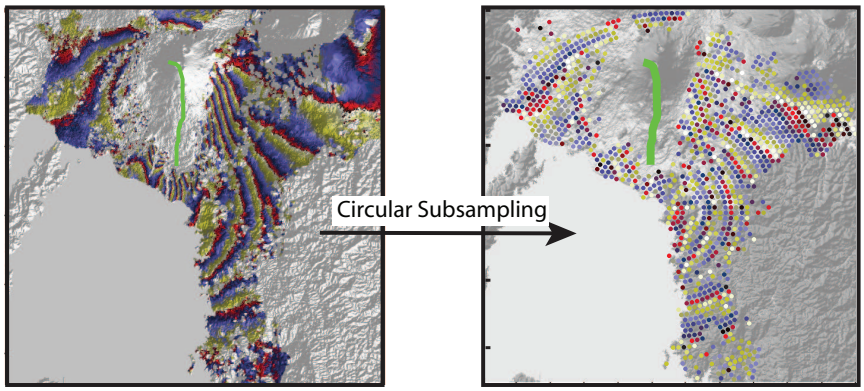

Figure 3.5: Example of the subsampling of a RADARSAT-1 descending interferogram covering the 2002 Nyiragongo eruption which decrease the number of points from 5.6 million to 1286.

The vector of observed LOS displacements is such that $u_o = u_o^{'} + off$, where off is the offset vector, with components corresponding to a constant offset for each interferogram. This offset vector off is determined for each forward model calculation in an inversion. It is such that the misfit between observed, u_o^i, and modeled, u_m^i, displacements of the ^{ith} interferogram is minimized:

$$off_i = \frac{1^{iT} C_d^{i-1} (u_o^i) - u_m^i}{1^{iT} C_d^{i-1} 1^i} \tag{3.2}$$

where C_d^{i-1} is the inverse of the covariance matrix of points in interferogram i, and $1^i = (1...1)^T$ is a unity vector with the same dimension as u_o^i and u_o^m.

InSAR data contain spatially correlated phase noise caused by propagation of the radar wave in the troposphere. Statistical studies of atmospheric noise are based on computations of either the autocorrelation or the covariance function [*Tarantola*, 1987]. Both can be fitted by exponential functions of the form:

$$C(r) = \sigma_d^2 \, exp(\frac{-r}{a}) \tag{3.3}$$

where r is the distance between two pixels, σ_d^2 is the variance of the noise, and a is the correlation length [*Fukushima et al.*, 2005] [*Parsons et al.*, 2006]. Except if explicitly mentioned, typical values determined from preliminary inversions residuals, of 10^{-4} and 300 m for the variance and correlation distance respectively, are used in inversions. These values are modified and an inversion rerun if they are too far from the values determined from the residuals of the best-fit model [*Fukushima et al.*, 2010].

To compare inversion results with a physically meaningful characteristic, we introduce an RMS error, expressed in centimeters. It is defined as:

$$RMS \;=\; 100 \;\times\; \sqrt{\frac{(u_o \;-\; u_c)^T \,(u_o \;-\; u_c)}{npts}} \tag{3.4}$$

where $npts$ is the number of subsampled data points. As both the RMS and misfits depend on the number of points, they will only be strictly comparable if the number of subsampled points is identical from one inversion to another.

The near-neighborhood algorithm searches for models that minimize the misfit within predefined model parameter bounds. The algorithm works as follows: n_1 (here often 200) initial acceptable models are chosen randomly. Misfits corresponding to the n_1 models are then calculated. For each new iteration, n new models are generated in the neighborhood of the n lowest misfit models and misfits for these new models are calculated. Iterations continue until the misfit is not lowered significantly anymore. The neighborhood around a model is defined by a Voronoi cell which covers the area closer to that model than any other model. When n is small, the search is fast but concentrated to a limited area of the parameter space; when n is large, the search is slow and the search is conducted exploring a larger portion of the parameter space. *Fukushima et al.* [2005] showed that values of 10, 30, 50 or 70 for n lead to reliable results. Here n is taken to be 10, except where otherwise specified. This value is discussed in Section 3.2.

The appraisal stage [*Sambridge*, 1999b] involves calculations of posterior probability density functions using misfit values calculated during the search stage. It allows for the estimation of several model statistical characteristics such as the mean model and marginal posterior probability density functions (PPD). The one-dimensional marginal PPDs provide confidence intervals for the model parameters, while the two-dimensional marginal PPDs indicate trade-offs between pairs of model parameters.

3.2 Synthetic Tests: parameter resolution and influence of multiple viewing geometries

Inversions of synthetic interferograms were performed in order to check: (1) which parameters of a single dike, oriented roughly N-S and entirely connected to the ground surface, are constrained by the inversions; and (2) how the use of InSAR data from various viewing geometries impacts on both the inversion results and the convergence speed. This dike is referred to as our *test model* and the corresponding parameters are listed in Table 3.1. To make tests close to a realistic problem, such as the 2002 Nyiragongo N-S eruptive fissure (Chapter 4, Section 4.1), a synthetic interferogram was constructed from a 3D-MBEM calculation of displacements associated with a shallow N-S dike entirely connected to the ground. Displacements are then projected onto the LOS of the three available interferograms for this event and a correlated noise with the same characteristics as the noise of the original interferograms (Table 4.1 in Chapter 4) is added. The same coherence threshold and masks as the original interferograms are used before subsampling with a circular gridded method.

Nine tests were done: seven tests corresponding to each possible combination of the three

considered viewing geometries, computing 10 forward models for each iteration; an eighth test performed with n = 30 forward models (instead of 10) for each iteration; and a ninth test, with 10 models computed at each iteration, and also including data close to the eruptive fissure to investigate how near-field data could influence the parameter resolution. Results of those tests are presented in Table 3.1.

Parameters are well constrained in each test and the mean and best-fit models are close to the *test model* (Table 3.1). Figure 3.6 shows the PPD obtained for the test considering the three swaths with the area close to the eruptive fissures masked out and n equal to 10. Most parameters have low confidence intervals, and with single-peaked 1D marginal PPD (Figure 3.6). The 95% confidence intervals of some parameters fail, however, to include the test model. In the tests considering all the viewing geometries, $P0$, *Botelv* and *Botang* are outside the confidence intervals, whereas some tests including only two viewing geometries were able to determine more parameters. This might result from the intrinsically random nature of the neighborhood search. The least well determined parameter is *Botelv*, as the 95% confidence interval for this parameter consistently fails to include the *testmodel*. According to the two-dimensional PPD, there are no significant trade-offs between the parameters (Figure 3.6).

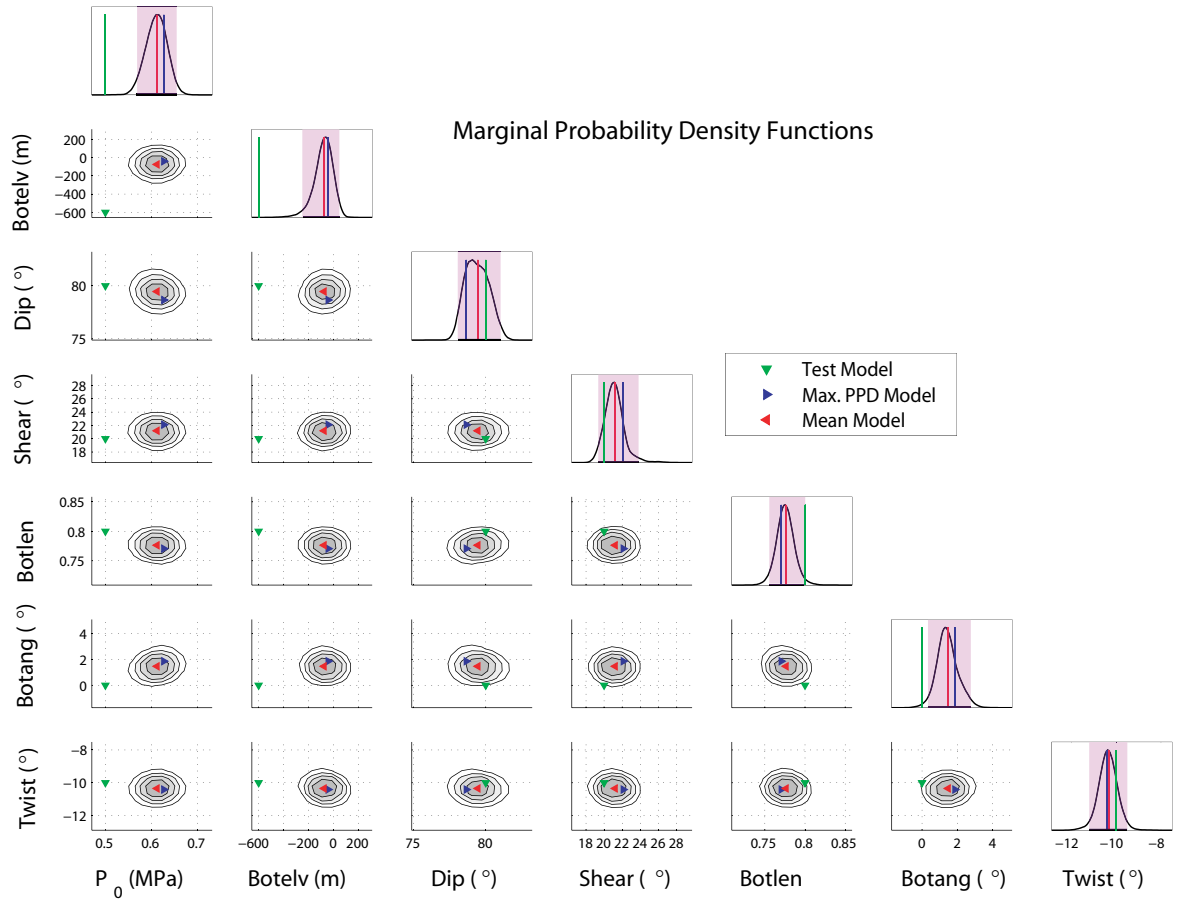

Figure 3.6: One-dimensional (curves) and two-dimensional (contour plots) marginal PPDs plotted with the test (bold green), maximum PPD (solid blue) and mean (dashed red) models, for the synthetic test considering a dike connected to the ground and inverting the three viewing geometries using the InSAR data (n 10 forward models for each iteration). Contour interval is 0.2 times the maximum value. The pink shaded areas, in the one-dimensional PPD plots, show the 95% confidence intervals.

In accordance with the results of *Dawson and Tregoning* [2007] on faults, source parameters are found to be quite accurately determined from one viewing geometry alone. The fact that InSAR measures displacements along oblique LOS directions can explain this observation. However, unlike these authors, who determined that combining several geometries decreased the parameter uncertainties by a factor of 1.5, combining several geometries are found to not reduce parameter uncertainties. Nevertheless, combining several geometries increases the efficiency of the inversion since the number of models needed for convergence is then strongly reduced (Table 3.1).

Furthermore, increasing the number of forward models at each iteration from $n = 10$ to $n = 30$ does not change the best model misfit value and only slightly improves the parameter determinations (Table 3.1), as the *Botang* parameter lies within the confidence interval for $n = 30$. Yet the total number of forward models needed with n = 30 models per iteration is almost twice as many as with n = 10 models per iteration, thus doubling the computation time. As our inversions consider several sources simultaneously, using n = 10 model computations per iteration is assumed to be a reasonable compromise.

Taking the area close to the eruptive fissures into account does not significantly change the test results, which means that the inversion is not sensitive to near field data. Moreover, the convergence speed is lower, probably due to the greater number of subsampling points considered (9204 points versus 7945 points for the other tests). Thus, masking the area close to the dike does not affect our modeling result, but does increase the convergence speed.

	RMS (cm)	N° acceptable forward models		P_0 (Mpa)	Botelv (km)	Dip (°)	Shear (°)	Botlen	Botang (°)	Twist (°)
			Test model	0.5	-0.6	80	20	0.8	0	-10
			Search intv.	[0; 2.5]	[-5; 1]	[60; 120]	[-40; 40]	[0.5; 1.5]	[-20; 20]	[-20; 20]
ERS asc.	1.1	23410	Max PPD	0.46	-0.78	81.3	13.1	0.76	0.45	-9.7
			95% conf. Intv.	[0.36; 0.52]	[-1; -0.7]	[79.2; 83.4]	[9.8; 16.8]	[0.73; 0.79]	[-0.63; 2.1]	[-10.4; -8.7]
RSAT desc.	1	8110	Max PPD	0.48	-0.78	80.8	23.7	0.75	3	-11.5
			95% conf. Intv.	[0.44; 0.51]	[-0.84; -0.7]	[79.2; 81.5]	[22.3; 26]	[0.74; 0.76]	[2; 3.1]	[-11.8; -11]
RSAT asc.	0.6	7410	Max PPD	0.46	-0.78	81.5	18.9	0.78	-1.3	-10.9
			95% conf. Intv.	[0.44; 0.63]	[-1; -0.61]	[80.5; 84.6]	[12.4; 20.2]	[0.73; 0.79]	[-3.5; -0.9]	[-11.8; -9.8]
ERS asc. + RSAT desc.	1.5	3080	Max PPD	0.64	-0.04	77.4	22.1	0.8	2.1	-10.4
			95% conf. Intv.	[0.56; 0.71]	[-0.08; 0.22]	[75.5; 80.5]	[17.8; 22]	[0.73; 0.8]	[0.37; 3.7]	[-12.7; -10.1]
ERS asc. + RSAT asc.	0.9	4470	Max PPD	0.46	-0.79	81.1	21.2	0.75	0.3	-10
			95% conf. Intv.	[0.39; 0.52]	[-0.94; -0.68]	[79.6; 82.9]	[19.9; 23]	[0.74; 0.81]	[-0.5; 1.6]	[-11.7; -9]
RSAT asc.+ desc.	1	4200	Max PPD	0.62	-0.055	78.4	25.4	0.75	2.3	-10.1
			95% conf. Intv.	[0.55; 0.7]	[-0.28; 0.24]	[76.5; 81.2]	[19.1; 27]	[0.73; 0.8]	[-0.3; 3.6]	[-12.4; -8.4]
ALL	1.2	2360	Max PPD	0.63	-0.04	78.7	22.1	0.77	1.86	-10.4
			95% conf. Intv.	[0.57; 0.65]	[-0.25; 0.05]	[78.1; 81]	[19.4; 23.4]	[0.76; 0.8]	[0.3; 2.7]	[-11.2; -9.5]
ALL (n=30)	1.2	5630	Max PPD	0.62	-0.05	78.8	21.4	0.77	1.7	-10.5
			95% conf. Intv.	[0.56; 0.7]	[-0.22; 0.11]	[78; 81.2]	[17.2; 21.7]	[0.75; 0.81]	[-0.45; 2.6]	[-11.7; -9.5]
ALL with PROX	1.1	10190	Max PPD	0.49	-0.79	80.2	21	0.75	-3.2	-10.3
			95% conf. Intv.	[0.49; 0.5]	[-0.81; -0.77]	[79.8; 80.3]	[20.7; 21.2]	[0.75; 0.76]	[-3.5; -3.1]	[-10.5; -10.3]

Table 3.1: Influence of the viewing geometries on the parameter determination for a synthetic model considering a shallow dike connected to the ground surface. The RMS values for the eighth test considering the data close to the fissure are not strictly comparable with the values from the other tests as the subsampled points are different.

Chapter 4

Volcanic and Seismic Events in the Kivu Area Studied by InSAR

The conventional InSAR technique allows us to capture the ground displacements related with several particular events, of seismic and/or magmatic origin, in the North Kivu area. When enough data are available, InSAR displacements are inverted and modeled using the 3D-MBEM approach, presented in the previous chapter, which proved to accurately retrieve dike characteristics, even with a reduced number of InSAR beams. Hence, the Nyiragongo January 2002 eruption is firstly described and modeled. Several possible models are compared, they involve a dike and reservoir, a dike and a fault, and several dikes. Using the Akaike Information criteria, the best compromise between the data fit and the number of inverted parameters is determined. These models are compared with other available data and studies. We also provide critical information for the risks associated with the interaction of magma with the Lake Kivu and we investigate the role of the rift extension in the triggering of the eruption. Secondly, the ground displacements of the last eruption of Nyamulagira, which occurred in January 2010, are captured by eight beams and simultaneously inverted leading to a detailed eruption model involving two independent dikes and a sill-like reservoir. Keeping this detailed eruption model in mind, the previous Nyamulagira eruptions captured by InSAR since 1996 are described and the InSAR data modeled when enough data are available. Finally, the displacements related to two seismic events, which occurred in February 2008 and October 2002 south of the Lake Kivu, are presented and modeled.

The term range decrease will be used when displacements are towards the satellite, while the term range increase in case of displacements away from satellite. A given mode of acquisition, from ascending or descending orbits, with a specific incidence angle - and thus LOS vector -, from a given satellite, will simply be called a beam.

4.1 Nyiragongo Volcano Eruption, 2002 *[Wauthier et al., submitted]*

On January 17, 2002, Nyiragongo erupted along an approximately 20 km-long fracture network extending from the northwestern flank of the volcano to the south, towards the airport and the city of Goma. Part of the 1977 fracture network was reactivated (Figure 4.1)[1]. The 2002 Nyiragongo eruptive fissures were mapped using a 1 meter resolution Ikonos image acquired in 2008 and a 2.5 meter resolution Spot image taken in 2009; the 1977 eruptive fissures were mapped from field observations. Locally, the N-S fracture system is almost parallel to the main local rift-related tectonic faults (Figures 4.1 and 1.7) and the observed opening is about 1-3 meters. A series of grabens, up to 10 meters wide, was observed along the southern segment and in Goma city. The fracture orientation, the emission of degassed magma at the beginning of the eruption [*Komorowski et al.*, 2002-2003]; [*Tedesco et al.*, 2007a], together with the draining of the lava lake lead *Komorowski et al.* [2002-2003] to suggest that the eruption was triggered by rift tectonics. The fracture that opened later released a gas-rich magma, associated with lava fountains, which is thought to come from a deeper reservoir [*Tedesco et al.*, 2007a]. The eruption lasted for 12 hours [*Tedesco et al.*, 2007a], whereas activity at some vents, lava fountains and explosive activity along the eruptive fissure were reported by unverified sources to last up to 48 hours [*Komorowski et al.*, 2002-2003]. The erupted volume is estimated to be approximately 14 - $34 \times 10^6 m^3$ [*Tedesco et al.*, 2007a].

[1]All the geocoded figures in this Chapter are shown in a UTM projection, zone 35S, and with the WGS84 Ellipsoid

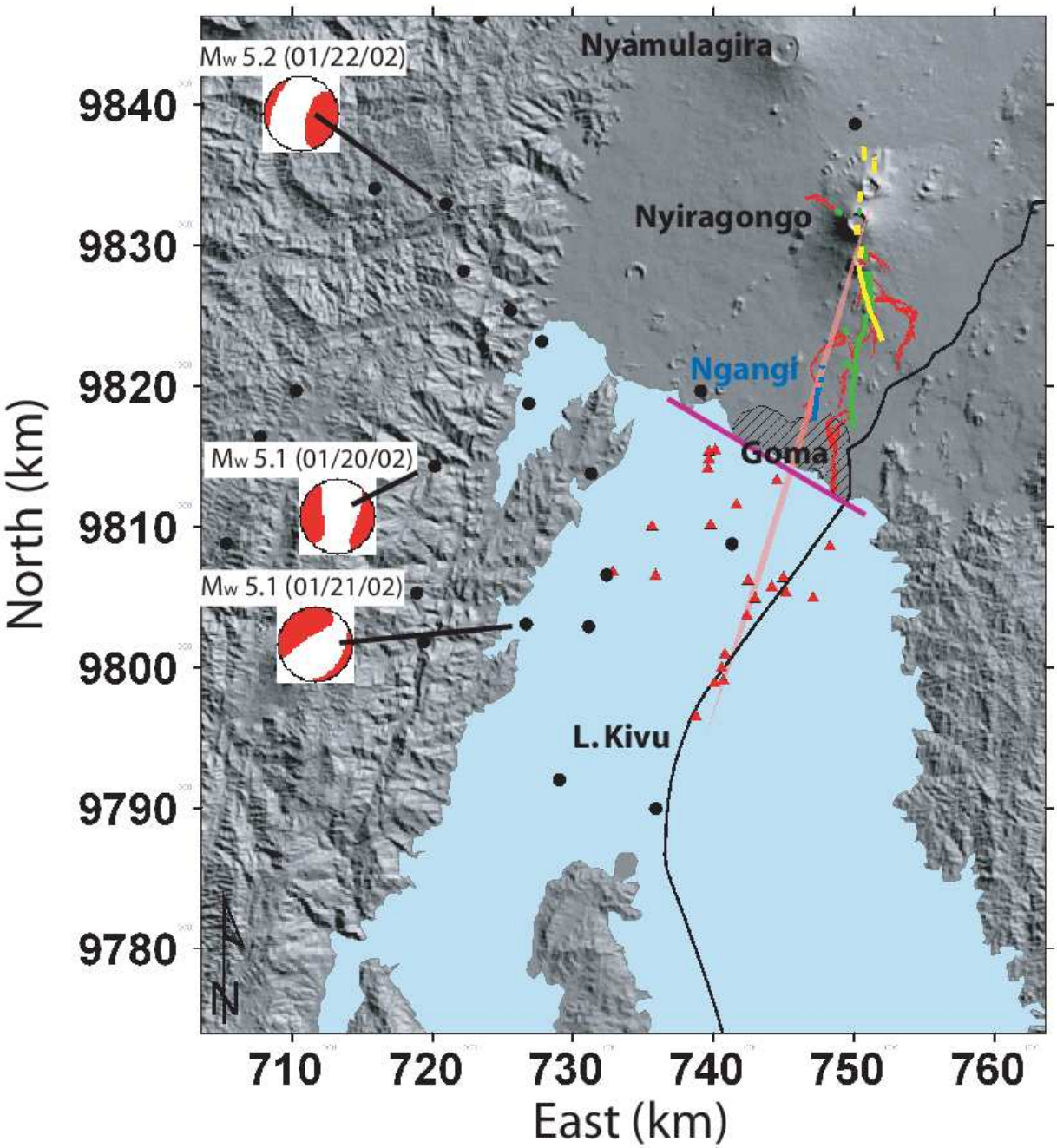

Figure 4.1: Shaded relief topographic map of the Goma area and Lake Kivu. The 2002 Nyiragongo eruptive fissures are in green, and were mapped from a 2.5 m resolution Spot image from 2009 and from a 1 m resolution Ikonos image from 2008. Fissures on the northern flank of the volcano were determined from the northernmost lava flow location. The main 2002 lava flows are drawn in red. The 1977 eruptive fissures, mapped from field observations, are in yellow. The Goma urban area is hatched in black, and the Ngangi fissures, determined from the Ikonos image, are mapped in blue. The red triangles represent the main volcanic cones on the floor of lake Kivu [*Capart*, 1955]; [*Schmid et al.*, 2010]. The black points indicate seismic events recorded in the USGS NEIC catalogue for January and February, with the CMT focal mechanisms of the three strongest events of the crisis. The pink shaded area is the deep dike projection of our preferred model presented in Section 4.1.5. The black line represents the border between RDC and Rwanda. Lake level changes were measured between Sake and Gisenyi along the direction indicated with a bold magenta line.

4.1.1 InSAR Data

Data selection

The ground displacements related to the January 2002 eruption were captured by C-band SAR sensors (wavelength of 5.6 cm) onboard satellites ERS-2 and RADARSAT-1 in different viewing geometries (*multibeam* data). Due to the fact that the perpendicular baselines are too large (projection of the distance between the two satellites perpendicular to the look direction), the descending ERS-2 interferograms spanning the eruption are affected by geometrical decorrelation [*Hanssen*, 2001], making them unsuitable for our modeling. Only a reduced number of ascending ERS-2 interferograms spanning the eruption are available either because the Doppler frequency shifts made images incompatible for the generation of interferograms [*Miranda and et al.*, 2004] or because perpendicular baselines between interferometric pairs were too large. In this study we use the most coherent ERS-2 ascending interferogram available (spanning 665 days) as well as one ascending and one descending RADARSAT-1 interferogram spanning respectively 48 and 72 days. The temporal decorrelation (due to the change of scattering properties within a pixel) is hence lower in the RADARSAT interferograms than in that from the ERS (Figure 4.2 and Table 4.1).

Satellite	LOS vector [East, north, Up]	Time span	Ha (m)	Frame(s)	Variance (m^2)	Correlation distance(m)
Nyiragongo 2002 Eruption						
ERS-2 (asc.)	[-0.36, -0.08, 0.93]	2000/09/06 - 2002/07/03 (665 days)	147	7158	$2.2 * 10^4$	10843
RSAT-1 (asc.)	[-0.59, -0.13, 0.80]	2001/12/31 - 2002/02/17 (48 days)	77	M: 7135 & 7150 S: 7136 & 7151	$4.6 * 10^5$	9152
RSAT-1 (desc.)	[0.50, -0.11, 0.86]	2001/12/21 - 2002/03/03 (72 days)	119	M: 3631 & 3646 S: 3631 & 3647	$7.1 * 10^5$	11925
24 October 2002 Earthquake						
RSAT-1 (desc.)	[0.51, -0.11, 0.85]	2002/10/05 - 2002/10/29 (24 days)	39	M: 3631 & 3646 S: 3635 & 3651	10^4	300

Table 4.1: Relevant characteristics of the three interferograms used in this section. The estimated variance and correlation length (characterizing the random correlated noise present in each InSAR data set) are determined in the undeformed areas.

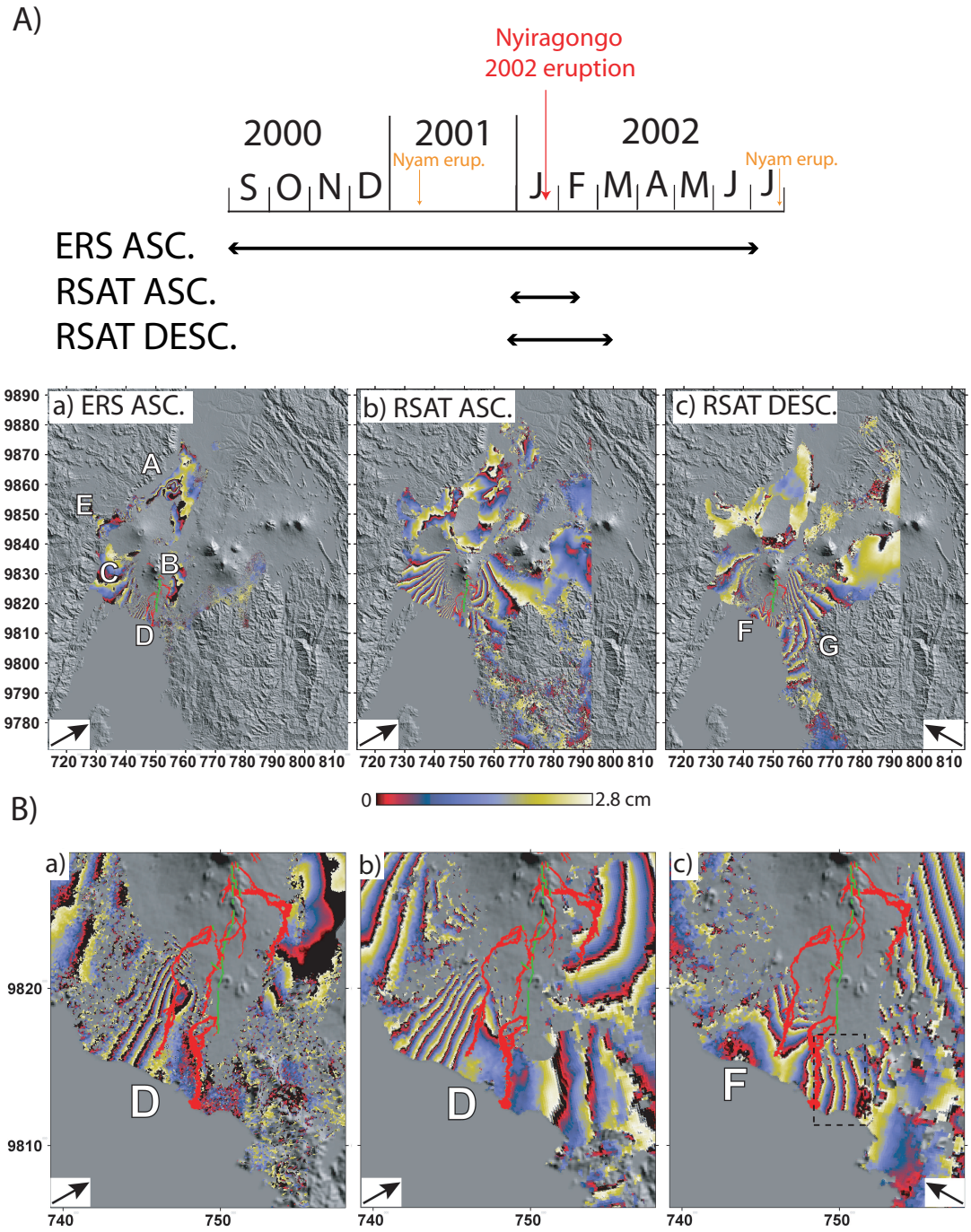

Figure 4.2: A) Three interferograms showing the deformations associated with the 2002 Nyiragongo eruption. One color cycle represents a 2.8 cm Line Of Sight (LOS) range change with positive fringe (red-blue-yellow) corresponding to a range increase. The arrows show Line Of Sight (LOS) direction. The shaded relief DEM is shown wherever the interferometric signal is incoherent. The 2002 lava flows are shown in red and eruptive fissures are drawn in green. See the text for the interpretations of signals referred to as A, B, C, D, E, F and G. a) ERS-2 ascending interferogram, b) Ascending RADARSAT-1 interferogram and c) Descending RADARSAT-1 interferogram. B) Close-up of the Goma-Gisenyi area for the three interferograms a) ERS-2 ascending interferogram, b) Ascending RADARSAT 1 interferogram and c) descending RADARSAT 1 interferogram. Black dashed square in c) shows the area of the RADARSAT-1 descending interferogram detailed in Figure 4.4.

Processing

We processed the interferograms with the Jet Propulsion Laboratory/Caltech repeat orbit interferometry ROI_PAC software [*Rosen et al.*, 2004]. A 1 arc second (about a 30x30m grid) digital elevation model (DEM) from the Shuttle Radar Topographic Mission (SRTM) [*Farr et al.*, 2007] was used to correct for the topographic phase. Two consecutive frames were used to form each of the RADARSAT-1 interferograms (Table 4.1). Interferograms are filtered with a power spectrum filtering, followed by an adaptive smoothing using Fast Fourier Transform [*Goldstein and Werner*, 1998]. We unwrapped the interferometric phases using the SNAPHU software [*Chen and Zebker*, 2001]. Before unwrapping, the ERS-2 interferogram was multilooked by factors of 10 and 2 in azimuth and range, respectively. The RADARSAT-1 interferograms were multilooked by factors of 20 and 4, except for the western area (G in Figure 4.2a), where, to improve the unwrapping, multilooking factors of 40 and 8 were used. The combination of multilooking factors allows the signal in the Goma area to be preserved (Figure 4.2b), where large deformation gradients are present, and enables the signal to be successfully unwrapped in the west (G in Figure 4.2a).

Orbital correction

Improper modeling of the orbital satellite trajectories results in large-scale parallel fringes in the interferograms. Both RADARSAT-1 interferograms were affected by such orbital phase ramps, which were empirically removed. In contrast, because of the lack of coherent data in the far field, unaffected by the 2002 eruption or by lava flow compaction, we were not able to accurately identify the orbital errors in the ERS-2 interferogram.

Interferograms description

Acquisition times of SAR scenes used to produce all the interferograms in our database [*d'Oreye et al.*, 2008]; [*Poland*, 2006] indicate that the main ground deformations observed took place between January 14 and February 13. InSAR data show complex ground displacements, with several overlapping fringe patterns, which could be associated with a combination of sources, both magmatic and regionally tectonic in origin. The Line-Of-Sight (LOS) range increase observed in the area marked A in Figure 4.2a corresponds to the compaction of a well-known Nyamulagira lava flow pile resulting from the 1958, 1967, 1980 and 1991-93 eruptions [*Smets et al.*, 2010a]. This signal is only clearly visible on the ERS-2 interferogram due to its larger time span. We do not attempt to model it as we focus here on the 2002 Nyiragongo eruption. Fringes with asymmetric LOS range change to the east and west of the eruptive fissure (B and C, Figure 4.2a), showing opposite range changes for the descending and ascending modes. Their pattern is consistent with dike intrusions and is presumably related to one or more dikes which fed the 2002 eruption. In the Goma area, a LOS range increase occurs in the three viewing geometries (D in Figure 4.2), indicating that the signal corresponds mainly to subsidence. The signal amplitude reaches approximately 15 centimeters in the LOS. A range decrease of about 1.5 fringes (F in figure 4.2) is also visible west of the lava flows, though only in the RADARSAT-1 descending mode.

Finally, one to two fringes, indicating a range increase northwest of Nyamulagira volcano (E in Figure 4.2a), are visible in both ERS and RADARSAT ascending viewing geometries. The

altitudes of ambiguity ha of the ascending ERS-2 and RADARSAT-1 interferograms are 147 and 77 meters, respectively. Parameter ha is the altitude difference that generates one topographic-related fringe. It characterizes the sensitivity of the interferogram to DEM errors [*Hanssen*, 2001]. A DEM error of such a high amplitude is unlikely and hence cannot be responsible for the signal observed in E. Furthermore, studying several independent ERS-2 interferograms in our database shows that the signal always corresponds to a range increase which varies from less than one to two fringes. As the signal is consistent, the main part of the signal is probably a deformation associated to the Nyamulagira volcano. The amplitude variation indicates that part of the signal could be an atmospheric effect or a small orbital error. Analyzing this volcano is outside the scope of this study, so we do not attempt to model the signal.

In the western part of the descending RADARSAT-1 interferogram (G in Figure 4.2a), a large extension signal is characterized by four to five fringes of LOS range decrease. The area corresponding to this signal is incoherent in the ERS-2 interferogram, and only just visible in the RADARSAT-1 ascending interferogram.

The InSAR displacements from the three beams were simultaneously used to compute the horizontal and vertical displacements in an area coherent in the three datasets (Figure 4.3B). The reference of each unwrapped interferogram was adjusted from the best-fitting model offset calculation (Equation 3.2). They show that the major part of the 2002 deformation is mainly due to horizontal displacements.

4.1.2 Comparison with field observations in Gisenyi (Rwanda)

The RADARSAT-1 descending interferogram shows two fringe discontinuities (Figure 4.4A) in the city of Gisenyi (Rwanda). In order to retain a fine resolution, this interferogram was neither multilooked in range (5 pixels in azimuth for 1 pixel in range) nor filtered. During a field investigation carried out in January 2010 we confirmed that almost all houses aligned along these two discontinuities were affected by open cracks (Figure 4.4B). The inhabitants of these houses confirmed that the initiation of the cracks was simultaneous with the January 2002 Nyiragongo eruption. New cracks also opened up after the eruption, some appearing in early 2009. The Rwandese Red Cross, which has been measuring the extension of some cracks in a building of the Gisenyi Hospital, confirmed that the crack widening is still ongoing. In some cases a vertical movement, with the western side moving down, was noticed. A one meter high west-dipping fault scarp was observed north of the Gisenyi airport.

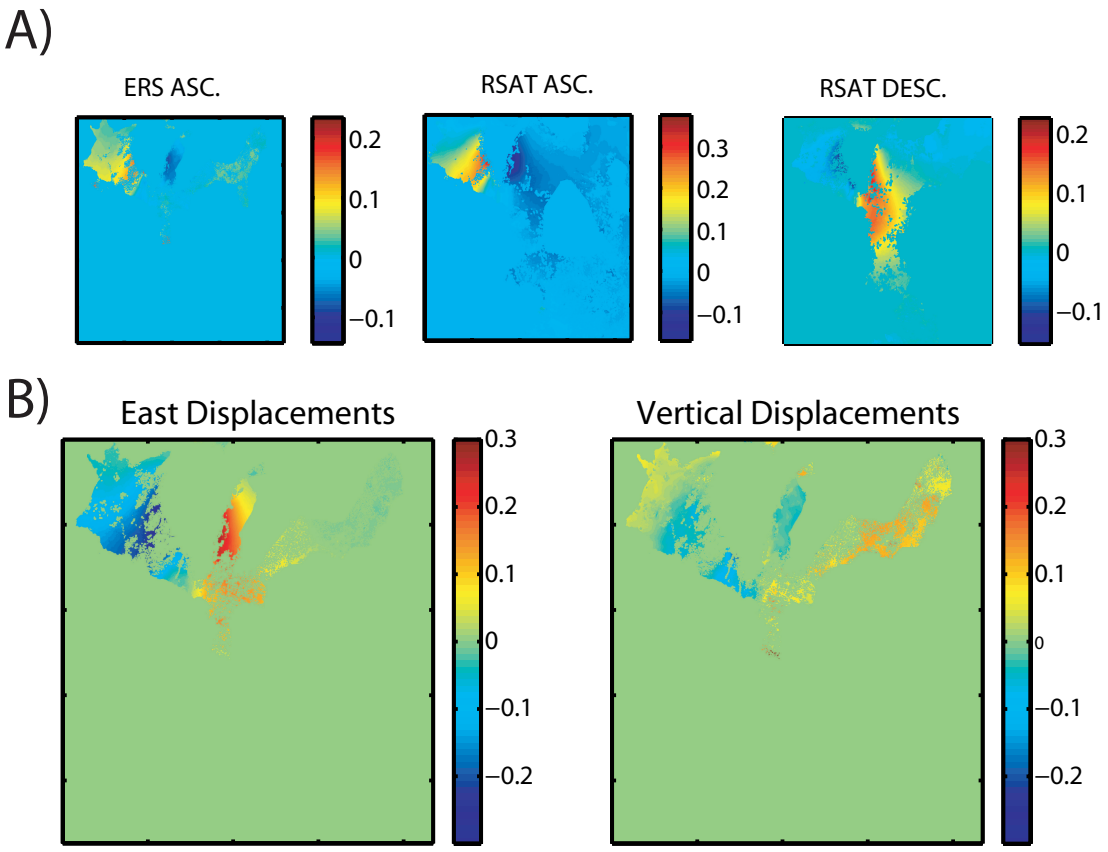

Figure 4.3: A) The same three interferograms showing the deformations associated with the 2002 Nyiragongo eruption unwrapped with Snaphu. All displacements are in meters. B) The InSAR displacements from the three beams were simultaneously used [*Wright et al.*, 2004] to compute the horizontal (left) and vertical displacements (right). The standard deviation are 1.1 cm and 3.4 cm, respectively.

4.1.3 Other Data

Field surveys conducted after the eruption provided geochemical data [*Tedesco et al.*, 2007a]; [*Tedesco et al.*, 2010] which indicate that up to three different magmatic sources were involved in the eruption. The southern part of the eruptive fissure is inferred to be fed by a much deeper source than the northern vents which emitted lava drained from the lava lake, possibly combined with input from a shallow magmatic reservoir located below the main Nyiragongo edifice.

After the eruption, carbon dioxide and methane emanations were observed around the eruptive fissures and in several locations in Goma [*Komorowski et al.*, 2002-2003]. Gas explosions were also reported during the eruption. This gas could have been stored in sediments filling the Lake Kivu basin, in methane-rich gas pockets, and may have been continuously released through tectonic fractures in the whole region. The sudden fracturing associated with the 2002 eruption could have promoted the degassing [*Tedesco et al.*, 2007a].

The two operating seismic stations showed that precursory seismicity occurred in the year preceding the eruption [*Kavotha et al.*, 2002/2003]. It was characterized by volcanic tremors, long-period and short-period earthquakes, sometimes followed by increased fumarolic activity [*Tedesco et al.*, 2007a]. Between January 4 and 16, 2002 [*Allard et al.*, 2002], and after the effusive activity had stopped, seismic activity remained high. In the whole Lake Kivu area, about

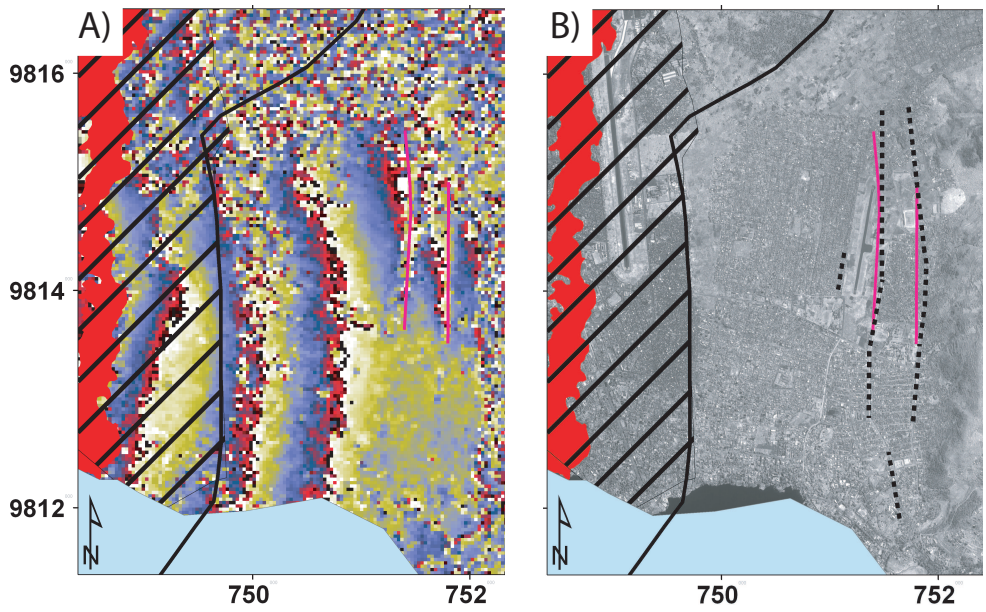

Figure 4.4: A) Detail from the descending RADARSAT-1 interferogram (see Figure 4.2B for location) which is here neither multilooked in range nor filtered in order to have the finest resolution for the discontinuities identification. Fringe discontinuities are indicated by bold magenta lines. The border between DRC and Rwanda is indicated by a bold black line. The city of Goma is showed by the shaded black area, and the 2002 lava flow is in red. B) Ikonos-2 image (Panchromatic 1 meter spatial resolution) from July 11, 2008 showing a comparison between the fault traces inferred from fringe discontinuities on the descending RADARSAT-1 interferogram (bold magenta lines) and from evidence of cracks in houses (black dotted lines) and by steplike topography.

100 tectonic earthquakes with magnitudes larger than 3.5 were recorded in the five days following the eruption [*Tedesco et al.*, 2007a], culminating in a magnitude Mw = 6.2 event on October 24, 2002. Unfortunately, the seismic network did not allow an accurate assessment of the location of the seismic events (Figure 4.1). The Harvard Centroid Moment Tensor (CMT) focal mechanisms of the three largest January 2002 earthquakes (moment magnitude, $Mw > 5$) indicate almost pure normal faulting mechanisms (Figure 4.1). The scalar moment of the three strongest shocks are $M_0 = 5.23 \times 10^{16} N.m$, $5.94 \times 10^{16} N.m$, and $7.41 \times 10^{16} N.m$, leading to magnitudes Mw = 5.1 for the two first shocks, and Mw = 5.2 for the strongest one (Figure 4.1).

After the eruption, local inhabitants reported a noticeable rise in the water level of the lake in some places along the shore line in the Goma area. Eleven days after the eruption, water level changes were estimated by measuring the depth of the immerged algae zone ($\tilde{3}$0 cm thick) that develops just below the water surface [J. Durieux, pers. com., 2005]. These measurements were repeated at irregular intervals until March 2002 [*Komorowski et al.*, 2002-2003]; [*Tedesco et al.*, 2007a] and showed an asymmetric increase in the water level of Lake Kivu, which reached a maximum of about 37 cm at the Goma shore (red profile A in Figure 4.5). Due to the agitation of the water surface by waves and given possible additional sources of perturbations (water discharge at the Ruzizi electric dam located 100 km to the south, seasonal effects, seiches, etc.), the uncertainty can conservatively be estimated to be of the order of +-15 cm. This water level change has been attributed to subsidence of the rift system around Goma as the asymmetry is consistent with the asymmetry of the graben in which the lake is located [*Komorowski et al.*,

2002-2003].

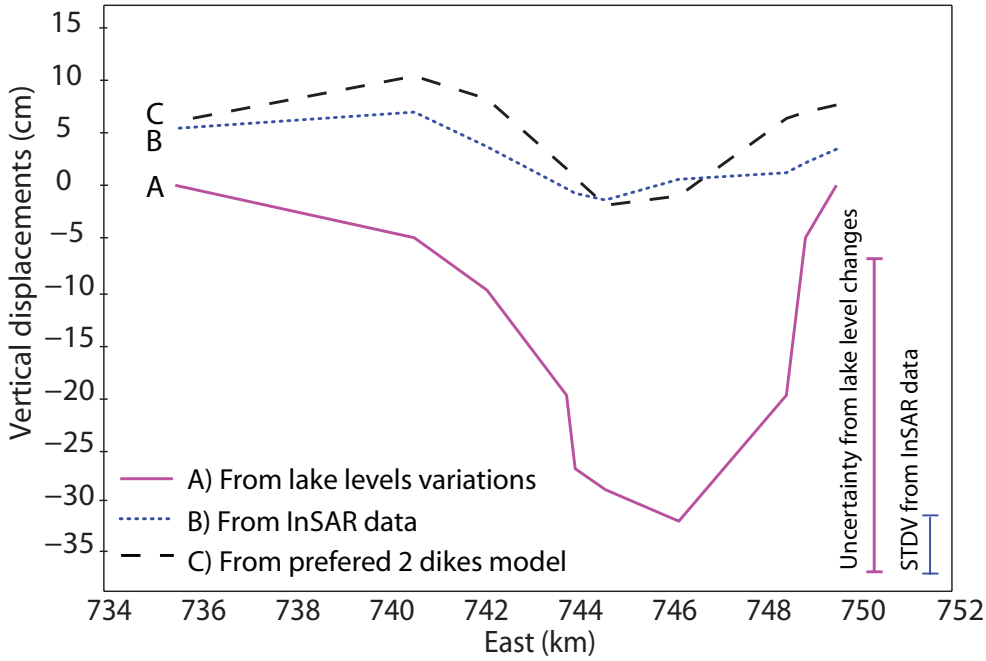

Figure 4.5: Vertical displacements along the northern coast of Lake Kivu (see Figure 4.1 for the profile location). A) The bold magenta line indicates the measured lake level variations from January 17 [Tedesco et al., 2007], for which the uncertainty is estimated to be about ±15 cm. B) The dotted blue line indicates vertical displacements computed from the different beams using InSAR data. Standard deviation on vertical displacements is 3.4 cm. C) The dashed black line indicates the vertical displacements from the preferred 2 dikes model.

4.1.4 Modeling and Inversions

Analysis of interferograms, eruptive activity and seismicity suggest that deformations associated with the 2002 eruptions could result from the combined effect of a dike intrusion connected to the observed eruptive fissure and some fault movements. Magma or gas reservoirs could also have been involved in the eruption.

3D Boundary Element Modeling

For the Kivu area, in situ elastic coefficients are estimated from a seismic velocity profile of the Virunga area [*Mavonga*, 2010] which showed that seismic velocities increase from 3.5 km/s at sea level to 7.3 km/s at 7500 meters b.s.l (Figure 4.6a). Experimental values of Poisson's ratio, for basalts range from 0.22 to 0.28 for low to high confining pressure corresponding to a depth of several kilometers [*Birch*, 1966]. We take an average Poisson's ratio of 0.25. The Young's modulus, density and Poisson's ratio contribute to the seismic velocities. Young's modulus can be determined from:

$$E_d \;=\; V_p^2\,\rho_r\,\frac{(1\,-\,2\nu)(1\,+\,\nu)}{(1\,-\,\nu)} \tag{4.1}$$

Based on studies in Hawaii [*Zucca et al.*, 1982], we assume that the density varies from 2500 kg/m3 at shallow depth, where vesiculated lava flows are present, to 2900 kg/m3 at greater depth where rocks are compacted (Figure 4.6b). In the absence of data we assume the density variation to be linear with depth. Density at shallow depth is consistent with the value of 2500 kg/m^3 estimated from a gravity survey around Nyiragongo and Nyamulagira volcanoes [*Mishina*, 1983]. From seismic velocities, the dynamic Young's modulus is estimated to increase with depth from 23 GPa to 124 Gpa (Figure 4.6c). Laboratory experiments show that static values of Young's modulus, Es, are always less than dynamic values, Ed, [*Cheng and Johnston*, 1981a] [*Jaeger et al.*, 2007] and that the Es/Ed ratio increases with confining pressure, and is inversely related to porosity and crack density. Here, confining pressure is estimated by integrating the density (Figure 4.6d). We further consider an elevated porosity and crack density close to the surface, leading to a lower ratio of Es/Ed of 0.1. This ratio is assumed to increase to Es/Ed = 0.25 at sea level. At greater depth we assume that the evolution of Es/Ed with confining pressure follows a value intermediate between the experimental curves derived by *Cheng and Johnston* [1981a] for westerly Granite and Ammonia Tanks Tuff (4.6e). Thus our first order estimate is that Young's modulus varies from 2.3 GPa close to the surface to 100 GPa at 9.5 km below the surface (Figure 4.6f). Preliminary models showed that the 2002 Nyiragongo eruption dike and other intrusions and faults involved in other events in the Kivu area, is probably shallow, thus we take a Young's Modulus of 5 GPa. Implications of the homogeneity assumption and possible underestimation of the Young's modulus will be discussed in the following section.

We assume that the 20 km long segmented fissure corresponds to a single dike at depth. As no interferometric data is available close to the eruptive fissure, we do not attempt to connect this dike to the exact echelons that were measured after the eruption (Figure 4.1), and we consider a single eruptive fissure instead.

The topographic mesh is constructed from the DEM used for the InSAR processing and further includes a rough bathymetry [*Capart*, 1955]; [*Schmid et al.*, 2010]. The size of the mesh

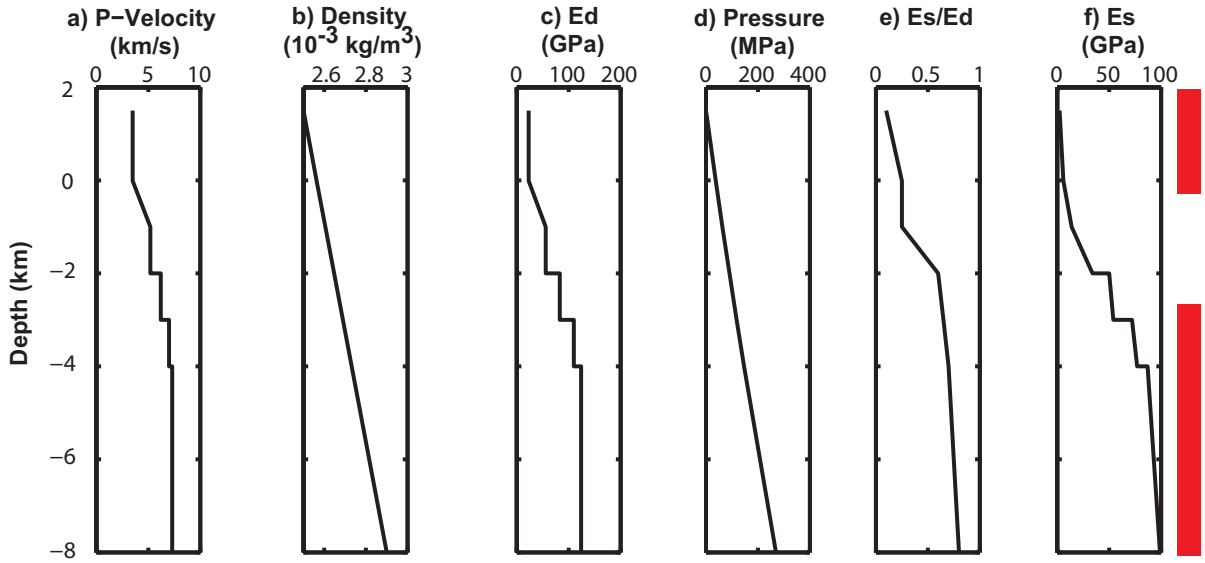

Figure 4.6: Estimated crustal structure in the Virunga area. a) Estimated P-wave velocity structure obtained in the Virunga area [*Mavonga*, 2010]. b) Density structure assumed to be similar to Hawaii. c) Inferred dynamic value of Young's modulus from Equation 4.1. d) Ambient lithostatic pressure computed from the presumed density structure. e) Ratio of dynamic to static Young's modulus from laboratory measurements [*Cheng and Johnston*, 1981a]. f) Estimated static value of Young's modulus. The thick red line indicates the depths of dikes from the best-fit model obtained for the Nyiragongo 2002 eruption, $z = 0$ corresponds to sea level.

is ten times greater (200 km in radius) than the length of the 2002 eruptive fissure, so that the limited extension of the ground surface has a negligible influence (around 2 %) on the computed displacements [*Cayol*, 1996]. The topographic mesh is dense close to the eruptive fissures in the Goma area where displacement gradients are greatest, and it becomes coarser further away. Figure 3.4 in the previous chapter, shows an example of one such topographic mesh, constituted of 3408 elements and 1706 nodes, which was used for the inversions.

A 400 meter mesh interval is used for the dike associated with the 2002 eruptive fissure and the elliptic reservoir, while an 800 meter mesh interval is used for the buried dike and faults.

Near Neighborhood Inversions

Only the southern part of the scene shown in Figure 4.2a is subsampled as we do not attempt to model deformations associated with lava flow pile compaction (A), or Nyamulagira (E). Data are subsampled at circular gridded points in such a way that the number of subsampled points is dense (800 m) in areas where displacement gradients are large, i.e. close to the 2002 eruptive fissure and in the vicinity of Goma, and coarser further away (Figure 4.7).

After subsampling (Figure 4.7), the 5.6 million points of the original InSAR data were reduced to 2432 data points; 284, 1286 and 862 for the ERS-2, RADARSAT-1 descending and ascending interferograms, respectively. Differences in the number of points in each scene can be explained by: (1) differences in the number of coherent pixels between interferograms, with fewer coherent pixels in the long time span ERS-2 interferogram, (2) differences in the area affected by deformations.

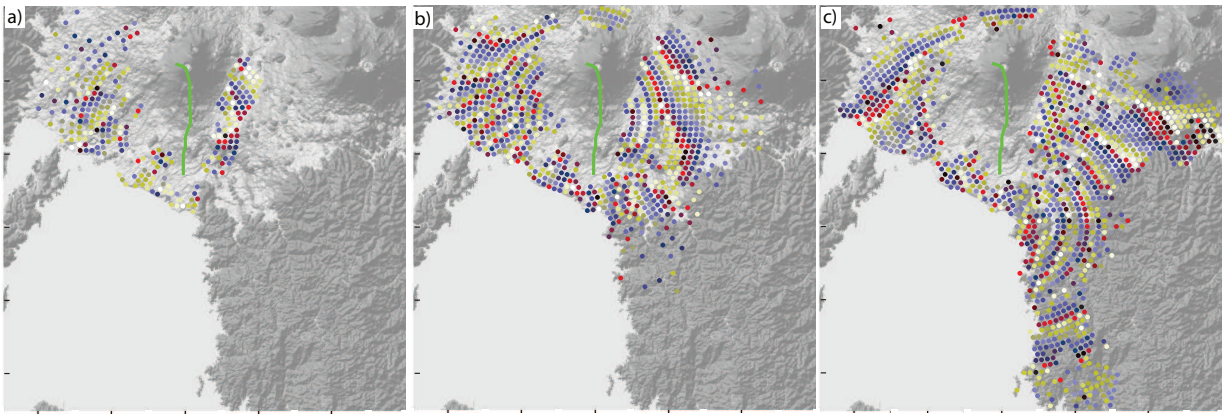

Figure 4.7: Data points subsampled for the three InSAR data sets: a) ERS-2 ascending interferogram, b) Ascending RADARSAT 1 interferogram and c) descending RADARSAT-1 interferogram.

4.1.5 Results for the 2002 Nyiragongo Eruption

The complex observed displacements could result from a combination of sources. Possible deformation sources are suggested by the observation of the various geological and geochemical changes associated with the eruption. The eruptive fissure indicates that one of the sources is a dike. The fact that methane and CO2 were released [*Komorowski et al.*, 2002-2003] could indicate the partial draining of a gas reservoir. One of the magma sources inferred from geochemical data [*Tedesco et al.*, 2007a] is either a magma reservoir, or a second, deeper dike. The seismic activity associated with the eruption, and the fissure orientation controlled by rift tectonics, suggest that faults may have been involved in the eruption.

To test these different hypotheses, we simultaneously invert the InSAR data corresponding to three viewing geometries. For each set of modeled sources there are a given number of parameters to invert: 1) 6 parameters for a single dike associated with the 2002 eruptive fissure, 2) 12 for a dike associated with the 2002 eruptive fissure and a deflating magma reservoir, 3) 17 for a network of normal faults, and 4) from 9 to 14 parameters for a dike associated with the 2002 eruptive fissure and a buried dike under the Goma and Lake Kivu area.

Single dike model

Simultaneous inversions of the three beams show that a sub-vertical dike associated with the eruptive fissure can account for the InSAR signal in the near field i.e. to the left and right of the eruptive fissure. For simplicity, the parameter shear is fixed to zero. The best-fit model only fits the data poorly, with a RMS error of 4.8 cm (Table 4.2, column 1). The best-fit dike is a subvertical structure about 4.5 km high (Table 4.3 and Figure 4.8), deep below the Nyiragongo edifice and shallower in the Goma area. The largest residuals (Figure 4.8) are in the Goma area and in the far field, towards Nyamulagira and east of Lake Kivu, where other sources probably cause the complex deformation observed.

	1 dike	1 dike and 1 deflation source	1 dike and 1 fault network	2 dikes (a)	2 dikes (b)	2 dikes (c)	2 dikes (d)	2 dikes (e)	2 dikes (f)*
N° of param. inv.	6	12	17	9	10	11	12	13	14*
RMS error (cm)	4.8	4.2	3.5	2.7	2.6	2.6	2.6	2.5	2.3*
AIC	3583	3256	3125	2883	2856	2858	2883	2842	2840*

(a) Inverted parameters: $P_0, Dip, Botelv, Botlen, Twist; P_{02}, D_{top2}, Strike_2$ and $Toplen_2$
(b) + Dip_2
(c) + $Botelv_2$
(d) + $Botlen_2$
(e) + $Botang$
(f) + $Botang_2$

Table 4.2: Comparison of the most relevant inversions results. The"*" denotes the preferred model.

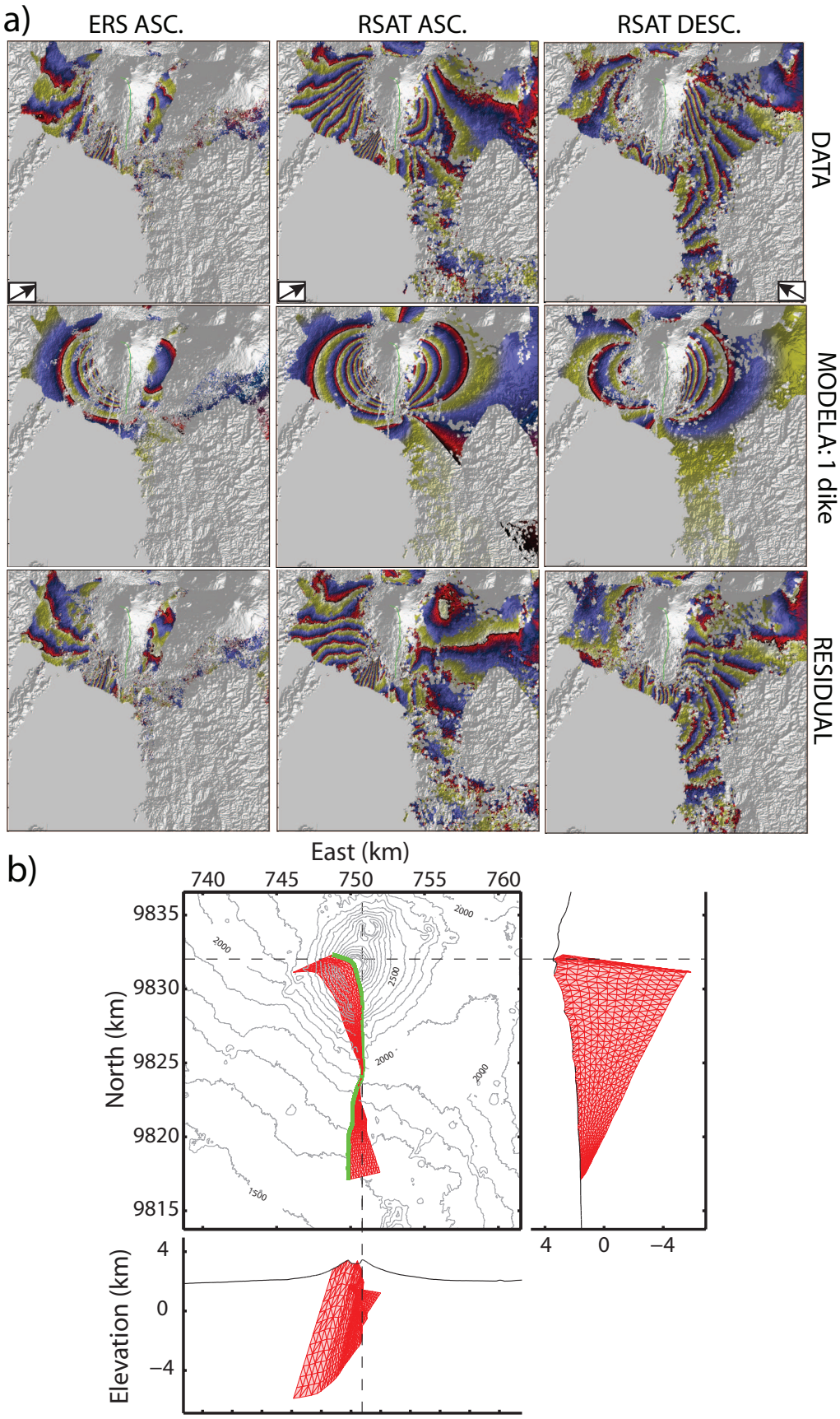

Figure 4.8: a) ERS-2 ascending , ascending RADARSAT 1 and descending RADARSAT 1 observed (upper row), modeled (middle row) and residual interferograms (lower row) obtained with a single dike intrusion associated with the 2002 eruptive fissure (in green). b) Geometry of the best-fit single dike model.

Quadrangular Dike Connected to the Ground								
	P_0 (MPa)	*Botelv* (km a.s.l)	*Dip* (°)	*Shear* (°)	*Botlen*	*Botang* (°)	*Twist* (°)	Average opening on the surface (m)
Max PPD	0.27	-2.5	94.6	0	1.1	-25.7	19.5	1.3
95% conf. intv.	[0.27; 0.28]	[-2.5; -2.4]	[94.4; 94.7]	fixed	[1; 1.1]	[-26; -25]	[19.2; 19.6]	-

Table 4.3: Best-fit parameters of the single dike model. Parameters are described in Figure 3.1 in Chapter 3.

A dike and a deflating reservoir model

We explore the possible involvement of a magma or gas reservoir by inverting simultaneously with an elliptical deflating source and a fissure dike. The best-fit model corresponds to a reservoir below the Goma area, but it fits the data poorly, giving an RMS error of 4.2 cm (Table 4.2, column 2).

A dike and a normal fault model

We simultaneously invert for a fissure dike and up to three westward-dipping normal faults located to the west of this dike. Such faults are mechanically consistent with the extensional tectonic context. In preliminary inversions, the dike geometry was fixed to the values determined in section 6.1 and the height and strike of the three faults were fixed to 1 km and 4°, respectively. We invert simultaneously for the dike overpressure and the three fault locations, geometries and shear stress drops, corresponding to 14 fault parameters (dip, length, location, and shear stress drop of the faults). These inversions show that the faults are aligned, so that they probably correspond to a single fault with different stress drops. Therefore, in the next step, we invert for a total of 17 parameters corresponding to a dike associated to the eruptive fissure and a single fault having three different stress drops, each acting over a different length (Table 4.4).

Adding this fault improves the data fit, leading to a RMS error of 3.5 cm (Table 4.2, column 3). The best-fit dike is a subvertical structure about 4 km high (Table 4.4 and Figure 4.9). The fault, located beneath the dike, is 1.2 to 1.6 km high, 49.5 km long and extends for 30 km under Lake Kivu towards Idjiwi. Both structures are mechanically consistent. Indeed, the normal fault can accommodate the dike opening and conversely, the dike opening can induce the normal fault slip. The scalar seismic moment corresponding to this fault network displacement is M0 = 7.2 $\times$ 10^{18} N.m (Table 4.4), leading to a M_w = 6.5. This value is much larger than the strongest event (Mw = 5.2) recorded during the 2002 eruption. Summing the scalar moments of the three strongest shocks, thus assuming a similar mechanism for the three shocks [*Kostrov*, 1974], leads to a total scalar seismic moment equal to 1.9 $\times$ 10^{17} N.m, which is about 30 times less than the model geodetic moment (7.2 $\times$ 10^{18} N.m). This could indicate that part of the slip on the fault occurred aseismically, similar to the results which *Biggs et al.* [2009] found for the rifting episode of Tanzania in 2007. The largest shocks recorded were located on the western rift border (Figure 4.1). Even considering a 10 km inaccuracy in the location [*Hellfrich*, 1997], these events are too far from the inverted fault to be attributed to slip on this fault, making the model quite unlikely.

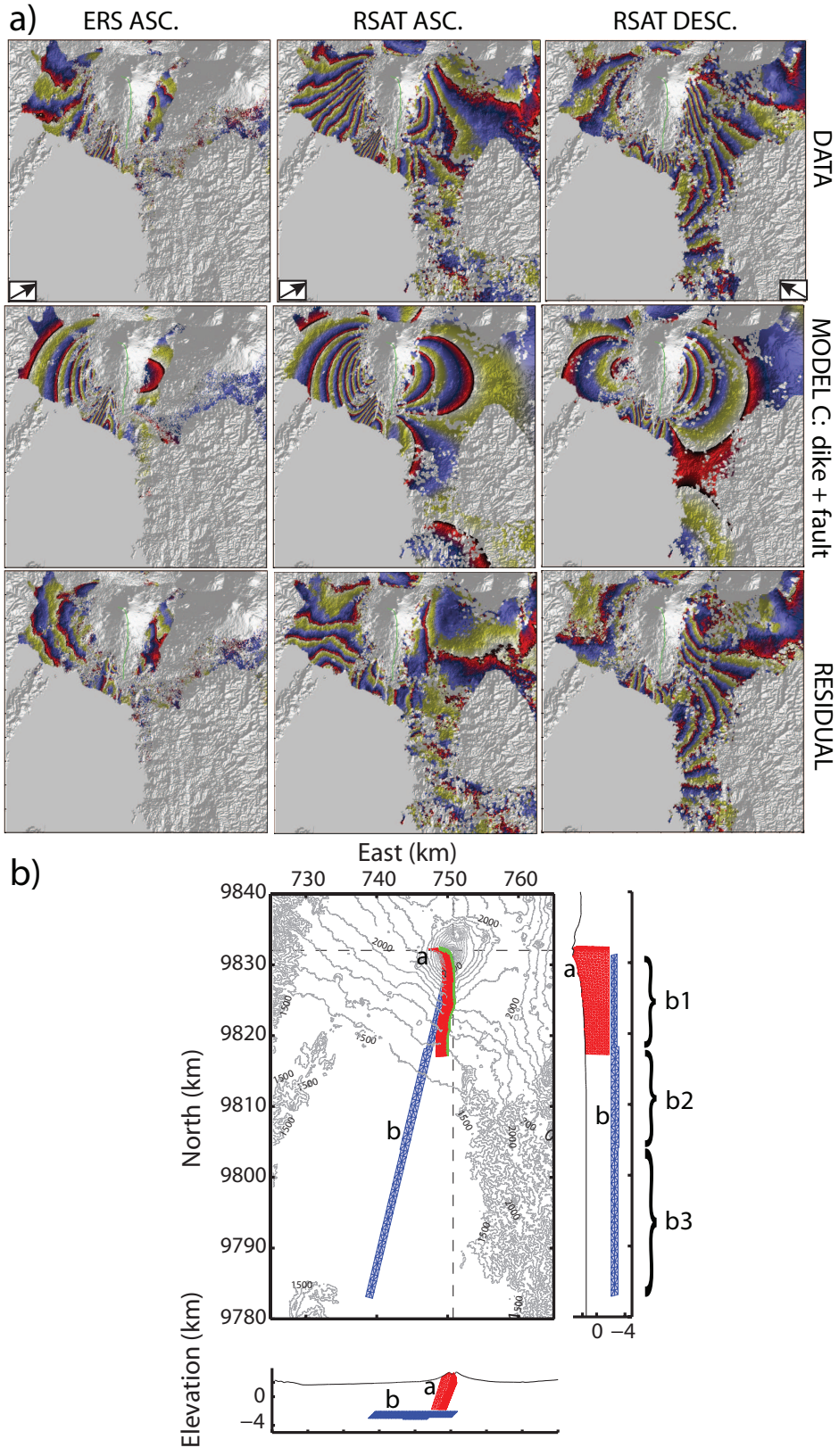

Figure 4.9: a) Observed, modeled and residual interferograms obtained with the model considering a dike and a normal fault structure. The 2002 eruptive fissure is mapped in green. b) Geometry of the best-fit dike and normal fault model. The dike associated with the 2002 eruptive fissure (green) is mapped in pink, while the three fault patches are mapped in blue.

Quadrangular Dike Connected to the Ground								
	P_0 (MPa)	*Botelv* (km a.s.l)	*Dip* (°)	*Shear* (°)	*Botlen*	*Botang* (°)	*Twist* (°)	Average opening on the surface (m)
Max PPD	0.24	-1.8	110	0	1	0	0	0.6
95% conf. intv.	[0.17; 0.58]	[-4.7; -2.2]	[105; 123]	fixed	fixed	fixed	fixed	-

Rectangular Fault Network															
	b1						**b2**			**b3**					
	σ_{drop}	*Midx*	*Midy*	*Midz*	*Length*	*Height*	σ_{drop}	*Length*	*Height*	σ_{drop}	*Length*	*Height*	*Strike*	*Dip*	M_0
	(MPa)	(km)	(km)	(km a.s.l)	(km)	(km)	(MPa)	(km)	(km)	(MPa)	(km)	(km)	(°)	(°)	(N.m)
Max PPD	4.8	749.4	9824.5	-2.1	13.5	1.2	1.1	14.7	1.6	11.4	21.3	1.4	13.5	44	$7.2 * 10^{18}$
95% conf. intv.	[4; 5]	[749; 749.6]	[9824.2; 9824.7]	[-2.1; 15.5]	[12; 15.5]	[1; 1.6]	[1; 1.5]	[11.6; 16.8]	[1.2; 2]	[10.7; 13.3]	[20.6; 23.2]	[1.1; 1.8]	[11; 14]	[37; 53]	-

Table 4.4: Best-fit parameters of the dike and normal faults model. Parameters are described in Figure 3.1.

Two dikes model

Lastly we consider a shallow dike associated with the eruptive fissure, and a second, deeper dike, with its northern end located around the Nyiragongo edifice, extending below Lake Kivu, and ending about 15 kilometers from Idjiwi Island.

Since we do not have InSAR measurements over the water surface, we assessed the position of the southern end of the deep dike based on the sole coherent InSAR data along the shores. It was fixed by trials and errors in preliminary inversions. A reasonable data fit was found with the southern end of the deep dike located at 743,000 N and 9,805,000E UTM (about -1° 45' S and 29° 11' E) (Table 4.5, Figure 4.10). The northern end of the deep dike is defined by two inverted parameters (Strike and Toplen). In order to discriminate between relevant parameters, we perform six inversions, increasing the number of inverted parameters from 9 to 14. All two-dike models provide a better fit than the previous models. The 14 parameters model (Figure 4.10) gives the best-fit with the data as it is associated with the lowest RMS (2.3 cm, Table 4.2). It is also the most likely as it has the lowest AIC.

With this model, the dike connected to the eruptive fissure is subvertical and shallow, with an average height of 2 km and a sub-horizontal bottom side, making the dike higher beneath Nyiragongo volcano (Figure 4.10 and Table 4.5) than beneath the city of Goma. The dike is associated with an overpressure of 0.91 MPa, corresponding to a mean ground surface opening of 3 meters, which is consistent with field measurements [*Komorowski et al.*, 2002-2003]. The other dike is deeper and has a 20 km long upper side at a depth of 3.3 km below the surface, an average height of 6 km, and a 40 km long bottom side. The dike depth is consistent with the estimated depth of the Nyiragongo magma chamber, which is estimated to range from 10 to 14 km below the ground surface [*Tanaka*, 1983]. Like the shallower dike, the deeper dike has a low overpressure of 0.4 MPa, corresponding to an average opening of 0.72 m.

west of the 2002 eruptive fissure, residuals are the smallest on the shortest time-span interferogram. This indicates that time dependent processes, such as a slow motion of the rift border or magma movements associated with Nyamulagira's 2002 eruption, might also have taken place. Residuals are also visible in the Goma area in all beams, probably due to an oversimplified shape of the deeper dike in this area. This could also be the reason for the residuals east of Lake Kivu, on the ascending RADARSAT interferogram.

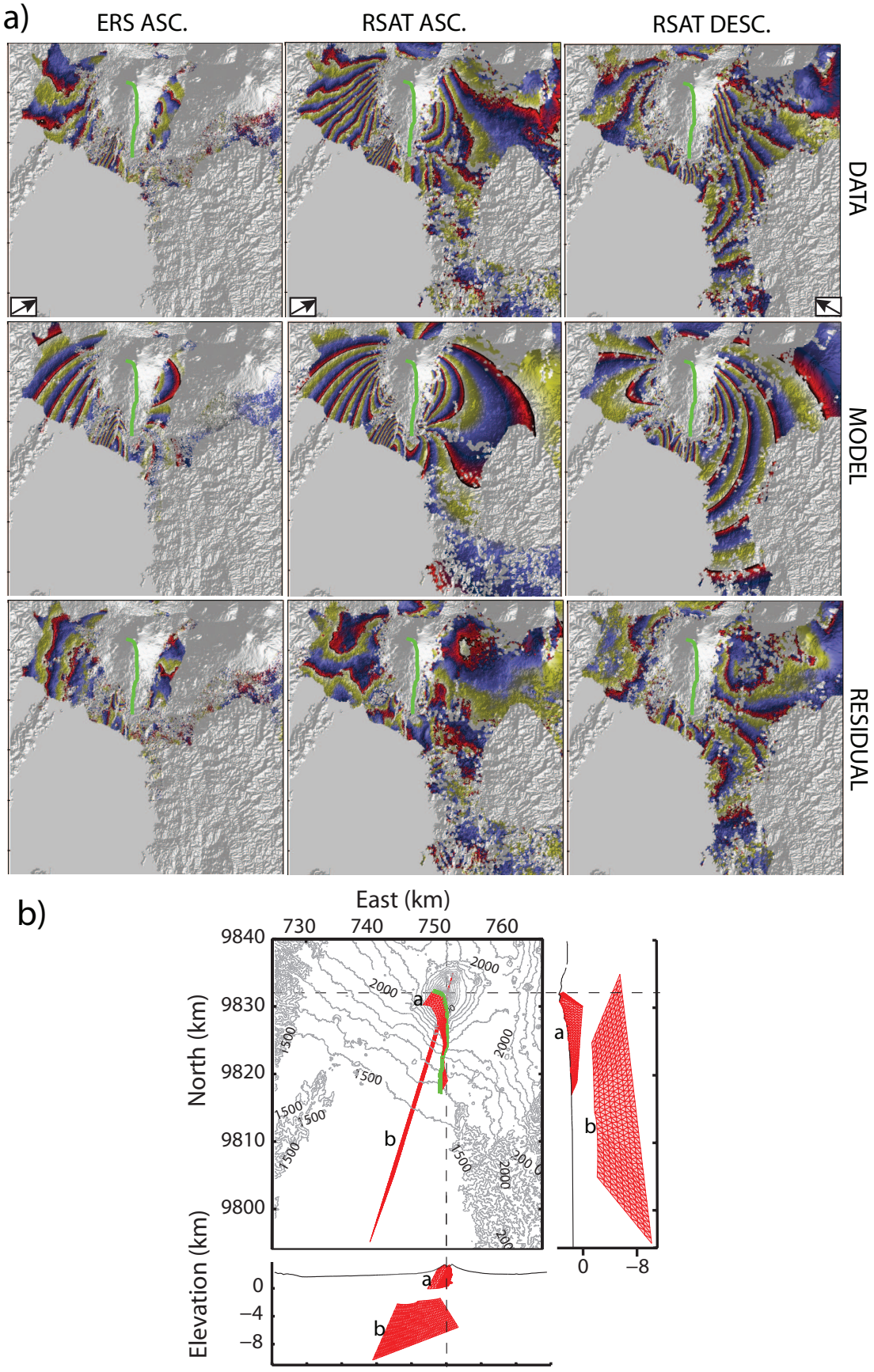

Figure 4.10: a) Observed, modeled and residual interferograms obtained with the preferred model considering two dike intrusions. This model also gives the lowest AIC. The 2002 eruptive fissure is mapped in green. b) Three views of the geometry of the preferred model with two dikes. The 2002 eruptive fissure is mapped in green.

Quadrangular Shallow Dike Connected to the Ground									
	P_0 (MPa)	*Botelv* (km a.s.l)	*Dip* (°)	*Shear* (°)	*Botlen*	*Botang* (°)	*Twist* (°)	Average opening on the surface (m)	Average opening (m)
Max PPD	0.91	0.33	105	0	0.78	-4	14	3	2.1
95% conf. intv.	[0.87; 0.94]	[0.28; 0.36]	[104; 106]	fixed	[0.76; 0.8]	[-5.1; -3]	[13.2; 14.7]	-	-

Quadrangular deep dike												
	P_{02} (MPa)	$Botelv_2$ (km a.s.l)	Dip_2 (°)	$Shear_2$	$Botlen_2$	$Botang_2$ (°)	$Twist_2$ (°)	D_{top2} (km)	$Strike_2$ (°)	$Toplen_2$ (km)	*southern end*$_2$ (km)	Average opening (m)
Max PPD	0.41	-7.9	95	0	2	6.5	0	3.3	17	20.8	(743, 9805)	0.72
95% conf. intv.	[0.39; 0.43]	[-8.1; -7.8]	[93.8; 05.7]	fixed	[1.99; 2.05]	[5.3; 7.7]	fixed	[3.27; 3.4]	[16.9; 17.4]	[20.5; 21.1]	fixed	-

Table 4.5: Best-fit parameters of the preferred model (two dikes with 14 model parameters (f)*) given with their 95% confidence intervals. Parameters are described in Figure 3.1.

	Nyiragongo lava lake altitude below the rim (m)	Volume drained from the crater ($*10^6 m^3$)	Intruded magma volume ($*10^6 m^3$)	Total erupted lava volume ($*10^6 m^3$)
2002	250 [Durieux, 2002/2003]	60 [Komorowski et al., 2002/2003]	60* [Komorowski et al., 2002/2003] 136 in the deep dike + 74 in the shallow dike = 210 [this study]	14-34** [Tedesco et al., 2007]
1977	155 [Durieux, 2008; Tedesco et al., 1007]	234 [Tazieff, 1977; Komorowski et al., 2002/2003]	212*** [Tazieff, 1977; Komorowski et al., 2002/2003]	22** [Tazieff, 1977; Komorowski et al., 2002/2003]

* estimated from the drained volume

** estimated from the lava flow volume

*** estimated from drained - lava flow volumes

Table 4.6: Altitudes of the Nyiragongo lava lake, intruded magma volume and erupted lava volumes estimated for the 1977 and 2002 eruptions. The crater rim is located at about 3,425 m above the sea level.

4.1.6 Discussion

Consistency with geochemical data

A model with two dikes is consistent with the geochemical analyses [*Tedesco et al.*, 2007a], which indicate that the northern lava flows were probably supplied by the lava lake and a shallow magma reservoir, while the southern lava flows were related to a second, deeper reservoir, probably located beneath Goma city and Lake Kivu. The dike volumes are consistent with this model, as the shallower dike has a slightly greater volume ($74 \times 10^6\ m^3$) than the volume of lava that drained from the summit crater ($60 \times 10^6\ m^3$, [*Komorowski et al.*, 2002-2003]), thus it could have been supplied by magma from the lava lake, a reservoir, and the deeper dike; while the deeper dike volume ($136 \times 10^6\ m^3$) could have been supplied by a deep source. We do not see any evidence of a shallow reservoir deflation but this deflation could be hidden by the large displacements associated with the dike intrusion, and the pressure in the reservoir could have been restored by gas exsolution in the magma chamber [*Rivalta and Segall*, 2008]. Here, the minimal estimated depth for the Nyiragongo magma chamber is 10 km below the ground surface [*Tanaka*, 1983]. Computing a volume balance between the lava lake and the inverted shallow dike, neglecting the deeper dike magma volume in the shallow dike, the maximum volume loss of the reservoir is estimated to be 14×10^6 m3. The subsidence would be greatest if the magma was incompressible, and would amount to 3 cm, an amplitude which could barely be detected. As the shallow dike was also probably filled with magma from the deep dike, and that magma is also incompressible, the subsidence associated with the deflation of the Nyiragongo magma chamber is probably undetectable.

The deep dike is not connected to the ground in our preferred model. This connection is

likely to be a fracture or dike, as they are the most efficient means of transporting magma in the lithosphere [*Rubin*, 1995]; [*Delaney and Pollard*, 1981]. When shortening the shallow dike and adding a 5 km long dike to connect the southernmost segment of the eruptive fissure and the deep dike, the data fit decays. We therefore think that the most likely scenario is a small dike between the deep dike and the shallow dike. In our preferred model, the two dikes have a minimal separation of about 2 kilometers (Figure 4.10), which makes the presence of a magma conduit between them likely. Such a path might be too narrow to cause detectable displacements. A similarly narrow path is also postulated for other volcanoes such as Piton de la Fournaise [*Fukushima*, 2006]; [*Traversa et al.*, 2010].

Comparison with lake level data

In order to compare the lake Kivu level data with the InSAR observations and our best fit deformation model, the InSAR displacements from the three viewing geometries were simultaneously used to compute vertical displacements along the lake shore as indicated by *Wright et al.* [2004]. Before computing vertical displacements, InSAR displacements are shifted by the amount that minimizes the misfit between observed data and the best-fit model (Equation 3.2). Standard deviations and unit LOS vectors considered for the displacement calculations are given in Table 4.1.

Comparison of the lake shore vertical displacement determined from the best-fit model, the InSAR data and the water level measurements (Figure 4.5) shows a similar shape of subsidence characterized by a maximum subsidence found approximately at the same location. However, lake level data show a larger maximum subsidence of 37 cm. In addition, whereas the lake level data indicate only a broad subsidence, the InSAR data and associated model predict uplift on each side of the subsiding sector. Because of the large uncertainties in the lake level measurements, we can attribute the discrepancies between the model, InSAR data and the lake level measurements to errors in the latter.

Discontinuities in the Gisenyi area

Two discontinuities are observed in the RADARSAT-1 descending interferogram in the Gisenyi area (Figure 4.4). These discontinuities might correspond to pre-existing faults, related to the eastern border of the rift, reactivated by the tensile stresses induced above the deep dike [*Rubin and Pollard*, 1988]; [*Rubin*, 1992]. As only local displacements are induced, the associated displacements are probably superficial and it is likely that the faults were only reactivated to a shallow depth. Such possible reactivation of faults has large implications for natural hazards in the city of Gisenyi, which could be investigated with further detailed studies including leveling campaigns, and the implantation of new seismic station, tiltmeters or GPS stations in the area.

Bias induced by the homogeneous elasticity hypothesis

A low value of the Young's modulus was considered for the inversions of both dikes (E = 5 GPa), corresponding to the Young's Modulus in the upper two kilometers of the crust. Although this is a reasonable assumption for the shallow dike, such a low value could lead to underestimating the depth of the deeper dike. Indeed models with depth dependent elastic properties, with compliant

layers at shallow depth and a less elastic lower layer, always lead to deeper source estimates, whether these sources are shear faults [*Arnadottir et al.*, 1991]; [*Montgomery-Brown et al.*, 2009] or magmatic reservoirs [*Masterlark*, 2007].

In addition, this low value might also lead to the underestimation of the overpressure of the deep dike. Considering the rigidity increase with depth estimated earlier for this area (Figure 4.6f), the Young's modulus reaches an average value of 90 GPa at 4 km, which is the mean elevation of the deep dike (Table 4.5). Thus, to yield the observed displacements with E = 90 GPa, the deep dike overpressure should be 7.4 MPa.

Low overpressure in a rift context

The deep dike overpressure value is smaller than values estimated in areas where extension is accommodated by normal faulting. Horizontal stresses needed for tectonic rifting are assumed to correspond to a critically stressed crust with hydrostatic pore pressure [*Rubin*, 1990]; [*Buck*, 2006]; [*Townend and Zoback*, 2000]. In such a case, an average overpressure of 54 MPa at 5 km depth could be reached. Instead, the overpressure determined here is close to values estimated when the stress state in the crust is lithostatic, such that the horizontal compressive stress equals the rock pressure. If the rock stress close to the dike was lithostatic, the overpressure at the center of the dike (corresponding to the mean overpressure), would be:

$$\Delta P(z_d) \;=\; \int_{z_d}^{Z_{ma}} (\rho_m \;-\; \rho_r(z'))g dz' \tag{4.2}$$

where ρ_m is the magma density and $\rho_r(z')$ is the rock density, linearly varying with depth, as indicated in Figure 4.6b. For the magma density ρ_m in the shallow dike, we take a value of 2650 kg/m3, which is the nephelinite density at Nyiragongo [*Carn*, 2002/2003], and for the magma density of the deeper dike we take = 2800 kg/m3. Equation 4.2 gives values of 1.1 MPa, and 4.5 MPa for the shallow and deep dikes, respectively. These values are close to the overpressures estimated from the inversion of ground displacements, which are 0.91 MPa for the shallow dike (Table 6) and 7.4 MPa for the deep dike after correcting for the low Young's modulus used for the inversions.

These small overpressures could result from the repetition of dike intrusions causing the compressive stress to increase at a higher rate compared to the tensional stress caused by rift extension. The previous eruption of Nyiragongo volcano occurred in 1977. Assuming the dike opening created by this eruption was similar to the average opening of the 2002 shallow dike, we get a 2.1 meter dike opening over the 25 year period. In North Kivu, a rift extension of 2.8 mm/year is estimated from geodetic data and earthquake slip vectors [*Stamps et al.*, 2008]. This rift extension corresponds to a 7 cm extension in 25 years, which does not balance the compression generated by the dike opening. Thus, it is likely that the compression generated by successive dike intrusions is only partially relaxed by the rift extension. This quasi-lithostatic compressive stress is achieved close to the area of repeated dike intrusions, where the crust is not affected by shear failure. This result indicates that, although the rift is immature, strain localizes in magmatic segments and the rift extension is driven by magma. In such a case, magmatic activity, by increasing minimum principal stresses, would diminish deviatoric stresses and suppress earthquakes driven by tectonic extension [*Parson and Thompson*, 1991]. However,

magmatic activity would trigger earthquakes on faults located close to the injected dikes [*Rubin and Pollard*, 1988]; [*Rubin*, 1992], such that observed earthquakes would be triggered by magmatic rather than tectonic activity. As faults scarps on the western rift border and magmatism are shown to have coexisted [*Wong and Herzen*, 1974], it is also likely that brittle/ductile extension on the rift borders and magmatic extension within the rift coexist, corresponding to heterogeneous stresses with critically stressed crust on the borders and lithostatic stresses inside the rift.

Influence of the rift extension

Both dikes are subvertical and more or less aligned with the rift axis, the shallowest dike being further from the rift axis than the deeper dike, which is found to be strictly perpendicular (N17°E) to the rift extension direction (N108°E ±10° [*Bilham et al.*, 1999]). At the level of the Nyiragongo edifice, the shallower dike follows the N20°W weakness direction [*Meyer*, 1953] joining Nyamulagira and Nyiragongo. Further south, the dike follows a north-south direction also taken during the course of the 1977 eruption. This direction is intermediate between the N20°W weakness direction and the N20°E rift direction, suggesting the combined effect of the area of weakness and the rift extension on the eruptive fissure emplacement. The fact that the direction of the deeper dike is perpendicular to the extension direction indicates that this dike direction is related to the rift extension. It is aligned with the Idjiwi horst (Figures 4.1 and 4.10), located to the south of Lake Kivu, where a seismic reflection experiment [*Wong and Herzen*, 1974] showed that the horst structure extended up to the northern shore of the lake. The horst bounding fault could have guided the magma path. The deep dike could be connected to another eruptive fissure located at Ngangi (Figures 4.1 and 1.7, 10 kilometers west of the 2002 fissure, which strikes N8°E. This undated fissure is associated with the alignment of several eruptive cones and hornitos, and, in some places, to about 10 meters of uplift (as confirmed by a field survey in January 2010). At the time of the January 2002 eruption, the local population reported smoke emissions along part of the Ngangi fissure. Eruptions beneath lake Kivu are probably common since bathymetric data [*Capart*, 1955]; [*Schmid et al.*, 2010] indicate the presence of numerous old volcanic cones on the lake floor (Figure 4.1). The southernmost cones are located above the deep dike determined from our inversions, indicating that this structure might have been active in the past and breached the lake floor.

Triggering of the eruption

Triggering of the eruption by nearby fault motions is unlikely. *Rubin* [1992] showed that, provided magma pressure exceeds horizontal stresses, dike intrusions occur before the compressive stresses are reduced sufficiently to initiate faulting. Moreover, we do not find any evidence of a precursory fault motion in the interferograms. Small tectonic events associated with normal faulting, such as the February 3, 2002 Bukavu event (Mw 5.9 [*d'Oreye et al.*, 2010]), or the October 24, 2002 south Lake Kivu event (Mw 6.2) (Figure 4.34), could remain undetected by interferometry if they occur beneath Lake Kivu or in areas of low coherence, but they would probably be too small to trigger decompression at depth and subsequent magma injection. Thus, it is most likely that the eruption was triggered by the supply of magma from depth, resulting from the melting of asthenosphere by adiabatic decompression due to the extension [*Ebinger and Casey*, 2001].

The most likely scenario (Figure 4.11), consistent with the *Tedesco et al.* [2007a] model, is that magma could have first been supplied to the deep dike, further inducing the opening of the shallow dike and the draining of the lava lake. Then magma coming from the deep source could have been supplied to the southern part of the shallow dike (Figure 4.11), as indicated by the geochemical data [*Tedesco et al.*, 2007a]. Even if the deep intrusion was initiated first, it could have breached the surface after the shallower intrusion as it was further from the surface and fracture toughness is depth dependent [*Rivalta and Dahm*, 2006]. Injection of magma from depth could have triggered the precursory short and long period earthquakes by inducing slip on faults adjacent to the dike [*Rubin*, 1992]. Injection of magma at depth could also be responsible for the harmonic tremor which started eleven months before the eruption. This injection might have remained undetected by interferometry as it was too deep.

Comparisons with the 1977 eruption

The 2002 eruption shares many characteristics with the 1977 event. The two estimated erupted lava volumes (lava flow volumes) are similar (Table 4.6, column 4), and both eruptions are associated with the draining of the summit lava lake. In 1977, the lava lake level was about 155 m below the crater rim, while it was about 250 m before the 2002 eruption (Table 4.6, column 1). Although the lava lake heights were similar, the diameter of the drained crater was larger in 1977 than in 2002 [*Durieux*, 2002/2003], leading to a much larger estimation of the drained volume in 1977 (234 $\times 10^6$ m3) [*Tazieff*, 1977b] compared to 2002 ($\times 10^6$ m3) [*Komorowski et al.*, 2002-2003] (Table 4.6, column 2).

In 1977, an intruded volume of 212 $\times$ 10^6 m^3 was estimated from the difference between the drained and the lava flow volumes [*Komorowski et al.*, 2002-2003]; [*Tazieff*, 1977b]. Following the same approach, an intruded volume of 60 $\times 10^6$ m^3 was estimated from the drained volume in 2002 (Table 4.6, column 3) [*Komorowski et al.*, 2002-2003]. However, inverting for deformation data, we find that a shallow and a deep dike were involved in the eruption, leading to an intruded volume of 210 $\times$ 10^6 m^3, more than three times larger than this estimate. The modeling is consistent with the lava lake draining in the shallow dike. This shows that, when estimating magma volumes, the drained volumes should be considered as minimum volume estimates.

In 2002, similar to in 1977, erupted volumes (14-34 $\times$ 10^6 m^3 and 22 $\times$ 10^6 m^3, respectively) are an order of magnitude smaller than the intruded volume (210 $\times$ 10^6 m^3 and 212 $\times$ 10^6 m^3, respectively) (Table 4.6). The large intruded versus extruded volume is consistent with the tensional context of the region, where the continuous rift extension partly relaxes compressive stress and permits for the intrusion of large volumes.

Both eruptions are associated with rift parallel fissure networks, indicating that the intrusion direction is related to the rift extension. However, it is likely that, in the same way as for the 2002 eruption, the 1977 eruption involved a deep source. Thus 8 months after that eruption, high frequency earthquakes with a depth range of 3 to 10 km were recorded south of Nyiragongo volcano along the rift axis [*Tanaka*, 1983]. They could have been aftershocks induced by the stress perturbation associated with the 1977 dike intrusion.

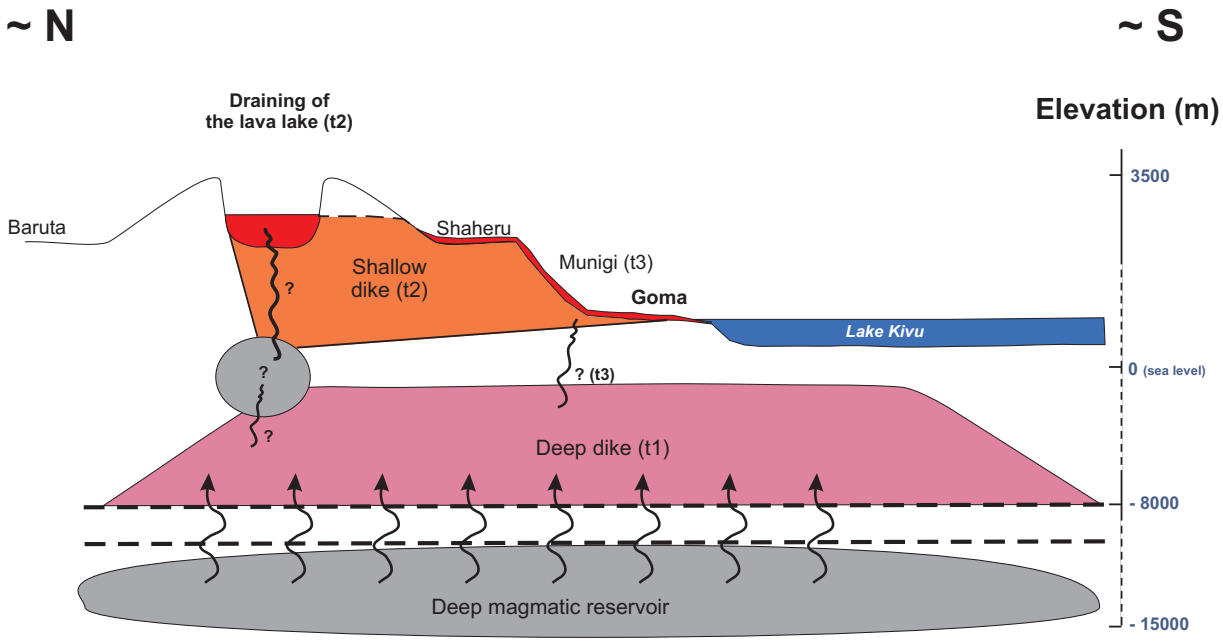

Figure 4.11: Magmatic plumbing system beneath the Nyiragongo volcano and the northern part of Lake Kivu, and possible eruption chronology, inferred from the modeling and consistent with a previous study by *Tedesco et al.* [2007a]. Note that the figure is not to scale.

4.2 Nyamulagira Volcano Eruptions

During the study period a total of 8 eruptions occurred at Nyamulagira volcano. Ground displacements related to the 1996, 2002, 2004, 2006 and 2010 eruptions were successfully recorded by InSAR, providing us the required input data for our modeling. Unfortunately, InSAR data spanning the other eruptions, 1998 2000 and 2001, were too noisy to clearly identify any significant and useful ground displacements. Lava flows associated to the eruptions captured by InSAR is shown in Figure 4.12.

4.2.1 Other available data

For single deformation events, the conventional InSAR is used to obtain ground displacement maps before modeling them. Other data, obtained from geology, seismology, geochemistry and fields investigations are used to better constrain and validate our numerical models. Even if ground-based geodetic networks (GPS and tiltmeters, see Figure 1.17) were installed after the January 2002 Nyiragongo eruption, the lack of data for the required periods or the location of the stations too far from the Nyamulagira volcano prevented us from using them. Thus, InSAR data are the only geodetic data we use.

4.2.2 Nyamulagira 2010 Eruption

A new eruption at Nyamulagira began on January 2, 2010, at 02:17 according to seismic data from the Goma Volcano Observatory (GVO) monitoring network. Lava erupted inside the caldera from the pit crater (located in the north-eastern part of the caldera) and along an ENE-WSW-trending fracture in the southern part of the caldera (Figure 4.13). A 600-m-long fissure opened on the SSE flank of the main edifice, about 1.5 km from the caldera rim. Lava fountains were higher than 300 m during the first days of the eruption (Figure 4.13a). Beginning on 11 January, this height began to decrease irregularly to 50-150 m high. A 150-m-high new volcanic cone was built. The main flows were 10.5-11 km long (Figure 4.12), and partly covered portions of the 2006 lava flow (Figure 4.13b) as well as the southern part of the 2001 lava flow (Figure 4.13c). The eruption lasted until 27 January 2010. The activity in the caldera associated with the northern eruptive fissure probably stopped on January 9. See *Smets et al. [in prep.]* for a detailed study of the different eruptive phases.

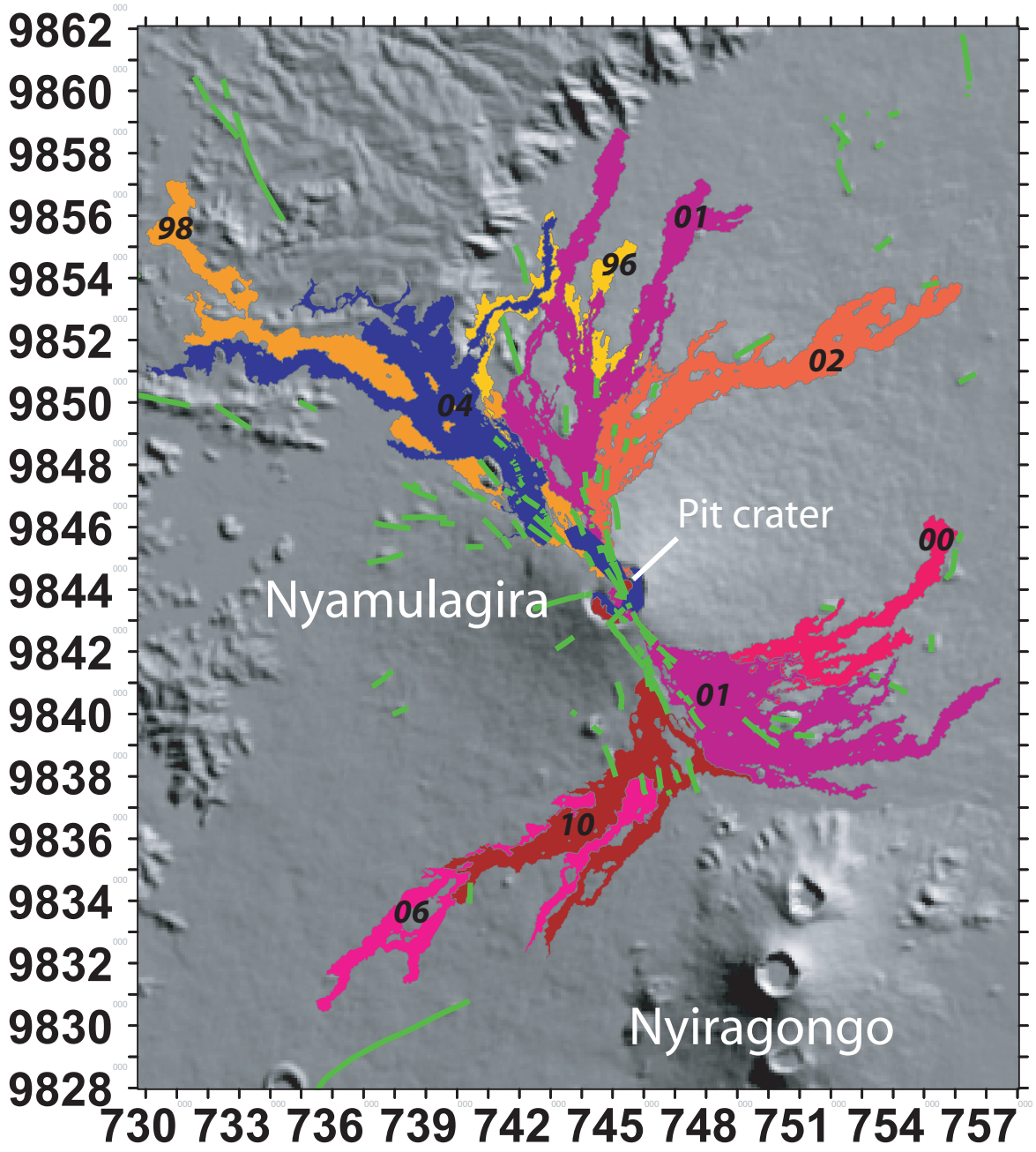

Figure 4.12: Nyamulagira lava flows from the 1996 to the 2010 eruptions are from *Smets et al.* [2010c], except for the 2004 lava flow mapped inside the caldera (as explained in the subsection 4.2.3). Volcanic features in green were identified by Smets et al. *[in prep.]* based on optical and radar images

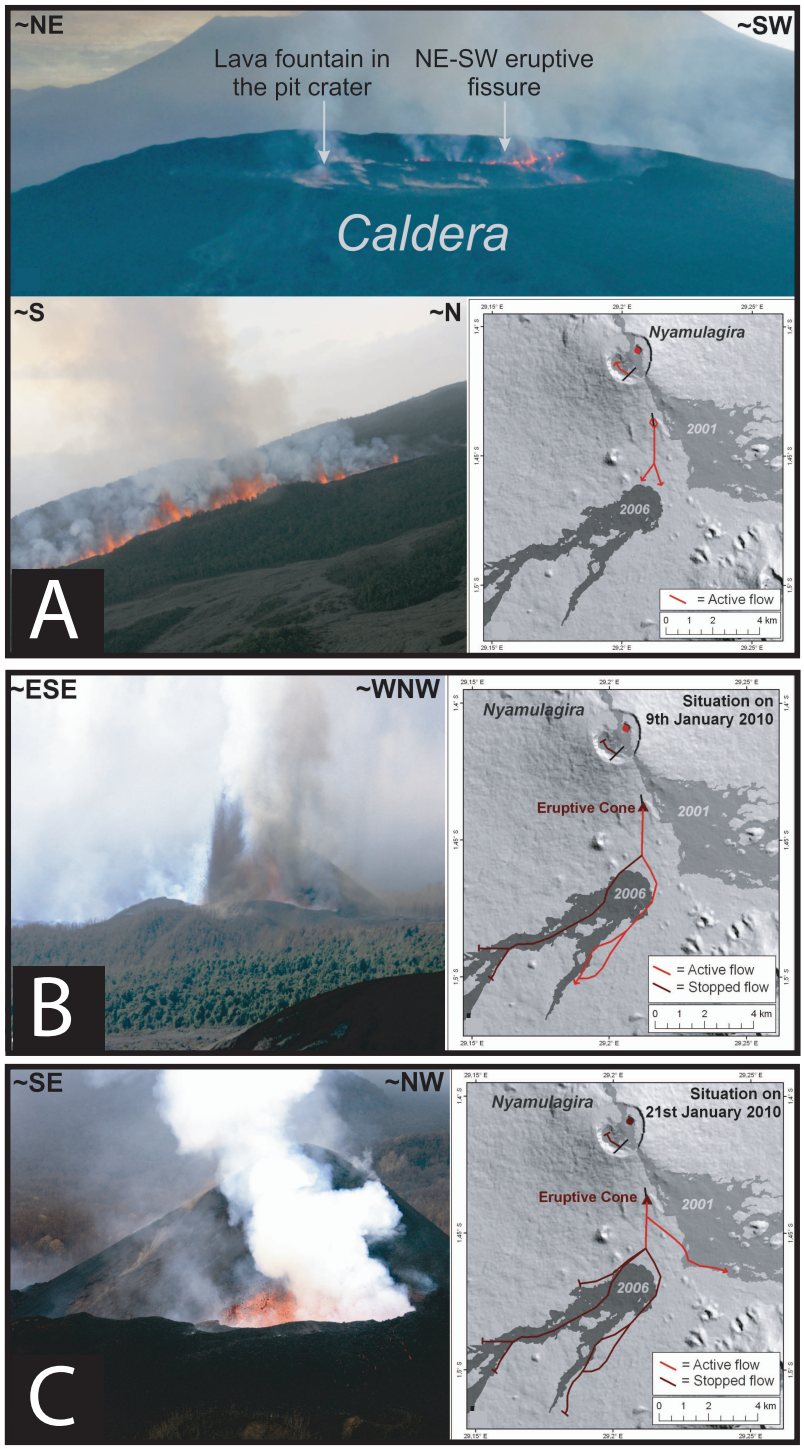

Figure 4.13: The main eruptive phases, after *[Smets et al., in prep.]*. Phase 1 (A): eruption started at 2h17 local time on January 2, 2010. Lava fountains appeared in the pit crater and along a NE-SW fracture inside the caldera, as well as along a 600 m long fracture on the SSE flank of the main edifice, about 1.5 km far from the caldera rim. Phase 2 (B), January 3 - 9, 2010: the eruptive activity inside the caldera concentrated in the southern part of the pit crater and corresponded to lava fountains and a small temporary lava lake. Lava fountains in the SSE flank of Nyamulagira were restricted to the central / S-half part of the eruptive fracture, at an elevation of about 2540 m (a.s.l.). The lava flows nearly reached their maximum length during this phase. Phase 3, January 10 - 16, 2010: the lava fountains and the small lava lake inside the caldera disappeared on January 10, 2010. (C) January 17 - 27, 2010: progressive decrease of eruptive activity until the end of the eruption.

InSAR data

Ground displacements related to the January 2010 eruption were captured by C-band SAR sensors (wavelength of 5.6 cm) onboard of satellites ENVISAT and RADARSAT-2 with different beams, and by L-band ASAR sensor (wavelength of 11.8 cm) onboard of satellite ALOS (Table 4.7). The wrapped and unwrapped interferograms are shown in Figures 4.14 and 4.16A, respectively.

Satellite	LOS vector [East, north, Up]	Time span	Ha (m)	Nb used in Figure 4.14
ENVISAT (asc., beam 42i5)	[-0.5, -0.1, 0.9]	2009/12/10 - 2010/02/18 (70 days)	45	1
ENVISAT (asc., beam 314i7)	[-0.6, -0.13, 0.8]	2009/12/29 - 2010/02/02 (35 days)	430	2
ENVISAT (desc., beam 35i2)	[0.3, -0.07, 0.95]	2009/12/10 - 2010/01/14 (35 days)	43	3
ENVISAT (desc., beam 493i4)	[0.45, -0.1, 0.89]	2009/12/07 - 2010/01/11 (35 days)	74	4
ENVISAT (desc., beam 221i6)	[0.54, -0.12, 0.83]	2009/12/23 - 2010/01/27 (35 days)	3200	5
ENVISAT (desc., beam 450i7)	[0.6, -0.13, 0.8]	2009/12/04 - 2010/01/08 (35 days)	32	6
RSAT-2 (desc.)	[0.5, -0.11, 0.86]	2002/03/03 - 2002/09/11 (144 days)	97	8
ALOS (asc.)	[-0.55, -0.12, 0.83]	2009/12/17 - 2010/02/01 (46 days)	704	9

Table 4.7: Relevant characteristics of the interferograms used for the modeling of the 2010 Nyamulagira eruption.

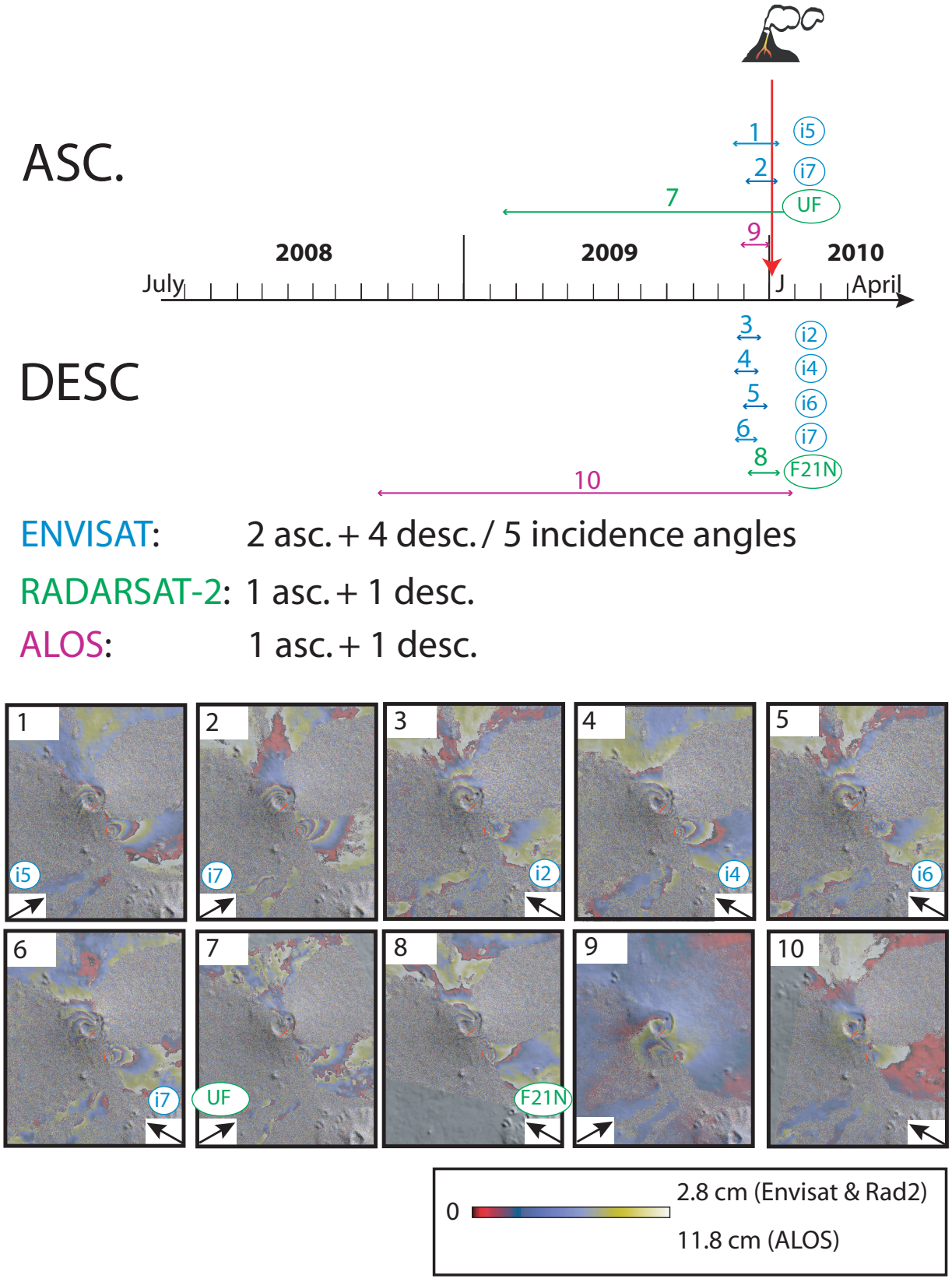

Figure 4.14: Available InSAR data superimposed on a shaded relief DEM covering the 2010 Nyamulagira eruption

In Figure 4.15, the signal A, east of the northern eruptive fissure corresponds to a range increase in the descending modes, but is not so clearly visible in the ascending modes. B and C signals, south east of the northern fissure and east of the southern fissure, respectively, correspond to range decreases in the descending mode, and to range increase in the ascending modes. Finally, D signal, which is only visible in the descending modes, corresponds to a small range increase.

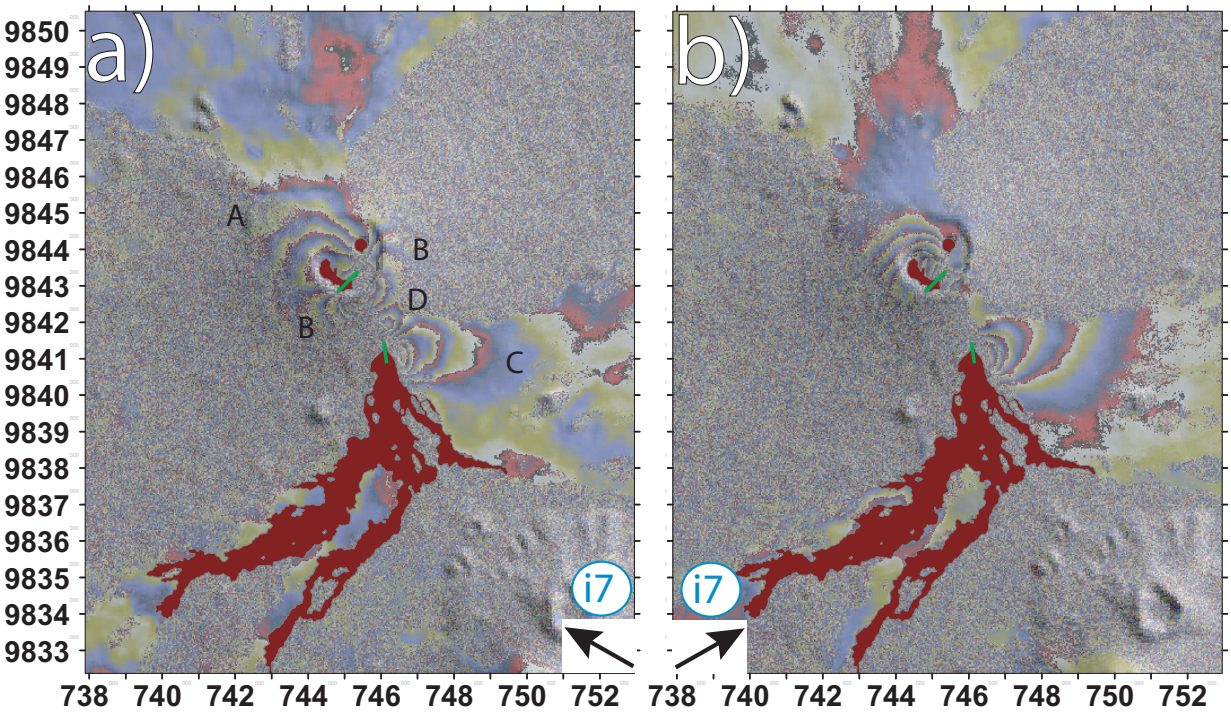

Figure 4.15: a) ENVISAT descending interferogram, from 2009/12/10 to 2010/01/14, $i7$ mode (Incidence angle of 38°), and b) ascending interferogram, 2009/12/29 - 2010/02/02, $i7$ mode (Incidence angle of 37° inc. angle); both superimposed on a shaded relief DEM showing the different deformation patterns associated with the main eruptive phase of the 2010 eruption. See text for A, B, C and D signals explanation

The InSAR displacements from the eight beams were simultaneously used to compute the horizontal and vertical displacements in an area coherent in the three datasets (Figure 4.16). The reference of each unwrapped interferogram was adjusted from the best-fitting model offset calculation as done in Section 4.1. They show that the main part of the 2010 deformation is due to horizontal displacements. These displacements correspond to a westwards subsidence east of northern eruptive fissures (A). They correspond to eastward displacements to the south east of the northern eruptive fissures (B) and east of the southern fissure (C) which reach a maximum of 0.24 meters south-east of the caldera and east of the southern eruptive fissure. However some vertical displacements are also observed, corresponding to an uplift of a maximum about 0.14 meters for the D signal, and to a slight subsidence of about 0.06 meters in the caldera.

The A, B and C signals are consistent with one or several dike intrusion(s) associated with the eruptive fissures, as the sense of ground displacements changes whether the orbits are ascending or descending and displacements have opposite directions on both sides of the dikes. This change in the sense of displacements is characteristic of displacements having mainly horizontal components (Figures 4.15 and 4.16B), such as those associated with a dike. Signal D could be induced by the sources interaction or by a fault movement (or reactivation). The small amplitude vertical

displacement (Figures 4.15 and 4.16B) centered on the NW flank of the volcano, can be attributed to a source distinct from a dike intrusion such as a deflating sill-like or spherical reservoir.

Our InSAR database reveals in some ENVISAT beams that deformation also occurred inside the caldera before the January 2010 eruption (discussed in Section 5). Excluding this caldera precursory deformation, our InSAR database constrains most ground deformations to have occurred between December 29, 2009, and January 10, 2010, which corresponds to the disappearance of volcanic activity inside the caldera (Figure 4.13). The eruptive phases (Phases 3 and 4 in Figure 4.13) from January 11 to January 27, 2010, were rather probably a passive extrusion of lava through open conduits at the SE flank vent. The numerical modeling of the multibeam InSAR data mainly assumes the presence of one to two dike intrusions, beneath the Nyamulagira south-east flank and the caldera, and connected to the surface through the two main eruptive fissures.

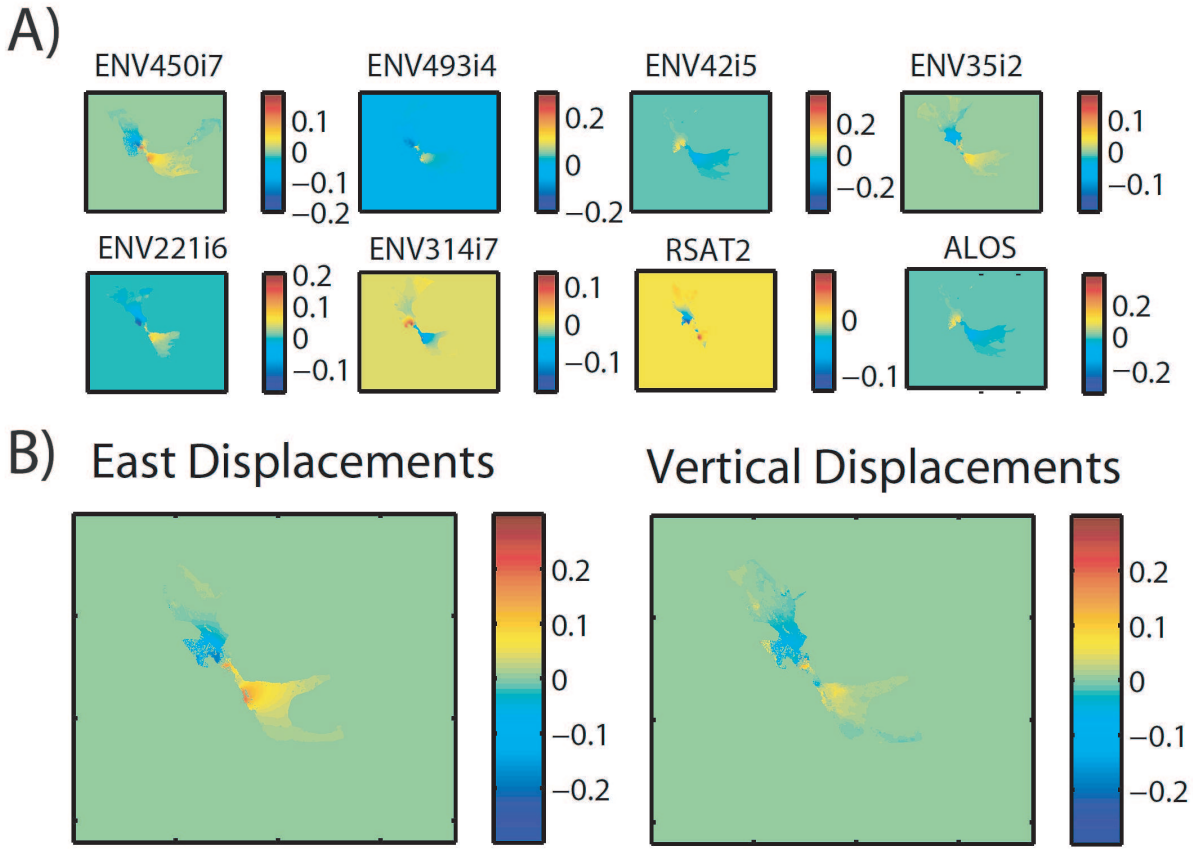

Figure 4.16: A) The eight selected interferograms showing the deformations associated with the 2010 Nyamulagira eruption after unwrapping with Snaphu. All displacements are in meters. B) The InSAR displacements from the three beams were simultaneously used [*Wright et al.*, 2004] to compute the horizontal (left) and vertical displacements (right). The standard deviation are 0.7 cm and 1.8 cm , on eastern and vertical displacements, respectively.

Other data

Only three GPS stations were operational during the eruption (BLG, OVG, RSY + the reference NURK in Kigali). The ground deformation recorded is not over 1 cm, which is roughly the detectability threshold of the InSAR technique in the most favorable conditions, even using Multi-Temporal InSAR techniques (see Section 5).

Several long-period (LP) seismic swarms were recorded between the 2006 and 2010 eruptions. A period of particularly high seismic activity occurred during 6 months following a 5.9-magnitude earthquake in Bukavu (128 km SSW) on 3 February 2008 [*d'Oreye et al.*, 2010]. However, there was no noticeable increase in seismic activity in the months preceding the January 2010 eruption. According to *Tedesco* [2010], both tectonic earthquake and tremors occurred simultaneously with the emission of lava at the surface. This observation lead *Tedesco* [2010] to suggest that magma was already close to the surface before the eruption.

Data from the Ozone Monitoring Instrument (OMI) of the EOS/Aura satellite allowed a monitoring of SO2 emissions from Nyamulagira. Those data provide the amount of emitted SO2, as well as the evolution and the dispersion of the gas plume during the eruption. MODIS images, processed with the MODVOLC algorithm, were used to follow the evolution of thermal emissions during the eruptions. Finally, Landsat 5 TM and 7 ETM+, EO-1/ALI and Terra/ASTER have also been used to map the new lava flows, cone and fractures, and to estimate the erupted lava surface. Considering an average 3 m thickness for the Nyamulagira lava flows, the estimation for the 2010 erupted volume is $46 \times 10^6\ m^3$ [*Smets et al.*, 2010c].

Modeling and inversions

For our modeling, we did not take into account the RADARSAT-2 ascending and ALOS descending interferograms, as they have too large time spans (Figure 4.14), leading to larger areas of decorrelation than other interferograms and moreover, including the possible pre- or post-eruptive ground deformations. The structure mesh interval is 200 meters, while the topographic mesh has 1222 nodes (with a 50 meters nodes interval along the two eruptive fissures).

The complex observed displacements probably result from a combination of sources. The eruptive fissures indicates at least one feeding dike. The southern eruptive fissure is a typical radial fissure, following the NNW-trend fracture network weakness area between the Nyamulagira and Nyiragongo volcanoes (Chapter 1), which is a preferential intrusion direction followed during many eruptions, such as in 2006 (Figure 4.13). However, the northern fissure is quite unusual as its direction makes a high angle of about 50° with the southern fissure (Figure 4.13), making them unlikely to be typical en echelon eruptive fissures. This fissure is roughly perpendicular to the steepest slope thus it could correspond to a superficial rotation of a deeper fracture aligned with the southernmost fissure, or might testimony of two different stress fields acting at two slightly different locations and times during the eruption. Two distinct feeding phases and therefore feeding systems, probably dikes, can thus be involved. Finally, as petrological and geophysical data suggest a shallow - 3 to 7 km beneath the volcano -, a magma reservoir might explain part of the deformation patterns. We will consider this reservoir as a planar source, closer to a sill than to a spherical source in analogy with systems studied in the Galapagos [*Amelung et al.*, 2000]. It is important to note that all the sources are simultaneously considered in a single 3D-MBEM model, so they can mechanically interact with each other.

To test these different hypotheses, we simultaneously invert the InSAR data corresponding to the eight selected beams. Three sets of modeled sources were considered: 1) a single dike associated with the two eruptive fissures, 2) a dike associated with the northern eruptive fissure in the caldera, and a second dike associated with the southern eruptive fissure on the southeastern flank of the volcano, 3) a dike associated with the northern eruptive fissure in the caldera, a second dike associated with the southern eruptive fissure on the SE flank of the volcano, and a deflating sill-like elliptic magmatic reservoir. The Akaike information (see Chapter 3) criterion (AIC) corresponding to each model is computed in order to determine which is the most likely.

Several inversions, considering different parameters were performed for each set of modeled sources. The most relevant inversions characteristics for the three sets of modeled sources are given in Table 4.8

	$1dike$	$2dikes$	$2\ dikes + deflating\ reservoir$
N° of param. inv.	8	8	10
RMS	2.9	2.6	1.8
AIC	7804	6779	5898

Table 4.8: Comparison of the most relevant inversions results for the 2010 Nyamulagira eruption

The selected inversion result for a single dike associated with the two eruptive fissures (Table 4.8, column 1) was obtained by inverting 8 parameters: the dike overpressure and seven parameters defining its geometry, *Dip*, *Botelv*, D_top and four parameters for the location of the upper side of the main rectangular part (*Botlen* was fixed to 1 and *Shear*, *Twist* and *Botang* angles were fixed to zero). The inversion shows that a single dike (Table 4.8, column 2), having a uniform overpressure, connected to the ground by the two eruptive fissures cannot satisfactorily explain the complex InSAR data (Figure 4.17). Inverting for increasingly large numbers of parameters and allowing more complex intrusion shape does not improve the inversions

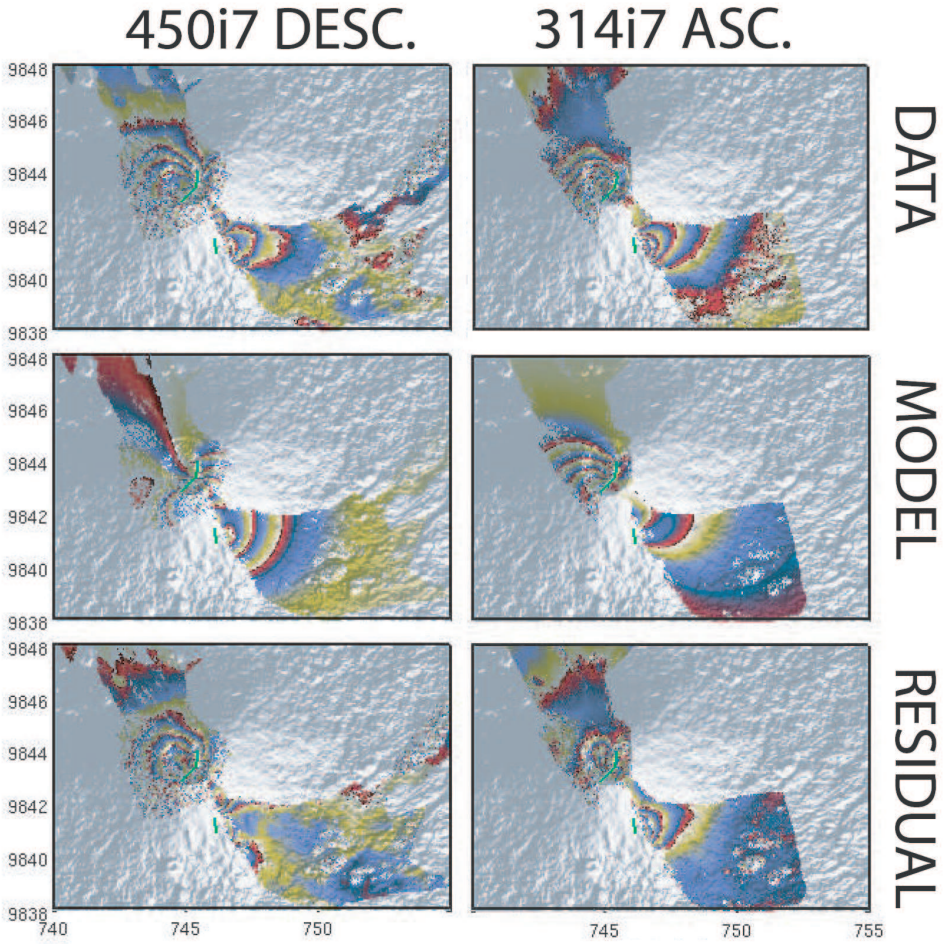

Figure 4.17: Observed, modeled and residual interferograms with a single dike intrusion associated with the 2010 eruptive fissures (in green). Note that all beams were however considered in the inversion.

The selected inversion result for two dikes, each connected to one of the fissure (Table 4.8, column 2) was obtained by inverting 8 parameters: P_0 and *Botelv* for the northern dike and P_0, *Botelv* and the location of the upper side of the main rectangular part for the southern dike, other parameters were fixed.

Such a model better explains the data in the southern part of the area (Figure 4.18, location *C* in Figure 4.15), the fringes pattern indeed is a closed feature as observed on the InSAR data. The signal there can thus be explained using a southern dike with a larger overpressure than the northern dike (2.2 for the southern dike versus 0.7 MPa for the northern dike). The northern part of the signal in the caldera is however not satisfactorily fitted.

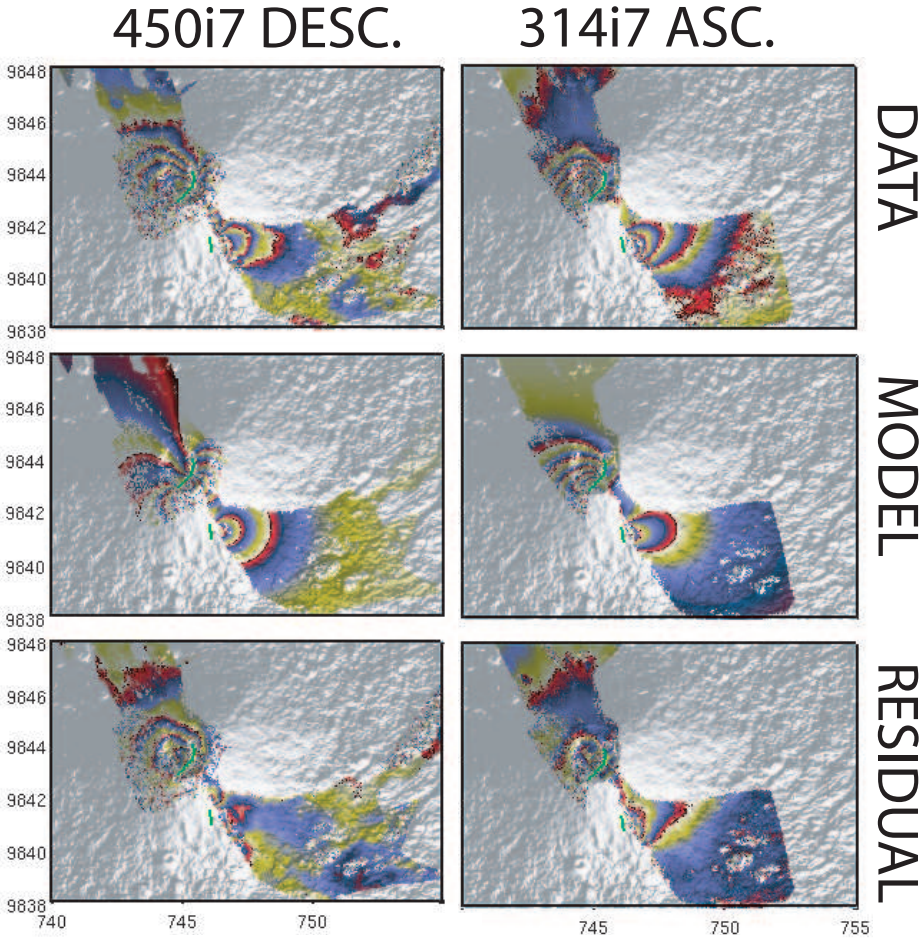

Figure 4.18: Observed, modeled and residual interferograms with two dike intrusions associated with the 2010 eruptive fissures (in green). Note that all beams were however considered in the inversion.

Because of the large number of sources and parameters that can be inverted, the following strategy has been used. First, an inversion considering 13 parameters, P_0, *Dip* and *Botelv* for both dikes, P_0, S_1 (ellipse major axis), S_2 (ellipse minor axis), *Rotplane* (strike of the major axis), and location of the ellipse center was done. Secondly, to refine the results of this test, a second inversion was done, with fixing some parameters thanks to test 1 results (indicated by * in Table 4.9), and allowing new parameters to be inverted, or larger search intervals than previous ones.

The best-fitting model, having to the lowest AIC (4.8), corresponds to two dikes with two independent overpressures and a deflating sill-like reservoir below the caldera. The parameters inverted are given in the Table 4.9. The model geometry is shown in Figure 4.19.

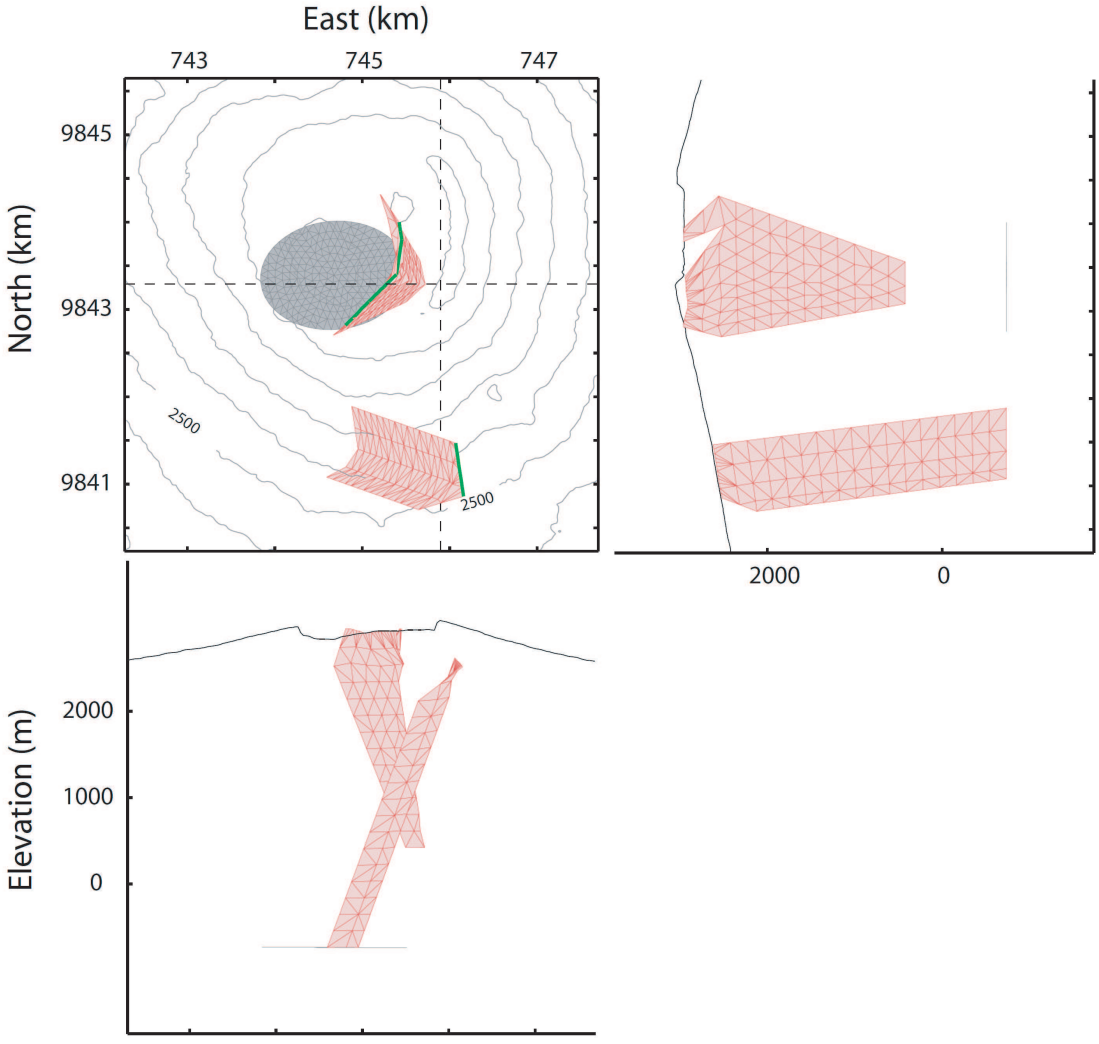

Figure 4.19: B) Geometry of the best-fit model.

The northern dike dips 77° towards the east, while the southern dike dips 70° towards the west. The northern dike reaches a shallower depth than the southern one, 2.6 km versus 3.7 km beneath the volcano summit, respectively. Both depths are consistent with the estimated depth of the Nyamulagira magma reservoir roof. The northern dike volume is 1.1×10^6 m^3, and 2.7×10^6 m^3 for the southern one. The sum of the two dikes volumes is thus about one order smaller the

estimated erupted volume (46×10^6 m^3 [*Smets et al.*, 2010c]). The northern dike overpressure is three times lower (1 MPa) than that of the southern dike (3 MPa). Both overpressures are consistent with typical values for the North Kivu area. The average opening on the surface is 0.3 and 0.8, for northern and southern dike respectively. Note that inversions considering also a dip for the elliptic sill-like reservoir do not improve the fit.

The RMS error for the best-fitting two dikes and deflating sill model is 1.8 cm (Table 4.8) leading to reasonable model residuals (Figure 4.20). The highest residuals in the Nyamulagira caldera.

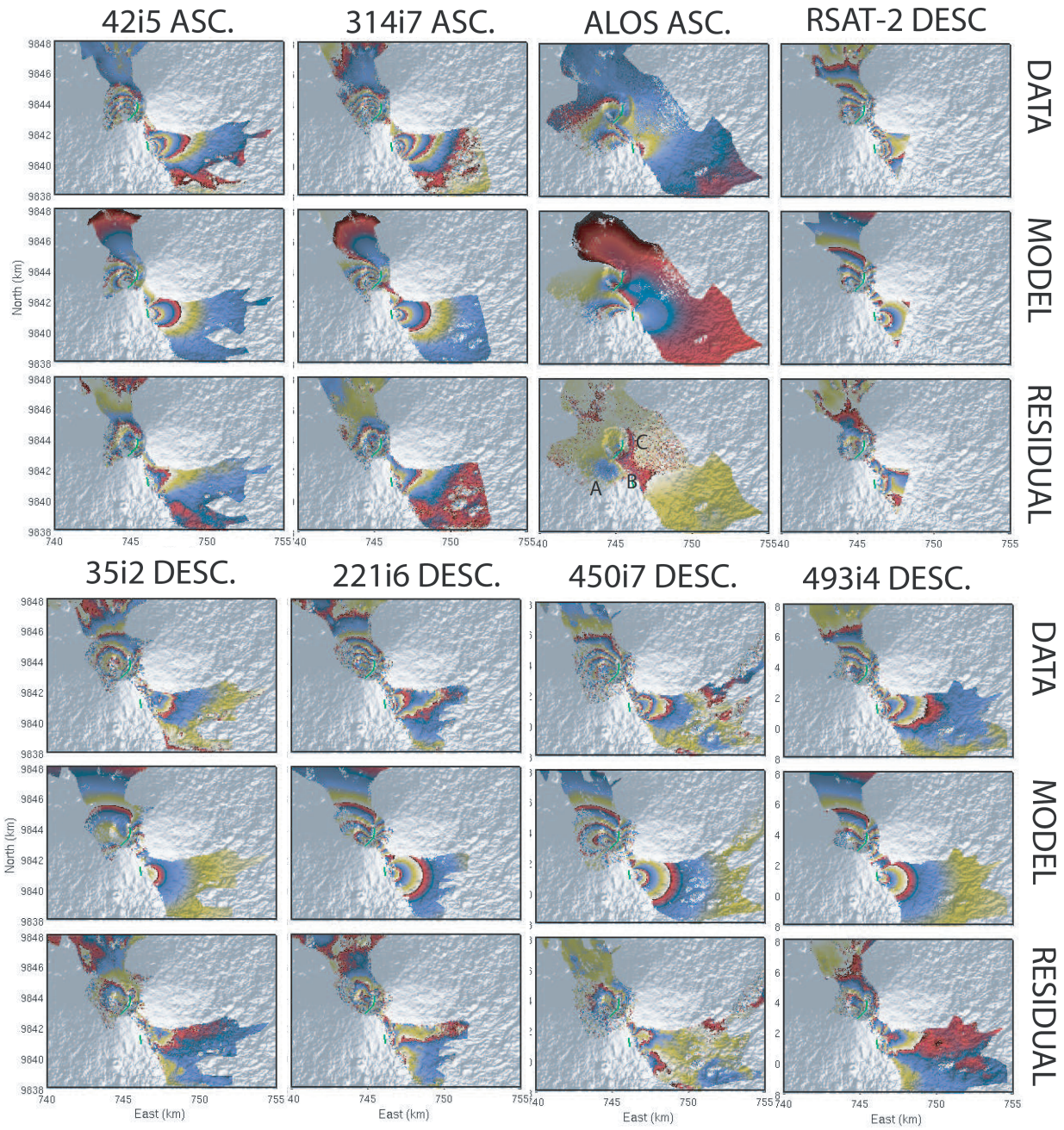

Figure 4.20: Observed, modeled and residual interferograms obtained with two dikes and an elliptic sill-like reservoir associated with the 2010 eruptive fissures (in green).

Because of the two distinct dike directions and overpressures, the two dikes probably indicate two different mechanisms under two different stress field conditions acting in the caldera summit and in the southeastern flank.

The northern dike bottom is about 1 km shallower than the modeled sill which is about 3.7 km beneath the volcano summit. However, if magma is buoyant, the connection between the dike bottom and the reservoir might have closed after the eruptive activity at the summit had stopped or the path linking them could be too narrow to be detectable by InSAR. Indeed, analytical models [*Weertman*, 1971], numerical models [*Dahm*, 2000] and laboratory experiments [*Rivalta and Dahm*, 2006] show that buoyant dikes propagate vertically closing their lower tip. The southern dike reaches the depth of the modeled sill but is about 1 kilometer southern of it. Again, there could be a narrow lateral path linking the two dike structures or the southern dike and the sill, undetectable by InSAR.

The L-band ALOS ascending interferogram, which has the highest coherence (Figure 4.20, row 1, column 3), shows three interesting residual patterns. Signal A, to the south of the summit caldera, indicates that the model still need to be refined to also explain this area, the northern dike or sill extensions could probably thus be revised. The same ALOS data also show a range increase pattern in B which is probably consistent with the on-going graben subsidence along the NNW fissures network linking the two volcanoes identified on optical images and photographed during the January 2010 helicopter flights (Figure 1.13). Signal C, is also a range increase which affects the eastern half of the Nyamulagira rim. This feature is probably indicating the progressive collapse of the eastern rim of the summit caldera, as noticed by circular fissures affecting the upper eastern flank (Figure 1.12) and is actually also visible on most of the ENVISAT coherence images from descending orbits acquired from 2003 in our InSAR database [*d'Oreye et al.*, 2008] as a half-circular loss of coherence (Figure 4.21). Events such as the 2010 Nyamulagira eruptions could promote the eastern summit flank collapse and the southeastern flank subsidence which are probably continuous.

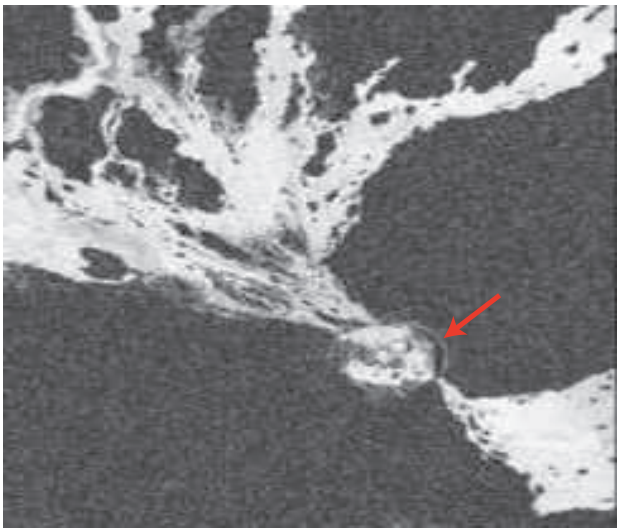

Figure 4.21: Close-up on the Nyamulagira volcano in a coherence image of the ENVISAT descending interferogram spanning the period from October 29, 2008 to January 7, 2009. Note that the image is not geocoded.

Northern dike										
	P_0 (MPa)	*Botelv* (km a.s.l)	*Dip* (°)	*Shear* (°)	*Botlen*	*Botang* (°)	*Twist* (°)	D_{top} (m beneath surf.)	*northern end* (km UTM)	*southern end* (km UTM)	Average opening on the surface (m)
Max PPD	1	0.4	77	0	0.26	0	0	400	745.1, 9844.5	744.5, 9842.6	0.3
95% conf. intv.	[0.76; 1.2]	[0; 0.6]	[74; 81]	fixed	[0.17; 0.32]	fixed	fixed	[400; 490]	[745; 745.2], [9844.3; 9844.5]	[744.4; 744.6], [9842.6; 9842.8]	-

Southern dike										
	P_0 (MPa)	*Botelv* (km a.s.l)	*Dip* (°)	*Shear* (°)	*Botlen*	*Botang* (°)	*Twist* (°)	D_{top} (m beneath surf.)	*northern end* (km UTM)	*southern end* (km UTM)	Average opening on the surface (m)
Max PPD	3*	-0.7*	111*	0	1	0	0	400	746.1, 9841.5*	745.8, 9841*	0.8
95% conf. intv.	fixed	fixed	fixed	fixed	fixed	fixed	fixed	fixed	fixed	fixed	-

Elliptic sill								
	P_0 (MPa)	S_1 m	S_2 m	*Rotplane* (°)	*Dipdir* (°)	*Dip* (°)	X_{center}, Y_{center} (km UTM)	Z_{center} (km a.s.l)
Max PPD	-5	1683*	1240*	5.5*	0	0	744.7, 9843.4*	-0.7*
95% conf. intv.	[-5.5; -5]	fixed	fixed	fixed	fixed	fixed	fixed	fixed

Table 4.9: Best-fit parameters of the two dikes and elliptic sill model for the 2010 Nyamulagira eruption. * denotes the results obtained and fixed after previous inversions.

4.2.3 Other Nyamulagira Eruptions

1996 Eruption

On December 1, 1996, a flank eruption started along two NNW eruptive fissures, 2.5 km from the caldera rim (Figure 4.22). The eruption lasted at least 4 days [*BGVN*, 1996a]. The estimated lava volume is 49.8 ± 16.6 10^6 m^3 [*Smets et al.*, 2010c]. The seismicity was higher than usual in September 1995 [*BGVN*, 1996b], and from November 15 to December 2 1995, with several hours of low amplitude tremors following each series of tectonic earthquake. An increase in seismicity occurred again in August 1996.

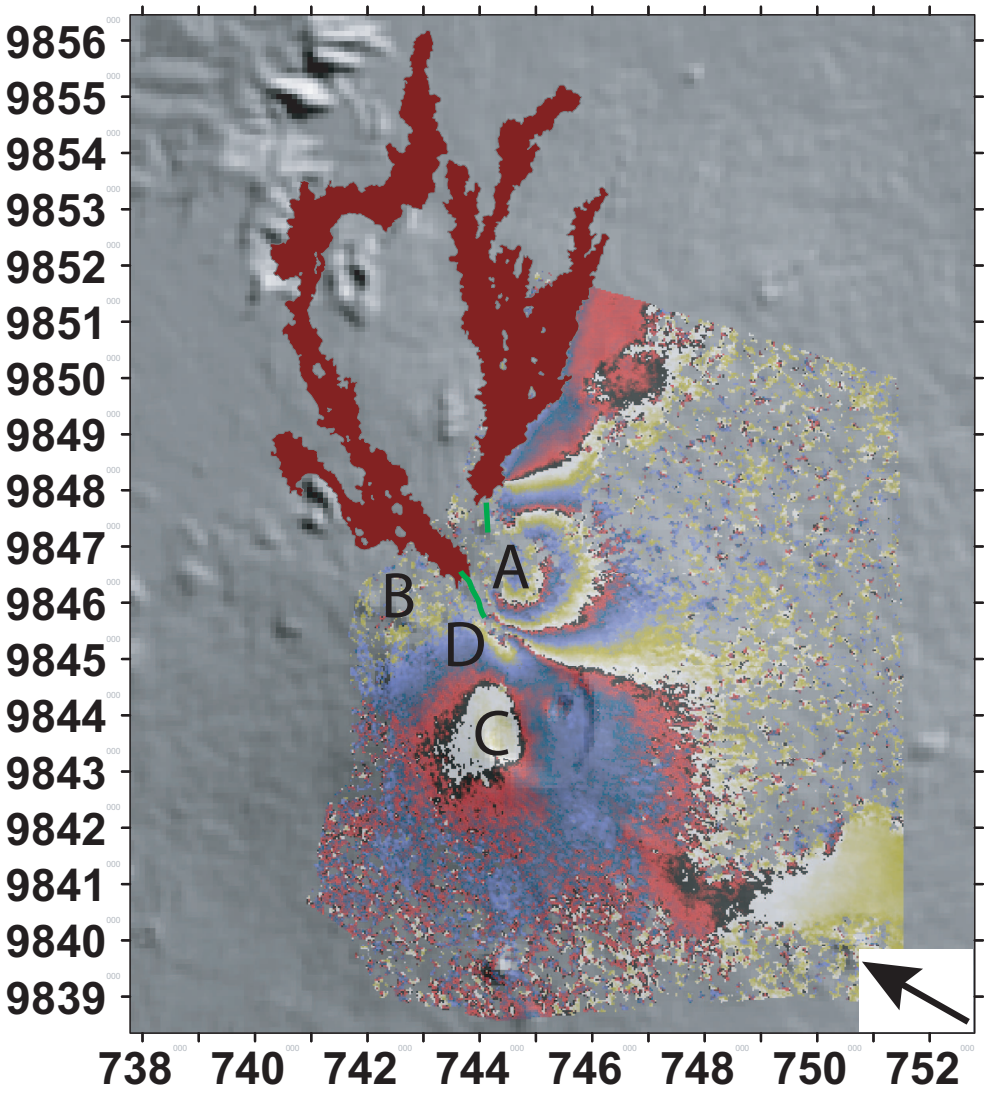

Figure 4.22: JERS Interferogram (1996/10/19 - 1997/02/28) spanning the 1996 Nyamulagira eruption, with the 1996 lava flows in dark red and the eruptive fissures in green. See text for A, B and C signals explanation. One color cycle represents a 11.8 cm Line Of Sight (LOS) range change with positive fringe (red-blue-yellow) corresponding to a range increase

InSAR Data A JERS interferogram (see Table 4.10), shows an 8 kilometers long extension of the deformation signal associated with the NNW flank eruption. In Figure 4.22, signal A, east of the eruptive fissures corresponds to approximately 3 fringes of range decrease (35.4 cm of displacements towards the satellite), while signals B and D correspond to small range increases of less than 1 fringe ($<$ 11.8 cm of displacements away from satellite). Finally, C signal corresponds to a small range decrease of less than 1 fringe.

Satellite	LOS vector [East, north, Up]	Time span	Ha (m)
	Nyamulagira 1996 Eruption		
JERS (desc.)	[0.54, -0.11, 0.83]	1996/10/19 - 1997/02/28 (132 days)	378
	Nyamulagira 1998 Eruption		
RSAT-1 (asc.)	[-0.59, -0.13, 0.79]	1997/02/19 - 1998/11/05 (624 days)	1480
	Nyamulagira 2000 Eruption		
RSAT-1 (desc.)	[0.51, -0.11, 0.85]	1998/10/26 - 2000/01/25 (456 days)	27

Table 4.10: Relevant characteristics of the interferograms used for studying the 1996, 1998 and 2000 Nyamulagira eruptions.

The asymmetric pattern of deformation is consistent with one or several dike intrusion(s) associated with the two eruptive fissures. The signal C if not explained by such dike intrusion(s) could also probably be explained by an inflating magma reservoir beneath the SW depression of the Nyamulagira caldera.

Other Data *Kitagawa et al.* [2007] has previously identified the deformation signal linked with this eruption. Their preliminary model is a dike 0.6 km high, 1.4 kilometers long, reaching a depth of 1 kilometer and creating an opening of 1.5 meters.

Modeling and Inversions The InSAR data were circularly subsampled with a 200 meters interval, leading to a 1966 data points vector. The sources mesh had 200 meters long triangular elements. A to D signals can satisfactorily be explained with a single vertical dike connected to the ground surface through the two eruptive en-echelon fissures. The best-fit dike model geometry and residuals are presented in Figure 4.23.

The best-fit dike model (Table 4.11) is vertical and is $\approx$ 3 km high. The two en-echelon fissures are connected 400 meters beneath the surface to the main quadrangular part of the dike.

The top of this main quadrangular part is more extended with respect to the surface eruptive fissures, but the bottom is smaller than the upper part ($Botlen = 0.26$). The overpressure of the dike is 1.3 MPa, which is consistent with typical overpressures found for Nyamulagira's and Nyiragongo's eruptions.

Discussion The highest residuals are located to the north of the eruptive fissures (see *a* in Figure 4.23). A supplementary echelon to the north, missing in the current fissures mapping, could maybe allow a better fit of the model in this area.

The best-fitting dike has its bottom side located at 3.4 km beneath the summit of the volcano, which is consistent with the presumed depth of the magmatic chamber of Nyamulagira (from 3.5 to 7 km). We also added an inflating reservoir to the dike, but the inversion lead to a zero overpressure for the reservoir, indicating that the eruption was not associated to a shallow reservoir pressure change large enough to be detectable on a JERS interferogram. Northern flank eruptions of this type occur quite frequently, and we can wonder whether the lack of detected magma reservoir deformation with InSAR is a feature common to all northern flank eruptions.

The dike has a volume of $5.56 \times 10^6\ m^3$, and induces an average opening of 0.75 m and a maximum surface opening of 1 m, which is consistent with typical values of Nyamulagira eruptive fissures opening. The intruded volume is an order of magnitude smaller to the estimated extruded volume. The dike has a larger extension than the preliminary model from *Kitagawa et al.* [2007]: about 3.4 km high and 2.2 km long on average in our study against 0.6 km high and 1.4 km long in *Kitagawa et al.* [2007]. Both openings are in the same order, in this study, the dike creates an average opening of 0.7 m while it creates an average of 1.5 m in *Kitagawa et al.* [2007].

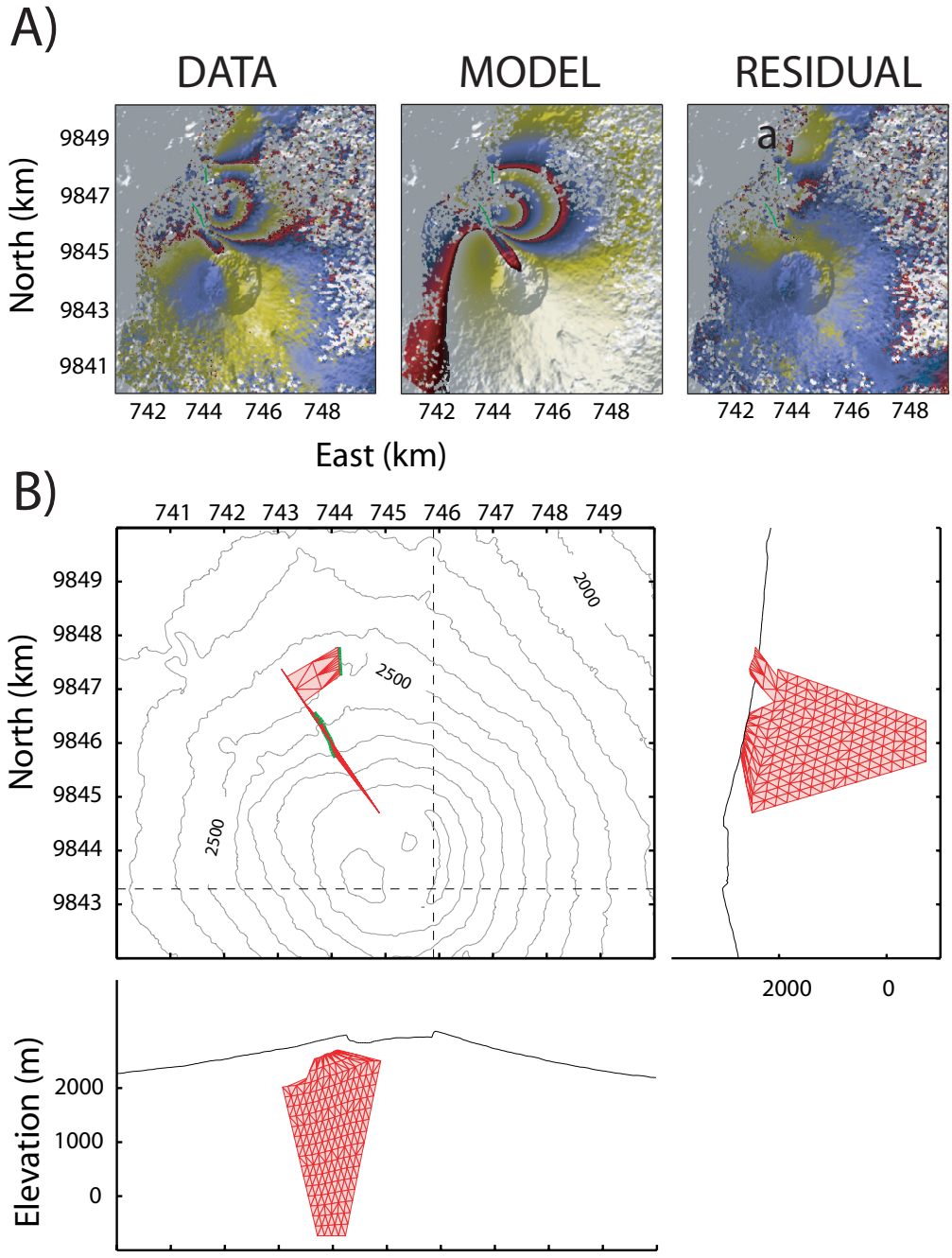

Figure 4.23: A) Observed, modeled and residual interferograms obtained with a single dike intrusion associated with the 1996 eruptive fissures (in green). B) Geometry of the best-fit single dike model.

Quadrangular Dike Connected to the Ground								
	P_0 (MPa)	Botelv (km a.s.l)	Dip (°)	Shear (°)	Botlen	Botang (°)	Twist (°)	D_{top} (m beneath surf.)
Max PPD	1.3	-0.7	90	0	0.3	0	0	400
95% conf. intv.	[0.9; 2]	[-2.8; 0.3]	[91; 111]	fixed	[0.1; 0.9]	fixed	fixed	[424; 891]
	Segmentgeom northern ech.	Segmentgeom southern ech.	northern end (km)		southern end (km)	Average opening on the surface (m)		RMS error (cm)
Max PPD	0 - 0.23	0.23 - 1 (fixed)	743, 9847		745, 9845	0.75		2
95% conf. intv.	[0; 0.1] - [0.22; 0.34]	[0.22; 0.34] - 1 (fixed)	[742; 744], [9847; 9848]		[744; 746], [9844; 9845]	-		

Table 4.11: Best-fit parameters of the 1996 dike model. Parameters are described in Figures 3.1 and 3.2.

1998 Eruption

On October 17, a flank eruption started which lasted at least 8 days [*BGVN*, 1998]. Figure 4.24 shows the eruptive fissure, starting from the caldera rim, which opened on the NW flank of the volcano. The estimated lava volume is 69.2 ± 23.1 10^6 m^3 [*Smets et al.*, 2010c].

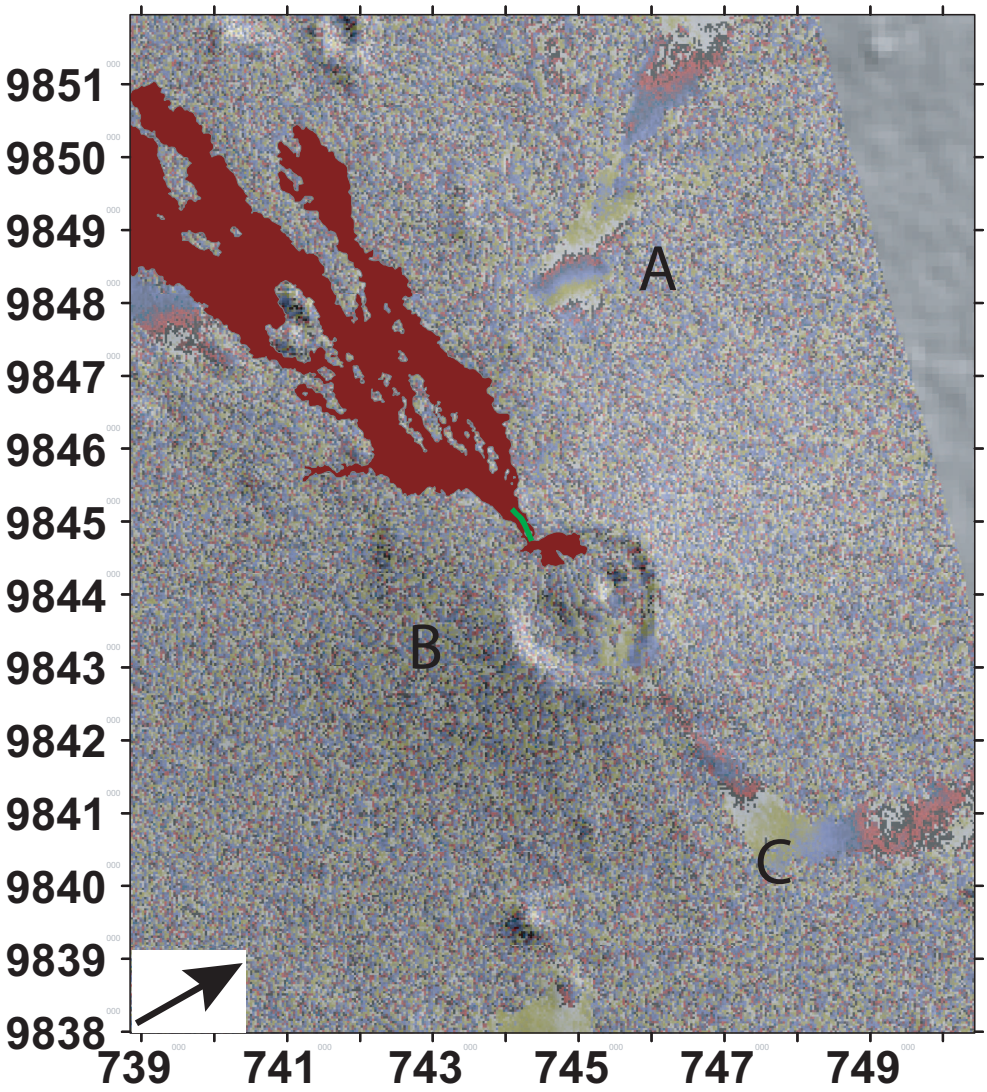

Figure 4.24: RADARSAT-1 ascending interferogram (1997/02/19 - 1998/11/05) spanning the 1998 Nyamulagira eruption, with the 1998 lava flows in dark red and the eruptive fissures in green. One color cycle represents a 2.8 cm Line Of Sight (LOS) range change with positive fringe (red-blue-yellow) corresponding to a range increase. See text for A, B and C signals explanation

InSAR Data A RADARSAT-1 ascending interferogram (Table 4.10) is the only interferogram where some deformation associated with the eruption is visible. However, due to the large time span, the coherence is low. Even if the data are noisy, we can see that signals A and C, correspond to a range increase to the right of the eruptive fissure, while signal B, corresponds to a range decrease to the left of the eruptive fissure.

The asymmetric pattern of deformation is consistent with one or several dike intrusion(s). But the data noise is too high, the signal too unclear for any in-depth modeling studies and to be more sure of the signal origin.

2000 Eruption

A flank eruption started on January 27 and lasted approximately 14 days [*BGVN*, 2000]. Figure 4.25 show the eruptive fissure, starting from the caldera rim towards the southeastern flank, and creating a new vent 1.3 km from the caldera rim. The estimated lava volume is 47.3 ± 15.8 10^6 m^3 [*Smets et al.*, 2010c].

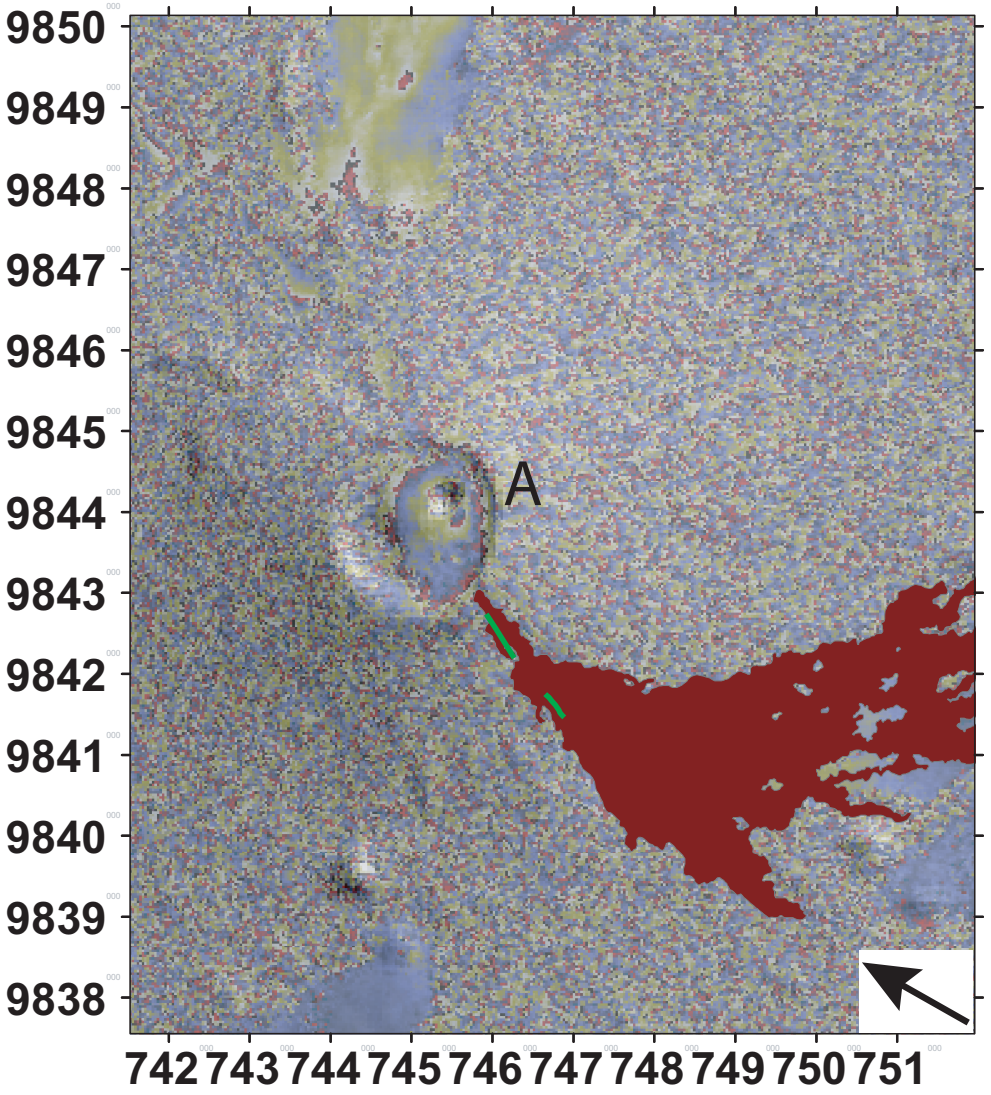

Figure 4.25: RADARSAT descending interferogram (981026 - 000125) spanning the 2000 Nyamulagira eruption, with the 2000 lava flows in dark red and the eruptive fissures in green. See text for A signal explanation

InSAR Data A RADARSAT-1 descending interferogram (Table 4.10) shows deformations associated with the 2000 eruption. Similarly as for 1998, the coherence is low. Signal *A* which corresponds to a range increase, centered on the pit crater inside the Nyamulagira caldera, is the only visible ground displacement.

Signal *A* could be associated with a reservoir deflation or with a dike intrusion. However, due to lack of coherent data, and the large time span, we cannot rule out that this signal is contaminated by lava flow compaction or by an atmospheric component.

2001 Eruption

This long-lived flank eruption occurred in February 6 and lasted 54 to 62 days [*BGVN*, 2001a] [*BGVN*, 2001b] [*BGVN*, 2001c]. The lava flowed towards the north and the south from the caldera rim, with the formation of two new cones. The estimated lava volume is 140.1 ± 46.7 10^6 m^3 [*Smets et al.*, 2010c].

We were not able to find a pair of SAR images suitable to capture even partially the deformation induced by this eruption. It is likely that the deformation is of limited extension on the incoherent volcano flanks. This observation is unexpected as the eruption duration is more than 50 days and the emitted volume large.

2002 Eruption

The eruption started on July 25 and lasted from 15 to 63 days [*BGVN*, 2002a] [*BGVN*, 2002b] [*BGVN*, 2003]. The fissure opened in the caldera towards the north, and the estimated lava flow volume is 56.7 ± 18.9 10^6 m^3 [*Smets et al.*, 2010c] (Figure 4.12). An increase of the seismicity had been observed around Nyamulagira since the end of February 2002. While a period of low seismic activity, characterized by shallow LP earthquakes, persisted for about a year following the July 2002 eruption [*Mavonga et al.*, 2006].

InSAR Data The event is covered by data from satellite ERS-2, from ascending orbits, and satellite RADARSAT-1, from ascending and descending orbits (Figure 4.26 and Table 4.12). Left of the eruptive fissure, a signal (signal *A* in Figure 4.26) corresponding to a range decrease is visible in all beams. On the RADARSAT ascending interferogram 15 narrow fringes corresponding to approximately 42 cm are visible. The sense of signal *A* switches to range increase in *D*, north of the eruptive fissure.

Satellite	LOS vector [East, north, Up]	Time span	Ha (m)
ERS-2 (asc.)	[-0.34, -0.07, 0.94]	2002/07/03 - 2003/01/29 (210 days)	3900
RSAT-1 (asc.)	[-0.59, -0.13, 0.8]	2002/02/17 - 2002/10/15 (240 days)	36
RSAT-1 (desc.)	[0.5, -0.11, 0.86]	2002/03/03 - 2002/09/11 (192 days)	23

Table 4.12: Relevant characteristics of the interferograms used for studying the 2002 Nyamulagira eruption.

On the RADARSAT descending interferogram, signal (A), corresponding to about 3 fringes of range increase, is also visible. However, the direction of the deformation changes when going south east (black arrow in Figure 4.26C), and a signal C, west of the eruptive fissure, corresponding to about 3 narrow fringes of range decrease is visible. A signal (B) east of the eruptive fissure, and SE of the caldera, corresponds to a range decrease (1.5 fringe).

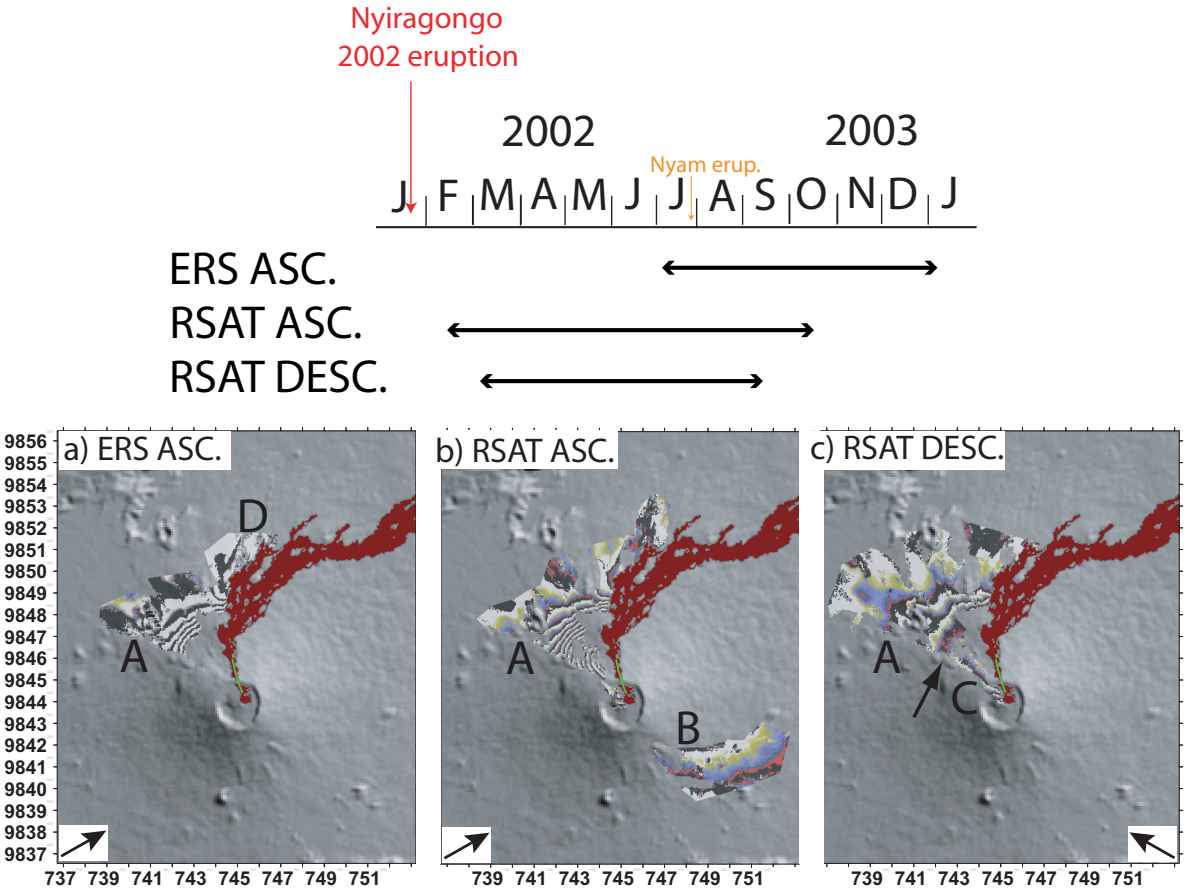

Figure 4.26: Three interferograms showing the deformations associated with the 2002 Nyamulagira eruption. The 2002 lava flow are shown in dark red and the eruptive fissure is drawn in green. See the text for the interpretations of signals referred to as A, B and C. a) ERS-2 ascending interferogram, b) Ascending RADARSAT-1 interferogram and c) Descending RADARSAT-1 interferogram.

The InSAR displacements from the three beams were simultaneously used to compute the horizontal and vertical displacements in an area coherent in the three datasets (Figure 4.27). The reference of each unwrapped interferogram was adjusted from the best-fitting model offset calculation as done in Section 4.1. They show that all the 2002 deformation captured is mainly due to westward horizontal displacements, which is consistent with displacements associated to a dike as most coherent pixels are all located west of the eruptive, reaching a maximum of 0.24 m close to the eruptive fissure. Vertical displacements are also observed, corresponding to an uplift of a maximum of 0.14 meters for the A signal (location in Figure 4.26), and to a small subsidence (smaller than 0.1 meter) for the area C.

A and D signals in ascending modes, and B signal in the descending mode, are probably associated with the opening of the eruptive fissure connected to one or several dike(s). B signal could also be linked with the dike intrusion, even if an atmospheric contamination or a lava flow

compaction origin could not be rule out as the number of fringes is small. After a quick check by generating coherent interferograms with other RARDARSAT descending pairs, we can rule out that signal C is generated by an atmospheric effect. Thus, it could indicate that another source, such as an inflating sill-like reservoir or another dike which has not reach the ground surface, is involved.

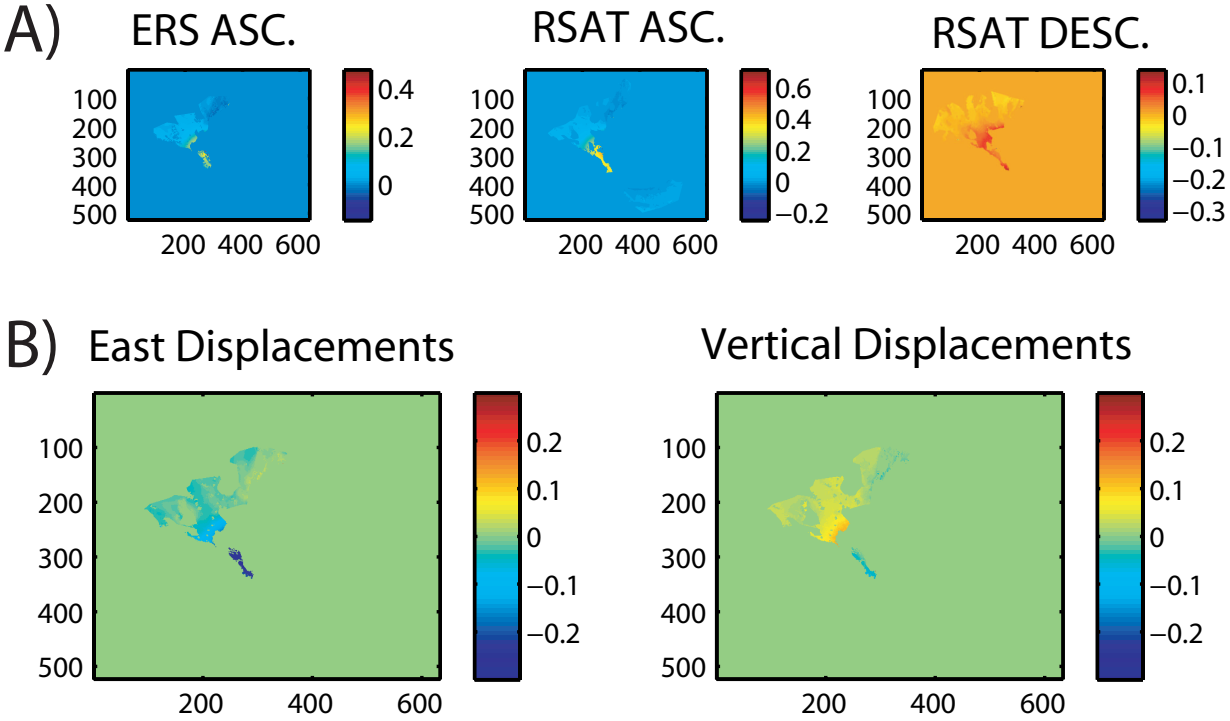

Figure 4.27: A) The three interferograms showing the deformations associated with the 2002 Nyamulagira eruption unwrapped with Snaphu. All displacements are in meters. B) The InSAR displacements from the three beams were simultaneously used [*Wright et al.*, 2004] to compute the horizontal (left) and vertical displacements (right). The mean standard deviation are 1.2 cm and 2.4 cm , respectively.

Other Data *Colclough* [2005] has previously identified the deformation signal linked with the 2002 eruption, but only on ERS interferograms. She concludes that a standard simple Mogi source was not able to reproduce the deformation pattern.

Modeling and Inversions Due to the asymmetry of the pattern associated with the eruptive fissure, the most likely source is a dike connected to the surface through the mapped eruptive fissure. The InSAR data were circularly subsampled with a 200 meters interval, leading to 157, 217 and 204 data points vectors for ERS, RSAT asc. and desc., respectively. The sources mesh had 100 meters long triangular elements. The topographic mesh has nodes separated by 50 meters close to the eruptive fissure as large gradients of deformation were identified on the RSAT ascending InSAR data.

The geometry of the best-fit model obtained when inverting the three subsampled interferograms using a model with 8 parameters is shown in Figure 4.28B. The RMS error is 2.2 cm (Table 4.13), the dike is larger at depth than the eruptive fissure length. It is dipping towards the east in its superficial part, while the bottom part (from $\approx$ 1 km beneath the volcano summit) is

dipping 44° towards west. Its bottom is 3.5 km beneath the volcano summit, which is consistent with the estimated depth of the Nyamulagira magma reservoir. The model residuals are small for the two ascending beams (Figure 4.28A), but large for the descending one. The dike volume is 27.10^6 m^3, hence about the half of the estimated erupted volume (56.7 ± 18.9 10^6 m^3). The dike overpressure is about 0.4 MPa, which is consistent with typical values for the North Kivu area. However, the average opening at the surface is 12 meters, which is larger than typical values of a few meters observed on typical Nyamulagira eruptive fissures, and much larger than the maximum westwards displacement identified in Figure 4.27. The shape of the dike considering only one echelon for the complex eruptive fissure could explain this observation. Pre-existing weakness features, such as faults inside the Nyamulagira volcano, could explained the particular shape of the dike, with a shallow east-dipping and a deeper west-dipping main part. However, as the model does not fit the RSAT descending data and moreover generates too much opening at the surface; the dike shape could thus be not adequate, other sources and thus more complex eruption mechanisms, are probably involved.

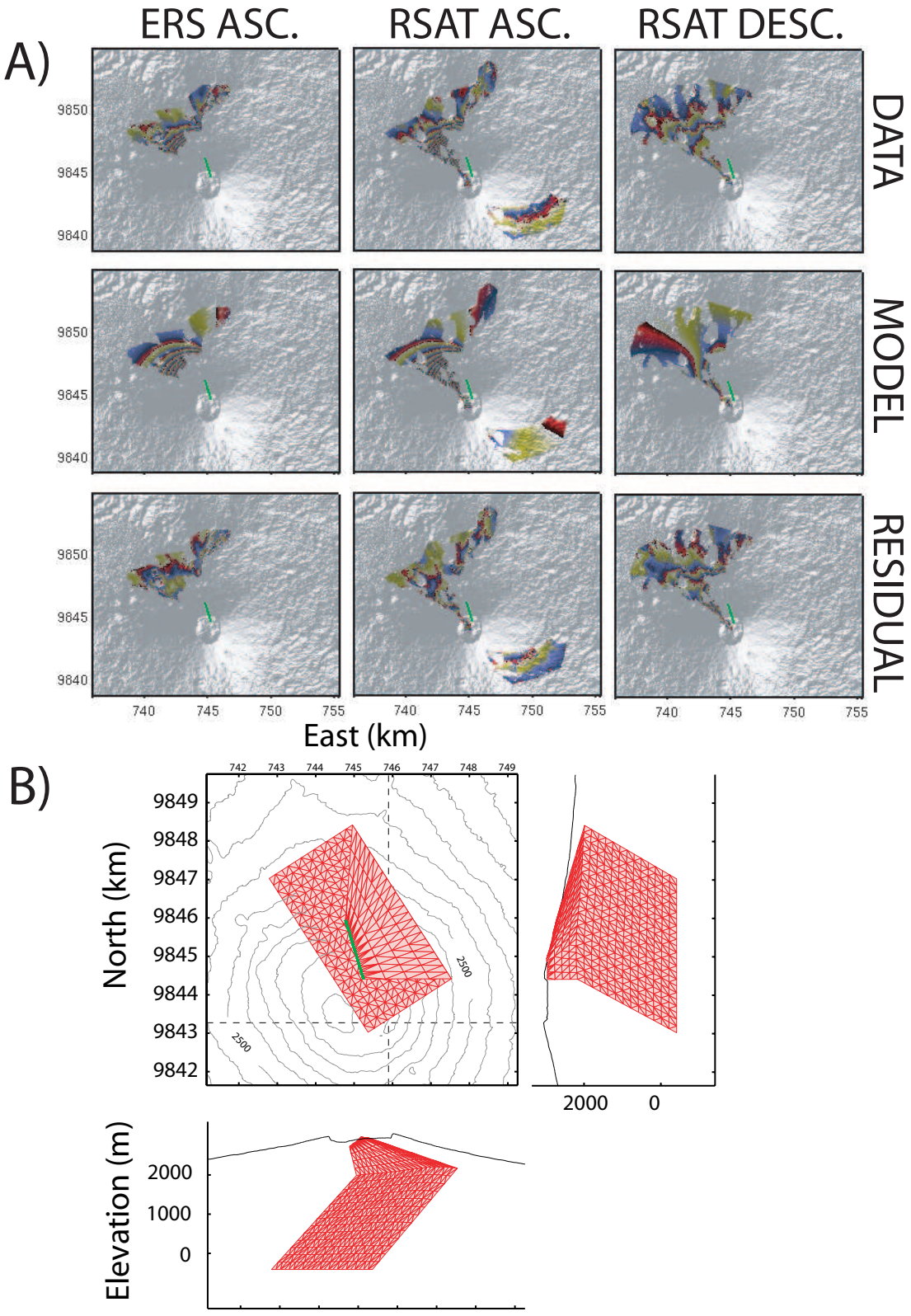

Figure 4.28: A) Observed, modeled and residual interferograms obtained with a single dike intrusion associated with the 2002 eruptive fissures (in green). B) Geometry of the best-fit single dike model.

Quadrangular Dike Connected to the Ground												
	P_0 (MPa)	*Botelv* (km a.s.l)	*Dip* (°)	*Shear* (°)	*Botlen*	*Botang* (°)	*Twist* (°)	D_{top} (m beneath surf.)	*northern end* (km)	*southern end* (km)	Average opening on the surface (m)	RMS error
Max PPD	0.36	-0.4	136	0	1	0	0	470	745.2, 9848.6	748, 9845	12	2.2
95% conf. intv.	[0.26; 0.5]	[-0.55; -0.37]	[133; 137]	fixed	fixed	fixed	fixed	[455 500]	[745.2; 745.3], [9848.6; 9848.6]	[747.8; 747.9], [9844.56; 9844.63]		

Table 4.13: Best-fit parameters of the single dike model for the 2002 Nyamulagira eruption. Parameters are described in Figures 3.1 and 3.2.

2004 Eruption

The eruption started on May 8 and lasted from 20 to 23 days. An eruptive fissure opened on the NW flank 1.9 km NW of the caldera rim (Figure 4.29) The estimated lava flow volume is $68.5 \pm 22.8\ 10^6\ m^3$ [*Smets et al.*, 2010c]. At the beginning of the eruption, the volcanic activity is reported to have also occurred inside the caldera and after to have migrated to the northern flank [*BGVN*, 2004a].

The seismic activity (LP earthquakes, attributed to the movement of magma in a deep conduit) increased around the Nyamulagira volcano about ten months prior the May 2004 eruption [*Mavonga et al.*, 2006]. A swarm of LP earthquakes, accompanied by tectonic events interpreted to be linked with the rift, began about 4 months prior to the eruption. About two months prior to the eruption, the number of deep LP events decreased and the number of shallow LP earthquakes increased. A major seismic swarm occurred on May 4-6 2004 and an important tectonic earthquake was felt in the Virunga north of Lake Kivu about 4 hours before the eruption. 2.5 hours before the eruption, a high amplitude long period earthquake occurred north of the Virunga. After the eruption, the seismic activity was dominated by shallow (0-5 km) LP events [*Mavonga et al.*, 2010b].

An unusual fumarolic activity was observed inside the caldera on May 2 2004 (seen from Goma). A lava lake was present inside the pit crater until at least May 12. Four new cones (30 - 50 meters high) were built on the NW flank during the eruption. [*BGVN*, 2004a] [*BGVN*, 2004b] [*BGVN*, 2006]

InSAR Data The event is covered by data from the ENVISAT satellite, from ascending orbits, and the RADARSAT-1 satellite, from ascending and descending orbits (Table 4.14).

Satellite	LOS vector [East, north, Up]	Time span	Ha (m)
ENVISAT (asc.)	[-0.34, -0.07, 0.94]	2004/03/24 - 2004/06/02 (70 days)	49
RSAT-1 (asc.)	[-0.59, -0.13, 0.79]	2004/03/26 - 2004/06/30 (96 days)	26
RSAT-1 (desc.)	[0.51, -0.11, 0.85]	2004/03/16 - 2004/08/07 (144 days)	30

Table 4.14: Relevant characteristics of the interferograms used for studying the 2004 Nyamulagira eruption.

As visible on the ENVISAT ascending interferogram, at least two distinct deformation patterns overlap (Figure 4.29). In the northern far-field (A signal), there is a small gradient deformation signal, which corresponds to a range increase in the ascending orbits, and a range decrease in

the descending orbits. There are large deformation gradient signals observed in the near-field NW of the caldera (B) and on its upper NW flank (C). There is a little coherence in the caldera in the descending orbit too, where some deformation is visible but not as clearly as in the ENVISAT ascending orbits. SE of the caldera, a small signal D, corresponding to a range increase, is visible in the RADARSAT ascending mode (and a bit on the descending one too).

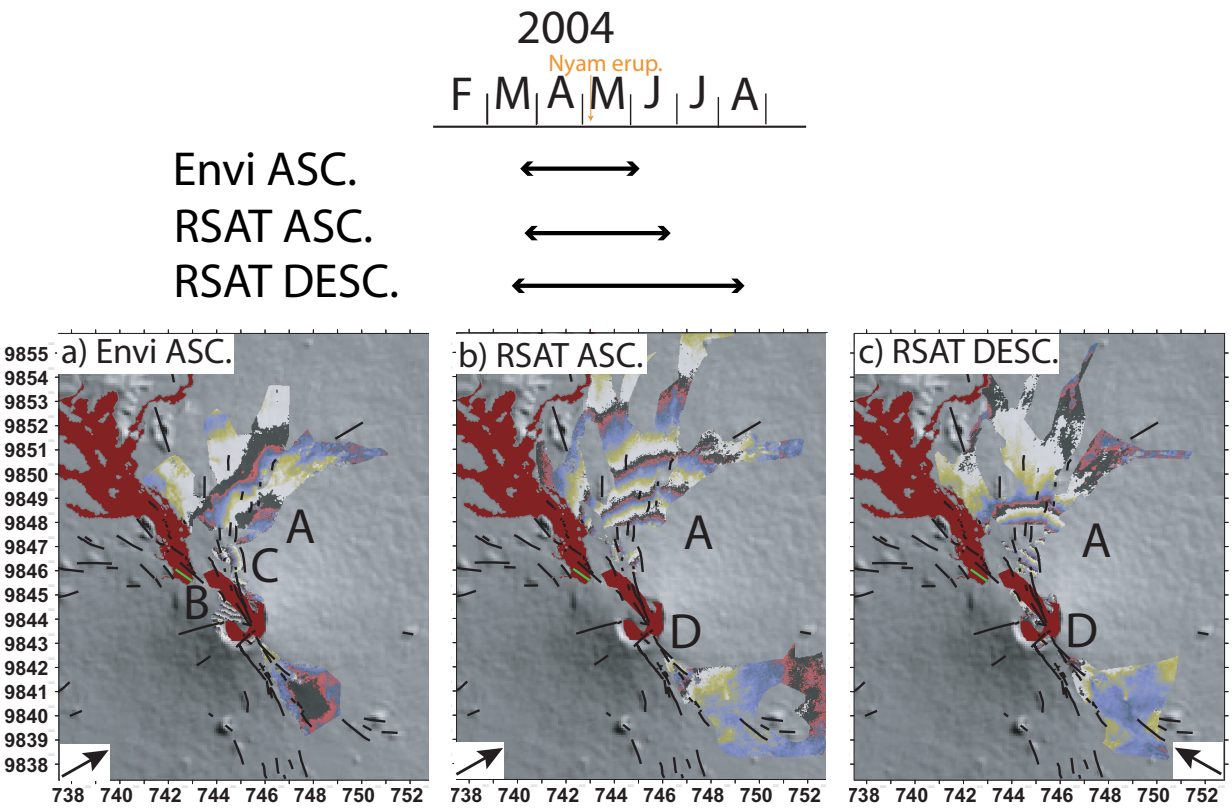

Figure 4.29: Three interferograms show the deformations associated with the 2004 Nyamulagira eruption. One color cycle represents a 2.8 cm Line Of Sight (LOS) range change with positive fringe (red-blue-yellow) corresponding to a range increase. The arrows show Line Of Sight (LOS) direction. The 2004 lava flow are shown in dark red and the eruptive fissure is drawn in green. See the text for the interpretations of signals referred to as A, B and C. a) ENVISAT ascending interferogram, b) Ascending RADARSAT-1 interferogram and c) Descending RADARSAT-1 interferogram.

Signal A could originate from the northern edge of the eruptive fissure, and be thus associated with a dike intrusion beneath it. The B and C signals probably correspond to a shallower phenomenon such as a dike or sill magma intrusion. The signal D could be contaminated by an atmospheric effect as it follows the volcano slopes, or it could be linked again to a dike intrusion or a magma reservoir. The InSAR displacements from the three beams were simultaneously used to compute the horizontal and vertical displacements in an area coherent in the three datasets (Figure 4.30). The reference of each unwrapped interferogram was adjusted from the preliminary best-fitting model offset calculation as done in Section 4.1. They show that all the 2004 deformation captured is mainly due to horizontal displacements eastwards, which is expected as the common coherent pixels corresponding to location A and C, are all located right of the eruptive fissures, reaching a maximum of 0.30 m close to it. A small vertical displacement is also observed in the coherent patch, corresponding to the location of signal C, close from the fissure, corresponding to an uplift of less than 0.1 meters.

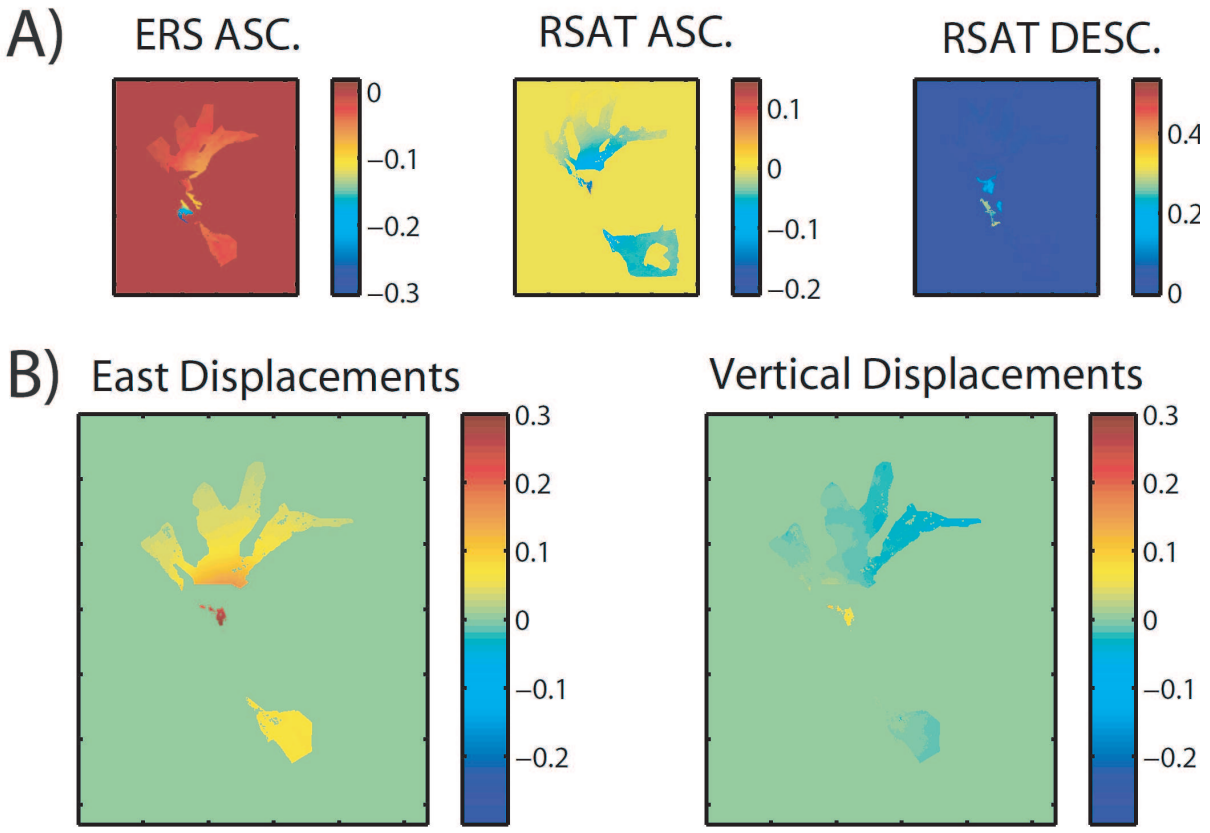

Figure 4.30: A) The three interferograms showing the deformations associated with the 2004 Nyamulagira eruption unwrapped with Snaphu. All displacements are in meters. B) The InSAR displacements from the three beams were simultaneously used [*Wright et al.*, 2004] to compute the horizontal (left) and vertical displacements (right). The standard deviation are 1.2 cm and 2 cm , respectively.

Modeling and Inversions A preliminary model for a dike intrusion connected to the surface though the NW eruptive fissure (location in green in Figure 4.29) mapped from Benoît Smets *[in prep.]* is shown in Figure 4.31. The northern far-field signal A could be explained by a shallow (bottom at 2800 meters below the Nyamulagira's summit) low 11° west-dipping dike, the intrusion is thus almost a sill, with an overpressure of about 3 MPa. However, the near-field data (B and C signals) and the southern data (D) cannot be satisfactorily explained by such a magma intrusion (Figure 4.31).

The volcanic activity is reported to have first occurred inside the caldera [*BGVN*, 2004a], but neither a lava flow nor an eruptive fissure were clearly visible on the available optical images [*Smets et al.*, 2010c]. However, having a closer look at an ENVISAT coherence images spanning the eruption (Figure 4.32), a lava flow is clearly visible inside the caldera and flowing north-westwards. A second eruptive fissure is thus missing, but we can assume from the ENVISAT deformation pattern inside the caldera, that it likely follows previous ones trending NNW or NW (see the arrow in Figure 4.29). However, we need extra information, such as from other optical images or field measurements, to identify exactly the eruptive fissures that were active during the first phase of the 2004 eruption.

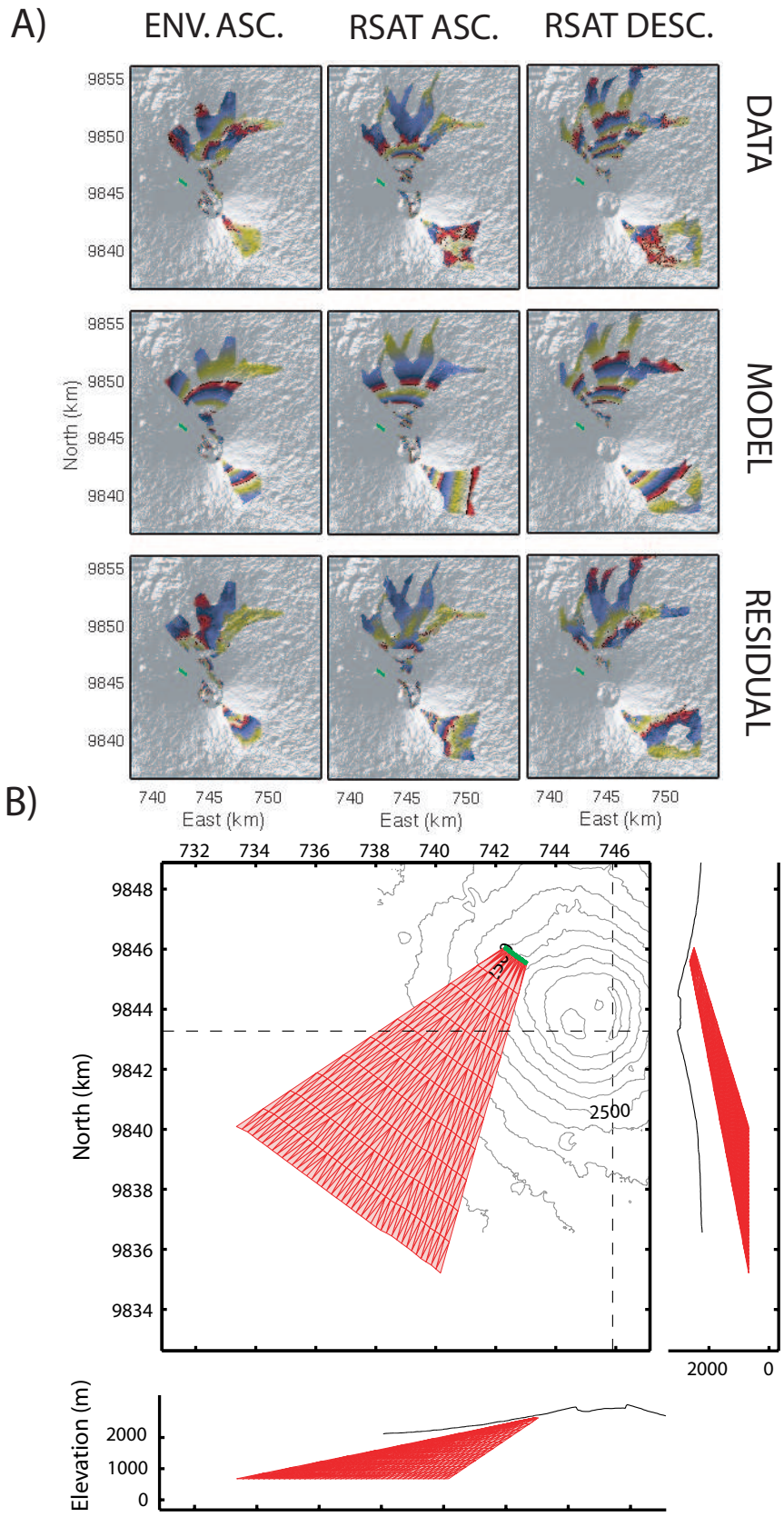

Figure 4.31: A) Observed (upper row), modeled (middle row) and residual interferograms (lower row) obtained with a single dike intrusion associated with the 2004 eruptive fissure (in green). B) Geometry of the best-fit dike model.

Considering a single dike connected to the NW eruptive fissure and an existing NW fissure inside the caldera starting from the pit does not fit the near-field data neither. We finally inverted for two dikes, a first one connected to the NW eruptive fissure, and a second one connected to the assumed fissure in the caldera, but again, the model cannot fit the near-field data.

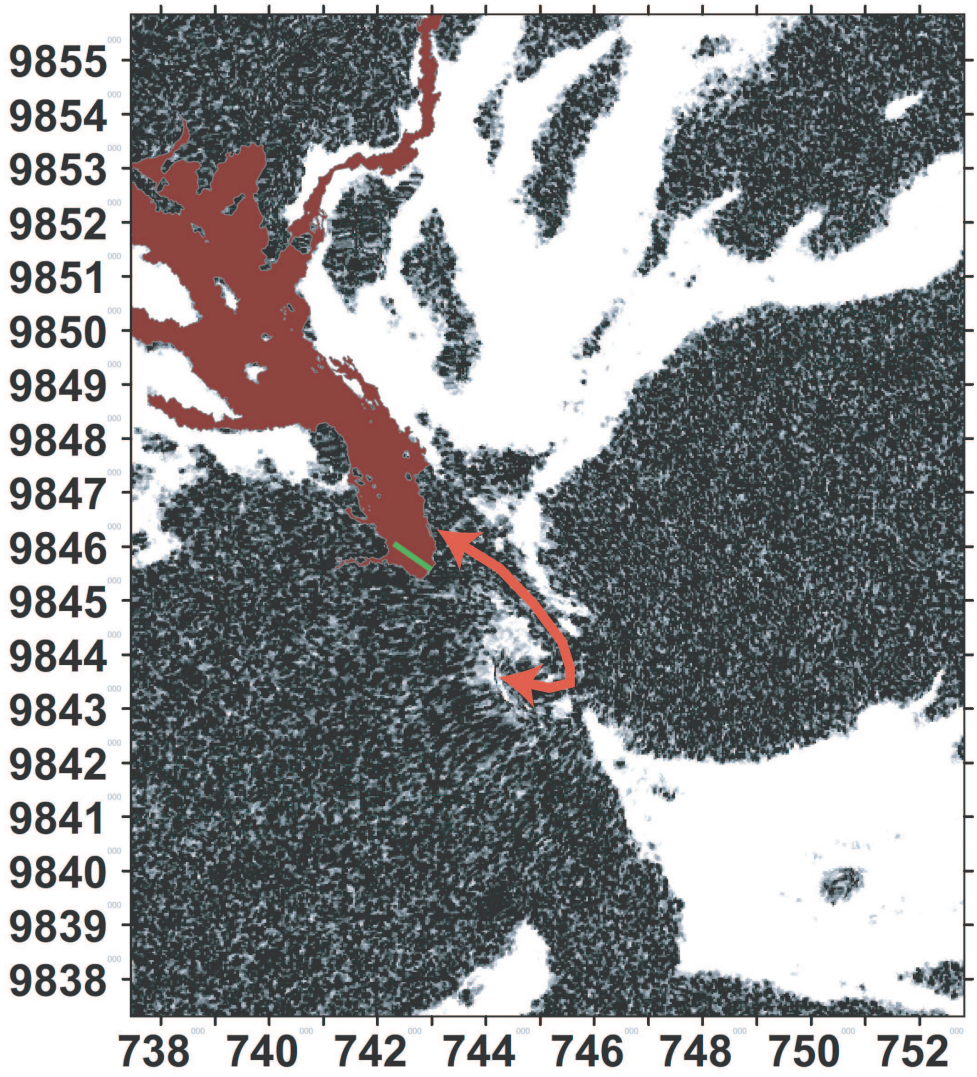

Figure 4.32: Coherence image of the ENVISAT ascending interferogram spanning the 2004 Nyamulagira eruption with the NW eruptive fissure in green, the lava flow mapped by *Smets et al.* [2010c] in dark red, and the newly identified lava flow path starting from inside the caldera in red

Discussion Our preliminary modeling studies show that the 2004 eruption cannot be explained simply with a single source associated with the NW eruptive fissure. At least two sources, likely one to several dike(s) and/or sill(s), should be involved. The missing eruptive fissures in the caldera, and possibly also on the NW flank, should be accurately mapped, from optical or maybe thanks to amplitude SAR images, before any further modeling fitting the near-field data could be realized.

2006 Eruption

This eruption started on November 27 with the opening of a 5 kilometers long eruptive fissure south of the caldera rim, located halfway between Nyamulagira and Nyiragongo (Figure 4.33). The lava flowed southwestwards and towards the Lake Kivu. The estimated lava volume is 44.2 $\pm$ 14.7 10^6 m^3 [*Smets et al.*, 2010c]. The eruption lasted 8 to 23 days.

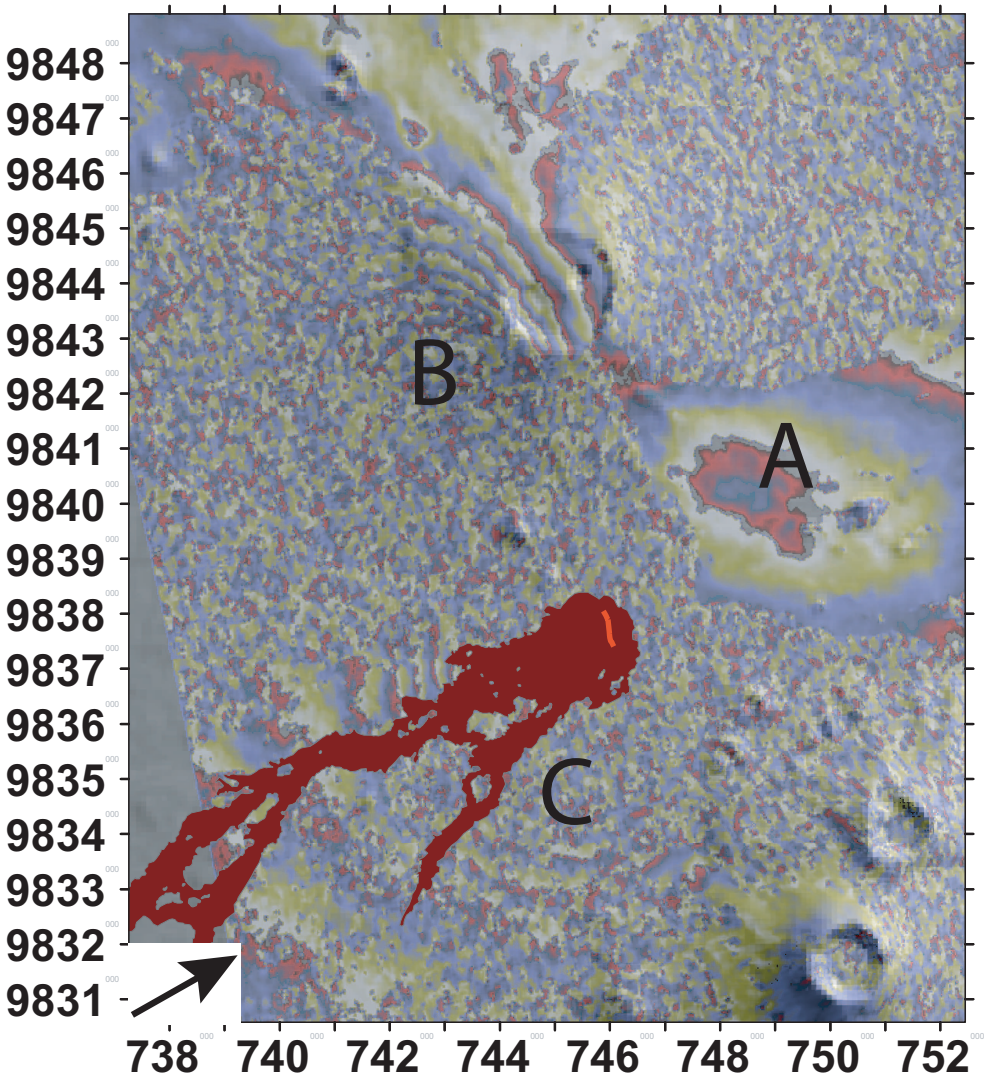

Figure 4.33: ENVISAT ascending interferogram (061031 - 061205, beam $\approx$ 38°) spanning the 2006 Nyamulagira eruption, with the 2006 lava flows in dark red and the eruptive fissures in green. See text for A, B and C signals explanation

Several LP seismic swarms, with deep (20-30 km) and shallow (0-5 km) events recorded and separated by an aseismic zone, stroke the volcano area about a year prior the eruption. The aseismic zone is interpreted as magma reservoir while the LP events could be generated by a flow of magma into the Nyamulagira shallow reservoir from a deep source located at about 20-30 km. The LP events were only shallow about 1-2 months before the eruption, probably because they were associated with the filling of the shallow reservoir. [*Mavonga et al.*, 2010b]

Furthermore, a magnitude 4.5 earthquake, with subsequent aftershocks, stroke the North Tanganika area on October 28, 2005. After this seismic event, a sustained seismic activity char-

acterized by long period events, interpreted as magma movements at depth, was recorded around the volcano. Hence, the month preceding the eruption was characterized by major swarms of long period events which occurred 10 km around the Nyamulagira [*BGVN*, 2007].

InSAR data This eruption was covered by C-band ENVISAT interferograms from four different beams, three acquired from descending orbits, and one acquired from ascending orbits. Only one interferogram from the ascending orbits had spatial and temporal baseline conditions allowing to overcome the vegetation induced coherence loss southwest of the volcano. This interferogram shows a signal over a 200 km^2 area east, north and south of the eruptive fissure (Figure 4.33). While, the interferograms from ascending orbits only show displacements over a 25 km^2 area east and north of the fissures *[Cayol et al., in prep.]*.

In the ascending orbits, signal A, located to the right of the eruptive fissures, corresponds to a range increase, while signals B and C, located to the left of the eruptive fissures correspond to range decreases. Signals B and C, although separated by incoherent areas, are consistent with one or several dike intrusion(s) associated with the eruptive fissures.

The unusual large extension of the deformation patterns suggest a large source dimension, compared to the size of the eruptive fissures at the surface. These large deformation patterns differ from the ground displacements related to past eruptions captured by InSAR. However, when comparing the petrological analysis performed on the 2006 lava samples *[Elisabet M. Head, pers. comm., 2008]* with analysis on other previous southern Nyamulagira lava flows, no significant differences in composition for the 2006 lava can be found.

Modeling and inversions Preliminary results show that a single dike fits the deformation patterns poorly. Two sources would actually be needed to explain the measured displacements. One of the sources corresponds to a dike located between Nyamulagira and Nyiragongo, which is aligned with the axis linking the two volcanoes. The other source, which is responsible for displacements measured north of Nyamulagira, could be an inflating sill-like source or a spherical reservoir.

4.3 Seismic Events

4.3.1 Kalehe Earthquake, October 2002

The largest earthquake ever recorded in the area, a magnitude $M_w = 6.2$ event, occurred on October 24, 2002. Figure 4.34 shows its approximate epicenter and the normal fault type focal mechanism (USGS NEIC catalog) corresponding to the event.

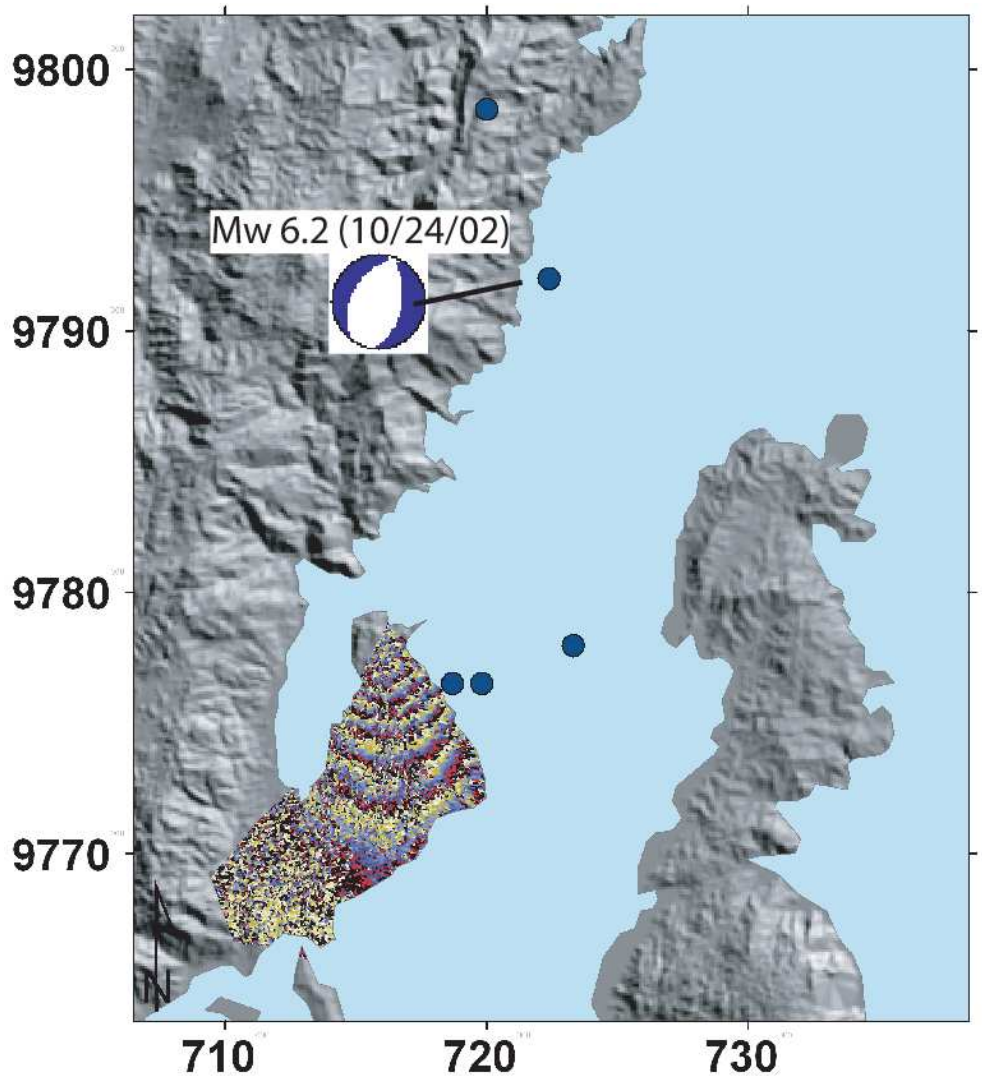

Figure 4.34: Subset of a RADARSAT-1 descending interferogram showing the October 24 M_w 6.2 earthquake, on a shaded DEM. The CTM focal mechanism of the event, indicating normal faulting, as well as the epicenter, are indicated. Dark blue points indicate other seismic events recorded for the October to December 2002 period (USGS NEIC catalogue).

InSAR data

A RADARSAT-1 descending interferogram (05 October 2002 - 29 October 2002) captured the event. About seven fringes, indicating a LOS range increase of 20 cm, are visible on the western lake shore (Figure 4.34). The InSAR deformation signal has only about 10 km^2 of spatial exten-

sion. Only part of it is visible on the interferogram because of vegetation-induced decorrelation on the rift shoulders and mainly because of the presence of the lake.

Other data

The focal mechanism of the main shock corresponds to a scalar seismic moment of 2.17 10^{18} N.m. The conjugated planes corresponding to this mechanism are 1) a 42° west-dipping fault striking 210°, and 2) a 50° east-dipping fault striking 9°. The latter east-dipping solution is the most likely because of the marked east-dipping border fault of the rift (Figure 1.6). Five smaller shocks, with undetermined focal mechanism solutions, were also recorder on October, 24 (Figure 4.34). The depth estimation of the events is about 10 kilometers.

Mavonga [2007] studied the temporal and spatial distribution of the aftershock sequences of the Kalehe earthquake. The aftershocks of the main shock extended from Kalehe to Idjwi island. They estimated the length of the fault plane to be about 25 km, and assuming that the deepest earthquake was at about 15 km, they estimated a 375 km^2 fault area.

Modeling and inversions

As the only InSAR data we have only covers only a small part of the deformation, it will not allow to determine the fault characteristic unambiguously, and the uncertainties will probably be large. Indeed *Dawson and Tregoning* [2007] showed that with a single InSAR data, it was possible to accurately determine fault characteristics, but that the uncertainties decrease when increasing the number of InSAR geometry. A rectangular east-dipping normal planar fault, with a shear stress drop of 1 MPa fits the RADARSAT data (Figure 4.35A) with a RMS of 0.6 cm. A total of 8 parameters were inverted and are show in Table 4.15.

	σ_{drop} (MPa)	Midx (km)	Midy (km)	Midz (km a.s.l)	Length (km)	Height (km)	Strike (°)	Dip (°)	M_0 (N.m)	RMS error (cm)
Max PPD	1	714.9	9780.3	- 3	7.4	6.1	18	35	$1.9 * 10^{18}$	0.6
95% conf. intv.	[0.7; 1.6]	[714.3 716.2]	[9780; 9782]	[-6.5; -0.75]	[6.1; 12]	[2.5; 7.4]	[11; 26]	[30.1; 43.6]	-	

Table 4.15: Best-fit parameters of the normal faults model for the October 2002 earthquake.

Discussion

As depicted in Figure 4.35B, the aftershock hypocenters are all roughly located at the same depth as the bottom of the fault, but only three are roughly at the same location as the fault. However, the expected error on the earthquake location is large (about 15 km), so they can be located differently as indicated. Moreover one can note the large confidence interval for the depth of the modeled fault ranging from -6.5 to -0.75 km b.s.l. The confidence intervals for the fault geometry parameters are large, as expected with only one InSAR beam [*Dawson and Tregoning*, 2007]. The confidence intervals are probably also large because of the lack of coherent data over the Lake Kivu.

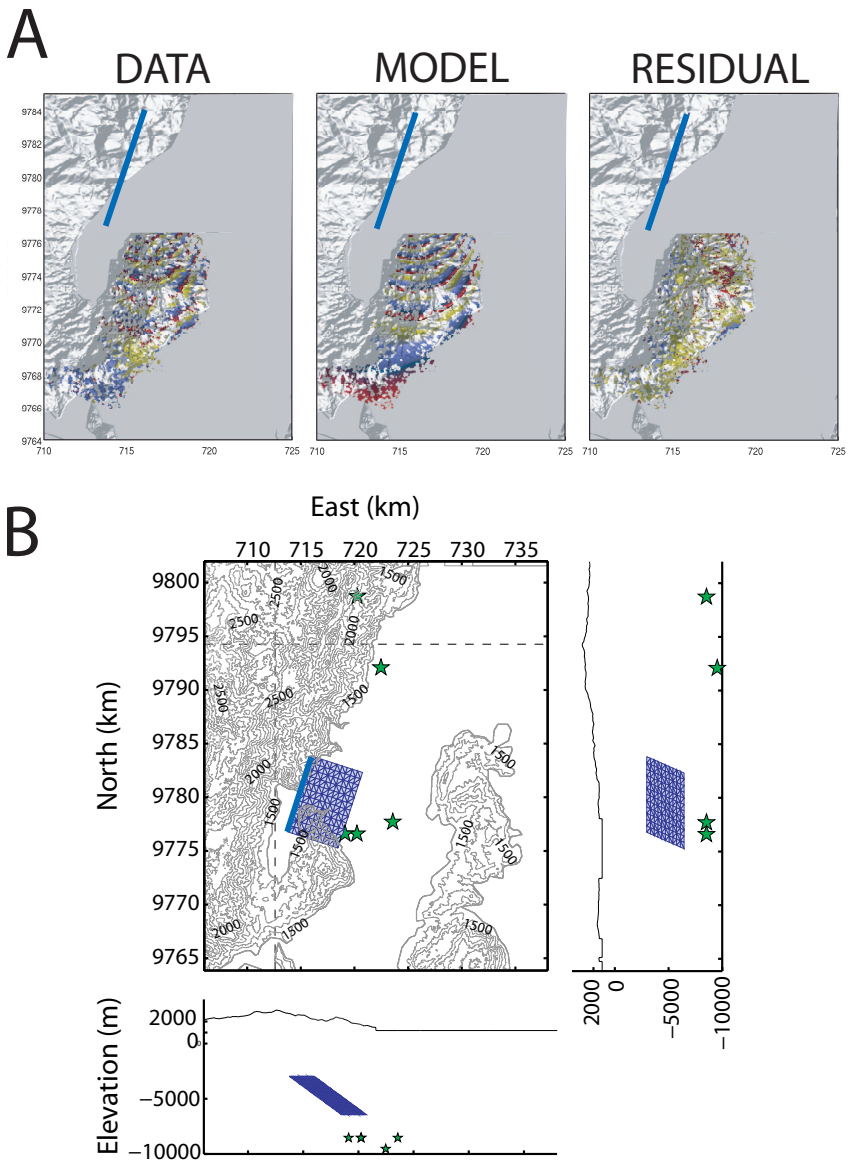

Figure 4.35: Observed, modeled and residual interferograms obtained with the best-fitting model considering one east-dipping rectangular normal fault. The top line of the fault is indicated in blue. B) Three views of the geometry of the best-fitting model in blue. The hypocenters of the 5 events are indicated by green stars.

The differences between the dip and strike inverted from the seismicity and the InSAR data could be explained by 1) the errors of the seismic-based estimations, typical values for the errors are about 10° [*Helffrich*, 1997], and 2) the fact that one single beam InSAR data captured the event, and only partially due to the vegetation and water-induced signal decorrelation.

The modeled fault geometry (Figure 4.35B) is in agreement with the 50° east-dipping striking 9° fault plane. Thus it is likely that such a structure created the observed seismicity. The geodetic moment M_0 of the best-fitting fault model is $1.9.10^{18}$ N.m and corresponds to an average slip on the fault of 1.4 m. However, as we only captured a small part of the displacements, we cannot rule out the possibility of the west-dipping fault. We have not evidence that this seismic event

is linked with a magma intrusion. It is probably a pure tectonic event linked with the western border rift fault reactivation. The geodetic and seismic scalar moments are indeed very similar, which confirms that the observed deformation is almost entirely caused by the fault motion, with no (detectable) magma movement involved.

4.3.2 Bukavu Earthquake, February 2008

On February 3, 2003, a Mw 5.9 earthquake stroke an area near the city of Bukavu (Figure 1.6). Ground displacements associated with this event were captured by descending ENVISAT and ascending ALOS data. The study and modeling of this event is presented in the GJI paper *d'Oreye et al.* [2010] given in Annexe 1. The Bukavu earthquake can be explained by a pure tectonic model including a normal fault striking almost N-S, 50-60° east-dipping, at a depth of 9 kilometers, in agreement with the result obtained when inverting the seismic data. As found for the Idjiwi October 24 seismic event, no major magma intrusion is involved in the event, at least, at shallow depth.

Chapter 5

The Complementary StaMPS Approach

Several volcanic events were successfully constrained using conventional InSAR and modeling. However, some eruptions were partly or fully missed and some residuals signals are hard to explain with the available data. As explained in Chapter 1, an interesting extension of the conventional InSAR is the new Multi-Temporal InSAR, i.e the PS and SBAS approaches. As we have a large database of ENVISAT and ERS-2 data from several beams and orbits configurations, we can go over a large period of our ground displacements history to check if such MT-InSAR methods could give us new complementary information to better constrain the previous established eruption models, or gain new insights on undetected eruptions, as well as on magmatic and tectonic activity. Furthermore, spanning long periods of time allows us to have a global view of the volcanoes dynamics rather than simply look at a single eruption snapshot. Such time-series methods can indeed help to find common threads between eruptions, study volcanoes endogeneous growth or identify eruptive cycles for instance.

5.1 Processing Strategy

As shown in Figure 2.20 in Chapter 2, the PS + SBAS combined approach leads to the largest number of selected pixels. The combined approach provides us with the largest amount of information about the ground deformation in the area. However, the consistency between the three methods results is checked systematically for all processed time-series. Table 5.1 shows all the time-series analysis processed in this study. Seven beams of ENVISAT have been processed, including three modes in ascending orbits, and four modes in descending orbits, covering different time spans from December 2002 to 2010. One ascending ERS-2 mode was also processed covering the period from June 1997 to January 2003.

5.2 ENVISAT Results

5.2.1 ENVISAT Beam 35i2 Results

The ENVISAT beam 35i2 (inc. angle 23°) is the longest time span available for a MT-InSAR study, running from 2003/01/16 to 2010/03/25 and including thus three Nyamulagira eruptions: May 2004, November 2006 and January 2010.

Beam	Orbits	Time Span	Master Image (PS Processing)	Nb of SAR Images	Nb of SBAS IFGS
		ENVISAT			
228i2 (18°)	asc.	2002/12/25 - 2008/04/02	2004/11/24	35	96
35i2 (18°)	desc.	2003/01/16 - 2010/03/25	2007/01/25	47	146
450i7 (38°)	desc.	2003/12/26 - 2010/03/19	2008/02/08	34	95
314i7 (38°)	asc.	2006/06/13 - 2010/04/13	2008/05/13	36	120*
493i4 (28°)	desc.	2008/04/21 - 2010/03/22	2009/11/02	16	41*
42i5 (31°)	asc.	2008/04/24 - 2010/03/25	2009/08/27	16	39**
221i6 (34°)	desc.	2008/05/07 - 2010/04/07	2009/07/01	17	52
		ERS-2			
20°	asc.	1997/06/04 - 2003/01/29	2000/09/06	15	46

* SBAS and MERGED results should be improved

** PS, SBAS and MERGED results should be improved

Table 5.1: Characteristics of the time-series processed in this study

The SBAS baseline plot is given in Figure 5.1. The first images were problematic as the perpendicular baseline differences were quite large, the most coherent couples allowing a good redundancy in the SBAS network have been thus added manually, and all the considered wrapped interferograms have been carefully checked for any coherence or coregistration problems.

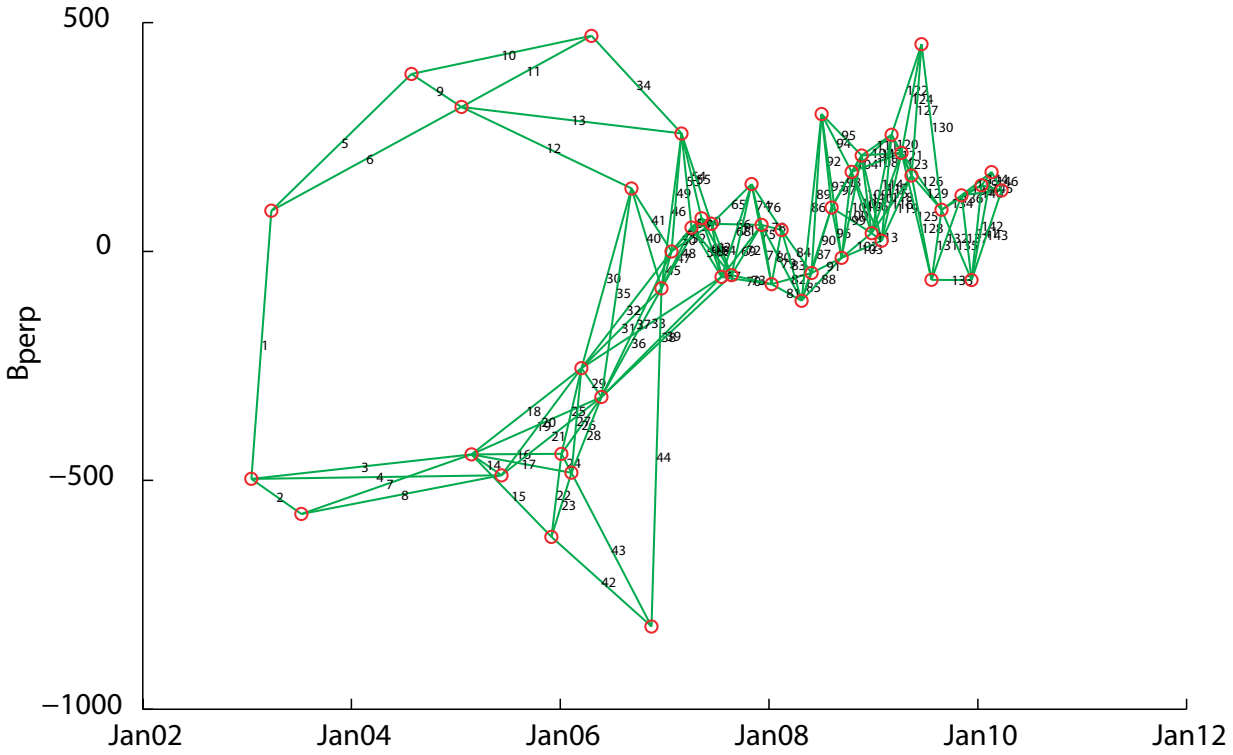

Figure 5.1: SBAS baseline plot for the ENVISAT 35i2 beam, descending orbits. A total of 47 SAR images and 146 SBAS inteferograms were used.

The combined approach seems to give the best results and the mean LOS velocity (MLV) corrected for the DEM error (Figure 5.2) is shown in Figure 5.3A. DEM errors (Figure 5.2), except for some isolated pixels, are small in flat areas, which is expected as the SRTM DEM used (mission done in February 2000) should be quite accurate in these areas. Large DEM inaccuracy are expected close to escarpments and high reliefs; as well as in locations where thick lava flows, volcanic cones and other topographic features were created after February 2000. The pixels in the Lake Kivu show the largest DEM error, but as we said previously in Chapter 2 in Figure 2.20, they are probably due to azimuth ambiguities remaining from the focusing processing and should not be taken into account. There are about three pseudo-circular shapes corresponding to the highest negative DEM error of about maximum 17 meters SE of the Nyamulagira volcano (to the right of *a* in Figure 5.2), aligned with the Nyamulagira-Nyiragongo faulted and weakness area direction, which could correspond to new topographic features such as the new volcanic cones built during the Nyamulagira 2001 eruption.

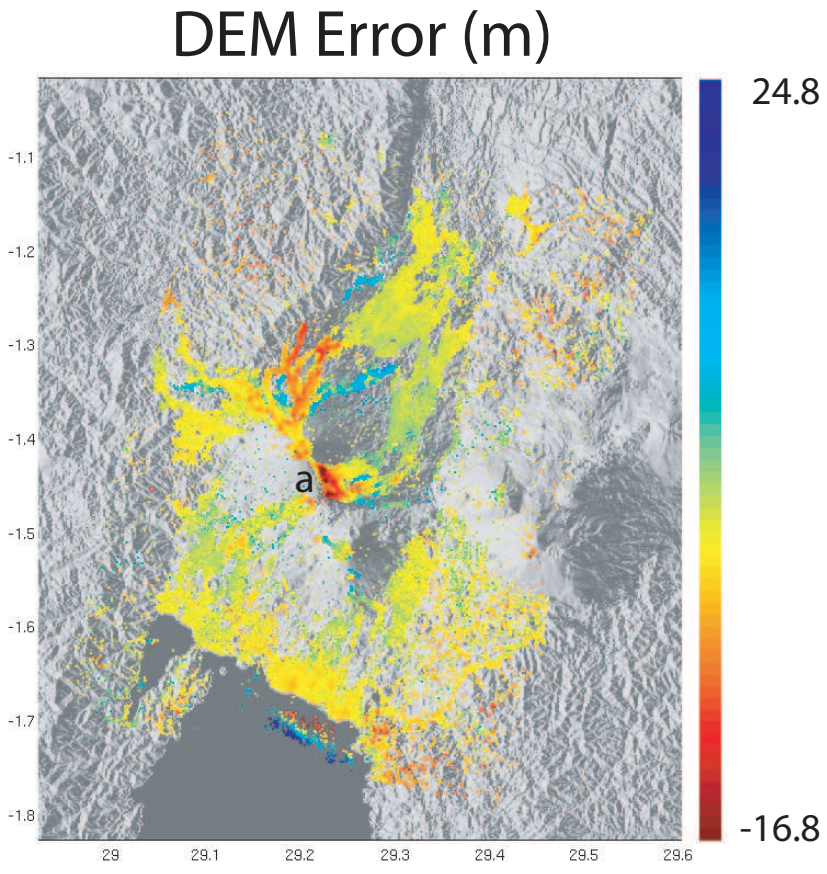

Figure 5.2: DEM error estimated for the ENVISAT 35i2 beam, descending orbits. A total of 47 SAR images were used.

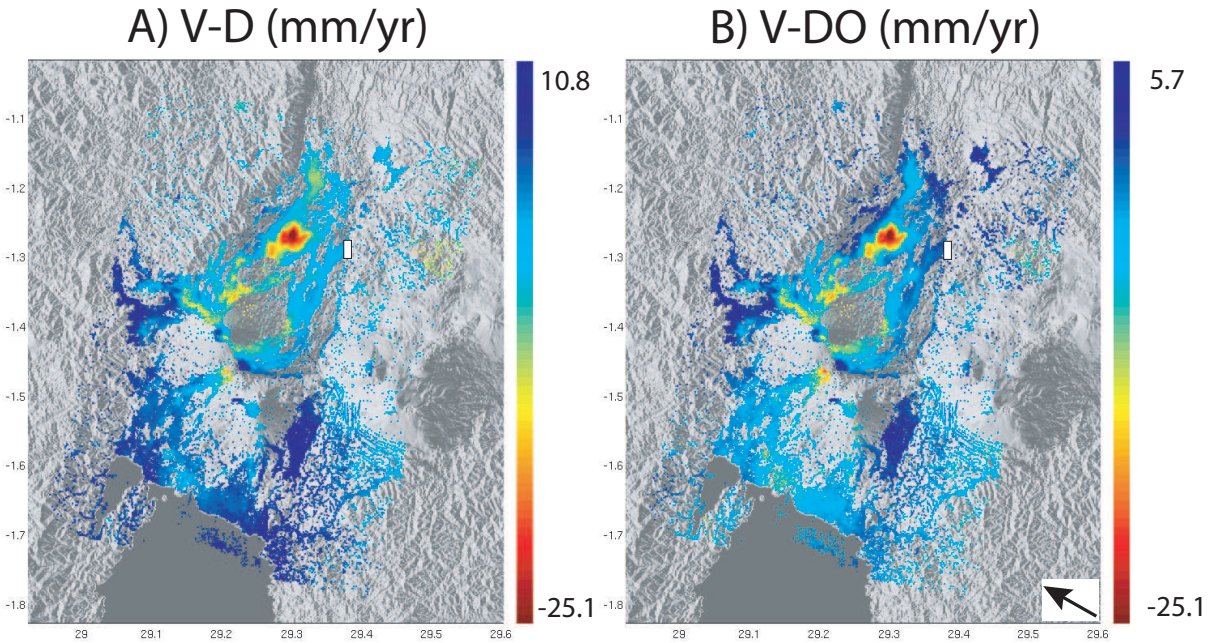

Figure 5.3: Mean LOS velocity (MLV) in mm/yr obtained with the combined (PS + SBAS) approach for the ENVISAT 35i2 beam, descending orbits, superimposed over the shaded DEM. 49,434 pixels (200 m) are selected. In A) The DEM error (Figure 5.2) has been subtracted, and in B) The DEM and orbital ramps have been subtracted. Positive velocities correspond to displacement towards the satellite. The reference master for the PS approach is 2007/01/25 and the baseline plot for the SBAS approach is given in Figure 5.1. The reference area is indicated by the white rectangle.

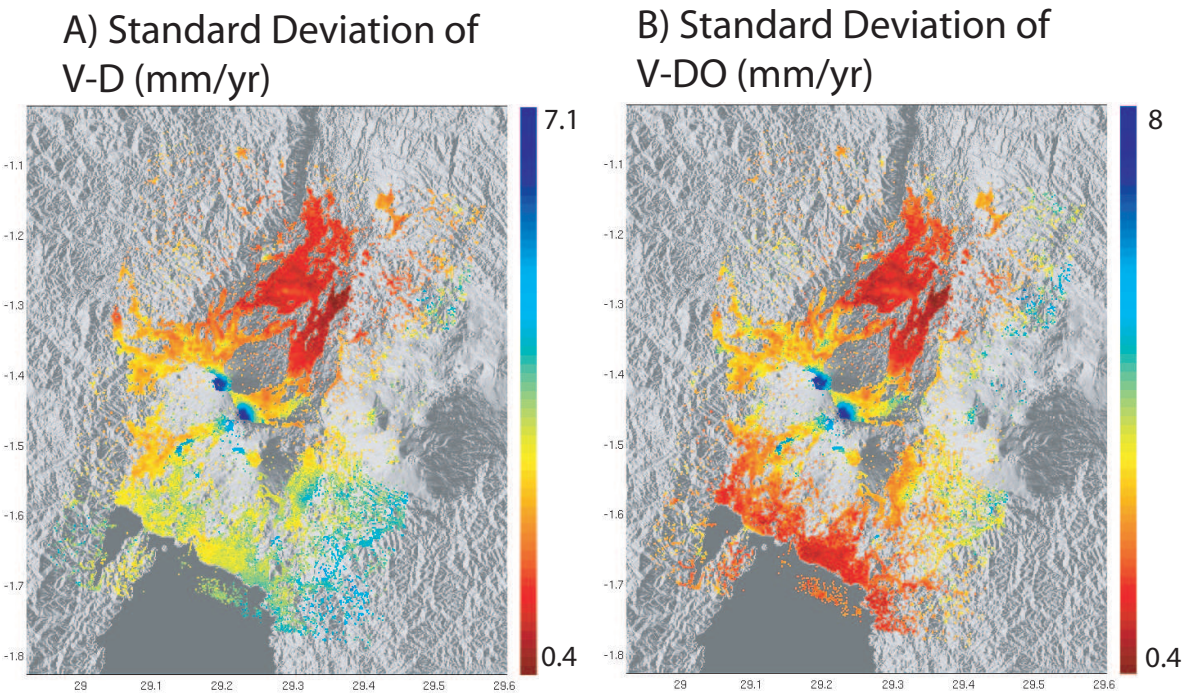

Figure 5.4: A) Standard Deviation of the MLV minus DEM error, B) Standard Deviation of the MLV minus DEM error and orbital error, estimated for the ENVISAT 35i2 beam, descending orbits.

Figure 5.3B shows the mean LOS velocity (MLV) also corrected for orbital errors, subtracting a linear orbital ramp for each interferogram. The visual inspection of the ENVISAT interferograms used shows that most of them are affected by small orbital artifacts as the ESA ENVISAT orbits are known with a good accuracy (generally less than 1 fringe of orbital ramp over the all scene). However, the standard deviation of the MLV minus the DEM error (Figure 5.4A) and also minus the orbital ramps (Figure 5.4B) shows that removing the orbital error significantly decreases the standard deviation in the southern part of the scene. Thus, we consider that the MLV minus the DEM and orbital errors (V-DO) is probably the most reliable result for the MLV estimation. Time-series plots for some areas known to be quite stable or with lava flow compaction (Figure 5.7), show variations in the deformation rate of the order of about 1 to 2 centimeters. The typical accuracy can be roughly estimated to about 1-2 cm. Signals below this threshold might therefore not be significant and should be interpreted with care.

5.2.2 Discussion about the reference area

Except in the case of difference in imaged scenes, the reference area is a rectangle of latitude comprised between -1.315 and -1.270, and longitude between 29.35 and 29.4 East. The choice of such a reference area was not trivial here as many parts of the Virunga area deform. Several tests were made before picking this area, which seems to give reliable results, with the lava flow pile NE of Nyamulagira continuously subsiding for instance. The different references tested were located west of the western border fault of the rift, at the edge of an other old lava flow, east of the city of Gisenyi. They all gave similar results. We finally choose an area corresponding to the edge of an old lava flow from 1981-82, so that its thickness at the edge is small and the subsequent lava compaction should be negligible. However, we are aware that the reference area is an issue in this case study, and should be taken into account for any interpretation, as any small movement affecting the reference area, could contaminate the displacements measured elsewhere. Such effect can be amplified when looking at areas far from the chosen reference.

5.2.3 Identification of Unstable Areas

Figure 5.5 shows that several areas were affected by ground displacements during the January 2003 - March 2010 period. Note that the i2 ENVISAT mode is almost vertical and is thus much more sensitive to the vertical component of displacements than to the horizontal displacements. At the beginning of the period covered by this beam, the density of images was a bit poor, moreover, the perpendicular baselines were not suitable (Figure 5.1), making the results quite noisy and difficult to interpret unambiguously until the Nyamulagira 2006 eruption. Note also that a MLV over such a large period of time can contain many non linear as well as reversed deformation signals, especially during eruptions where different dike orientations occur. It is particularly the case for Nyamulagira considering the fissures distribution and modeling results. One should hence check carefully time-series plot for small groups of pixels, and MLV or LOS cumulated displacements for smaller time period, for instance between two eruptions. Hence non linear signals could also be studied with MT-InSAR means.

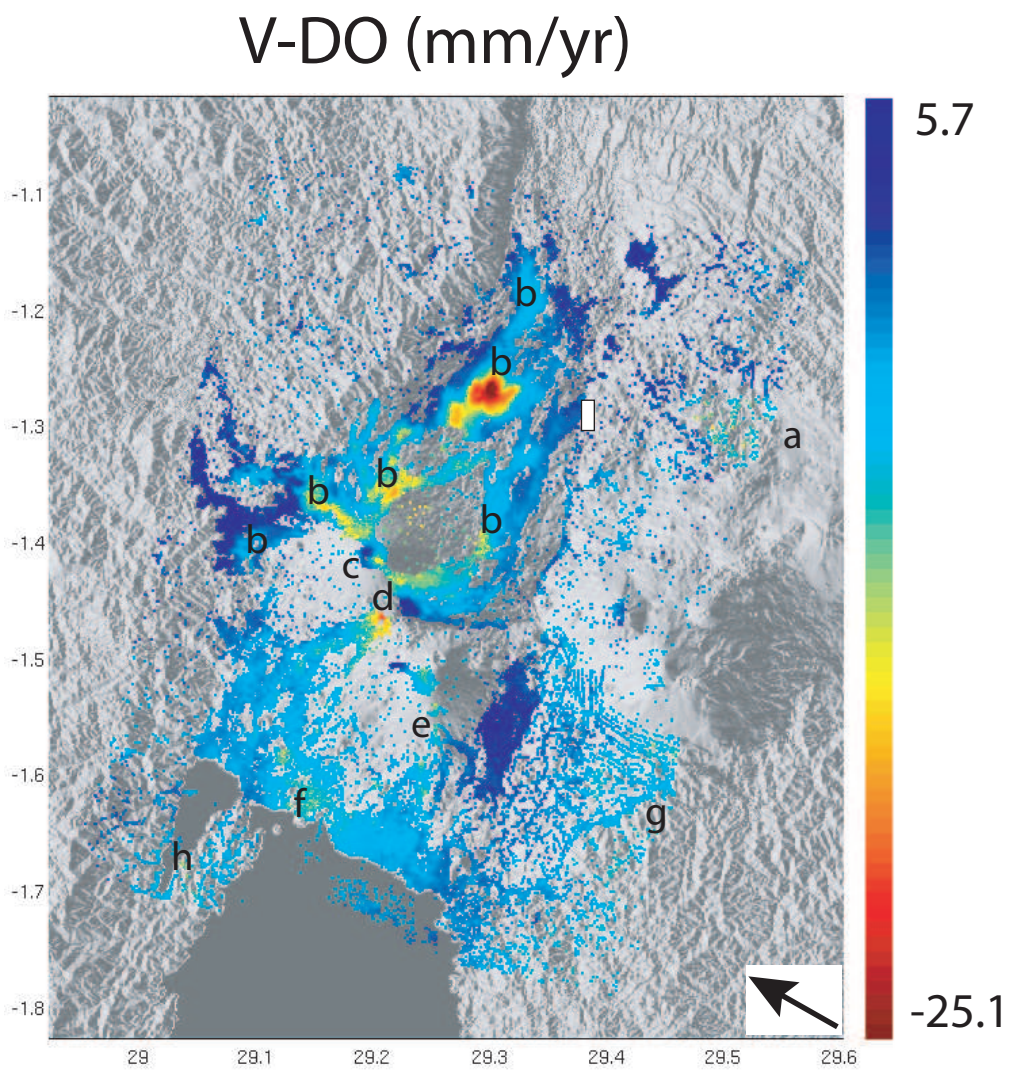

Figure 5.5: MLV minus DEM and orbital errors, see text for a, b, c, d, e, f and h explanation. The reference area is indicated by the white rectangle.

The area a, east of the scene is affected by a global range increase of about 20 mm/yr. The time-series plot for this area is given in Figure 5.6 and shows a cumulated range increase displacement of about 40 mm from end of year 2005, with a sudden 30 mm range increase from December 2005 to March 2006. Before the end of 2005, the area seemed quite stable but this is poorly constrained as the number of images is low. The range increase behavior seems to stop end of the year 2008.

Several areas of range increase can be identified corresponding to recent lava flow compaction (referred to as b). Interestingly, sometimes even old lavas, as for instance from the northernmost Nyamulagira 1958 lava flow (location given in the volcanological map in Figure1.14, Chapter 1) are still compacting, probably because of their large lava thickness.

The area NW of the Nyamulagira caldera (c) is characterized by a very interesting time-series deformation history, as depicted in Figure 5.8. This area appears first stable to slightly range increasing from January 2003 to the beginning of September 2006. A few displacements peaks of about 20 mm are visible but could not be confirmed unambiguously due to the small number of images used. The area experiences then a strong range decrease of about 80 mm from September

to December 2006, related to the November, 27, 2006 eruption. A precursor range decrease deformation seems thus have affected this area a few months before the eruption. After the 2006 eruption, the area is characterized by a continuous small range increase again until August, 27, 2009, a date from which the behavior changes again to a sharp range decrease just before the January 2010 eruption which induced a large sudden range increase until January, 14. The last two dates after January, 14, show that the behavior seems to switch again to a range decrease. Note that the area NW of the Nyamulagira caldera is almost free of lava flows, and thus the lava flow compaction could not explain the identified range increase patterns.

The time-series plot of the SE area of the caldera is shown in Figure 5.9. The overall deformation behavior is quite similar with the observation made in the NW part, with this time a dominating range increase in this area and less marked deformation peaks for the 2006 and 2010 events. Also, many lava flows were emplaced in this area, especially in the SW depression which is about 1000 m deep (Figure 1.10), and their compaction signal should play an important role in this area. The last lava flows were emplaced there during the 2001 and 2004 eruptions.

The beginning of the time-series for an area west of the point d (Figure 5.10) is characterized by two cycles including a range decrease followed by a range increase, the first one from January 2003 to July 2004, and the second one after July 2004 until April 2006. The range starts decreasing suddenly from September 2006 to December 2006 too, similarly as what was observed NW of the caldera. After the 2006 eruption, the behavior is a range decrease until the January 2010 eruption. The behavior is completely different in an area west of point d, which is indeed dominated by a range increase (Figure 5.11), with a larger rate from the November 2006 eruption. This observation is consistent with the new lava flow emplaced during 2006 eruption, which began to subside too.

An almost linear NS feature e of range decrease is observed from Nyiragongo to the city of Goma.

The area f SW of the Nyiragongo volcano is characterized by several patches of range increase reaching a maximum of about 70 mm of cumulated range increase. Several parts of the area are thus undoubtedly deforming with a general range increase behavior. Several small changes in behavior can be observed too (Figure 5.12), but they are often close to the method accuracy and cannot be interpreted unambiguously.

Several small anomalies of range increase (in the proximity of g) are also identified south of the Virunga volcanoes Mikeno and Karisimbi. These areas include many culture in terraces on the relief slopes, and the existence of these paths explain the linear trends of the reflectors in this area.

An area of range increase is finally identified in h in the Mbuzi peninsula.

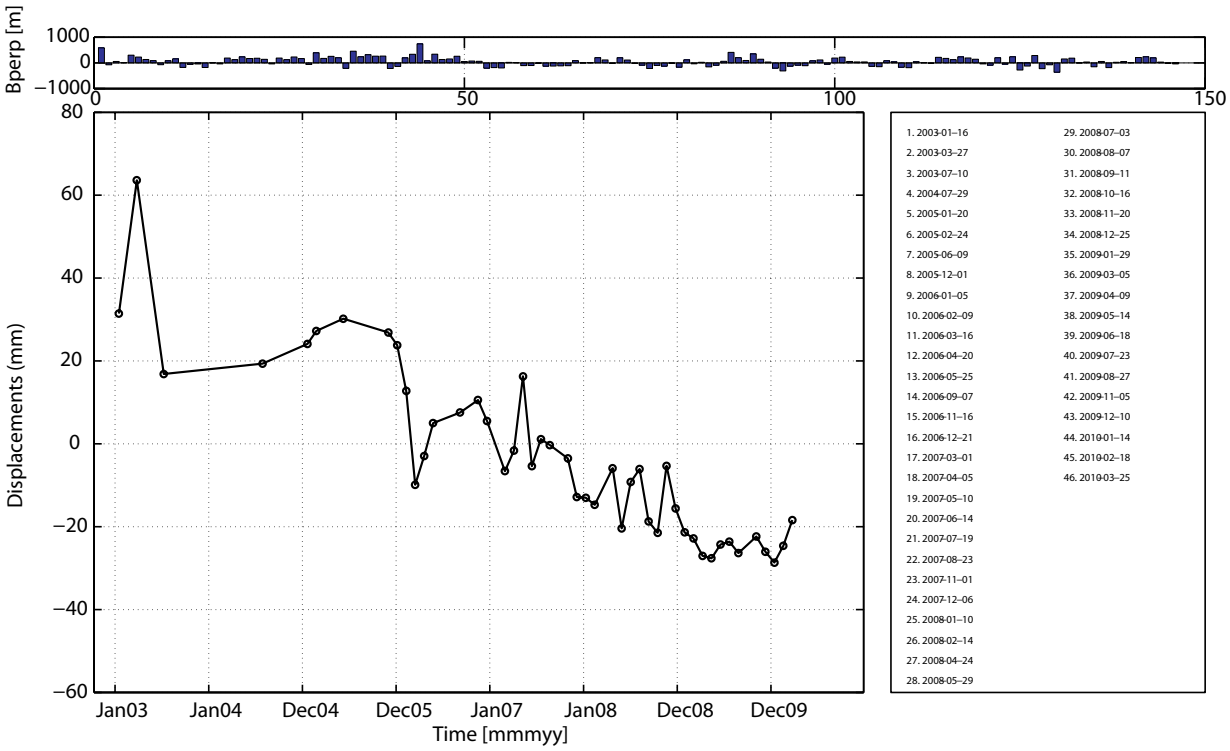

Figure 5.6: Time-series plot for the point *a* in Figure 5.5. The time reference (zero displacement) is 2007/01/25.

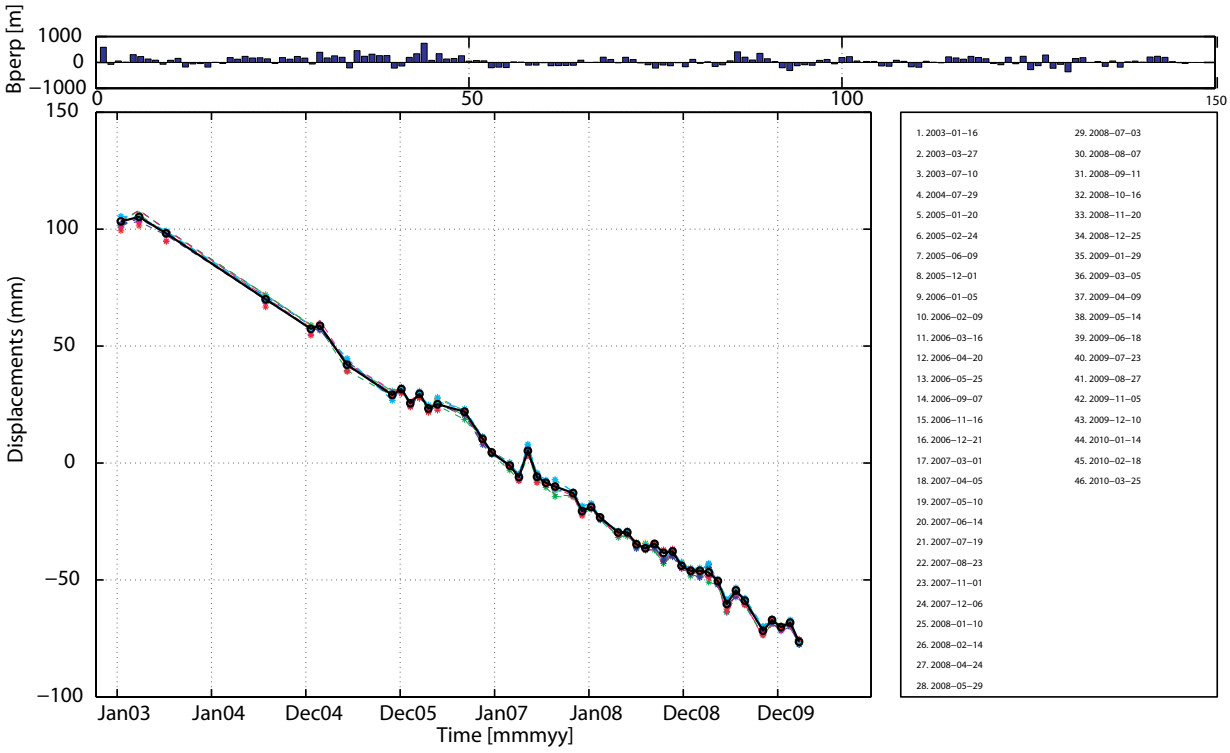

Figure 5.7: Time-series plot for the point *b* NE of the Nyamulagira in Figure 5.5, in the lava flow pile from Nyamulagira resulting from the 1958, 1967, 1980 and 1991-93 eruptions. The time reference (zero displacement) is 2007/01/25

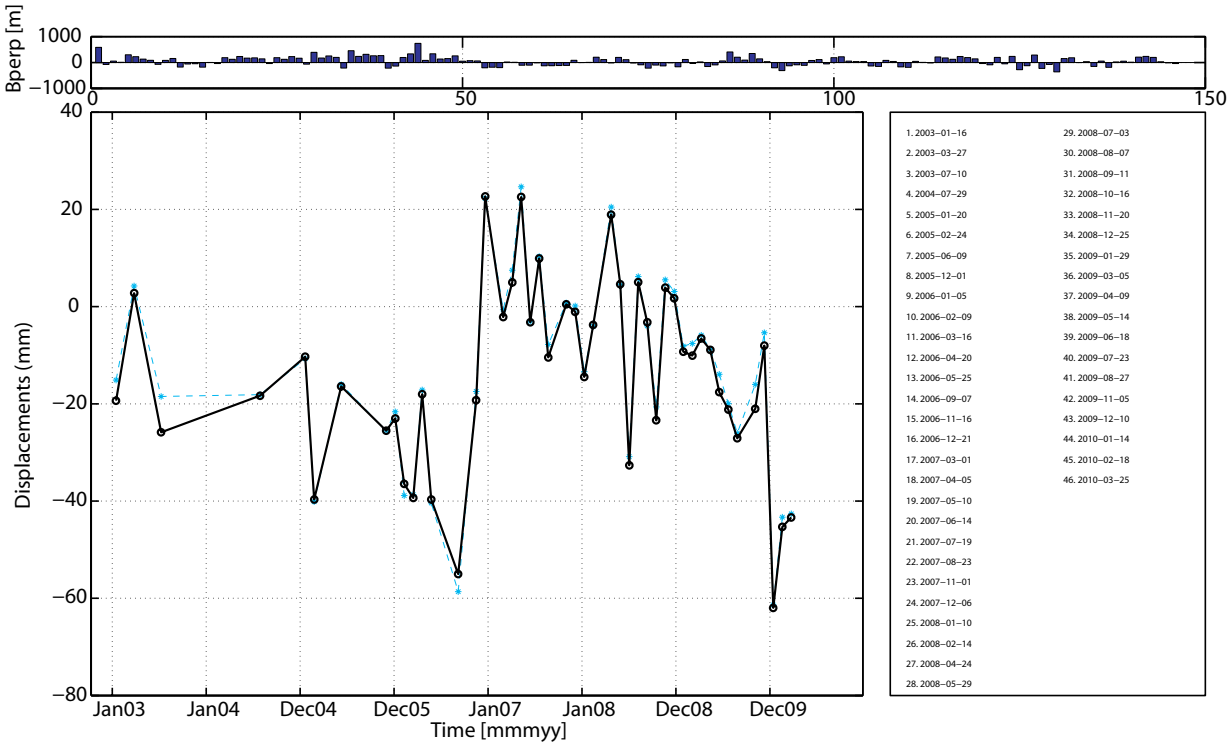

Figure 5.8: Time-series plot for the NW area of the Nyamulagira caldera close to point *c* in Figure 5.5. The time reference (zero displacement) is 2007/01/25

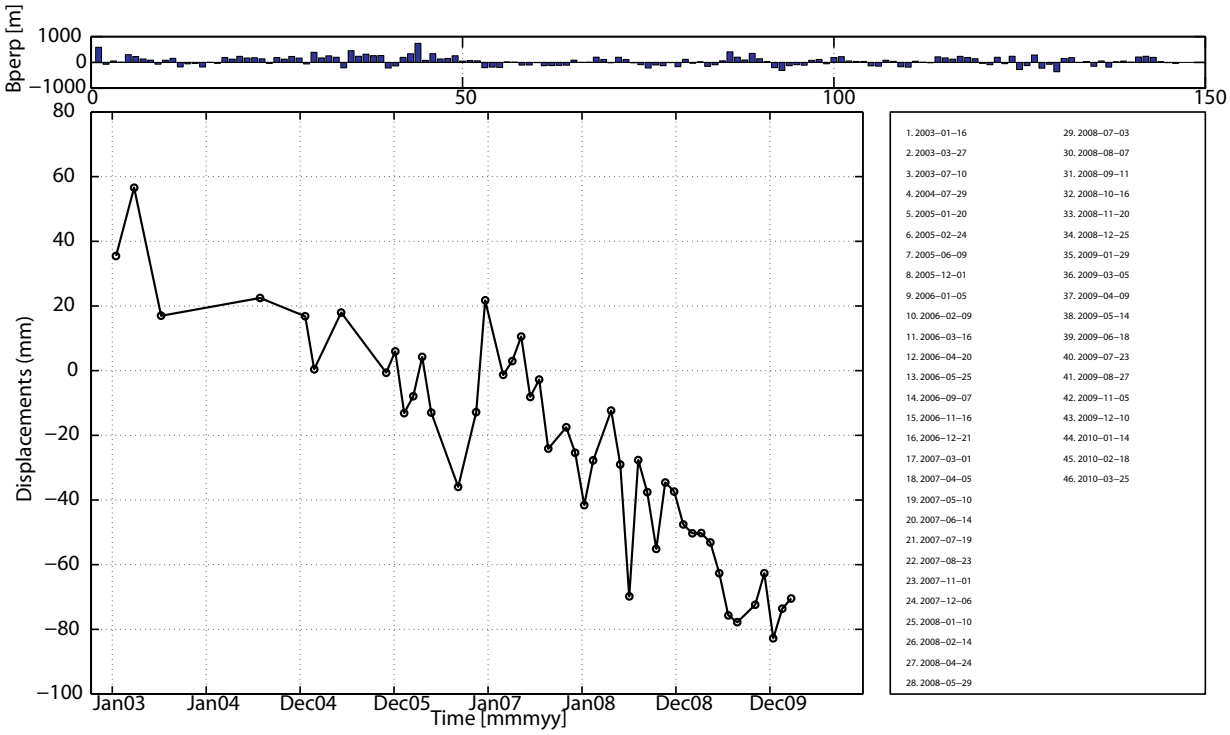

Figure 5.9: Time-series plot for the SE area of the Nyamulagira caldera close to point *c* in Figure 5.5. The time reference (zero displacement) is 2007/01/25

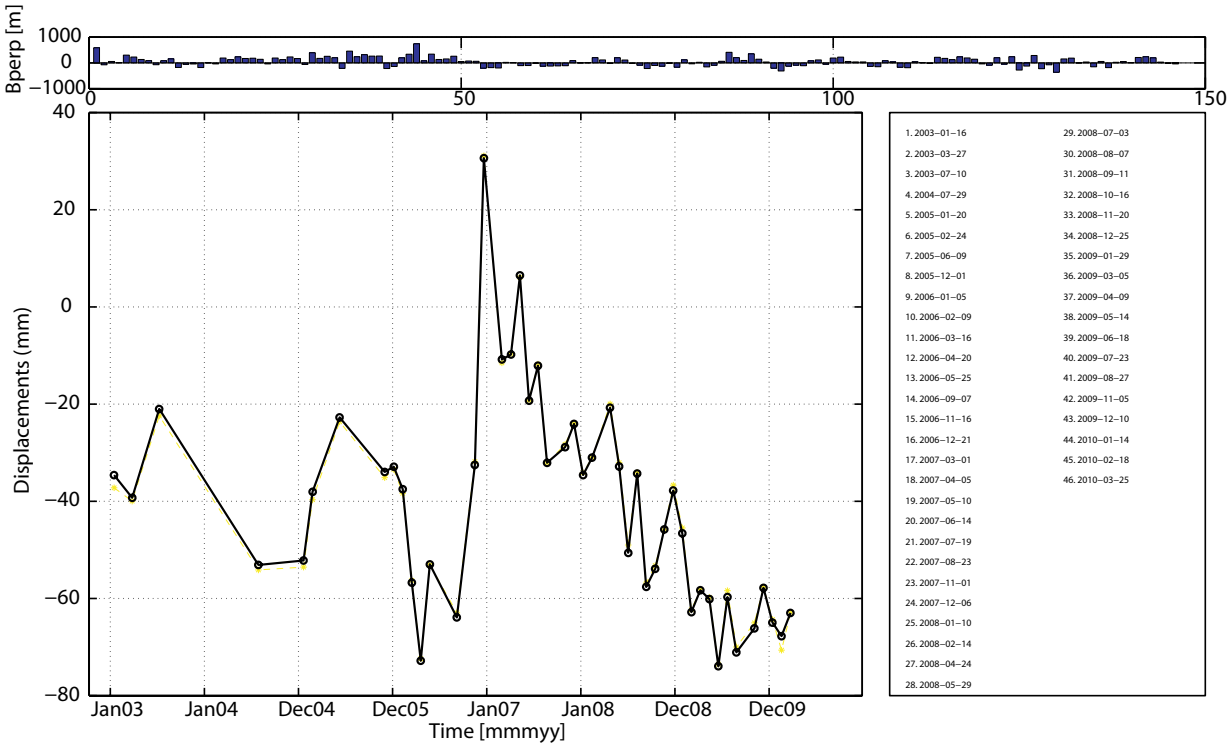

Figure 5.10: Time-series plot for an area east of the point d in Figure 5.5. The time reference (zero displacement) is 2007/01/25

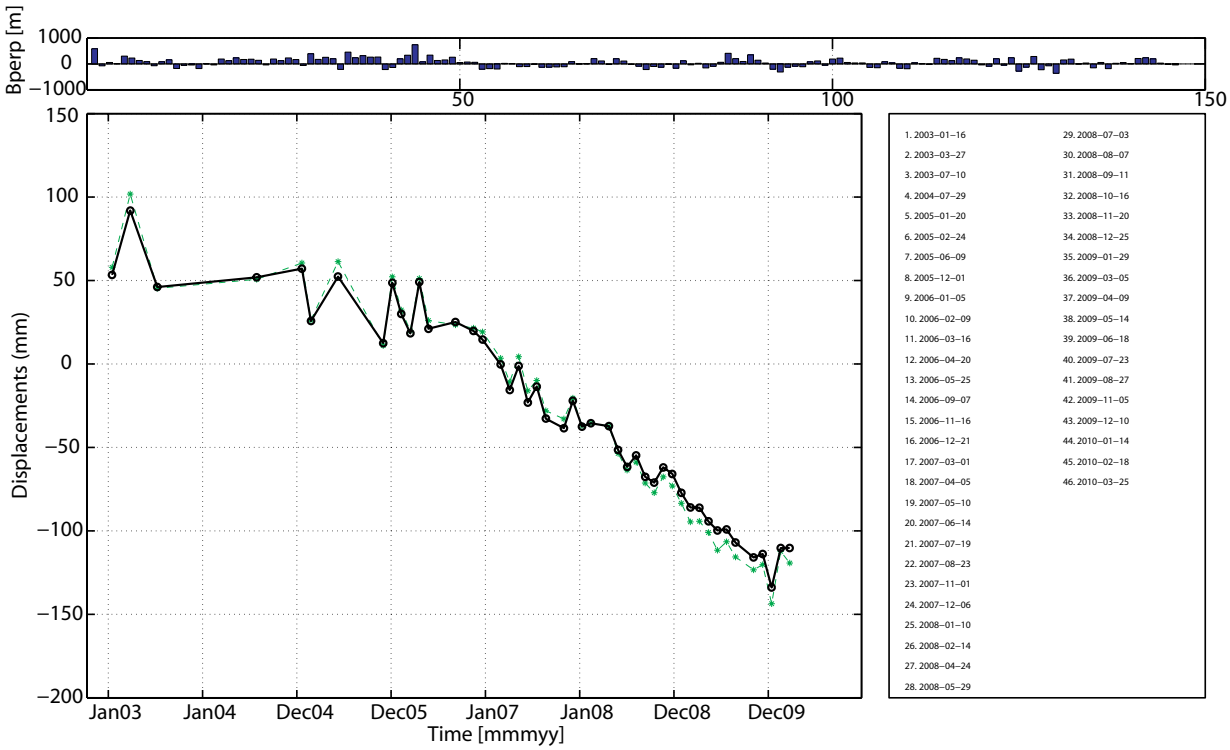

Figure 5.11: Time-series plot for an area west of the point d in Figure 5.5. The time reference (zero displacement) is 2007/01/25

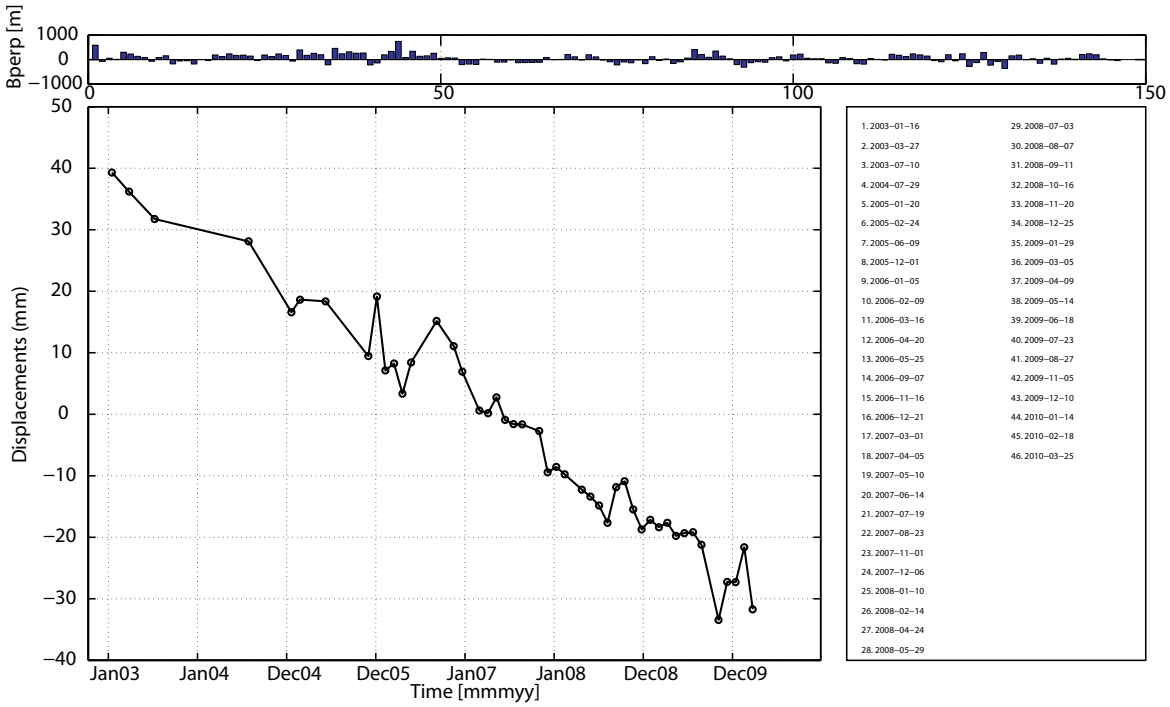

Figure 5.12: Time-series plot for an area surrounding the point f in Figure 5.5. The time reference (zero displacement) is 2007/01/25

5.2.4 Comparison with SBAS IREA Results

When comparing [*Wauthier et al.*, 2010] the MLV results obtained with the StaMPS method and the SBAS method developed at IREA, we can conclude that the two methods give consistent and quite similar results, identifying the same deforming areas but with slightly different velocities estimations, likely because of different filters, The IREA method suing indeed a strong filter for atmospheric delays to smooth the general aspect of the time-series. The StaMPS method allows generally to have a best density of selected pixels, even on the volcanoes flanks, where the IREA method fails to select any reliable pixels.

5.2.5 Comparison with other Beams and Interpretation

The MLV obtained for all the other ENVISAT beams are shown in Figures 5.13, 5.15, 5.16, 5.17. The PS results for the beams 450i7, 314i7, 493i4 and 42i5 are shown as the SBAS or combined (PS+SBAS) results were not estimated reliable enough. The PS results for the 42i5 beam (Figure 5.16, right image) are affected by large errors in the southernmost part of the scene, one or more images should be removed from the processing, and these southernmost pixels are thus estimated to be unreliable.

The range increase anomaly identified in a on the 35i2 beam results (Figure 5.5) could not be further investigated for the other ENVISAT beams as the area a is systematically outside the imaged scene. This area includes several topographic features and small villages and is located on Precambrian basement exposure. No strong seismic activity occurs there from end of 2005, as most of the seismic activity is localized in the western part of the rift, along the western border rift fault. However, there are faults in the Precambrian basement which can be reactivated *(Benoît Smets, pers. comm., 2011)*.

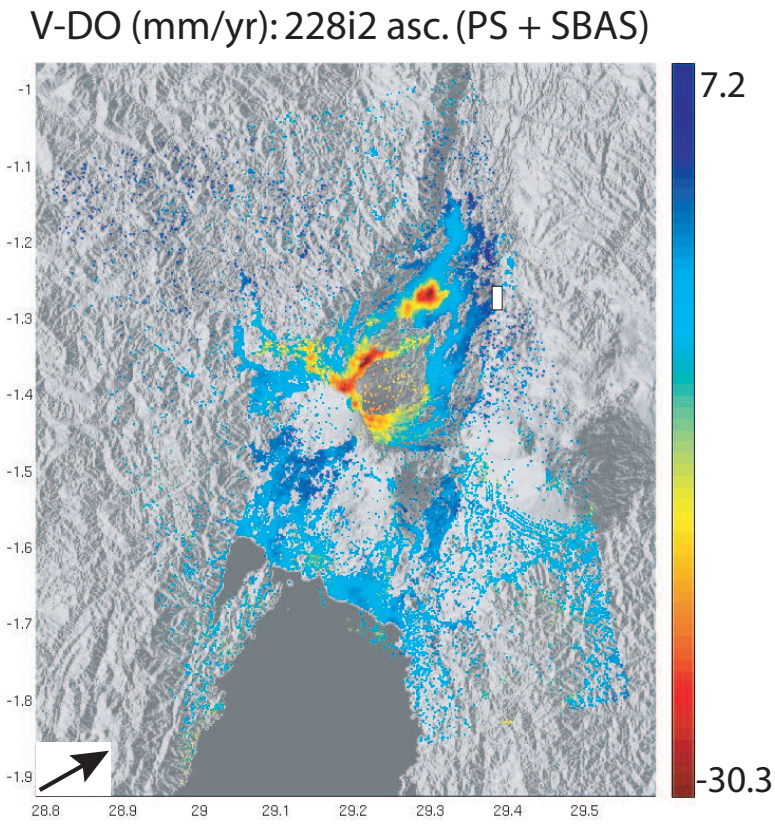

Figure 5.13: Mean LOS velocity (MLV) in mm/yr obtained with the combined (PS + SBAS) approach for the ENVISAT 228i2 beam, ascending orbits, surimposed over the shaded DEM. 33,949 pixels (200 m) are selected. The DEM and orbital ramps have been subtracted. Positive velocities means displacement towards the satellite. The reference master is 2004/11/24 and the baseline plot for the SBAS approach is given in Figure 5.14. The reference area is indicated by the white rectangle.

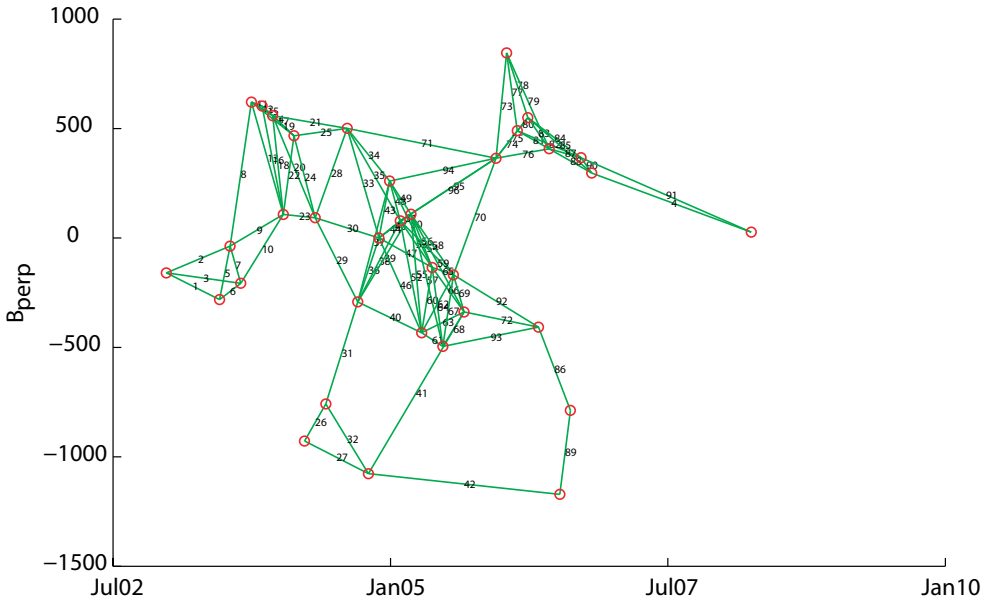

Figure 5.14: SBAS baseline plot for the ENVISAT 228i2 beam, ascending orbits. A total of 35 SAR images and 96 SBAS inteferograms have been used.

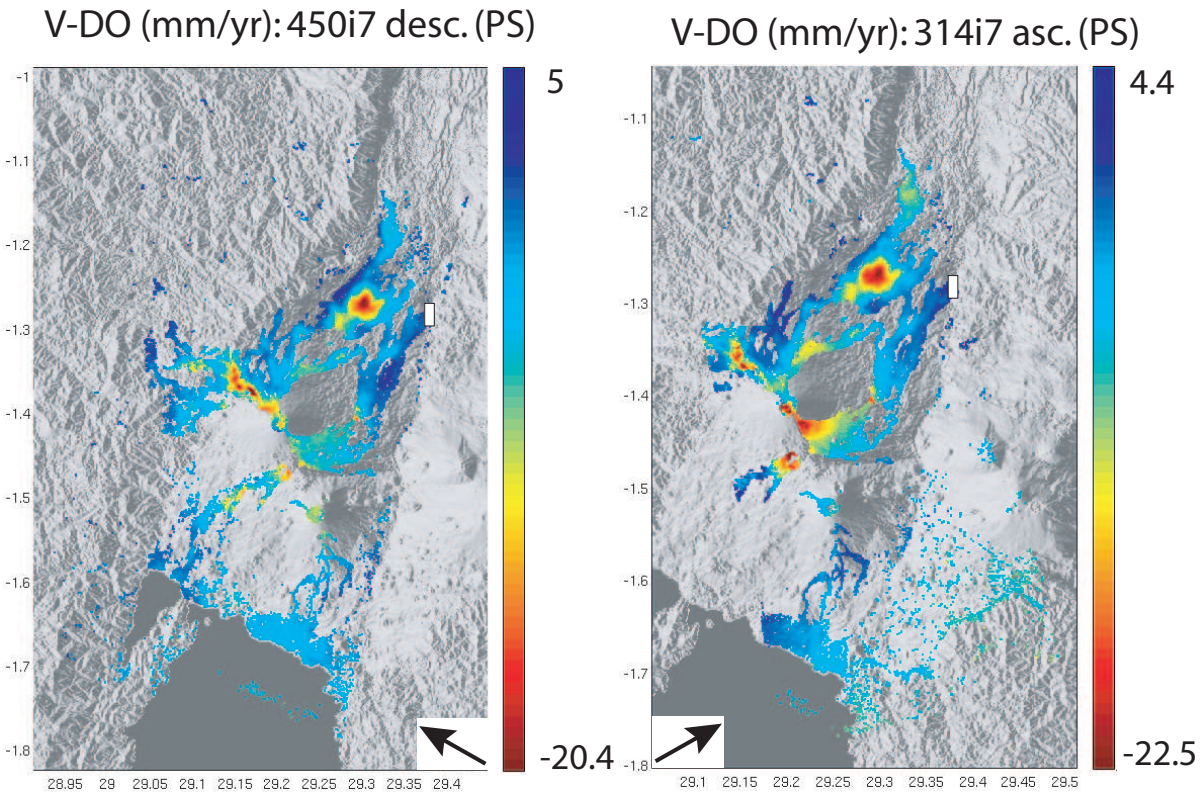

Figure 5.15: Left Image: Mean LOS velocity (MLV) in mm/yr obtained with the PS approach for the ENVISAT 450i7 beam, descending orbits, surimposed over the shaded DEM. 24,998 pixels (200 m) are selected. The DEM and orbital ramps have been subtracted. Positive velocities means displacement towards the satellite. The reference master is 2008/02/08. Right Image: Mean LOS velocity (MLV) in mm/yr obtained with the PS approach for the ENVISAT 314i7 beam, ascending orbits, surimposed over the shaded DEM. 11,254 pixels (200 m) are selected. The DEM and orbital ramps have been subtracted. Positive velocities means displacement towards the satellite. The reference master is 2008/05/13. The reference area is indicated by the white rectangle.

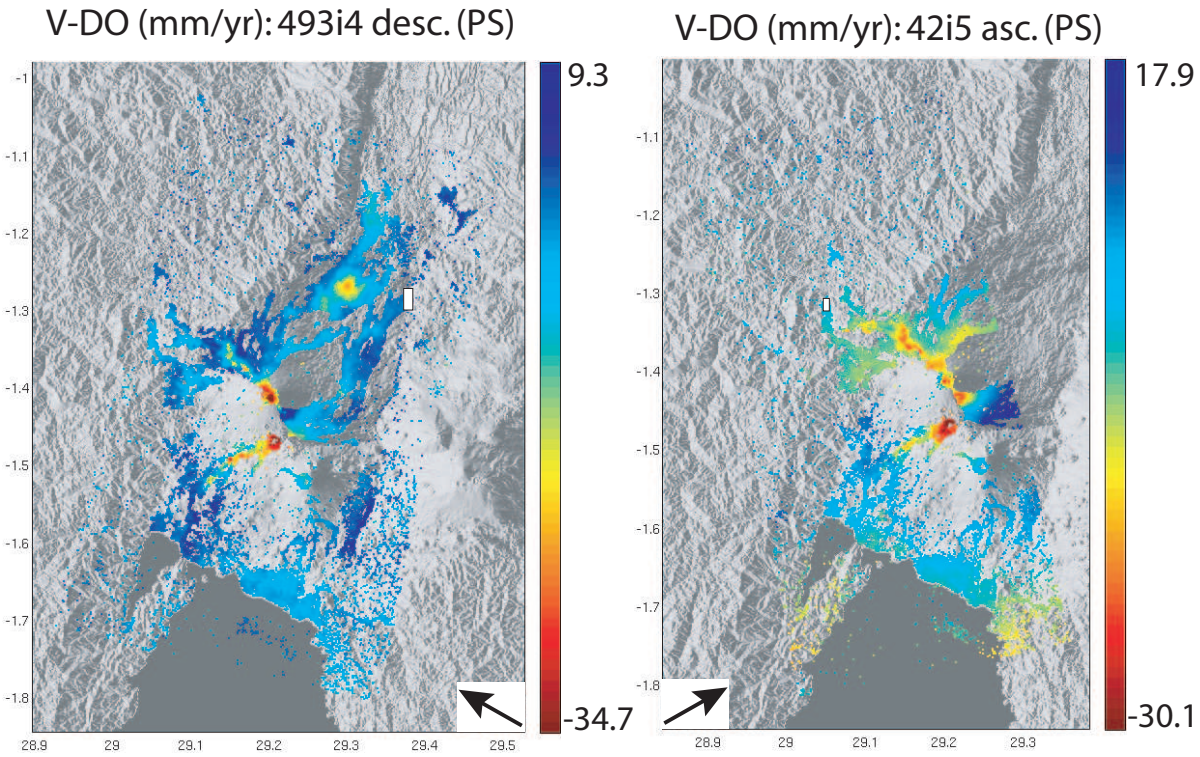

Figure 5.16: Left Image: Mean LOS velocity (MLV) in mm/yr obtained with the PS approach for the ENVISAT 493i4 beam, descending orbits, surimposed over the shaded DEM. 19,499 pixels (200 m) are selected. The DEM and orbital ramps have been subtracted. Positive velocities means displacement towards the satellite. The reference master is 2009/11/02. Right Image: Mean LOS velocity (MLV) in mm/yr obtained with the PS approach for the ENVISAT 42i5 beam, ascending orbits, surimposed over the shaded DEM. 12,997 pixels (200 m) are selected. The DEM and orbital ramps have been subtracted. Positive velocities means displacement towards the satellite. The reference master is 2009/08/27. The reference area is indicated by the white rectangle.

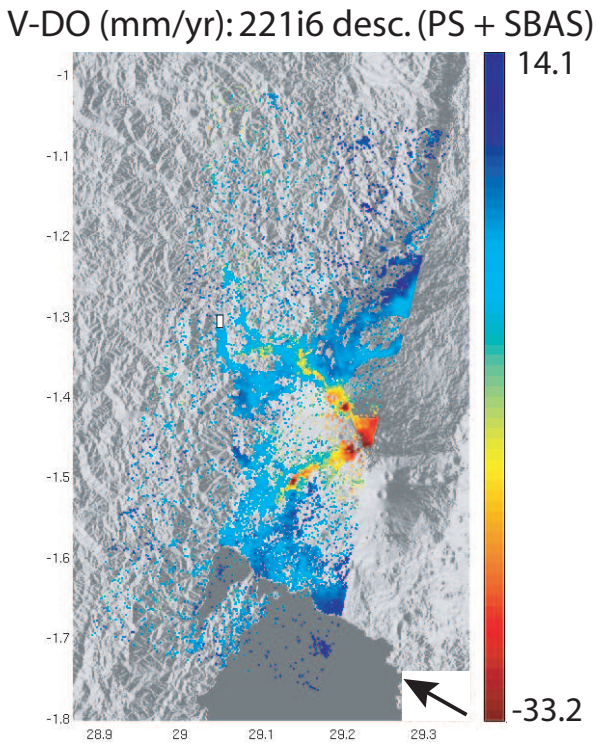

Figure 5.17: Mean LOS velocity (MLV) in mm/yr obtained with the combined (PS + SBAS) approach for the ENVISAT 221i6 beam, descending orbits, surimposed over the shaded DEM. 15,092 pixels (200 m) are selected. The DEM and orbital ramps have been subtracted. Positive velocities means displacement towards the satellite. The reference master is 2009/07/01 and the baseline plot for the SBAS approach is given in Figure 5.18. The reference area is indicated by the white rectangle.

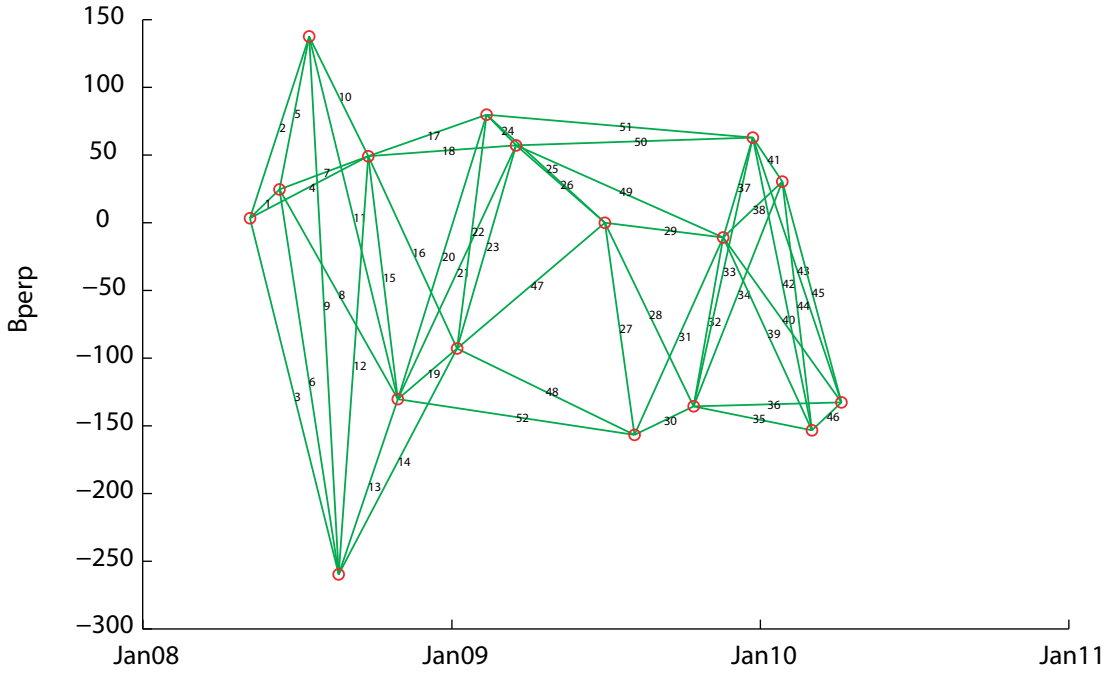

Figure 5.18: SBAS baseline plot for the ENVISAT 221i6 beam, descending orbits. A total of 17 SAR images and 52 SBAS inteferograms have been used.

Lava flow compactions (see *b* areas in Figure 5.5) such as the lava flow pile NE of Nyamulagira are visible and consistent on all times-series results. The strongest lava flow compaction is observed for the lava flow pile from Nyamulagira resulting from the 1958, 1967, 1980 and 1991-93 eruptions. This area cumulates indeed about 200 mm of cumulated range increase (LOS subsidence) over the all 35i2 period (Figure 5.7), for a MLV of about 25 mm/yr, and corresponding mainly to lava flow compaction [*Murray*, 1988] and underlying substrate subsidence by creep thermal relaxation [*Delorme*, 1994] [*Stevens et al.*, 2001]. Moreover, for the considered time period, we can observe that the rate of compaction is still not decreasing but follow more a linear decreasing law, even if the last lava flows emplaced there are about 20 years old.

The linear NS feature *e* of range decrease, observed from Nyiragongo to the city of Goma, could be associated with the 2002 eruptive fissure of Nyiragongo. It could result of the shallow dike thermal cooling. The Nyiragongo 2002 lava flows are not affected by strong small lava compaction effects, although they are visible, very likely because of smaller thickness and difference in composition and thus in compaction behavior with respect to the Nyamulagira lava flows. Interestingly, the Goma-Gisenyi area does not seem to be affected by clear extended deformation, except for some isolated pixels, and those located on the 2002 lava flows affected thus by small lava flow compaction effects.

StaMPS results for all ENVISAT beams including the area *f* are consistent with deformation corresponding to a general linear range increase of the southern area north of Lake Kivu, and is thus likely to be more a vertical movements as both ascending and descending results show the same sense of movements. The ground subsidence could be linked with gas release of the groundwater system. The two most subsiding areas, f_1 and f_2 (Figure 5.19), reaching a maximum subsidence of about 15 mm per year, correspond indeed with the presence of many *mazuku*[1] which are dry gas vents, i.e. depressions where carbon dioxide accumulates. They were mapped by *Smets et al.* [2010b], as depicted in Figure 5.19D. f_1 corresponds to the Bulengo and west of Goma areas where a large amount of *mazuku* have been mapped [*Smets et al.*, 2010b], and f_2 is located at the Rumoka volcanic vent, which was built during the 1912 Nyamulagira eruption and is the area releasing the largest amount of carbon *(Benoît Smets, pers. comm, 2011)*. The f_3 range increase anomaly, visible on the three beams, is located just southwest of the horseshoe-shaped old phreatomagmatic cone could corresponds to the compaction of the 1986 lava flow southernmost end. Three other range increase anomalies are identified on the 228i2 ascending beam only, mainly because of a largest number of pixels in this mode, but we cannot rule out that they are noisy pixels: f_4 which does not correspond to any specific feature on the field, f_5 which is located in Sake where several *mazuku* have been mapped too [*Smets et al.*, 2010b], and f_6 could correspond to the Mubambiro *mazuku*. The intense degassing at these *mazukus* could induce the ground subsidence.

The small oscillations observed in the time-series plots for these areas could be attributed to noise or to small seasonal variations. Other small isolated *mazuku* mapped by *Smets et al.* [2010b] on the lake shore and in Goma could explained the small range increase of other isolated smaller groups of pixels in the StaMPS results.

The small anomalies of range increase (in the proximity of *g*) could be generated by noisy pixels or be induced by farming.

[1]The word *mazuku* in Swahili means evil wind

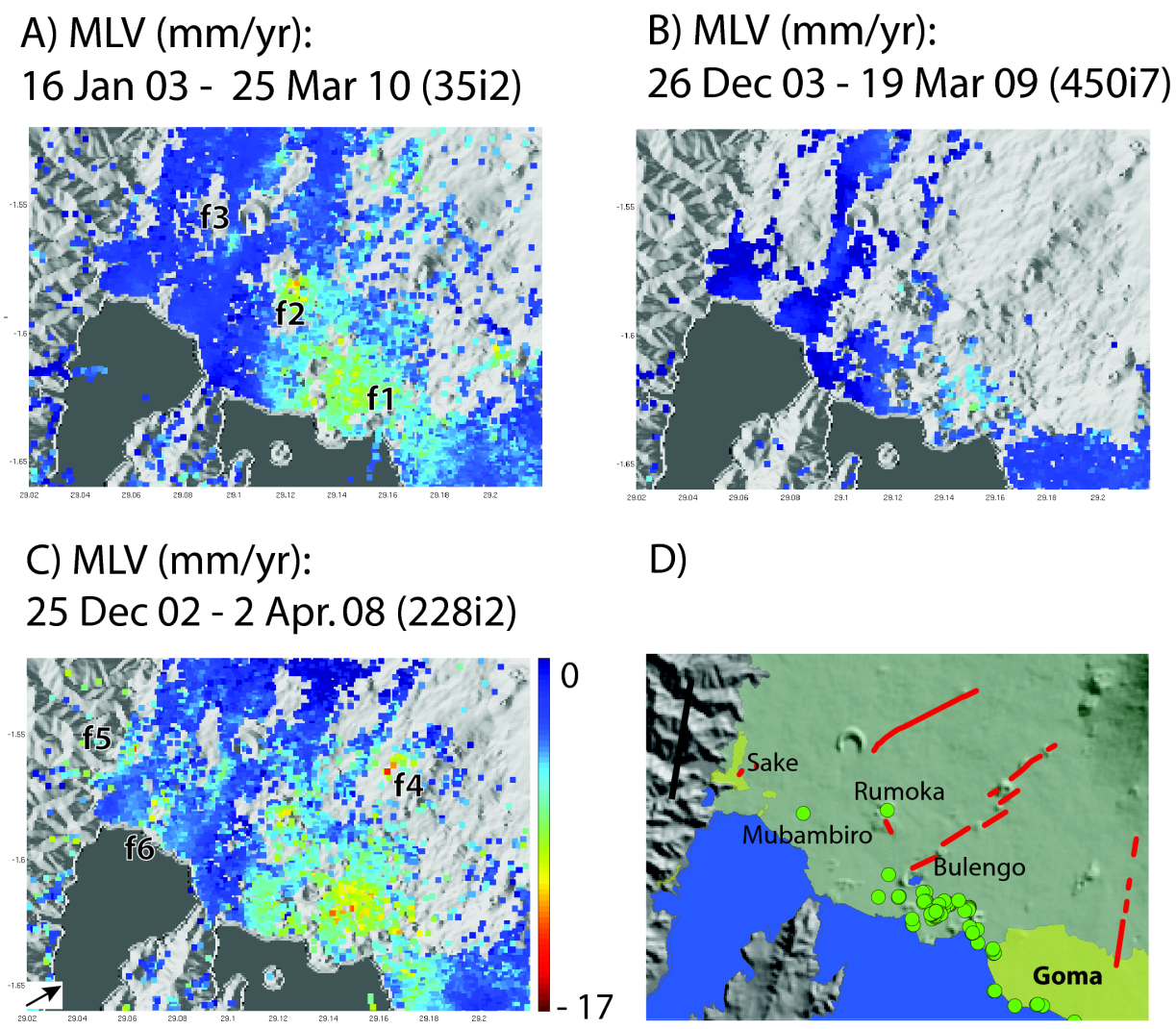

Figure 5.19: Mean LOS velocity (MLV) in mm/yr obtained with A) the combined (PS + SBAS) approach for the ENVISAT 35i2beam, descending orbits, A) the PS approach for the ENVISAT 450i7beam, descending orbits, C) the combined (PS + SBAS) approach for the ENVISAT 228i2beam, ascending orbits, all surimposed over the shaded DEM. Positive velocities means displacement towards the satellite. D) shows the *mazuku* location after [*Smets et al.*, 2010b]

The few pixels affected by range increase identified in h in the Mbuzi peninsula in the 35i2 results, is not clearly visible on other beams results and could thus be an artifact generated by a few noisy pixels.

5.2.6 Close up on the Nyamulagira Volcano Activity

The 228i2 ascending mode offers the best coverage in SAR images before the May 2004 Nyamulagira eruption. The LOS cumulated displacements for the period June 03 - April 04 is shown at Figure 5.20. West and NW of the caldera is affected by about 3 cm of range decrease, which can be due to magma input in a shallow reservoir or sill. A pseudo-triangular area SE of the caldera is slightly range increasing, with an average rate of about 1 cm in 315 days thus. This area corresponds likely to the shape mapped for the 2001 lava flow inside the caldera which after flow outside of it on the SE flank (Figure 4.12).

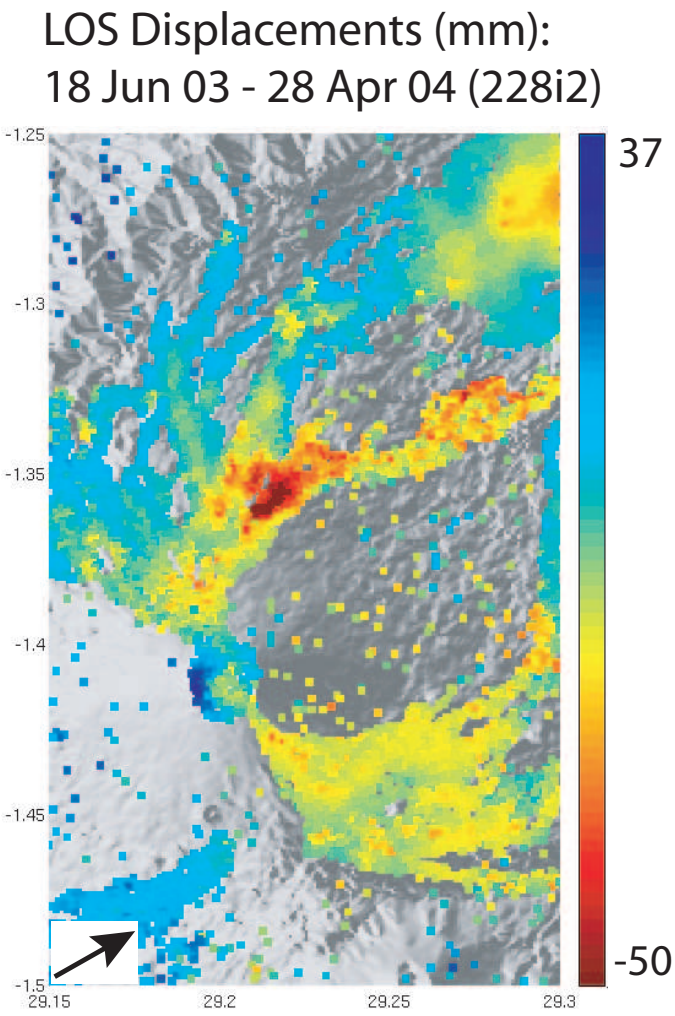

Figure 5.20: LOS Displacements in mm before the 2004 Nyamulagira eruption (18 Jun 03 - 28 Apr 04) for the ENVISAT 228i2 beam, ascending orbits, surimposed over the shaded DEM. The DEM and orbital ramps have been subtracted.

The 2004 syn-eruptive signal is visible on the 228i2 ascending beam (Figure 5.21) with a similar pattern as what was observed on the interferogram (Figure 4.29). The spatial coverage is better here but the information could be unreliable as 1) large phase gradients and noisy pixels could create unwrapping errors in the signal with a merging of 200 meters for the unwrapping as it was used here, and 2) there was a lava flow which emplaced in the caldera during the eruption as explained in Section 4.2.3.

The pattern of the LOS displacements between the 2004 and 2006 eruptions for the two i2 beams, ascending and descending, are given in Figure 5.22. The compaction of the 2004 lava flow on the NW flank and for other lava flows is clearly visible of course, reaching about 6 cm in 840 days, i.e. about 26 mm per year. A same intensity range increase is identified SE of the caldera and could also be due to lava flow compaction from 2002 as already noticed before the 2004 eruption, and, especially of the new 2004 lava flow emplaced in the caldera.

Three beams captured the 2006 eruption as depicted in Figure 5.23. The 228i2 beam result is not presented here as there is no data between October 2006 and April 2008. The signal *A*, located east of the 2006 eruptive fissure (see Figure 4.33), is consistent with the fissure opening

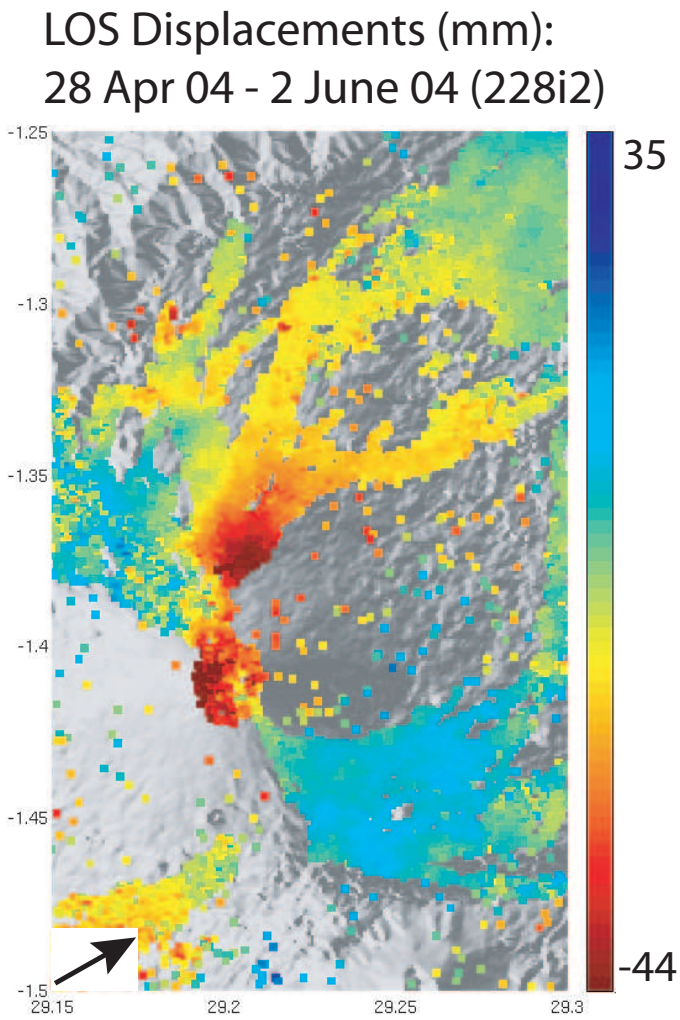

Figure 5.21: LOS Displacements in mm spanning the 2004 Nyamulagira eruption (28 Apr 04 - 2 Jun 04) for the ENVISAT 228i2 beam, ascending orbits, surimposed over the shaded DEM. The DEM and orbital ramps have been subtracted.

signal due to a dike as its sense is changing in ascending and descending modes. The signal B seems to have a different origin as it shows a similar sense of deformation (range decrease) in all modes. This could be due to an inflating sill-like reservoir as postulated by *Cayol et al. (in prep)*. The pixels in the patch C are unreliable as they are located on the 2006 lava flow (see Figure 4.33). Some pixels on the western flank of the volcano in the 35i2 beam could give new insights about the deformation pattern as the western flank is decorrelated in the conventional interferograms spanning the event, however, large phase gradients are expected there and unwrapping errors can therefore affect these pixels.

Three beams cover the period between the 2006 and 2010 Nyamulagira last eruptions (Figure 5.24). The compaction of the 2006 lava flow is clearly visible in A, the lava subsides with an average rate of maximum about 3.5 mm/yr at the proximal vent and fissure location for the 35i2 beam.

The same pseudo-triangular pattern of subsidence SE of caldera, B, is visible in all modes, with a rate of about 2.5 for both i7 beams, and 3.5 mm/yr for 35i2 beam. The lava flow compaction rates differs from one beam to another, this can be explained by a more vertical incidence angle

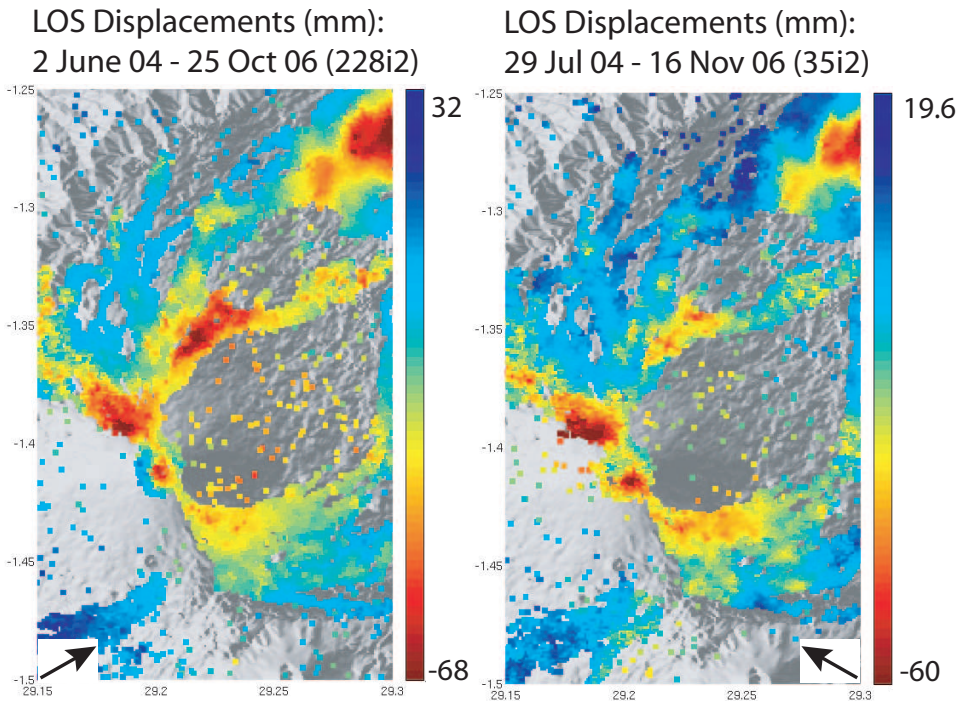

Figure 5.22: LOS Displacements in mm between the 2004 and 2006 Nyamulagira eruptions for A) the ENVISAT 228i2 beam (2 Jun 04 - 25 Oct 06), ascending orbits, and B) 35i2 beam (29 July 04 - 16 Nov 06), descending orbits, surimposed over the shaded DEM. The DEM and orbital ramps have been subtracted.

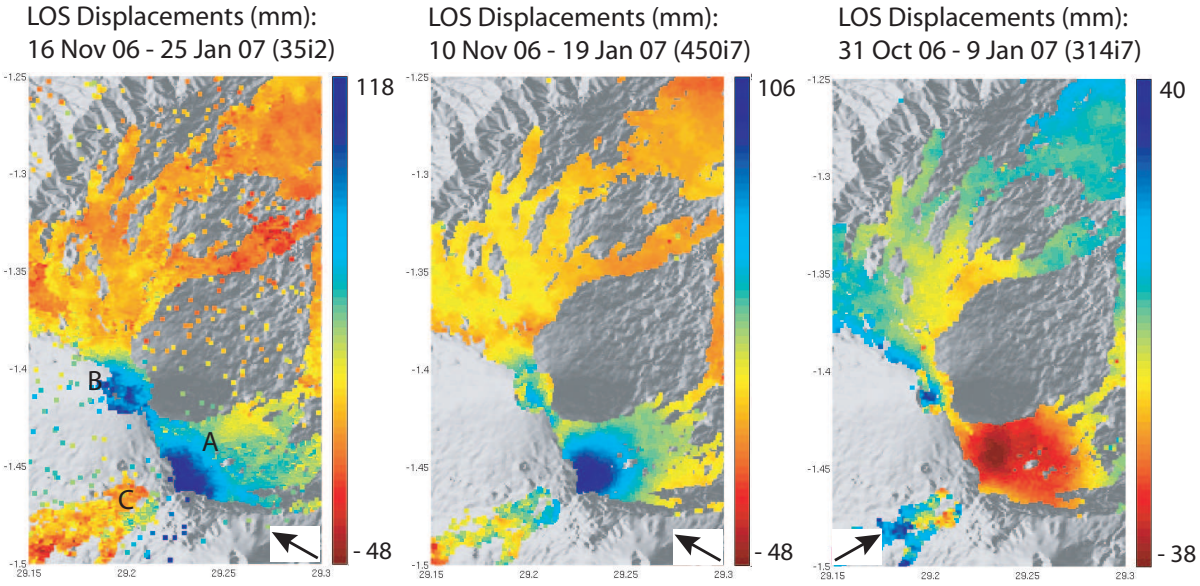

Figure 5.23: LOS Displacements in mm for the 2006 Nyamulagira eruption for A) 35i2 beam (16 Nov 06 - 25 Jan 07), descending orbits, B) 450i7 beam (10 Nov 06 - 19 Jan 07), descending orbits, and C) 314i7 beam (31 Oct 06 - 9 Jan 07), ascending orbits, surimposed over the shaded DEM. The DEM and orbital ramps have been subtracted.

of the 35i2 mode ($\approx 18°$ versus $\approx 38°$), mode thus more sensitive to the vertical component of ground displacement which dominates in the case of lava flow subsidence. The time-series plot for the area B are given in Figure 5.25. They all show an almost linear range increase, with the maximum in the 35i2 plot. However, several fluctuations are also visible, the first one, marked by

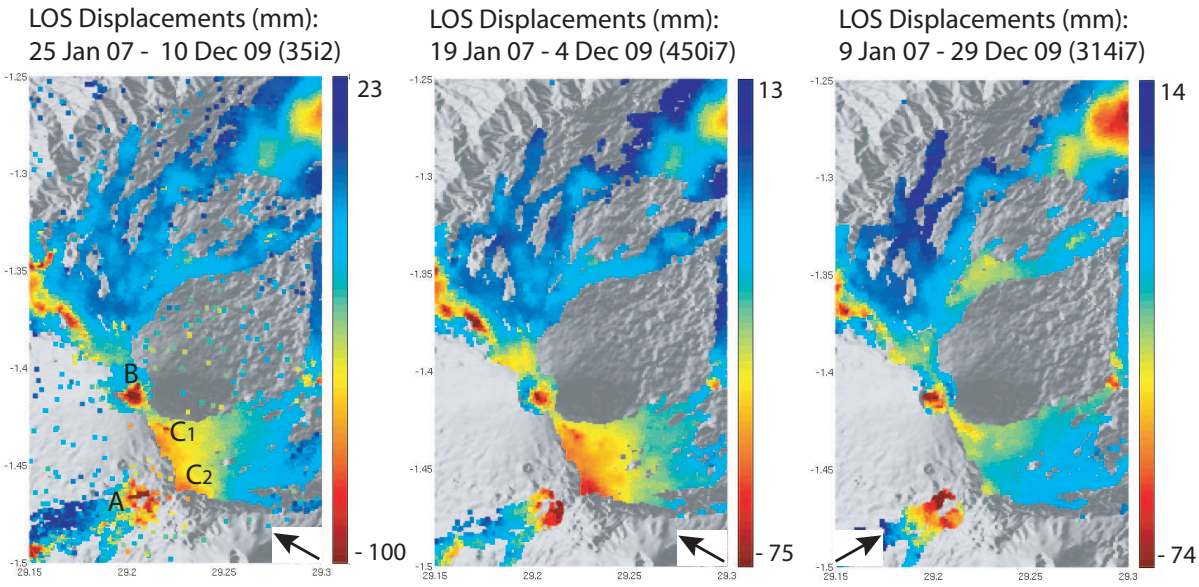

Figure 5.24: LOS Displacements in mm between the 2006 and 2010 Nyamulagira last eruptions for A) 35i2 beam (25 Jan 07 - 10 Dec 09), descending orbits, B) 450i7 beam (19 Jan 07 - 4 Dec 09), descending orbits, and C) 314i7 beam (9 Jan 07 - 29 Dec 09), ascending orbits, surimposed over the shaded DEM. The DEM and orbital ramps have been subtracted.

the green vertical line, could indicate a range decrease behavior of about 20 to 30 mm consecutive to the 2006 eruption, maybe indicating new input of magma in a shallow magmatic chamber. The 35i2 plot shows large oscillations around March-April 2008 (highlighted by the blue line), and some similarities can be found in the two other plots, even if the amplitude is less important. This period corresponds to a strong decrease in tremor activity *(Benoît Smets, pers. comm., 2011)*, and interestingly, a stabilization in the Nyiragongo lake level *(Benoît Smets and N. d'Oreye, pers. comm., 2011)*. Finally, a last change in behavior to range decrease seems to occur a few months before the 2010 eruption, as indicated by the red line. This behavior could be the sign of magma rising to shallower levels and can actually be observed for all pixels in the whole caldera, for instance in the NW part of it (Figure 5.8). Other beams show also this behavior but it is hard to be sure of this precursor signal as we have only an image every 35 days, and that the amplitude of this range decrease is in the method accuracy order.

The SE Nyamulagira flank also presents a very particular deformation pattern. Both descending modes show indeed a range increase behavior, which seems to be centered in C_1 and C_2, located on the weakness fissures network linking both volcanoes, and where the 2006 and 2010 eruptive fissures and vents opened. The time-series plots, given in Figure 5.26, show a global linear range increase for all modes for this period. The cumulated range increase is about 70 mm for the two descending beams, while it is only of about 30 mm for the ascending beam. This could indicate that the movements has not only a pure vertical component, but has also an oblique component of displacement which descending beams are more sensitive with. Deflating magma reservoirs beneath the SE flank and promoting the on-going graben subsidence identified in Figure 1.13 could also be involved but further modeling needs to be done to confirm this hypothesis.

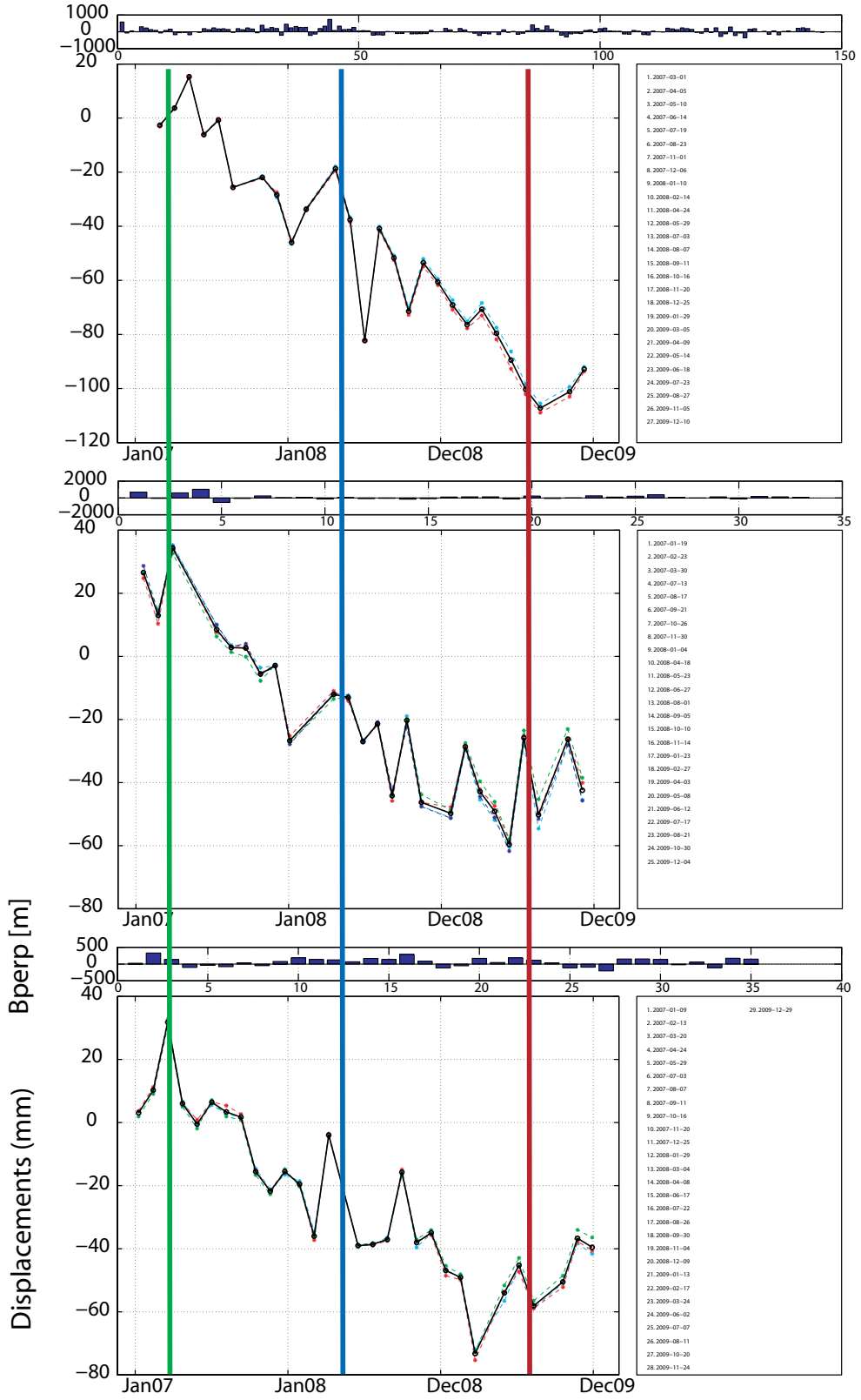

Figure 5.25: Time-series plot for an area close to the point B in Figure 5.24. Up: 35i2, descending, with the time reference 2007/01/25. Middle: 450i7, descending, with the time reference 2008/02/08. Low: 314i7, ascending, with the time reference 2008/05/13.

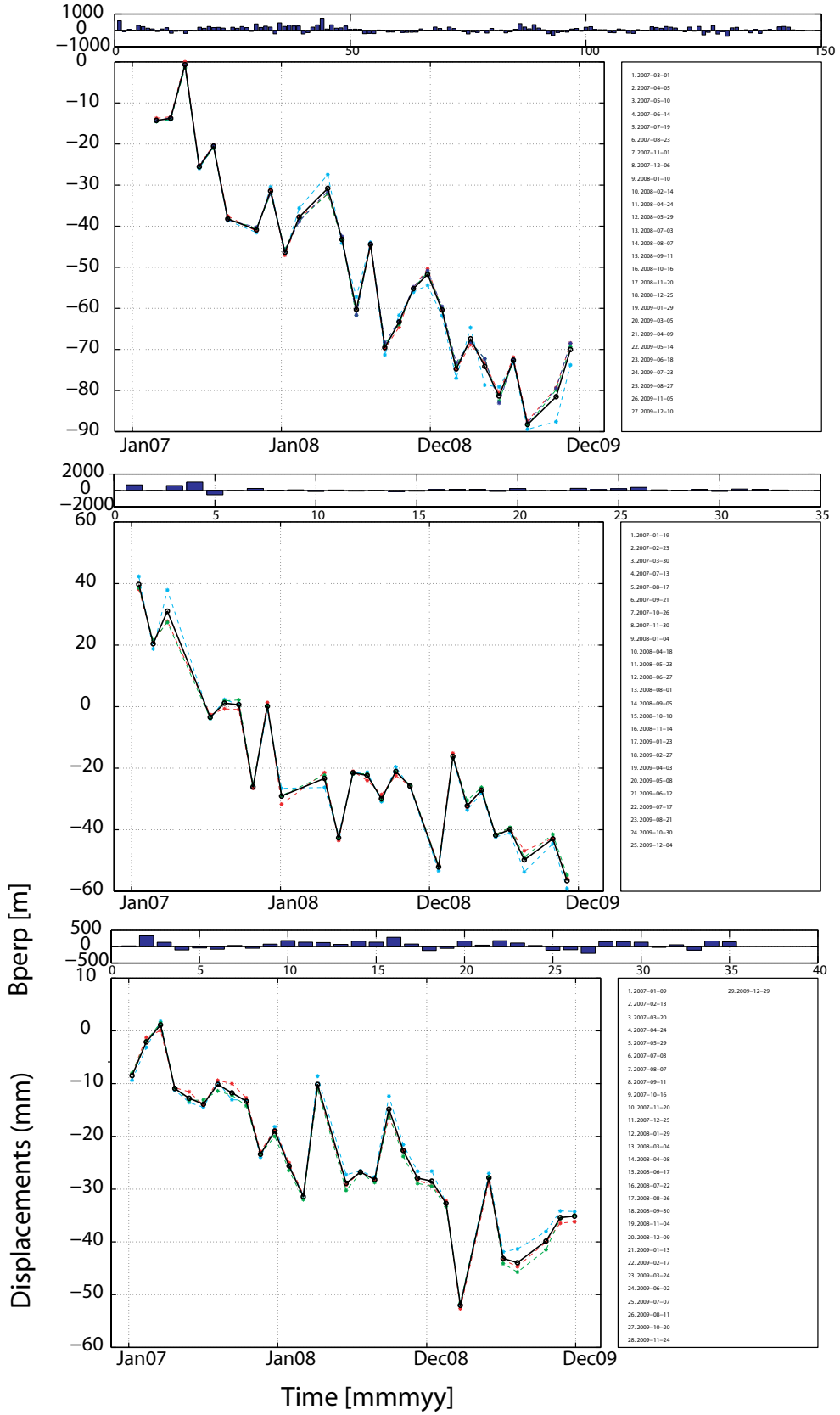

Figure 5.26: Time-series plot for an area close to the point C_2 in Figure 5.24. Up: 35i2, descending, with the time reference 20070125. Middle: 450i7, descending, with the time reference 20080208. Low: 314i7, ascending, with the time reference 20080513.

The 2010 syn-eruptive signal is of course clearly visible in all beams (Figure 5.27). Ground displacements of the reliable pixels located on the volcano flanks could bring extra information than conventional InSAR (Section 4.2.2). Only the ALOS interferogram shows indeed good coherence on the volcano flanks. It could be worth to also invert the ENVISAT StaMPS displacements to try to better constrain the model as there were some residuals on the southeastern flank of the volcano visible with ALOS (Figure 4.20, row 1, column 3).

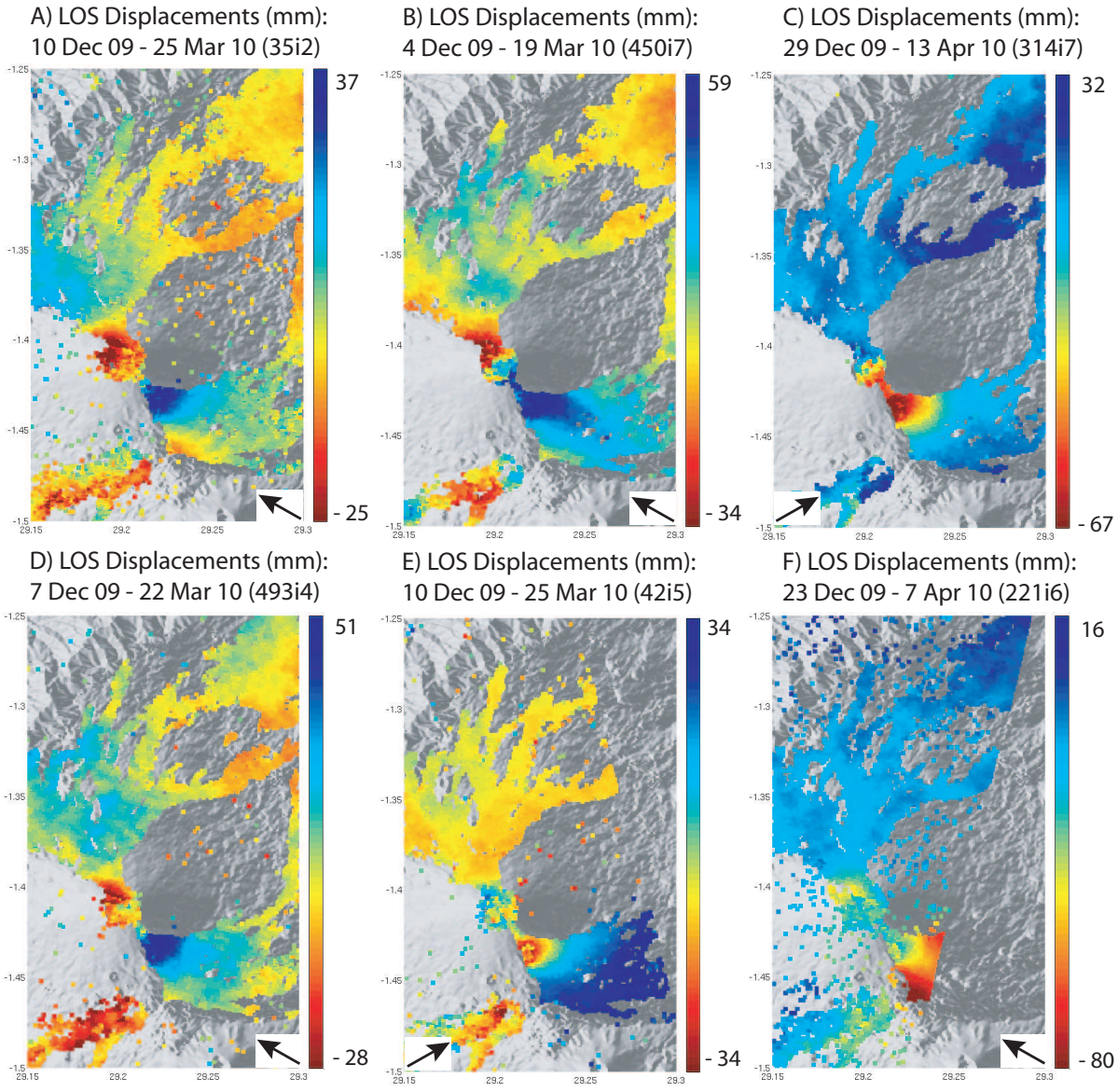

Figure 5.27: LOS Displacements in mm for the 2010 Nyamulagira eruption for A) 35i2 beam (10 Dec 09 - 25 Mar 10), descending orbits, B) 450i7 beam (4 Dec 09 - 19 Mar 10), descending orbits, C) 314i7 beam (29 Dec 09 - 13 Apr 10), ascending orbits, D) 493i4 beam (7 Dec 09 - 22 Mar 10), descending orbits, E) 42i5 beam (10 Dec 09 - 25 Mar 10), ascending orbits, and F)221i6 beam (23 Dec 09 - 7 Apr 10), descending orbits, surimposed over the shaded DEM. The DEM and orbital ramps have been subtracted.

5.3 ERS-2 Results

The inspection of the ERS-2 wrapped interferograms shows that some of them are affected by orbital trend, thus we will interpret the MLV minus DEM error and orbital ramps. The SBAS results shows a quite small density of selected pixels, the SBAS network is indeed not very favorable as the images frequency is generally very low, and the perpendicular baselines are high (Figure 5.29). The PS and thus the combined - PS + SBAS (Figure 5.28A) - approaches lead to more pixels selected, but some of these pixels, especially in the far field, outside the rift are probably not all reliable and should be interpreted carefully. Due to the unfavorable images frequency and large baseline, we therefore think that the accuracy of the results is likely less good than for the ENVISAT time-series results. For instance, when looking at the lava flows pile NE of Nyamulagira (*a*: location in Figure 5.28A, and time-series plot in Figure 5.30), the time-series plot shows an overall range increase pattern, but also some range decrease peaks, about maximum 22 mm, for instance in May 2000 or in July 2002, which are quite unlikely as no particular seismic or volcanic events occurred at that periods. These unlikely peaks of range decrease were smaller, reaching a maximum of about 10 mm, for the ENVISAT results (Figure 5.6).

The large extent major deformation signals related to the Nyiragongo 2002 eruption are obviously visible and dominate the southern part of the area, showing opposite sense of movement west and east of the 2002 eruptive fissure (see the arrows in Figure 5.28A and B). The deformation might also extend further W and SW to the Mbuzi peninsula (see *c*) and likely extends further E and SE in Rwanda (*d*). The latter observation was identified on the RADARSAT-1 interferograms spanning the event but not on the event most coherent ERS-2 interferogram (Figure 4.2). Note that the pixels on the Nyiragongo flanks, close to the 2002 eruptive fissure, are expecting to be affected by strong deformation gradients, as about 3 meters of fissure opening was modeled for the shallow dike in Section 4.1. Therefore, unwrapping errors due to fringes aliasing can likely affect these pixels which are likely unreliable, and this observation can explained the discrepancy between the previously unwrapped ERS-2 interferogram (Figure 4.3) and the converted cumulated LOS displacements given in Figure 5.28.

Other clear deforming areas can be identified on this dataset for of course the flow compactions (*b*). Some deformation are identified also on the Nyamulagira volcano, in the caldera and on upper flanks, linked to the 1998, 2000, 2001 and 2002 eruptions (Figure 5.31A, B, C and D, respectively). The 1998 eruption generates hence about 63 mm of range increase N and NW of the caldera. This observation was only very partially visible with the classical InSAR and only on a RADARSAT-1 interferogram (Figure 4.24). A range increase is also observed on some pixels S of the caldera, and a range decrease of about 20 mm could be visible just SE of it. During the 2000 eruption, the conventional InSAR reveals only one fringe of range increase centered on the pit crater (Figure 4.25) again on a RADARSAT interferogram. The StaMPS results also show range increase of maximum 108 mm N and NW of the rim itself. The 2001 eruption was completely missed by conventional InSAR, however, we do see some deformation corresponding to range decreases, of about maximum 60 mm, in the Nyamulagira caldera, and also on the NW, S and SE flanks of the volcano. The N flank seems to be affected by a range increase of about 60 mm. The 2002 Nyamulagira eruption was captured partially by the conventional InSAR (Figure 4.26), however, the best ERS-2 classic interferogram only gave useful coherent information on the deformation pattern about 3 km NW of the caldera rim. In the StaMPS results, we also do see that the

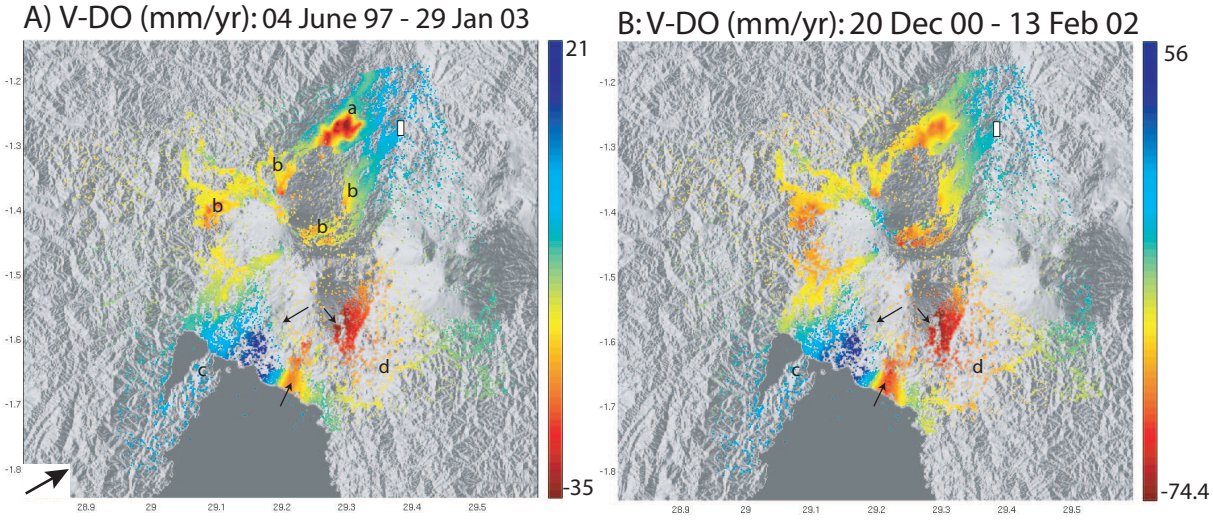

Figure 5.28: Mean LOS velocity (MLV), minus DEM error and orbital ramps, in mm/yr obtained with the combined (PS + SBAS) approach for the ERS-2, ascending orbits, surimposed over the shaded DEM. 19,148 pixels (200 m) are selected. Positive velocities means displacement away from the satellite. The reference master is 2000/09/06 and the baseline plot for the SBAS approach is given in Figure 5.29. The reference area is indicated by the white rectangle. Time span: A) all period: 1997/06/04 - 2003/01/29, and B) spanning the 2002 Nyiragongo eruption (and the 2001 Nyamulagira eruption): 2000/12/20 - 2002/02/13. The velocity can be converted in LOS cumulated displacements for this period (420 days) and ranges from -86 to 64 mm.

deformation pattern corresponding to a range decrease, of maximum 45 mm, extends actually inside the caldera rim, and is not limited to its NW flank, as it was actually observed when looking at the RADARSAT-1 interferograms covering the event.

The StaMPS results on the ERS-2 dataset do not agree with the observation made by Manoochehr Shirzaei and Thomas Walter *(pers. comm., 2010)* using a WABInSAR time-series approach [*Shirzaei and Walter*, in press], indicating that two areas of post-rifting deformation were visible W and N of the Nyamulagira volcano, close to the western border fault escarpment.

Even if the ERS-2 StaMPS results are not very accurate, they show some deformations in the Nyamulagira caldera and on its upper flanks, associated to its eruptions and likely magma intrusions. With the exception of the 2002 event, the conventional InSAR using ERS-2 data completely missed these deformations.

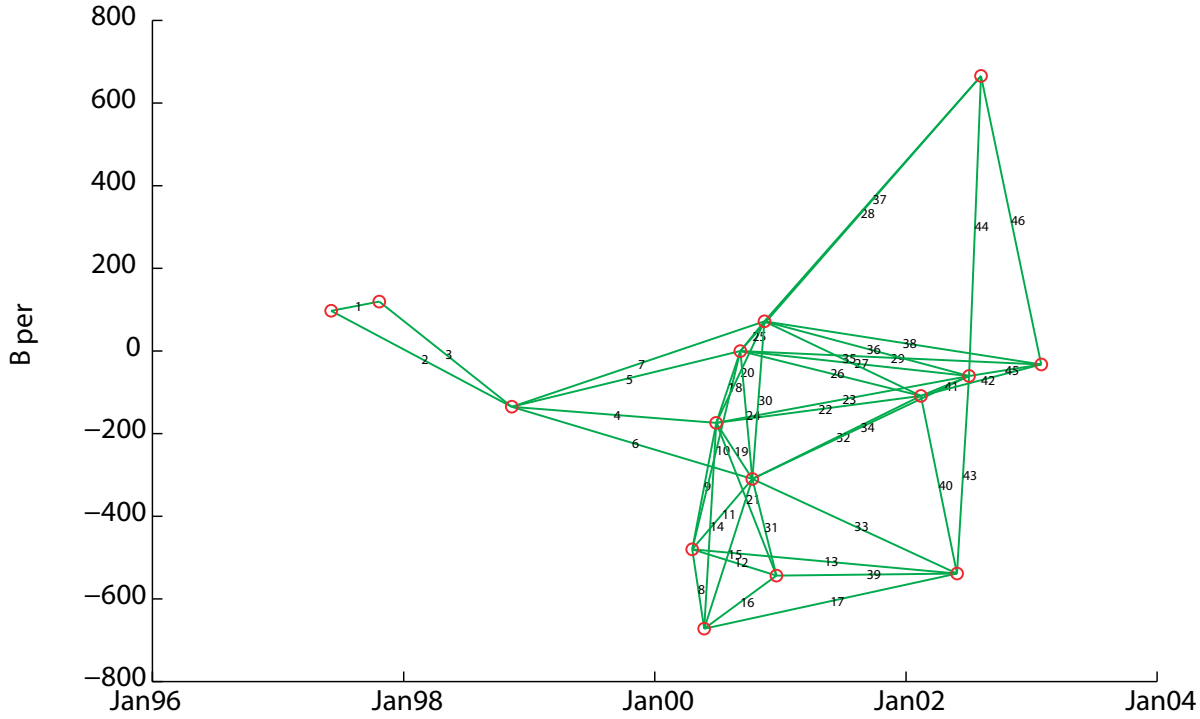

Figure 5.29: SBAS baseline plot for the ERS-2, ascending orbits. A total of 15 SAR images and 46 SBAS inteferograms have been used.

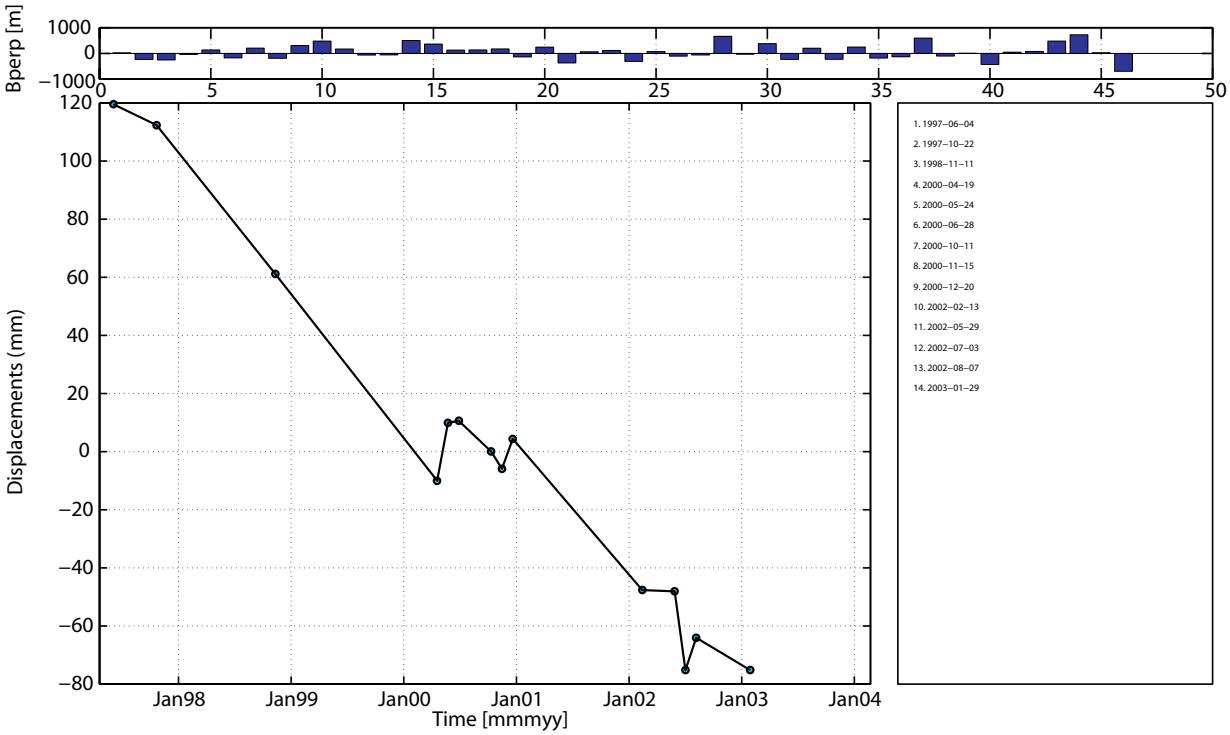

Figure 5.30: Time-series plot for the point a in Figure 5.28. The time reference (zero displacement) is 2000/09/06.

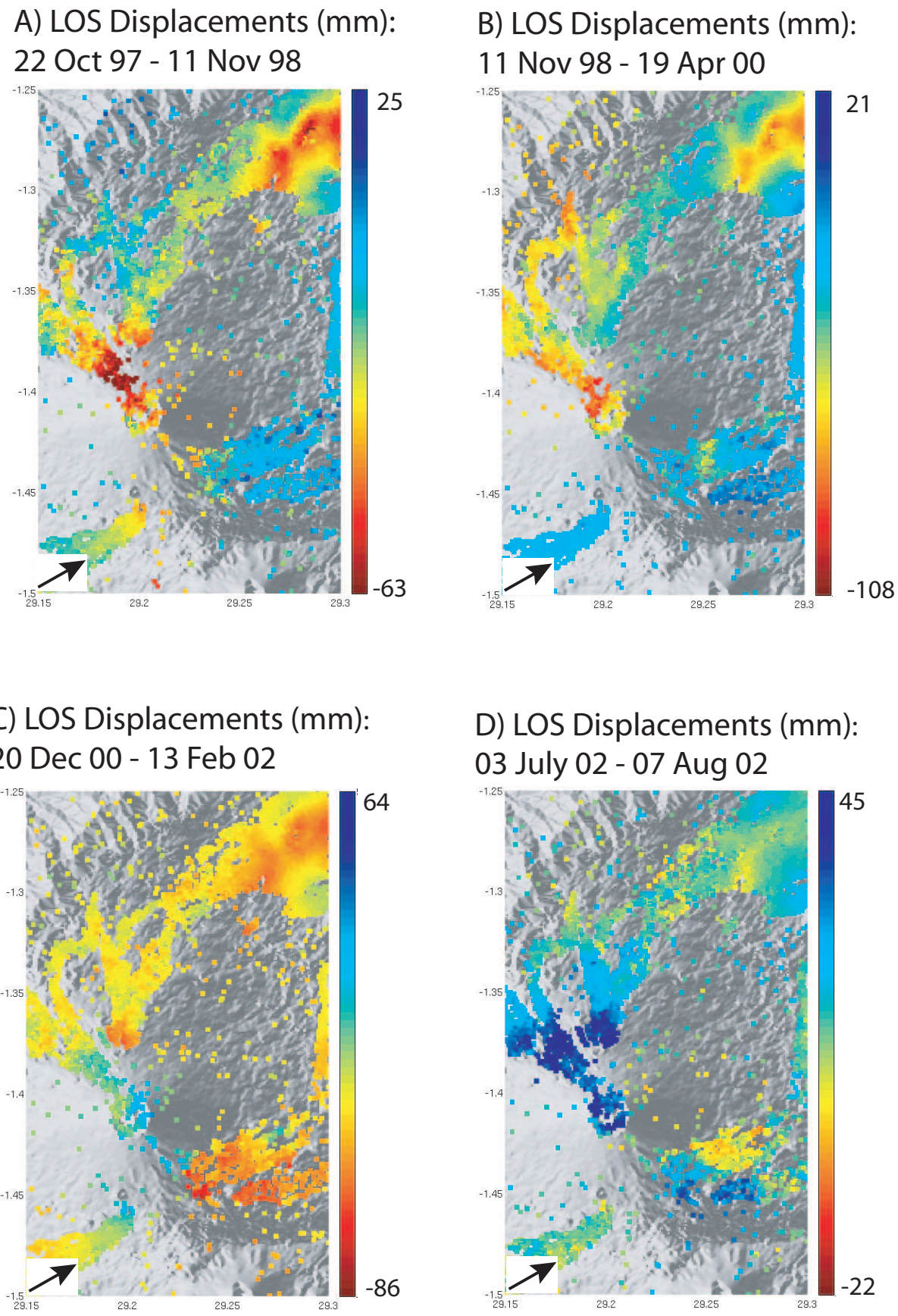

Figure 5.31: LOS Displacements in mm for a period covering A) the 1998 Nyamulagira eruption, B) the 2000 Nyamulagira eruption, A) the 2001 Nyamulagira eruption, A) the 2002 Nyamulagira eruption. Positive value means range decrease (i.e displacement towards the satellite).

Chapter 6

How do the Field Measurements help to constrain the InSAR Modeling of the Natron Crisis

The 2007 July-August Natron sismo-magmatic crisis is a nice case-study to show the importance of InSAR to constrain field investigations, and the major input and insights obtained from the field to better constrain the numerical modeling of the InSAR data. The information gathered during the field mission and subsequent interpretations have allowed an accurate modeling of the available InSAR data which leads to several important publications, including one in Nature [*Calais et al.*, 2008].

6.1 The Natron Crisis

More than 30 km of surface fractures opened on the southern and eastern flanks of the Gelai volcano in the Natron area (Figure 1.5 in Chapter 1) during a seismic swarm, which began on July, 12, culminates with the strongest shock on July, 17, 2007, with a body-wave magnitude (M_w) of 5.9, and lasted up to the September, 8. This seismo-magmatic crisis promoted a diking event, the first ever captured geodetically in a youthful continental rift [*Calais et al.*, 2008].

Soon after the main event of July, 17, two Tanzanian researchers, R. Ferdinand (a seismologist) and E. Sariah (a geophysician) visited the site and reported the presence of important surface fissures on the ground, but without mapping them in detail. They also re-measured the Engaresero GPS site (location showed in Figure 2 of [*Calais et al.*, 2008] given in Annexe 2) and installed seismic stations at Engaresero and Gelai villages.

In the framework of the SAMAAV project (Belgian Science Policy - Belspo - and Luxembourg FNR Action-1 project and ESA Cat-1 project n° 3224), several SAR images (from the ENVISAT satellite, descending orbits) were acquired and processed. We obtained thus interferograms showing the opening of two main fractures systems delimiting a NNE-trending graben on the Gelai southern flank (Figure 6.1). Some fissures were also detected on the eastern flank of the volcano. Preliminary modeling realized with the 3D-MBEM method in September 2007 in Luxembourg, suggested that the structure observed on the interferograms could be best interpreted in a se-

quence of deformation involving the emplacement of a subvertical dike at depth under the graben structure.

In October 2007, the Royal Museum for Central Africa sent a team of scientists (Dr. Damien Delvaux, Benoît Smets and Ir. Christelle Wauthier) to collect field data before the next rain season. The main objective were: 1) to map the surface fissures related to the seismo-magmatic crisis, 2) to constrain the advanced modeling studies thanks to these field data, and thus to better understand and interpret the event, (3) to record the volcanic activity of the Oldoinyo Lengai volcano, and (4) to re-measure the Engaruka GPS site and to install and measure additional GPS points across the graben structure. Two Tanzanian scientists joined and helped the RMCA team during this mission: Athanas S. Macheyeki and Elifuraha Saria.

The results of this mission summarized here were mainly compiled from two scientific mission reports, [*Smets and Wauthier*, 2007] and [*Delvaux et al.*, 2007]. These results were furthermore presented in several conferences (among others, [*d'Oreye et al.*, 2008], [*Oyen et al.*, 2008], [*Delvaux et al.*, 2009], [*Wauthier et al.*, 2009]) and strongly help to constrain the advanced modeling studies ([*Calais et al.*, 2008], [*Oyen*, 2009], and [*Oyen et al.*, 2010]).

6.2 Field Mission Results

6.2.1 Mapping of Observed Fissures

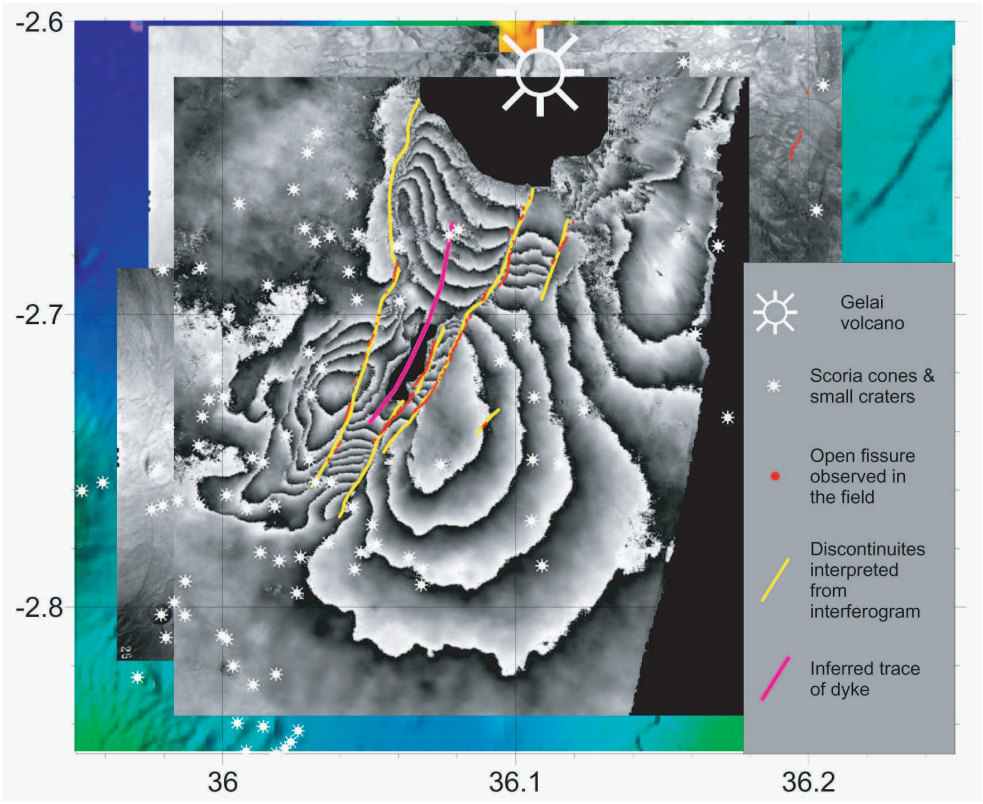

Figure 6.1: General overview of the mapped fractures (red lines and dots) surimposed on a descending ENVISAT interferogram spanning the crisis. After [*Delvaux et al.*, 2009]

Figure 6.1 shows the GPS points where surface fractures have been observed. On the field,

the fractures often appear as a series of relatively small segments, arranged in an en-echelon way, with both left- and right overstepping. Only one fracture system was mapped on the western side of the structure, while five different fracture systems were found on the eastern side (E1-5). They were further subdivided into segments according to their field characteristics: segments W-1, W-2, W-3 for the western fracture system, and segments E1-1, E1-2, E1-3, E2-1, E2-2, E2-3, E2-4, E3, E4 and E5 for the eastern fracture system (Figure 6.2). The western fracture system has not been mapped entirely doe to the lack of time and problematic field accessibility, but it is likely that it continues more to the north.

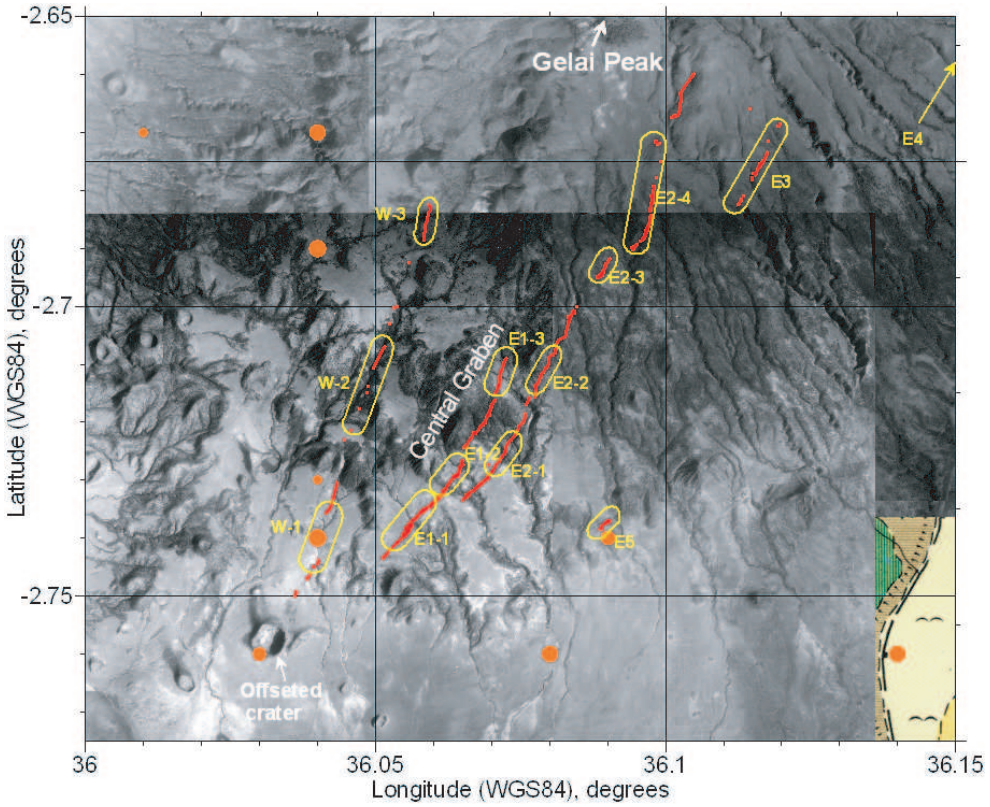

Figure 6.2: Mapped fractures (red lines and dots) surimposed on geo-referenced aerial photographies. The encircled data and labels in yellow correspond to the fault segments for which the average values of displacement are reported on table 1. Segment E4 located on the northeastern extremity of the mapped structure is outside the limits of the map (to the NE, see Figure 6.1). The expected Gelai seismo-magmatic graben is located between the western and the eastern fault systems. Geodetic coordinates in degrees, WGS84 datum, 0.05° corresponding to 4.5 km. After [*Delvaux et al.*, 2007].

The surface fractures observed are commonly subvertical at the surface. For one of them (along segment E1-2), we could measure a minimal vertical depth of 8.5 m using a measuring tape loaded with a stone. They appear in the field as open tension cracks of limited lateral extent, with a general en-echelon arrangement from a metric to a kilometric scale. They also often show a vertical offset. Both horizontal opening (dilation) and vertical offset are at the scale of a few centimetres to decimeters. The vertical downfaulting observed along the western fault system is on the eastern side of the fault, and along the eastern fault system, on the western side (with the exception of the segment E1-3). The ground portion comprised between the two fracture systems defines thus a subsiding graben (Figure 6.1 and 6.2).

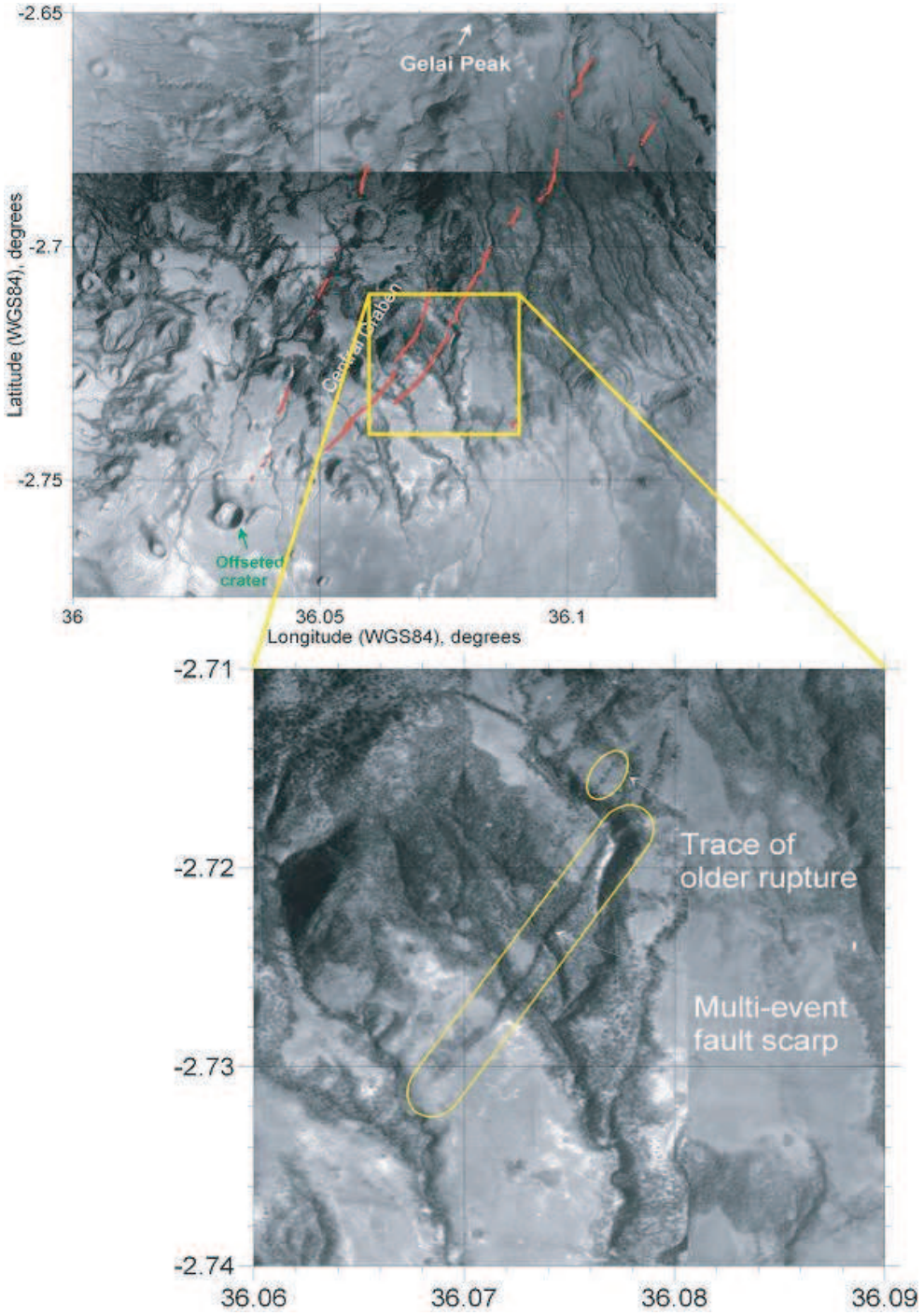

Figure 6.3: Detail of the relay between the two eastern faults delimiting the graben. According to field observations and photo-interpretation, the fractures E2 are found to correspond to a reactivation of older faults and ruptures. Geodetic coordinates are in degrees, WGS84 datum, 0.01° corresponding to 900 m. After [*Delvaux et al.*, 2007]

As depicted in Figure 6.1, the mapped surface fractures correspond very well with fringe discontinuities identified on the interferograms spanning the crisis. The fringe discontinuities, however, extend generally laterally further than the open fractures observed in the field. This apparent discrepancy could be explained by 1) an incomplete observation in the field as for the northern portion of the western fracture system which could not be mapped, and/or 2) isolated

or weakly expressed fractures were missed in the area mapped, and/or 4) subsurface deformation could occur without the opening of visible tension fracture at the surface; such a deformation can be accommodated with discrete and/or diffuse zone of extension.

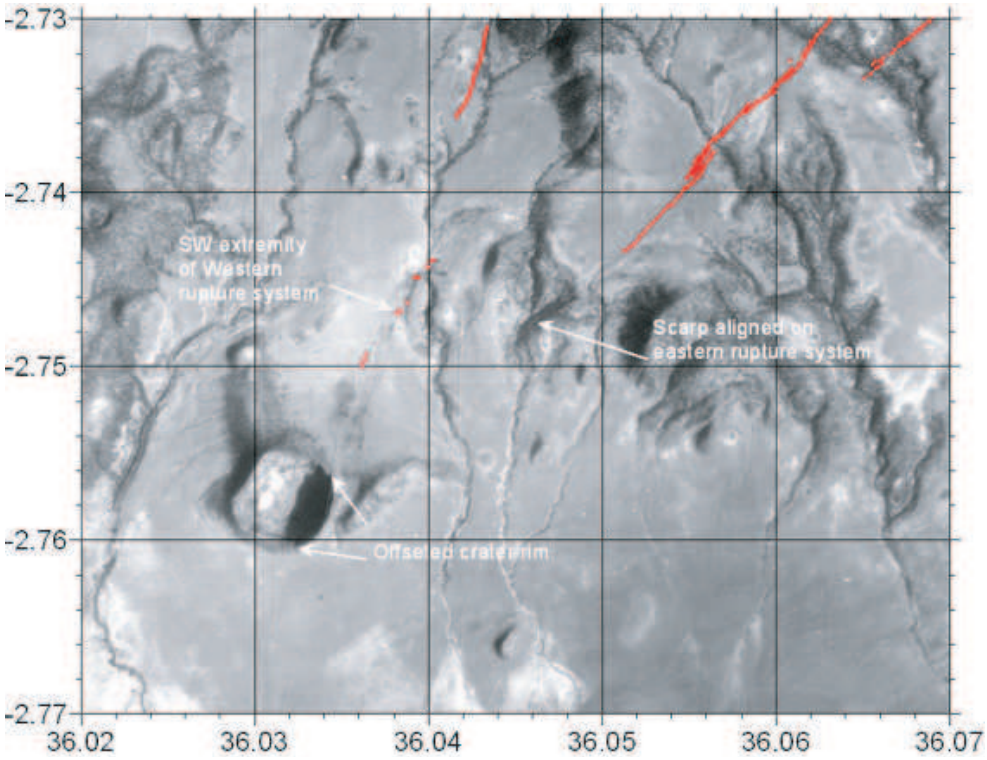

Figure 6.4: Detail of the southwestern closure of the fault graben enclosed between the western fault (center - north of the map) and the eastern fault system (SE corner of the map). The two fault systems apparently continue southwestwards further than the last surface fractures opened during the during the 2007 July-August event are observed. They seem to intersect at the location of a circular crater whose rim is offset by a recent fault at two locations. Geodetic coordinates in degrees, WGS84 datum: 0.01° corresponding to 900 m. After [*Delvaux et al.*, 2007]

The Figure 6.3 shows that the fault E2 is developed at foot of a multi-event morphological scarp and on older ruptures highlighted on the air photo by a line of darker vegetation. The 2007 surface ruptures follow those scarp and rupture.

The two fault systems progressively narrow the graben by converging in the southwestern direction. If the lines of the observed surface fractures are prolonged southwestwards, they would join in the middle of a morphologically fresh volcanic crater, composed of several layers of pyroclastic deposits (Figure 6.4) likely indicating a past explosive activity for that vent. Figure 6.5 shows that the rim of this crater is actually cut and shifted at two points by a fault which seems to form the southwards prolongation of the western fault system. A field check confirms that the fractures which affect the crater rim are subvertical, with down-to-the-east movement. However, no fresh fractures or proof of reactivation directly related to the July-August 2007 event could be identified undoubtedly.

A landslide can be observed on the Gelai summit, probably promoted by the intense seismicity (Figure 6.6). Several Masai's houses were cut and damaged by the opening of the fracture systems (Figure 6.7).

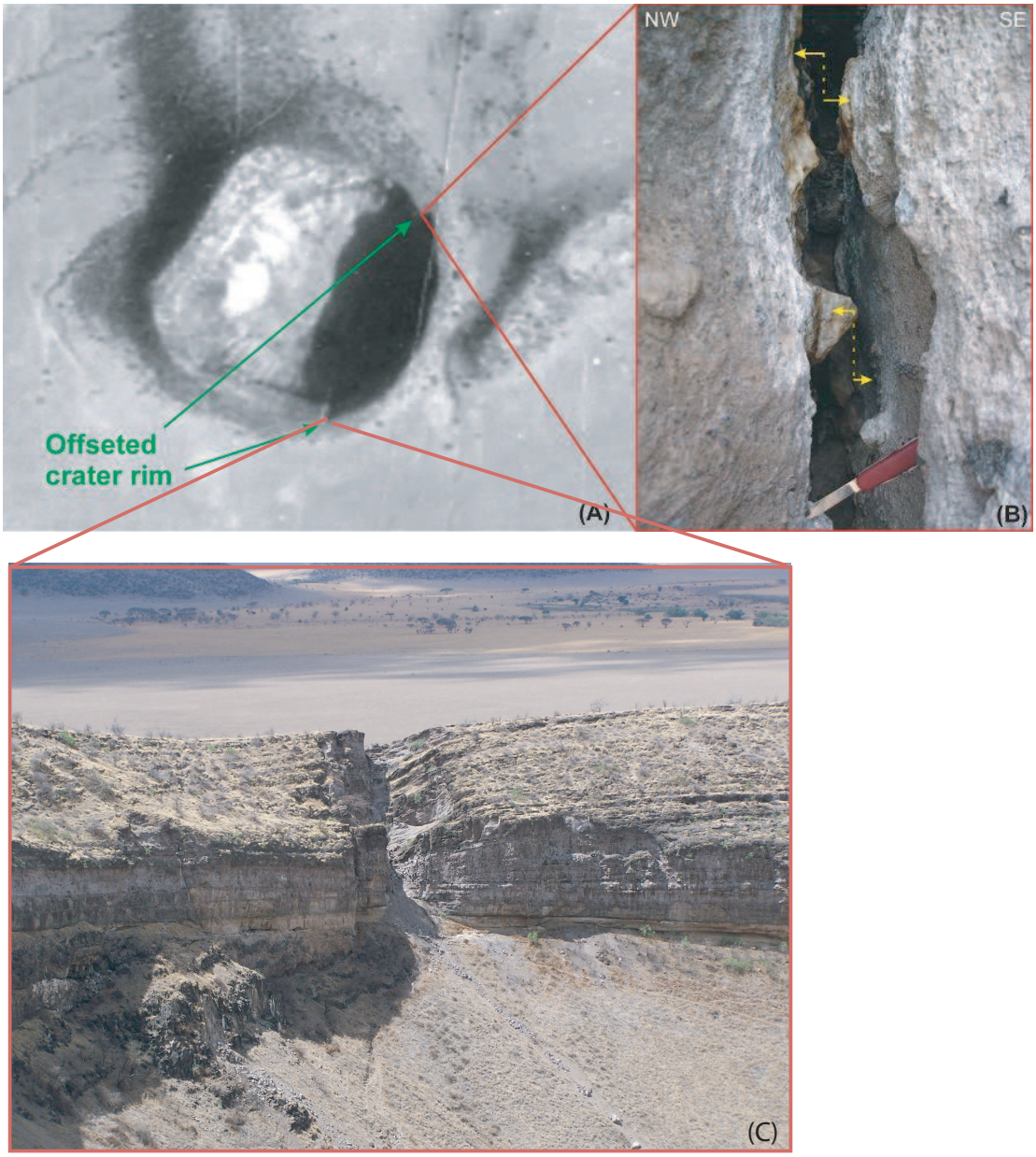

Figure 6.5: A) Zoom on Figure 6.4, corresponding to the crater whose rim is cut by a fault at two locations. B) Details of an older fissure in the the north-east displaced crater rim. The vertical offset is about 5 cm. C) Details of the older fissure in the south-east displaced crater rim. Modified after [*Delvaux et al.*, 2007]

Figure 6.6: Gelai summit viewed from south towards north. A landslide is visible on the Gelai's summit and the house cut by a crack is showed in Figure 6.7. Modified after [*Smets and Wauthier*, 2007]

Figure 6.7: Masai's house cut by a crack which opened during the July crisis. Modified after [*Smets and Wauthier*, 2007]

6.2.2 Displacement Profiles

Together with the mapping of the surface fractures, the measurement of both horizontal opening - or dilation (Δ_h) - and vertical offset (Δ_v) have been made, taking into account the possible collapse of fracture margin. To illustrate the variation of the dilation and vertical offset along the fault systems, displacement profiles were constructed to show the horizontal opening and vertical offset in function of the distance along the faults, using the southernmost observation point as origin (Figures 6.8 and 6.9).

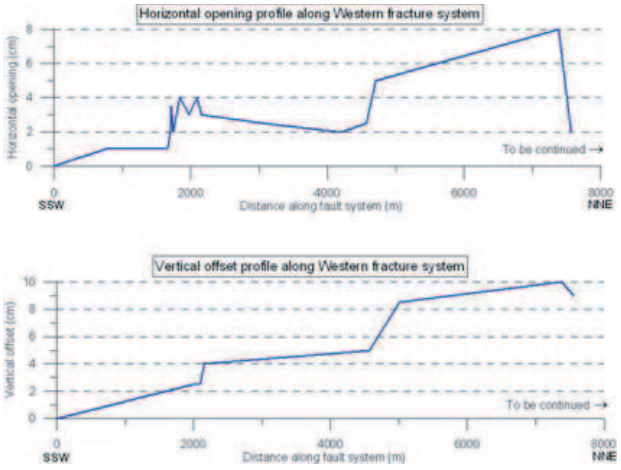

Figure 6.8: Displacement profiles for the western fracture system, showing the horizontal opening (Δ_h) and vertical offset (Δ_v) in function to the distance along the fault from the first fractured observed at the southerwestern side of the fault. Note that only the southern part of the western fracture system has been mapped. Vertical offset is down to the east. After [*Delvaux et al.*, 2007].

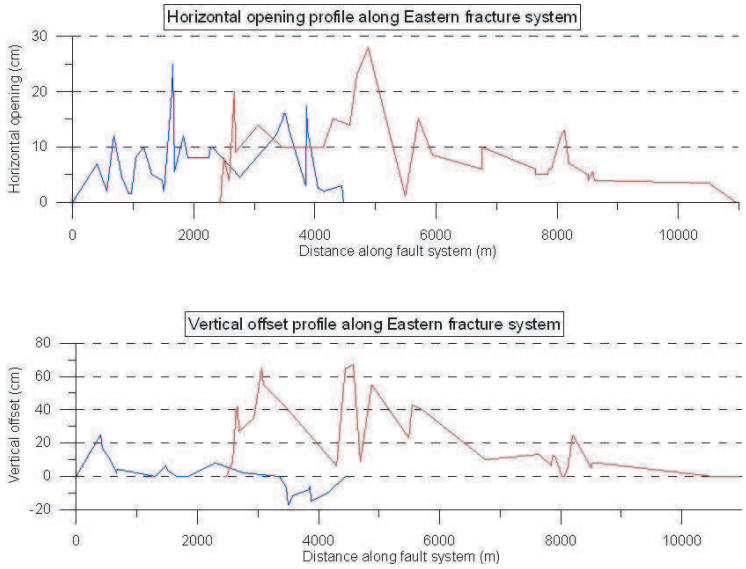

Figure 6.9: Displacement profiles for the eastern fracture system. Blue lines for the fracture E1 and red lines, for fracture E2. Vertical and horizontal scales as in Figure 6.8. Vertical offset is down to the west (positive values and down to the east (negative values). After [*Delvaux et al.*, 2007].

6.2.3 Average Displacement Parameters

As can be seen from the displacement profiles (6.8 and 6.9), the values for horizontal opening (Δ_h) and vertical offset (Δ_v) are rapidly fluctuating along the trend. This is probably due to the highly segmented and sometimes discontinuous nature of the fractures. Moreover, it was not always possible to measure these values due to local outcrop conditions. Therefore, instead the values were averaged for the different segments.

Most average values of Δ_h as Δ_v are within a centimeter scale, with the smallest values for the western segment. The largest values are seen for the E2 fault, especially along its southernmost segments E2-1 and E2-2. They show average of Δ_h respectively of 10.8±5.5 and 14.3±8.4 cm with maximum measured values of 20 and 28 cm. Their vertical Δ_v offset are respectively 31.5±22.3 cm and 41.3±22.6 cm, with maxima at 65 cm for both segments. The average values have in general high standard deviation, reflecting probably the segmented and discontinuous character of the fractures.

For all the fractures observed, no significant lateral displacement could be measured.

6.2.4 Open fracture - Normal fault relationship

The frequently observed combination of horizontal opening and vertical offset associated to the subvertical fractures observed at the surface can be explained using the typical geometry of fracture systems that has been evidenced in northern Iceland by *Angelier et al.* [1997].

They established a geometrical and genetic relation between subvertical tension fractures at the surface and shear faults with dips between 60 and 75° at depths (Figure 6.10). In the absence of strike-slip movements, which seems the case also here, they evidenced an approximately linear relationship between Δ_h and Δ_v for a large number of surface fractures measured. Based on this relation and combining structural observations at different structural level, they propose a model in which the open subvertical fractures near the surface change abruptly into normal faults dipping 60-72° at moderate depth. Therefore, combining the Δ_h and Δ_v values of a fracture observed at subsurface, one can obtain the dip-angle of the underlying fault and the associated net slip. In the present case, the dip angle and net slips were computed on the average values of Δ_h and Δ_v for each segments when possible.

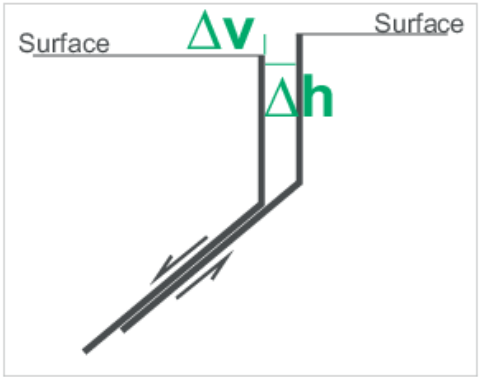

Figure 6.10: Fault geometry. Modified after [*Angelier et al.*, 1997].

It is interesting to note that the values obtained generally fall between 60 and 72°, in accor-

dance with *Angelier et al.* [1997] observations. The rather low angle obtained for the segment E2 (22.5°) is not considered to be significant as it forms the transition between the west-dipping E1-1 segment and the east-dipping E1-3 segment.

The nature of the transition between the vertical surface fissures and the normal faults at depth is still being discussed. Using structural observations combining surface fractures and shear faults at deeper structural level, *Angelier et al.* [1997] conclude that an abrupt change from the open vertical fissures near the surface to normal faults at moderate depth is more likely. They also found that the most frequent dip angle of these normal faults are between 60 and 72°, similarly as what we obtained in this study. Although they could not investigate directly the depth of the transition between the vertical fissures and normal faults, the same authors observe that the extensional deformation at depths of 1-2 km is dominantly accommodated by normal faulting. They also suggest that at mid crustal depth (2-5 km), the effective tension plays an important role, promoted by magma injection.

6.2.5 Listric versus planar fault at depth and Reactivations

A DGPS profile was realized across segment 1 of the eastern fracture system E2, where the July 2007 fissures appear at the base of the existing morphological scarp visible on Figure 6.4. A detail of that profile is depicted in Figure 6.11 (segment location in Figure 6.2). The red and blue lines represent the fits to the planar portions of the topographic surface which have been displaced by repeated faulting. Unfortunately the topographic profile was not measured far enough to the SE (to the right on the figure). Despite of this, the slope difference between these two surfaces is less than 1 ° (0.86°). Should the profile be continued more to the right, probably a close parallelism would be obtained. This suggests that no component of block rotation is involved in the long-term faulting and that the fault profile at depth should be straight and not listric as would be the case if block rotation occurred. In absence of block rotation, the vertical separation between these two surfaces represents the cumulated vertical offset associated with repeated faulting along the scarp since the constitution of the reference planar topographic surface.

In conclusion, the analysis of this AA' DGPS profile shows that the normal fault at depth, under the transition with the vertical fracture, should be planar. It also indicates that the 2007 event is just the last of a series of similar events that occurred earlier in the same area.

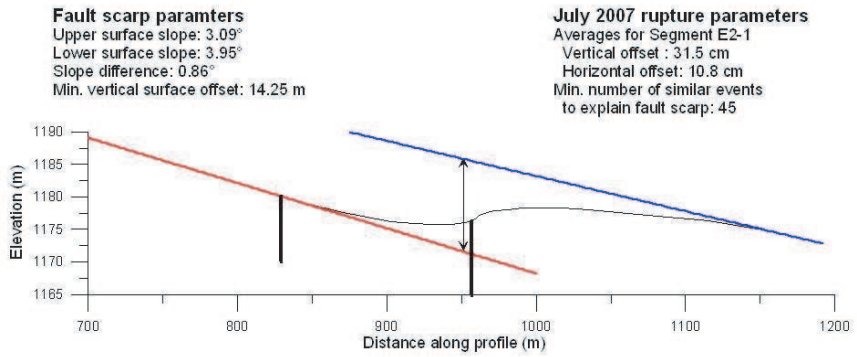

Figure 6.11: Detail of the DGPS topographic profile realized across the segment E2-1 (location on Figure 6.2) showing location of the 2007 surface fissures in relation to the long-term morphological fault scarp (the main fracture on the right side). After [*Delvaux et al.*, 2007].

6.2.6 Constrain on the Top Dike Geometry

In the previous paragraph, it is suggested that the observed subvertical fractures with both horizontal dilation and vertical offset are likely to reflect normal faulting along 60 to 72° dipping normal faults at depth. Furthermore, these fractures are aligned along two systems that show opposed sense of displacement delimiting a graben. We can calculate the point at which the faults intersect by extrapolating the continuation of these underlying faults at depth. It has been shown above that it is suspected that the July-August moderate-magnitude earthquake swam crisis might correspond to a seismo-volcanic event during which a dike emplaced at depth under the southern flank of the Gelai volcano. An intrusion of dike is furthermore typically marked at the surface by a subsiding graben [*Rubin and Pollard*, 1988] [*Rubin*, 1992].

According to this model, the graben between the two convergent fault systems should be underlained by a thin subvertical dike injection. The top of such a dike should correspond approximately to the intersection of the lines extending the two normal faults (even if physically the faults do not join the top of dike). Hence, a differential GPS topographic profile was measured in the field, orthogonal to the direction of the central graben and intersecting fault segments W1 (49°E) and E1-1 (61°W). The calculation of the X and Y coordinates of the top of dike and its elevation Z is illustrated in Figure 6.12.

The coordinates of the normal fault intersection, assumed to be close to the top of dike along selected topographic sections is calculated using a model where the vertical open fractures observed at surface change sharply into shear faults whose inclination is given by the ratio between the vertical offset and the horizontal opening of the surface fractures. For this calculation, the height of the vertical surface fractures is assumed to be 50 meters for all fractures. Measurement on one point along fracture E1-2 gives a minimum value of 8.5 m for the vertical fractures. Field data alone cannot constrain this parameter. Two assumptions can be made here. First, it can be assumed that the height of the vertical fractures is everywhere the same, as was done in this work. Secondly, the value imposed for that height should be at least 8.5 m but cannot be further constrained. Therefore, this should be either studied in the field by geophysical means, or considered as an unknown parameter that has to be estimated by modeling.

In order to map the top end of the dike under the central graben, a series of 6 topographic sections were extracted from the SRTM DEM at a right angle of the graben axis (Figure 6.13). In plane view, the top of dike displays a curved geometry, aligned between the summits of the Gelai and the Kerimasi volcanoes (Figure 6.1 and 6.13). Our data do not allow assessing the dip of the dike. For profile 5, the dip angle of the underlying normal fault along the western side of the graben is constrained by only 2 values of Δ_h and Δ_v for the segment E2-3. This is not considered to be significant. Therefore, three different calculations were made, with dip values of 65, 68 and 70°, intermediate between the dip of 71° calculated for segment E2-2 (11 data) and of 62° obtained for segment E2-4 (18 data). From dip values of 65 to 70°, the calculated top of dike is progressively deeper, but also at a greater distance from the origin of the section, further to the SE.

The dike top geometry forms thus a slightly but regularly curved line on plane view when using the first solution for Profile 5 (with the western normal fault dipping 65° to the east). This solution is also giving the shallowest depth for the top of dike (-2067 m a.s.l.), higher than the average level found along profiles 1 to 3 (-2480 to -2580 m). The last solution for Profile 5

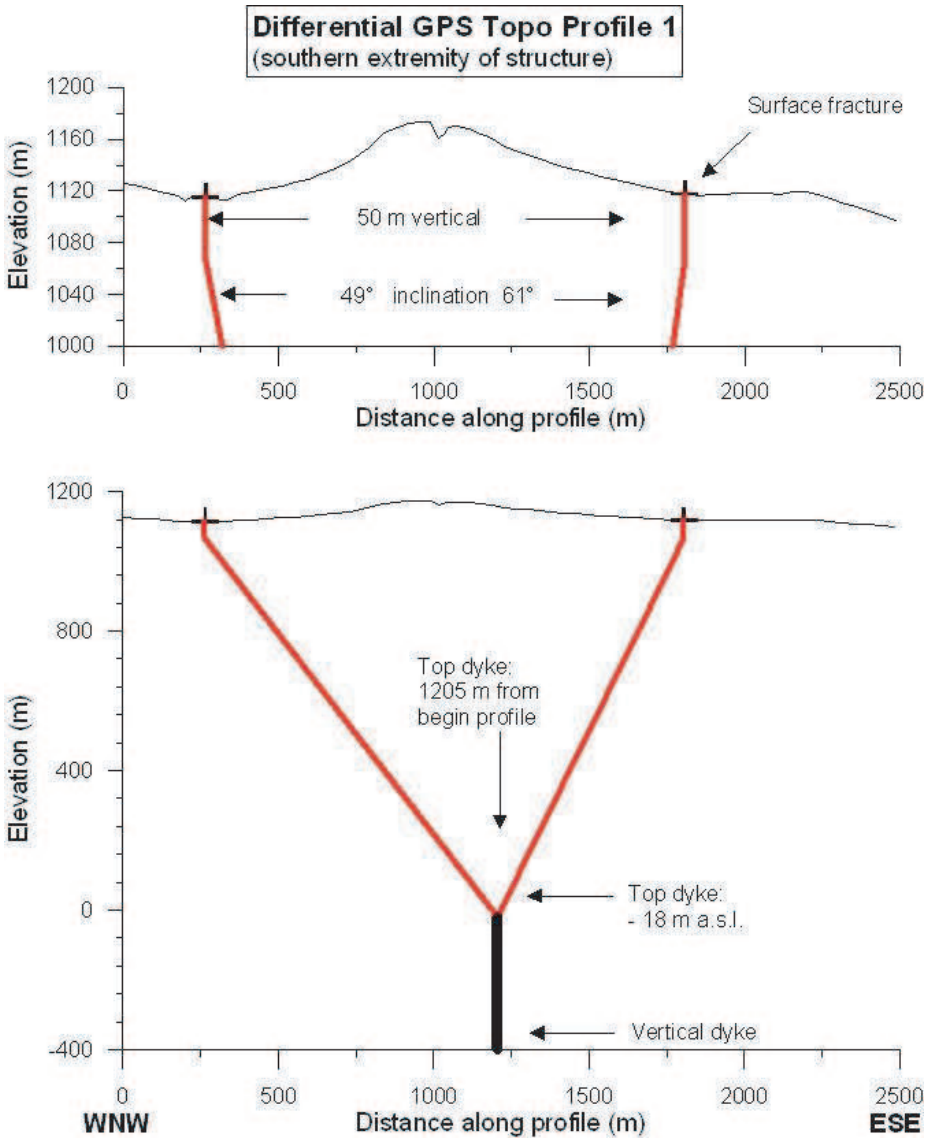

Figure 6.12: DGPS profile AA' across the Gelai seismo-magmatic graben (close to SRTM profile 1 in Figure 6.13) illustrating the calculation of the position of the top end of the inferred underlying dike. The crosses show the intersection of the fault segment on the profile. The fractures are drawn vertically to a depth of 50 m, after which in a sharp transition, they evolve in normal faults whose slope is constrained by the average values of Δ_h and Δ_v for the respective segments. The downward projection of the two faults intersects at an elevation of -18 m and at a distance of 1205 m from the origin of the profile on its northwestern side. After [*Delvaux et al.*, 2007].

(70°dip) gives a deeper level for the top of dike (-2480 m), in alignment with the results obtained for profiles 1 to 3. However, in this case, the geographic coordinates of the top of the dike are shifted along the profile to the SE, giving a broken line aspect to the map projection of the top of dike. Therefore, we prefer the first solution with a dip angle of 65° to respect the overall curvature of the dike in plane view.

A longitudinal profile extracted from the SRTM DEM passing through calculated dike coordinates and the summits of both the Kerimasi and Gelai volcano (Figure 6.13) is shown in Figure (Figure 6.14). For profiles 2 to 6, the inferred top of dike fluctuates between -2840 m a.s.l. (4750 m beneath the topographic surface) and -2070 m a.s.l. (3700 m beneath the topographic surface), with an average elevation close to -2500 m a.s.l (Figure 6.14 and 6.15).

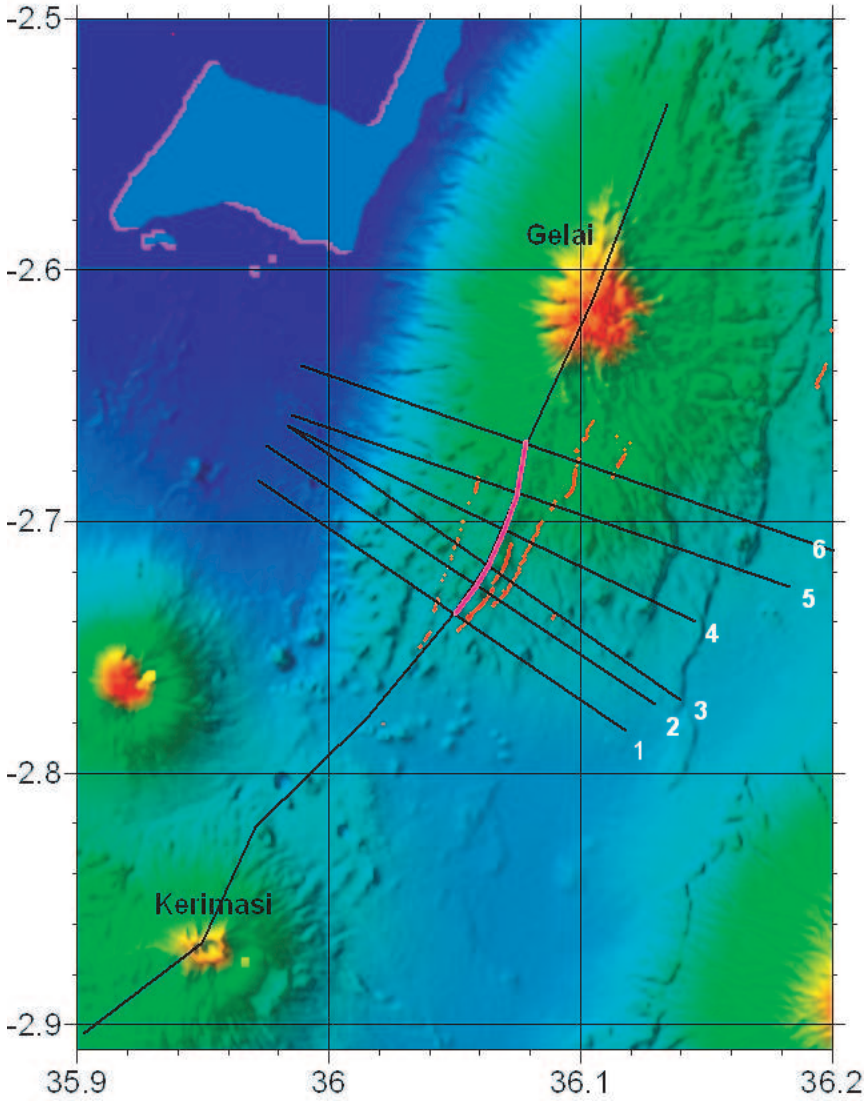

Figure 6.13: Location of the transversal and longitudinal profiles extracted from the SRTM-DEM. Geodetic coordinates in degrees, WGS84 datum: 0.1° corresponding to 9 km. After [*Delvaux et al.*, 2007].

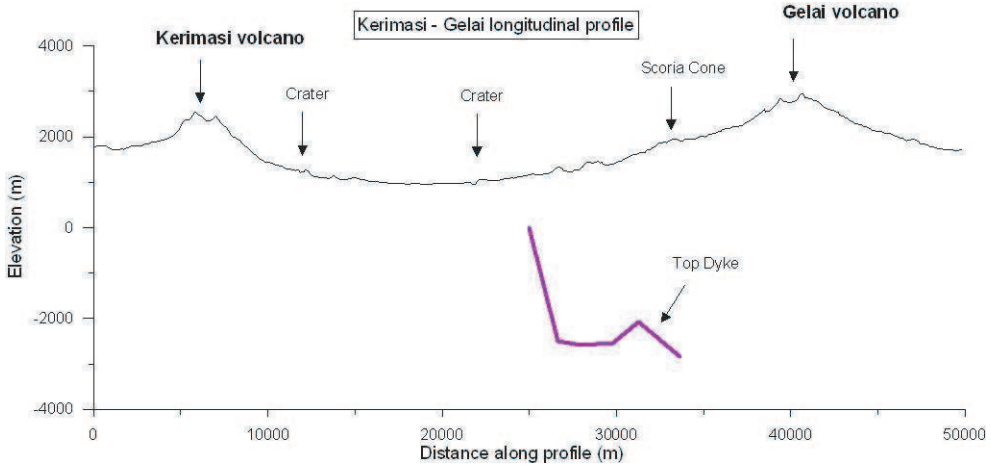

Figure 6.14: Longitudinal topographic profile extracted from the SRTM-DEM at 90-m resolution, passing through the surface projection of the mapped top of dike. After [*Delvaux et al.*, 2007].

At the level of profile 1, the calculated top of dike is significantly higher, reaching -3m a.s.l., 1747 m under the topographic surface. This corresponds to the narrower part of the graben, between the western fault and the eastern 1 fault. It should be noted that for the other profiles (2-6), the depth of the top of dike is constrained on the eastern side of the graben, by the eastern 2 fault instead of the eastern 1 fault as for profile 1. In spite of this shift, the geometry of the top of dike still follows a nice curve in plan view, suggesting that the dike has been injected to a higher level, but along a similar plane (assumed vertical).

The surface projection of the mapped dike corresponds to several volcanic vents as seen on the referenced geological map (Figure 6.16). The calculated depth for the top of dike along profile 1 suggests also that the magma injection at the southern extremity of the dike is approaching the surface, in the vicinity of the crater which marks the southern termination of the graben system, and corresponds to the lateral intersection of the two fracture systems. This time, the magma did not reach the surface but it certainly did in the recent past during a similar event.

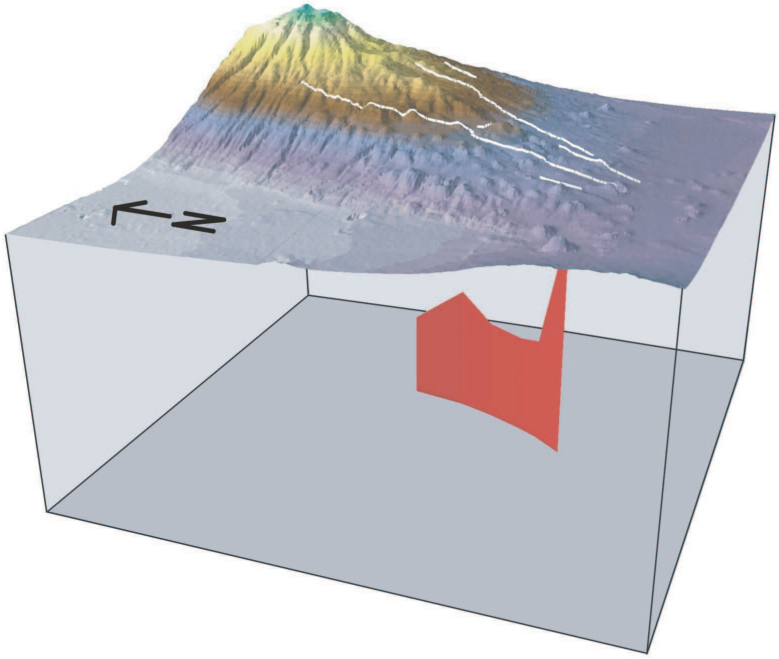

Figure 6.15: Inferred dike geometry in a 3D view. After [*Delvaux et al.*, 2009].

6.2.7 Summary of field observations and Interpretations

In summary, the field mapping of the surface fractures that appeared during the July-August volcano-seismic Gelai crisis confirms the preliminary interpretation of the interferograms and provided structural and deformation data that allow to reconstruct at depth the geometry of the top of the magmatic dike which is believed to be responsible for the observed surface fractures and ground deformation (Figure 6.20).

The geometry of the dike top draws a regular curved line in a plan view but with irregular elevation in a vertical longitudinal section. The magma injection could have thus occurred along a (sub)vertical plane, curved in plan-view.

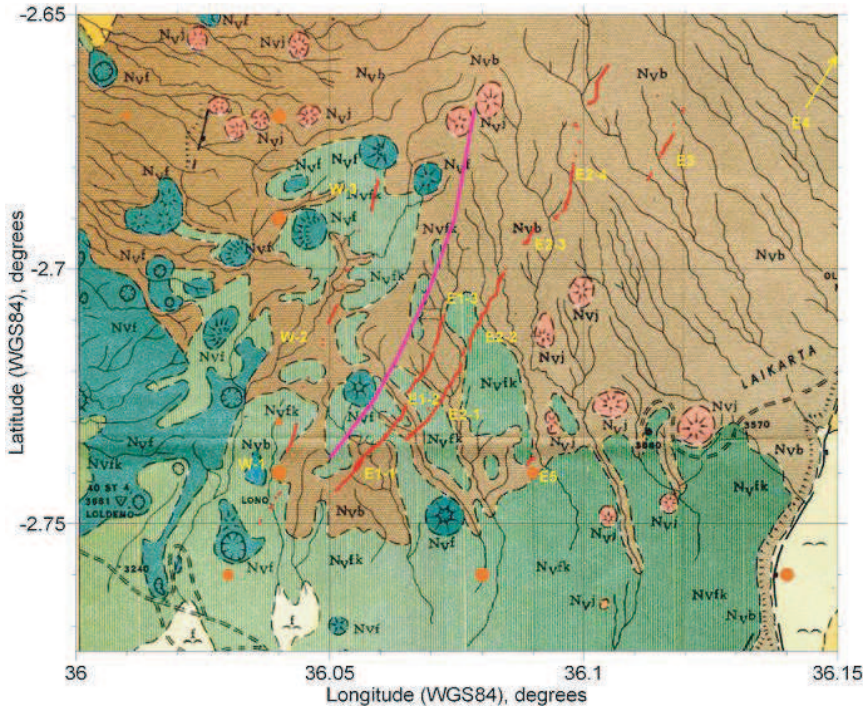

Figure 6.16: Plot of the fracture system (red lies and dots) and the surface projection of the calculated top of dike (violet) with as background the geo-referenced 1/250,000 geological map (QDS 40 - 1 Gelai). The volcanic vents are indicated as Nvj (recent scoria cones) and Nvf (Older tuff and agglomerate craters). After [*Delvaux et al.*, 2007].

Field data show that this event is not unique in the local geological history as we observed several signs for fault reactivation during the past.

6.2.8 Lengai Activity

During the field mission, the active volcano close to the Gelai, the Lengai, was erupting. The eruption was quite unusual for this volcano as it included many explosive phases (Figure 6.17) with ash fall deposits about 3 mm thick on the Engaresero village. New cones were constructed (Figure 6.18) during the eruption, with several plumes varying in color (white to dark gray during explosive pulses) and in height (a few hundred meters to km).

6.3 Advanced InSAR Results and Modeling

The Figure 6.19 summarizes the field observations and interpretations which will help to constrain further modeling studies.

The Figure 6.20 shows all the InSAR data available spanning the crisis. As depicted in Figure 6.20, the ALOS L-band satellite provides us with the only ascending SAR data because unfortunately, no images were available from the ascending orbits for that area and time period because of a failure in the ARTEMIS satellite relaying Envisat data to the ground.

Calais et al. [2008], given in Annexe 2, conclude that most of the strain during the July-August 2007 crisis was released aseismically. The major part of the registered deformation was created by slow slip on a normal fault which promoted a dike by stress unclamping. We thus

Figure 6.17: Several picture taken during the field mission of a small explosive plume on October, 17 (15h45 local time). After [*Smets and Wauthier*, 2007]

Figure 6.18: New cones in the Lengai crater rim, 17 (15h45 local time). After [*Smets and Wauthier*, 2007]

suggest that, even in such a youthful continental rift before significant crustal thinning (step 1 in Figure 1.4 in Chapter 1), rifting seems to be strongly magma-assisted.

Oyen et al. [2010], given in Annexe 3, perform a in-depth InSAR analysis of the crisis, dividing the crisis in three main parts, according to the InSAR data and seismicity, following [*Calais et al.*, 2008]. We show that the sequence begins (part I in Figure 6.20) with a 1.35 m slip along a long buried west-dipping fault. Part II of the swarm, covering the diking episodes, is mainly modeled

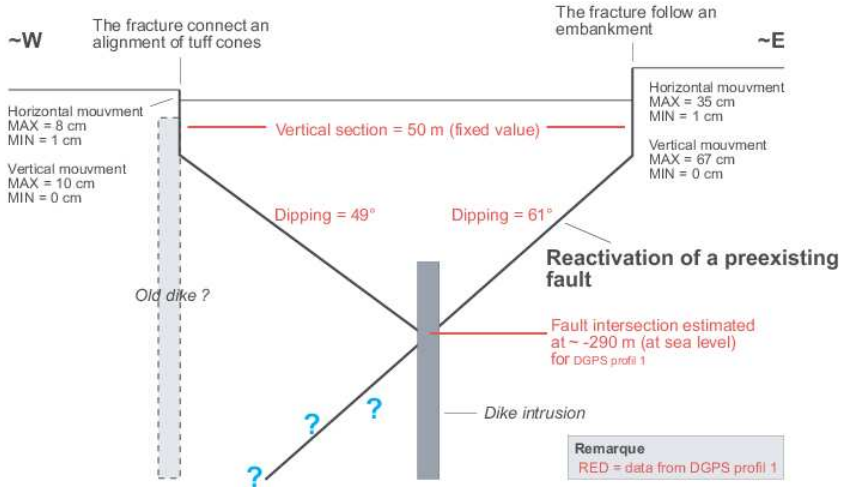

Figure 6.19: Summary of the field observations and interpretations to better constrain the in-depth modeling studies, after [*Smets and Wauthier*, 2007]

by a dike triggering a slip along the Graben Bounding Faults, corresponding to the mapped fracture systems. Additionally, two fault movements were modeled, both in the direction of the migration of the dike intrusions (north- and southwards respectively). Finally, part III of the swarm is modeled by slip along two east-dipping faults reaching the surface on the southeastern flank of the Gelai volcano. The final results and detailed chronology, strongly in line with the field observations and interpretations (Figure 6.19), and established by [*Oyen*, 2009], are presented in Figure 6.21. The dike modeled is subvertical with a volume of $63 * 10^6$ m^3 and has a low overpressure value of 1.5 MPa [*Oyen*, 2009].

Interestingly, two other studies by *Baer et al.* [2008] and *Biggs et al.* [2009], also present a slightly different modeling of the Gelai sequence. [*Oyen*, 2009] generally agrees with [*Baer et al.*, 2008] except for the dike location. *Baer et al.* [2008] indeed suggest a quite unrealistic location for the dike, not beneath the graben axis, and passing the Gelai by its western flank instead of beneath it. These authors also think that the magma comes from the Lengai magma reservoir, which is very unlikely. Finally, [*Biggs et al.*, 2009] present a simpler model, with a less number of sources and achieve to fit the far-field signal. However, they masked out the problematic graben near-field signal and had not attempt to model it. This issue is well solved by [*Oyen et al.*, 2010] and [*Oyen*, 2009], which are thus assumed to give the most realistic modeling results, in agreement with the field observations and interpretations, and taking into account a realistic topography through the advanced 3D-MBEM approach instead of simple Okada or Mogi approaches.

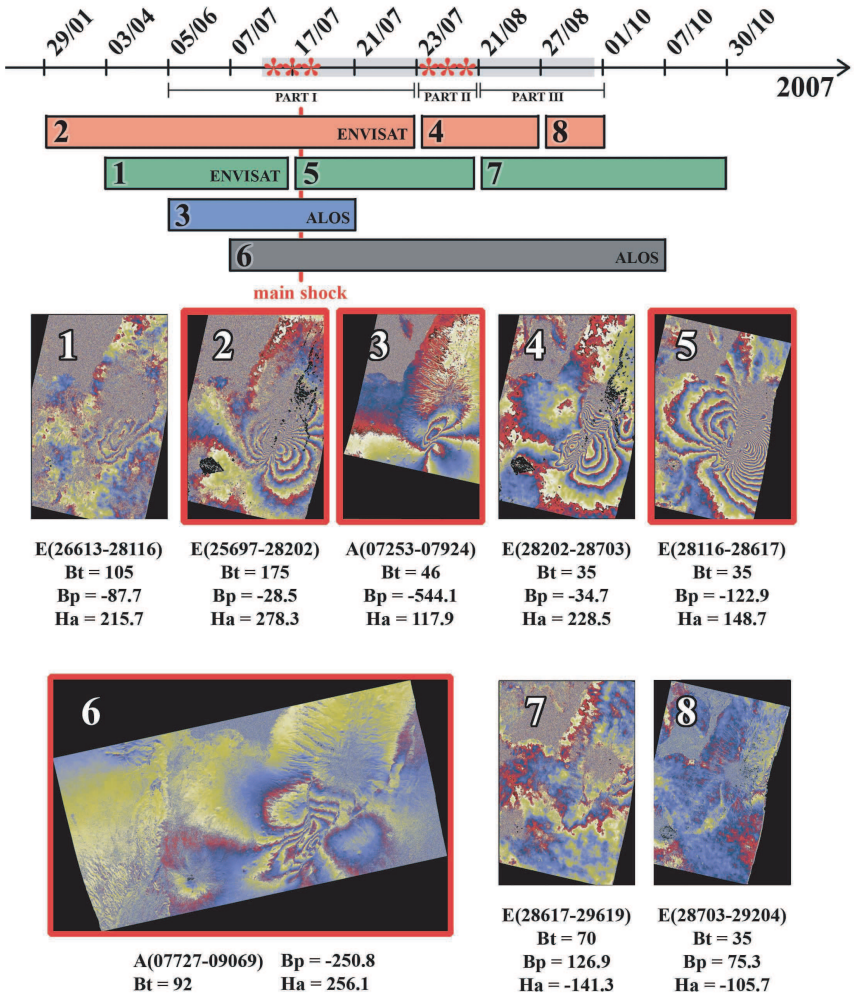

Figure 6.20: Summary of the differential interferometric results from 07/01/29 to 07/10/30. Green and red indicate respectively the Envisat track 6 (beam is6) and the Envisat track 92 (beam is2) interferograms. The descending and ascending ALOS interferograms are represented by blue and black respectively. Some important parameters of the interferograms, which are named by their respective orbit numbers, like temporal baseline (Bt), perpendicular baseline (Bp) and height ambiguity (Ha) are listed next to each interferogram. The > 5 M_w earthquakes of the seismic swarm, that started in the beginning of July 2007 and lasted up to September 2007, are indicated by the red stars on the time line. More specifically, the main shock is indicated by the vertical red line in the time line. The interferograms that contain this main shock are marked by the red boxes. The seismic swarm itself is indicated by the gray rectangle (July 2007 - September 2007). After [*Oyen et al.*, 2010]

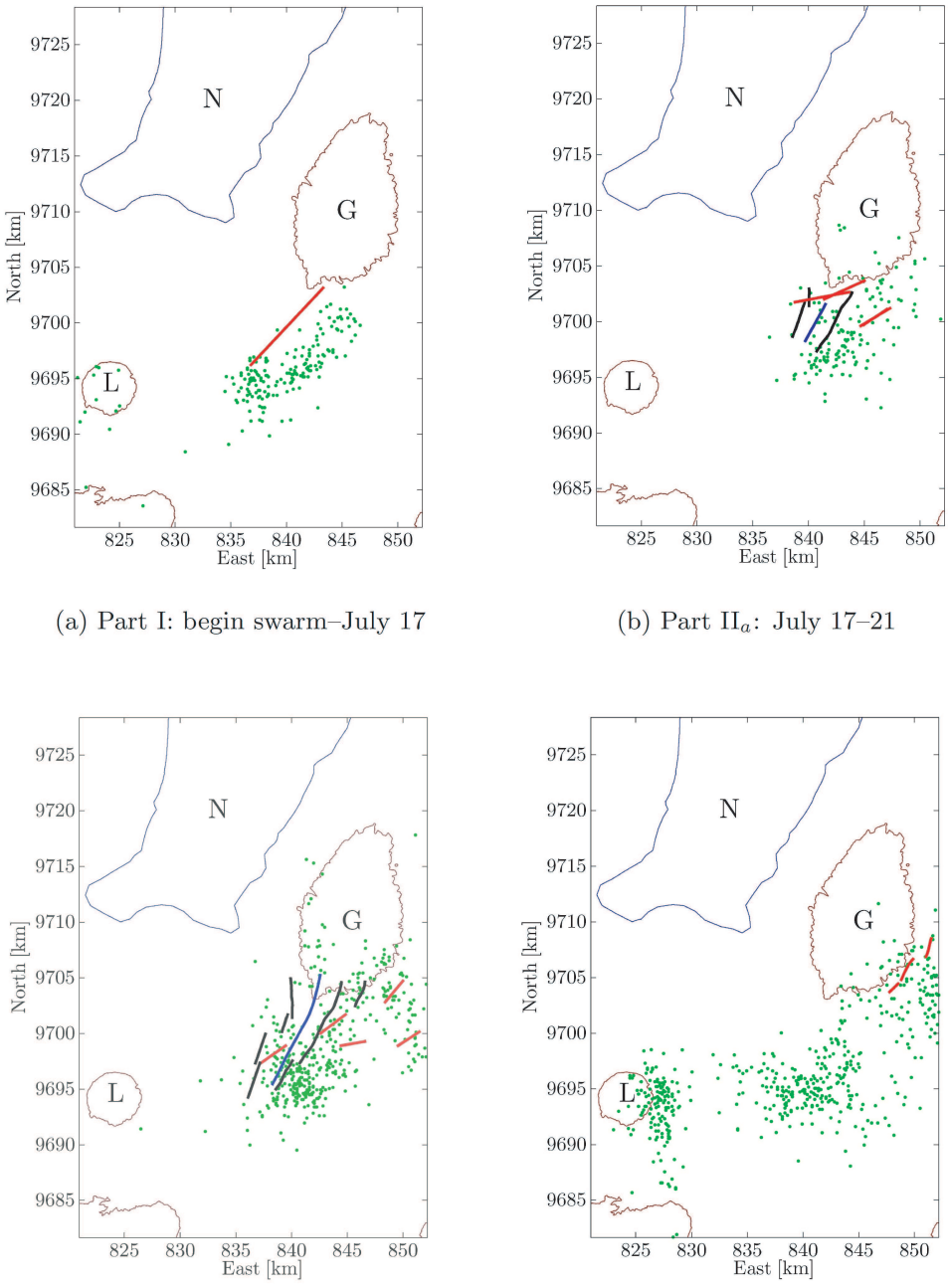

(a) Part I: begin swarm–July 17

(b) Part II$_a$: July 17–21

(c) Part II$_c$: July 23–August 28

(d) Part III: August 28–end swarm

Figure 6.21: Chronology of the Gelai seismo-magmatic crisis. The green dots are the relocated epicenters, red lines are faults, blue lines are dikes, and black lines represent the graben bounding faults (GBFs), after [*Oyen*, 2009]

Chapter 7

Discussion and Perspectives

The main purpose of this chapter is to discuss the major characteristics of the InSAR modeling, eruptions and inter-eruptive activity studied in the Virunga area for Nyamulagira and Nyiragongo volcanoes and to check if common characteristics can be determined. Secondly, new insights concerning the North Kivu rift dynamics and its link with the volcanism are given. Thirdly, a comparison between the North Kivu and the Natron areas, located each in a different branch of the EARS, is done. Finally, several perspectives of the work are proposed.

7.1 Discussion

7.1.1 North Kivu Area

Nyamulagira Volcano

		1996	2002	2006	2010
Fissures Location		N flank	N flank and summit	SE flank	SE flank and summit
$(P_0)_{dike_1}$	(MPa)	1.3	0.4	0.2*	1
$(P_0)_{dike_2}$	(MPa)	-	-	-	3
Reservoir center	(km)	-	-	744 , 9843*	744.7, 9843.4
Reservoir dimensions	(km)	-	-	1 × 1*	1.7 × 1.2
Reservoir depth	(km below summit)	-	-	1.5*	3.7
$(\Delta_V)_{reservoir}$	$(*10^6 m^3)$			+ 1.5*	- 2
V_{dike_1}	$(*10^6 m^3)$	5.6	27	1.2*	1.1
V_{dike_2}	$(*10^6 m^3)$	-	-	-	2.7
$V_{intruded}$	$(*10^6 m^3)$	5.6	27	2.7	3.8
$V_{erupted}$	$(*10^6 m^3)$	49.8 ± 16.6	56.7 ± 18.9	44.2 ± 14.7	46

* from *Cayol et al.* [2010]

Table 7.1: Relevant characteristics of modeled Nyamulagira eruptions. The model for the 2004 eruption is considered too preliminary and is thus not taken into account here.

The erupted volumes for Nyamulagira's eruptions are systematically larger than the modeled intruded volumes: They are about one order of magnitude larger for the 1996, 2006 and 2010 eruptions and twice larger for the 2002 eruption. However, the intruded volume estimations from the modeling will always be a minimum value as the magma could take the same path several times if the conduit remains open during the eruption.

For the 2010 eruption, the shallow reservoir is affected by a volume loss of $2*10^6 m^3$. However, the erupted volume, taking into account the intruded magma in dikes, is about $50*10^6 m^3$, which is more than 20 times larger than the volume loss in the reservoir. However, several factors must be taken into account: 1) the ENVISAT interferograms do not show useful signals to the south and southwest of the caldera but the ALOS residuals show that the current best-fitting model should be adjusted to explain a residual signal on the southwestern flank of the volcano. The sill and/or dike(s) extension could be larger than proposed in the current model, or another shallow deflating reservoir could be involved. The intruded volume could therefore be larger than the current estimation. 2) The modeled volume change in magma reservoirs will always be a minimum value since these models assume incompressible magma [*Rivalta and Segall*, 2008] [*Mastin et al.*, 2009]. Indeed, dissolved volatiles increase the magma compressibility and restore the pressure in magma reservoirs when they exsolve [*Johnson*, 1992] [*Johnson et al.*, 2000] [*Huppert and Woods*, 2002] [*Mastin and et al.*, 2008]. 3) This reservoir might be a summit reservoir fed by a larger deeper reservoir. If the emitted volume is small with respect to the deeper reservoir dimension and this deeper reservoir is volatile rich, its deformations might be unseen while the summit reservoir deformations will be visible on the interferograms. This summit reservoir will only be a zone where magma will be temporarily transferred. It will inflate or deflate depending on the volatile content of the emitted magma, and on the hydraulic connection between the different parts of the volcano plumbing system.

The southern eruptive fissure for the 2010 eruption opened almost at the same location as the 2006 eruptive fissure. Moreover, the preliminary modeling of the 2006 InSAR data shows that a spherical reservoir is involved, when this reservoir was considered to be a flat elliptical sill for the 2010 eruption. The reservoir is determined to be inflating in 2006 and located 1.5 km below the summit, while it is determined to be deflating in 2010 and located 3.7 km below the summit. The same reservoir was probably involved in both eruptions. This change in volume variation can obviously not be explained by the reservoir shape, however the change in the estimated depths could result from the different reservoir shapes considered in the studies.

No magma was emitted in the caldera in 2006 and 1996. However, during the 2002, 2004 and 2010 eruptions, magma was also emitted in the caldera and associated with fissures in the caldera floor and lava fountaining. Simultaneously, or just after the initiation of the summit activity, lateral fissures and vent(s) opened on the northern flank in 2002 and 2004, and on the southeastern flank in 2010. As the 2002 and 2004 eruptions were apparently not associated to any summit reservoir deformation, we can wonder whether the lack of magma reservoir deformation is a feature common to all northern flank eruptions.

Seismic data [*Hamaguchi and Zana*, 1983] indicate a magma reservoir with a roof located from 3.5 to 7 km beneath the Nyamulagira summit. This could correspond to the magma reservoir found by the modeling of the 2006 and 2010 eruptions. The location of this inferred reservoir is consistent with the SW depression resulting from the collapse of a shallow magma reservoir

which occurred during the major eruption of 1938-40.

Moreover, in the same area, range decreases were identified on the StaMPS results a few months before the 2004, 2006 and 2010 eruptions, while an overall range increase behavior in other periods occurred (Figure 5.8). This observation could indicate the refill of the summit magma reservoir a few months before each eruption. Furthermore, *Mavonga et al.* [2010a] found that LP earthquakes, preceded both the 2004 and 2006 eruptions of Nyamulagira. About ten months prior each eruption, a steady increase in seismicity was observed which is attributed to the movement of magma in a deep conduit. The last 1 or 2 months before each eruption, the hypocenters of LP earthquakes became shallower [*Mavonga et al.*, 2010a], which is consistent with our interpretation of a refill of magma in a shallower reservoir from a deeper source. According to the StaMPS results, the largest refill of the magma reservoir occurs before the 2006 eruption. The overpressure in the magma reservoir was probably high and this could explain why magma intrusion(s) in 2006 have created such a large extension deformation pattern, by propagating until about 15 kilometers to the south and south-east.

A schematic model for the possible Nyamulagira's plumbing system is shown in Figure 7.1. *A* is the area just beneath the volcano summit where the intrusions feed the summit eruptions and the pit crater. There could be very shallow reservoirs involved inside the edifice. *B* could be the superficial magma reservoir detected in 2010 located beneath the SW depression. *C* is the deep reservoir which feeds the superficial reservoir *B*, and could be responsible for the refills observed before the 2004, 2006 and 2010 eruptions. The depth of *C* is constrained from the seismic studies of *Mavonga et al.* [2010a] who estimated the location of a deep source at about 20-30 km. *D* could be the deflation sources identified on the StaMPS results for the 2006 - 2010 period. To promote the graben subsidence, magma could be stored in a dike-like reservoir and be close to the surface of the southeastern volcano's flank, and thus an other reservoir might be involved beneath the SE flank.

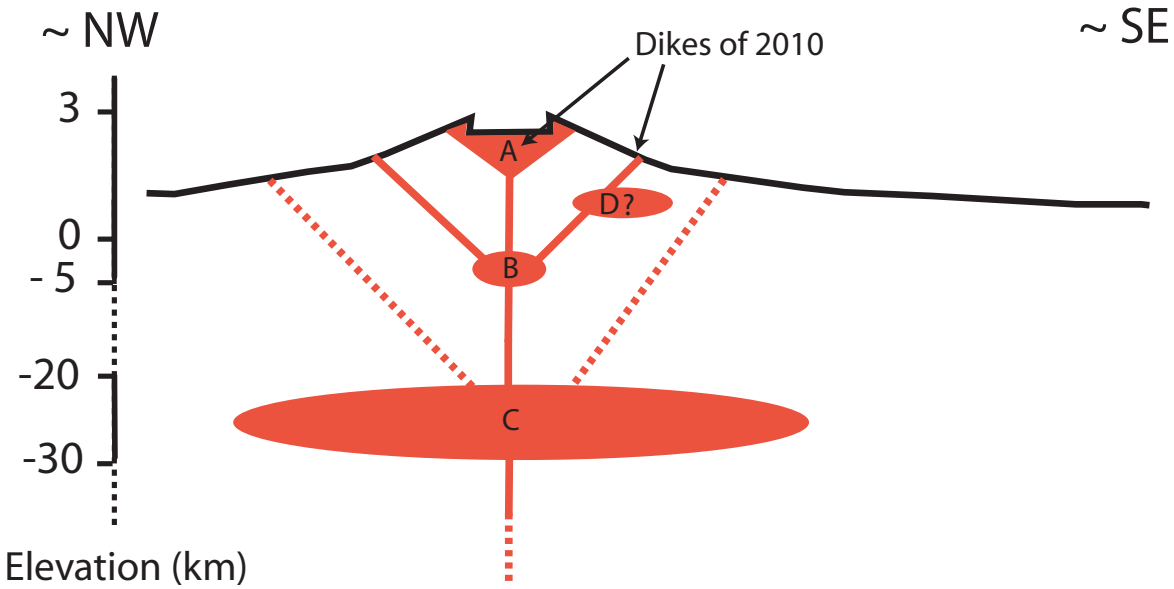

Figure 7.1: Conceptual sketch of the possible Nyamulagira magma plumbing system, adapted from [*Delorme*, 1976] and [*Smets et al.*, 2010a]. Note that the figure is not to scale.

The eastern flank of Nyamulagira is continuously subsiding, as indicated by: 1) the morphological circular collapse features (Figure 1.12) and the major east-facing scarp identified from inside the caldera on the southeastern flank (Figure 1.13), 2) the loss of coherence observed on some interferograms and coherence images around the eastern half part of the Nyamulagira rim, and 3) the signal observed on the ALOS interferogram and model residuals. The NNW-trending fracture network, which may be due to the stress field generated by the interplay between the magmatic systems of both volcanoes [*Gudmundsson and Andrew*, 2007] or, more likely, to the reactivation of Precambrian basement faults [*Smets et al.*, 2010a], is probably contributing to this progressive collapse (Figure 1.9). This process is probably going on from several (tens of) years. It could progress by steps, activating when new dikes intrude and further trigger the eastern flank displacements. This progressive collapse could leads to the eastern flank collapse unleashing the pressure in the Nyamulagira magma reservoir(s) *Pinel et al.* [2010].

Nyiragongo Volcano

The StaMPS results do not allow to identify features linked with the discontinuities observed in Gisenyi on the RADARSAT-1 interferogram spanning the January 2002 eruption, and further confirmed on the field during the January 2010 field mission. The merging size of pixels, 200 meters, used in the StaMPS processing could however smooth the signal and thus be too large to identify such motions.

The possible Nyiragongo plumbing system, deduced from geochemical and geodetic data of this study, was presented in Figure 4.11. Lava lake draining, shallow dike intrusions from a shallow magma reservoir, and southern flank fissural eruptions is a common feature of past Nyiragongo eruptions. However, the deep subvertical intrusion identified below Goma and the Lake Kivu, aligned with an old eruptive fissure networks (Ngangi) and several phreatomagmatic cones, is an evidence that the Nyiragongo magmatic activity has a narrow link with the local rift opening setting. As this dike extends for about 20 kilometers beneath the lake, it could have represented a considerable hazard if magma had reached the lake as its waters contain high concentrations of dissolved carbon dioxide and methane. Such deep dikes probably interacted with the lake in the past as evidenced by the presence of volcanic cones along the Lake Kivu shore [*Cahen*, 1954]; [*Newhall and Tuttle*, 1988] or on the lake floor [*Capart*, 1955]; [*Schmid et al.*, 2010]. They are certainly a common feature of Nyiragongo eruptions and they represent a serious threat for the population living around the lake.

Comparison Between Nyamulagira and Nyiragongo Volcanoes

Even if the two volcanoes are located 15 kilometers from each other, they differ in several aspects. In term of morphology and petrology of course, but also from a magmatic and volcanic activities point of views. An interesting feature is that the modeled volumes intruded for the 2002 eruption of Nyiragongo are about one order of magnitude larger than the erupted volumes, which is the opposite of what is observed for the Nyamulagira. Hence, the endogenous growth could be more important at Nyiragongo than at Nyamulagira. As shown before (Chapter 4, Section nyir02), magma coming from below the rift is probably now driving the rift extension at the location of Nyiragongo volcano and the preferential magma path identified south of the volcano. On the

other hand, Nyamulagira eruptions are probably permitted by the Precambrian basement faults, following an axis which is not favorably oriented with respect to the rift extension. Thus it does not accommodate much of the rift extension while Nyiragongo volcano does, leading to smaller intrude volumes than for Nyiragongo volcano.

New Insights Concerning the North Kivu Basin

The typical overpressure values found by our modeling range between 1.1 and 4.5 MPa for the Nyiragongo volcano intrusions, and from 0.2 to 3 MPa for the Nyamulagira intrusions. As we explained in the Section 4.1, the dikes might induce compressions are not relaxed by the rift extension. For instance, at Nyamulagira, at least seven fissure eruptions opened since 1980 on the southeastern flank of Nyamulagira, inducing a possible compression rates of 5 cm/yr [*Cayol et al.*, 2010]. The dikes-induced compressions could create a lithostatic stress state close to the intrusion pathway. These lithostatic stresses do not favor the intrusion of magma. Thus the intrusion of magma in the rift is forceful, and caused by the supply of magma not because of the rift extension. To the north of the North Kivu basin, although the rift is considered immature, the rift extension seems to be driven by the supply of magma from depth (magma-driven rift), rather than the tectonics. In this study, overpressures estimated from geodetic data were used as indicators of the rift maturity. Thus, following *Ebinger* [2005], we can conclude that a fifth criterion can be used to identify the stage of continental break up a rift area is experiencing.

From the modeling of the seismic and volcanic events detected by InSAR in the Kivu area, we find that two distinct regimes coexist to accommodate the rift extension. The south of the North Kivu basin, starting about from Idjiwi to the Bukavu area, seems to accommodate the rift extension with faulting, with no major magma intrusion detected. While in the northern part of the North Kivu basin, from the Virunga Volcanic Province to Idjiwi, the rift extension seems to be driven by the supply of magma. Although the North Kivu basin has been considered as an immature rift (Stage 1: onset of continental break-up [*Ebinger*, 2005]), we find that only the southern part of the basin is at such a stage. These differences are consistent with the younger age of the southern part of the Kivu basin [*Ebinger*, 1989a].

7.1.2 Comparison Between the Lake Natron and Kivu Areas

A subvertical dike with a volume of $63 * 10^6\ m^3$ [*Oyen*, 2009] below the southeastern flank of an important edifice, the Gelai volcano, is found by the InSAR modeling of the Natron crisis. Many faults are also involved, some faults only responding passively to the dike opening, and others (1.5 meters of slip [*Oyen*, 2009]) undergoing slip before the eruptive crisis. The dike overpressure also has a low value of 1.5 MPa [*Oyen*, 2009], which could indicate that the stresses are close to being lithostatic in the Natron area too and the rift is magma-driven. In such a case, it is likely that the observed seismicity is induced by magmatic rather than tectonic activity.

7.2 Perspectives

7.2.1 Modeling

Similarly as what was done for dikes, we could explore how the parameters describing a magmatic reservoir, whether it is assumed to be a sill or a sphere are resolved by the Inversion of InSAR data and these results could be used to improve the of the Nyamulagira eruptions involving a reservoir. The residuals of the 2010 best-fitting model on the ALOS data especially further need to be studied and explained as it could lead to significant differences in the intrusions geometries, probably for the northern dike and/or the sill. The graben subsidence and eastern flank collapse could be taken into account by adding new boundaries to the model, such as the eastern circular rim and the graben faults identified, which could respond passively to the dike intrusions. The 2002 eruption dike model is still not able to successfully explain the descending RADARSAT data, and future work could be done to improve the data fit. Further modeling studies could be done for the 2004 eruption once the eruptive fissures location will be constrained by other data. For the 2002 and 2004 eruptions, the involvement of a sill could be investigated.

The eastern flank collapse and graben subsidence should be studied in details by 1) investigating the ALOS inteferograms which provide a coherence to the northern and eastern flank of the volcano, and 2) studying in details the ENVISAT StaMPS displacements results.

7.2.2 MT-InSAR

The time-series StaMPS results should be investigated in details and can be refined for several beams probably by removing some interferograms that were badly unwrapped. The identified deformation signals in the Bulengo area could be constrained by other data, such as meteorological data and analysis of the springs and *mazuku* in this area. The eruptive precursory signals identified in the caldera could be inverted to try to constrain the magma reservoir(s) location and behavior. The range increase signals identified along the NNW trend on the southeastern flank of Nyamulagira between 2006 and 2010 should be modeled too to better constrain the mechanisms involved: is there magma movements close to the surface which promote the graben opening, are there deflating magma reservoirs involved? However, the main limitation is currently the mixing of possible inter-eruptive range increase signals with lava flow compaction and subsidence as almost all the area is covered by lava flows.

New insights on the inter-eruptive deformation could come from the generation of RADARSAT-1 time-series as the temporal sampling will be better with a 24 days revisit cycle. However, large shifts in Doppler frequency occur preventing us to focus the data with the ROI-PAC package and the orbits are difficult to handle.

The StaMPS displacements obtained over single eruption may also be joined in the inversions as new pixels, especially on the volcanoes flanks, could better constrain the models. However, one should take into account possible large gradient of deformation and maybe thus reduce the merging pixel size to avoid unwrapping errors.

7.2.3 POLInSAR

The POLInSAR approach has not be tested on our African targets due to the lack of full polarimetric (QUADPOL) ALOS data covering these areas because of the only experimental full polarimetric mode of ALOS. Moreover, the ALOS revisiting cycle and observation strategy is not favorable enough for significant coherence, and interferometric phase quality improvement (Eric Pottier and Laurent Ferro-Famil, Pers. Comm., July 2009). The benefit of such an extension of conventional InSAR could however be investigated using full polarimetric data from the RADARSAT-2 satellite for instance.

A new potentially strong technique could combine the benefits of both MT-InSAR and POLInSAR approaches. For instance, *Samsonov and Tiampo* [2011] proposes a new technique for selecting persistent scatterers (PS) based on their polarization phase differences. They obtained displacements maps using six full polarimetric images over the San Francisco area which have a better PS density and accuracy than if a standard PSI technique applied alone. An other interesting approach could be to generate optimized interferograms thanks to the POLInSAR approach, and then to use them for generating accurate time-series results with a dense spatial coverage.

Conclusion

InSAR has proven to be a valuable tool to study several volcanic and seismic events in two areas of the East African Rift System (EARS): the Lake Kivu (DRC) and the Lake Natron areas, as both areas are poorly studied and monitored by ground-based methods. The study and monitoring of these two areas by InSAR was thus of great value to the understanding of magmatism, and its link with the rifting as well as for hazard assessment.

Concerning the InSAR-related techniques used, conventional InSAR remains the preferred tool to study rapid deformation event, such as eruptions or fault ruptures associated to earthquakes. However, the use of a Multi-Temporal approach, such as the StaMPS method, brings extra information on areas where no coherence was obtained through conventional InSAR. The StaMPS method has proven to be a useful tool to detect continuous linear deformations over long periods of time. For instance constant rate subsiding areas have been identified in correlation with gas emanations on the northern shore of Lake Kivu. Insights were also given on the possible deformation cycle affecting a reservoir below Nyamulagira caldera and a linear subsidence has been detected beneath the fractures network trending NNW on the southeastern Nyamulagira flank. Multi-Temporal techniques, such as the PS, SBAS or combined approach from the StaMPS method, are therefore powerful complementary tools to conventional InSAR.

Using synthetic models and eight possible combinations of one to three beams (Chapter 3, Section 3.2), we showed that the six geometrical parameters and the overpressure which define a north-south trending dike can be satisfactorily determined by inversions. Test model parameters were, in most cases, within the 95% confidence interval, with the exception of the basal elevation of the dike which did not lie within the confidence intervals in 6 cases out of 8, showing that the inversions do not always succeed in resolving the extension of dikes at depth. By comparing results obtained inverting data from one to three beams, we find that using a single beam, we are able to satisfactorily retrieve the model parameters. When increasing the number of beams, we find that, the confidence intervals are not significatly reduced but that fewer forward models are needed to get convergence, indicating that the inversion efficiency is increased.

The major conclusions of our study of the Nyiragongo 2002 eruption using multibeam InSAR data (Chapter 4, Section 4.1) can be summarized as follows:

1. The best fit model describing the 2002 co-eruptive deformation, which was also the most likely, according to Akaike criteria, corresponds to two subvertical dike intrusions. The first

shallow dike, 2 kilometers high on average, is associated with the 20 kilometers long eruptive fissures network. The modeled mean surface opening is 3 meters, which is consistent with field measurements. This dike volume is consistent with a magma supply by the draining of the summit lava lake combined with a deeper source, a result which is also consistent with the geochemical data. The second dike is deeper, 6 kilometers high and located 3.3 kilometers beneath the city of Goma. It has a rift parallel strike, and a basal length of 40 kilometers. It is consistent with the deep magma source of the southernmost fissure, as inferred from geochemical data. As this dike extends for about 20 kilometers beneath the lake, it could have represented a considerable threat if magma had reached the lake as its waters contain high concentrations of dissolved carbon dioxide and methane. Such magma intrusions located beneath the Lake Kivu are likely to occur again and have to be taken into account for the hazard assessment as the magma could find its way to the Lake Kivu floor.

2. It is not easy to establish whether the deeper dike was injected before the shallower dike since magma injection in either dike could lead to injection in the other. It is likely that the deep injection triggered the pre- eruptive and post- eruptive seismicity and fault movements such as the superficial fault movements observed in Gisenyi.

3. The rift parallel directions of the dikes, as well as their sub-vertical dips, indicate that their direction of emplacement is controlled by the rift extension. The low overpressures determined for both dikes indicate that the stresses are close to being lithostatic. Such stresses indicate that successive dike intrusions are only partialy relaxed by the rift extension and thus that rift extension is induced by magma supply rather thand the tectonics.

The major conclusions of our study of the Nyamulagira volcano (Chapter 4, Section 4.2 and Chapter 5) are:

1. A magma reservoir has been identified thanks to the 2006 and 2010 eruptions modeling. This reservoir is located a few kilometers beneath a depression, southwest of the caldera, which results from a collapse during the 1938-40 eruption. The depth of this reservoir is consistent with seismic data. The time-series results suggest that this reservoir was probably affected by refill a few months before the last Nyamulagira eruptions.

2. The magma budget between the reservoir and the emitted magma indicates that reservoir is probably connected to a deeper source. Thus this shallow reservoir is probably storing magma temporarily.

3. The eastern flank of the volcano is collapsing along the NNW-trend fractures network linking Nyamulagira and Nyiragongo volcanoes. This phenomenon probably promotes the magma uplift by diminishing stresses in the edifice. A subsidence behavior has been identified during the 2006-2010 period on this direction linking the 2010 vent on the southeastern flank to the caldera rim. This is consistent with the graben feature identified at the same location on the field, likely induced by magma intrusion(s) close to the surface.

Chapter 6 showed the interest of field measurements to give constrain on the modeling of the InSAR data. A model of a subvertical dike, intruded below a dormant volcano, inducing slip on graben bounding faults, was established in accordance with the field investigations and subsequent interpretations.

The low overpressures found in the Kivu and Lake Natron areas indicate that, although the

rift is considered immature in both areas, the rift extension is driven by the supply of magma from depth, rather than the tectonics. A new criterion to identify the rifting stage can thus be added to the criteria proposed by *Ebinger* [1989a]: the stress state. In the southern part of the rift, tectonic activity dominates, indicating that the tectonics is probably driving the rift opening there. These different behaviors of the northern and southern parts of the Kivu basin are consistent with the age of the rift. The younger part of the Kivu basin, located to the south, is still accommodating strain by faulting, while the older part of the basin, to the north, is accomodating strain by magmatic activity.

Bibliography

Allard, P., P. Baxter, M. Halbwachs, and J.-C. Komorowski, The january 2002 eruption of nyiragongo volcano (dem. repub. congo) and related hazards: observations ans recommendations, *submitted to the Ministry for Foreign Affairs, Paris, France, Foreign Office, London, United Kingdom and respective Embassies in Democratic Republic of Congo and Republic of Rwanda, Paris, unpublished report*, p. 24 pp., 2002.

Amelung, F., S. Jonsson, H. Zebker, and P. Segall, Widespread uplift and "'trapdoor"' faulting on galapagos volcanoes observed with radar interferometry, *Nature*, *407*, 993 – 996, 2000.

Angelier, J., F. Bergerat, O. Dauteuil, and T. Villemin, Effective tension-shear relationships in extensional fissure swarms, axial rift zone of northeastern iceland, *Journal of Structural Geology*, *19*(5), 673 – 685, 1997.

Aoki, K. I., and T. Yoshida, *Petrological and geochemical studies on the 1981-1982 lava from Nyamuragira volcano*, pp. 91 – 96, H. Hamaguchi (Ed.), Volcanoes Nyiragongo and Nyamuragira: Geophysical Aspects, The Faculty of Science, Tôhoku University, Sendai, Japan, 1983.

Aoki, K. I., T. Yoshida, K. Yusa, and Y. Nakamura, Petrology and geochemistry of the nyamuragira volcano, zaire, *Journal of Volcanology and Geothermal Research*, *25*(1-2), 1 – 28, 1985.

Arnadottir, T., P. Segall, and P. Delaney, A fault model for the 1989 Kilauea south flank earthquake from level and seismic data, *Geophysical Research Letters*, *18*(12), 2217 – 20, 1991.

Ayele, A., D. Keir, C. Ebinger, T. Wright, G. Stuart, W. Buck, E. Jacques, G. Ogubazghi, and J. Sholan, September 2005 mega-dike emplacement in the manda-harraro nascent oceanic rift (afar depression), *Geophysical Research Letters*, *36*, 2009.

Baer, G., Y. Hamiel, G. Shamir, and R. Nof, Evolution of a magma-driven earthquake swarm and triggering of the nearby oldoinyo lengai eruption, as resolved by insar, ground observations and elastic modeling, east african rift, 2007, *Earth and Planetary Science Letters*, *272*, 339 – 352, 2008.

Bamler, R., and P. Hartl, Synthetic aperture radar interferometry, *Inverse Problems*, *14*, 54 pp., 1998.

Bamler, R., and D. Just, Phase statistics and decorrelation in SAR interferograms, *Proc. Int. Geosci. Remote Sens. Symp.*, pp. 980 – 984, 1993.

Bassi, G., Relative importance of strain rate and rheology for the mode of continental extension, *Geophysical Journal International*, *122*, 195 – 210, 1995.

Beauducel, F., P. Briole, and J. Froger, Volcano wide fringes in ers synthetic aperture radar interferograms of etna (1992-1999): Deformation or tropospheric effect?, *Journal of Geophysical Research*, *105*(B7), 16,391 – 16,402, 2000.

Bellon, H., and A. Pouclet, Datations k-ar de quelques laves du rift-ouest de l'afrique centrale: Implications sur l'évolution magmatique et structurale, *Geologische Rundschau*, *69*, 49 – 62, 1980.

BGVN, Nyamuragira, *Bulletin Global Volcanism Network, Smithonian Institution*, *21/10*, 1996a.

BGVN, Nyamuragira, *Bulletin Global Volcanism Network, Smithonian Institution*, *21/01*, 1996b.

BGVN, Nyamuragira, *Bulletin Global Volcanism Network, Smithonian Institution*, *23/10*, 1998.

BGVN, Nyamuragira, *Bulletin Global Volcanism Network, Smithonian Institution*, *25/01*, 2000.

BGVN, Nyamuragira, *Bulletin Global Volcanism Network, Smithonian Institution*, *26/01*, 2001a.

BGVN, Nyamuragira, *Bulletin Global Volcanism Network, Smithonian Institution*, *26/03*, 2001b.

BGVN, Nyamuragira, *Bulletin Global Volcanism Network, Smithonian Institution*, *26/12*, 2001c.

BGVN, Nyamuragira, *Bulletin Global Volcanism Network, Smithonian Institution*, *27/07*, 2002a.

BGVN, Nyamuragira, *Bulletin Global Volcanism Network, Smithonian Institution*, *27/10*, 2002b.

BGVN, Nyamuragira, *Bulletin Global Volcanism Network, Smithonian Institution*, *28/01*, 2003.

BGVN, Nyamuragira, *Bulletin Global Volcanism Network, Smithonian Institution*, *29/04*, 2004a.

BGVN, Nyamuragira, *Bulletin Global Volcanism Network, Smithonian Institution*, *29/05*, 2004b.

BGVN, Nyamuragira, *Bulletin Global Volcanism Network, Smithonian Institution*, *31/01*, 2006.

BGVN, Nyamuragira, *Bulletin Global Volcanism Network, Smithonian Institution*, *32/01*, 2007.

Biggs, J., F. Amelung, N. Gourmelen, T. Dixon, and S.-W. Kim, Insar observations of 2007 tanzania rifting episode reveal mixed fault and dyke extension in an immature continental rift, *Geophys. J. Int.*, *179*, 549 – 558, 2009.

Bilham, J., R. Bendick, K. Larson, P. Mohr, J. Braun, S. Tesfaye, and L. Asfaw, Secular and tidal strain across the main ethiopian rift, *Geophys. Res. Lett.*, *26*, 2792 – 2984, 1999.

Birch, F., Compressibility; elastic constants, *Handbook of physical constants, GSA memoire*, pp. 97 – 173, 1966.

Birt, C., blabka, and blabla, The influence of pre-existing structures on the evolution of the southern kenya rift valley - evidence from seismic and gravity studies, *Tectonophysics*, *278*, 211 – 242, 1997.

Blom, R., and C. Elachi, Spaceborne and airborne imaging radar observations of sand dunes, *J. Geophys. Res.*, *86*, 3061 – 3073, 1981.

Bürgmann, R., P. Rosen, and E. Fielding, Synthetic aperture radar interferometry to measure earth's surface topography and its deformation, *Annual Reviews of Earth and Planetary Sciences*, *28*, 169 – 209, 2000.

Buck, W. R., *Consequences of asthenospheric variability on continental rifting*, pp. 92 – 137, Columbia Univ. Press, 2004.

Buck, W. R., The role of magma in the developments of the africo-arabian rift system, *The Geological Society of London, Special publication*, *259*, 43 – 54, 2006.

Buckley, S., Roi-pac documentation. repeat orbit interferometry package, *Abridged version of Chapter 3 of a PhD thesis written by Sean Buckley CSR, UT, Austin*, p. 63 pp., 2000.

Cahen, L., *Géologie du Congo Belge*, H. Vaillan-Carmanne, Liège, Belgium, 1954.

Calais, E., et al., Strain accommodation by slow slip and dyking in a youthful continental rift, east africa, *Nature*, *456*, 6 pp., doi: doi:10.1038/nature07478, 2008.

Capart, A., L'échosondage dans les lacs du congo belge. techniques et résultats acquis, *Bull. Agric. Congo Belge*, *46*(5), 1075 – 1110, 1955.

Carn, S., Eruptive and passing degassing of sulphur dioxide at nyiragongo volcano (d.r.congo) : The 17 january 2002 eruption and its aftermath, *Acta Vulcanologica, The January 2002 eruption of Nyiragongo volcano and the socio-economical impact, Vol. 14 (1-2) and vol. 15 (1-2)*, 75 – 86, 2002/2003.

Cayol, V., Analyse élastostatique tridimenseionnelle du champs de déformations des édifices volcaniques par éléments frontières mixtes, Ph.D. thesis, Université de Paris VII, 1996.

Cayol, V., and F. Cornet, 3d mixed boundary elements for elastostatic deformations fields analysis, *Int. J. Rock Mech. Min. Sci. Geomech. Abstr.*, *34*, 275 – 287, 1997.

Cayol, V., C. Wauthier, N. d'Oreye, F. Kervyn, and G. TEAM, Insar displacements associated with the november 2006 and january 2010 nyamulagira eruptions, *AGU Fall Meeting Abstracts*, 2010.

CCR, *Fundamentals of Remote Sensing - A Canada Centre for Remote Sensing Remote Sensing Tutorial*, Canada Centre for Remote Sensing, Natural Resources Canada, 2011.

Chaabane, F., A. Avallone, F. Tupin, P. Briole, and H. Maitre, A multitemporal method for correction of tropospheric effects in differential sar interferometry : Application to the gulf of corinth earthquake, *IEEE T. Geosci. Remote*, *45*(6), 1605 – 1615, 2007.

Chen, C. W., and H. A. Zebker, Two-dimensional phase unwrapping with use of statistical models for cost functions in nonlinear optimization, *Journal of the Optical Society of America A (Optics, Image Science and Vision)*, *18*(2), 338 – 51, 2001.

Cheng, C. H., and D. H. Johnston, Dynamic and static moduli, *Geophys. Res. Let.*, *8*(39642), 1981a.

Cheng, C. H., and D. H. Johnston, Dynamic and static moduli, *Geophysical Research Letters*, *8*(1), 39 – 42, 1981b.

Chorowicz, J., The east african rift system, *Journal of African Earth Sciences*, *43*(1-3), 379 – 410, doi: DOI: 10.1016/j.jafrearsci.2005.07.019, phanerozoic Evolution of Africa, 2005.

Cloude, S., and K. Papathanassiou, Polarimetric sar interferometry, *IEEE trans. on geoscience and remote sensing*, *36*(5), 1998.

Cloude, S. R., Pol-insar training course, *Lecture notes*, p. 44 pp., 2007.

Cloude, S. R., and K. Papathanassiou, Polarimetric optimization in radar interferometry, *Electronic Letters*, *33*(13), 1176 – 1178, 1997.

Colclough, S., Investigations of nyamuragira and nyiragongo volcanoes (drc), using interferometric synthetic aperture radar, Ph.D. thesis, University of Cambridge, 2005.

Crouch, S. L., Solution of place elasticity problems by the displacements discontinuity method, *Int. J. Numer. Meth. Eng.*, *10*, 3001 – 3433, 1976.

Dahm, T., On the shape and velocity of fluid-filled fractures in the earth, *Geophys. J. Int.*, *142*, 181 – 192, 2000.

Dawson, J., and P. Tregoning, Uncertainty analysis of earthquake source parameters determined from insar: A simulation study, *J. Geophys. Res.*, *112*(B09406), 2007.

Dawson, J. B., Neogene tectonics and volcanicity in the northern tanzania sector of the gregory rift valley, *Tectonophysics*, *204*, 81 – 92, 1992.

Dawson, J. B., H. Pikerton, G. E. Norton, and D. M. Pyle, Physicochemical properties of alkali carbonatite lavas: Data from the 1998 eruption of oldoinyo lengai, tanzania, *Geology*, *18*, 260 – 263, 1990.

Delacourt, C., P. Briole, and J. Achache, Tropospheric corrections of sar interferograms with strong topography. application to etna, *Geophysical Research Letters*, *25*(15), 2849 – 2852, 1998.

Delaney, P., and D. Pollard, Deformation of host rocks and flow of magma during growth of minette dikes and breccia-bearing intrusions near ship rock, new mexico, *U.S. Geol. Surv. Prof. Paper*, pp. 1202 – 1263, 1981.

Delorme, H., Volcanologie du rift de l'afrique centrale, le nyamuragira dans les virunga, essai de magmatologie du rift, Ph.D. thesis, University of Paris-Sud Orsay, France, 1976.

Delorme, H., Apport des déformations à la compréhension des méchanismes éruptifs: le piton de la fournaise, Ph.D. thesis, Université Paris VII, France, 1994.

Delvaux, D., B. Smets, C. Wauthier, and A. Macheyeki, Brief scientific report of the october 2007 field work in northern tanzania - field mapping of the surface ruptures associated to the july-august 2007 gelai volcano-tectonic event, *Unpublished Field Report*, p. 18 pp., 2007.

Delvaux, D., B. Smets, C. Wauthier, A. Macheyeki, E. Saria, and A. K. F. N. d'Oreye N.4, Oyen, Surface structures related to the july 2007 natron dyking event, n-tanzania, *TSG - Keele 2009*, 2009.

Demant, A., P. Lestrade, T. L. Ruananza, A. B. Kampunzu, and J. Durieux, Volcanological and petrological evolution of nyiragongo volcano, virunga volcanic field, zaire,, *Bull. Volcanol.*, *56*, 47 – 61, 1994.

Deraw, D., Polinsar, *Lecture notes*, p. 11 pp., 2007.

d'Oreye, N., et al., Systematic insar monitoring of african active volcanic zones: What we have learned in three years, or an harvest beyond our expectations, *Proc. of 2008 Second workshop on USE of Remote Sensing techniques for Monitoring Volcanoes and Seismogenic Areas, Naples, Italy,*, 2008.

d'Oreye, N., et al., Source parameters of the 2008 Bukavu-Cyangugu earthquake estimated from InSAR and teleseismic data, *Geophysical Journal International*, *184*(2), 934–948, doi: 10.1111/j.1365-246X.2010.04899.x, 2010.

Dunbar, J. A., and D. S. Sawyer, How pre-existing weaknesses control the style of continental breakup, *J. Geophys. Res.*, *94*, 7278 – 7292, 1989.

Durieux, J., Volcano nyiragongo (d. r. congo): Evolution of the crater and lava lakes from the discovery to the present, *Acta Vulcanologica, The January 2002 eruption of Nyiragongo volcano and the socio-economical impact*, *Vol. 14 (1-2) and vol. 15 (1-2)*, 137 – 144, 2002/2003.

Ebinger, C., G. Karner, and J. Weissel, Mechanical strength of extended continental lithosphere: constraints from the western rift system, east africa, *Tectonics*, *10(6)*, 1239 – 1256, 1991.

Ebinger, C. J., Tectonic development of the western branch of the east african rift system, *Geological Society of America Bulletin*, *101*(7), 885 – 903, 1989a.

Ebinger, C. J., Geometric and kinematic development of border faults and accommodation zones, kivu-rusizi rift, africa, *Tectonics*, *8*(1), 117 – 133, 1989b.

Ebinger, C. J., The bullerwell lecture: Continental break-up: The east african perspective, *Astronomy and Geophysics*, *46*, 16 – 21, 2005.

Ebinger, C. J., and M. Casey, Continental breakup in magmatic provinces: An ethiopian example, *Geology*, *29*, 527 – 530, 2001.

Ebinger, C. J., and T. Furman, *Geodynamical setting of the Virunga volcanic province, East Africa*, vol. 14, pp. 9 – 16, Acta Vulcanologica - Istituti Editoriali e Poligrafici Internazionale, 2002 - 2003.

Ebinger, C. J., Y. Poudjom Djomani, E. Mbede, A. N. Foster, and J. B. Dawson, Rifting archean lithosphere: Eyasi-manyara-natron rifts, east africa, *J. Geol. Soc. Lond.*, *154*, 947 – 960, 1997.

Ebinger, C. J., et al., Extensional basin geometry and the elastic lithosphere, *Philosophical Transactions: Mathematical, Physical and Engineering Sciences*, *357*(1753), 741 – 765, 1999.

Elachi, C., *Spaceborne radar remote sensing : Applications and techniques*, The Institute of Electrical and Electronics Engineers IEEE Press, New York, 1988.

Farr, T. G., et al., The shuttle radar topography mission, *Rev. Geophys.*, *45*(RG2004), 2007.

Ferretti, A., C. Prati, and F. Rocca, Permanent scatterers in SAR interferometry, *IEEE Trans. Geosci. and Remote Sens.*, *39*(1), 8 – 20, 2001.

Fielding, E., Roi-pac internals, *InSAR Short Course, UNAVCO, 16-18 August 2010*, 2010.

Foster, A., C. Ebinger, E. Mbede, and D. Rex, Tectonic development of the northern sector of the east african rift system, *J. Geol. Soc. London*, *154*, 689 – 700, 1997.

Foster, M. R., and N. J. Guinzy, The coefficient of coherence : its estimation and use in geophysical data processing,, *Geophysics*, *32*(4), 602– 616, 1967.

Fournier, T., M. Pritchard, and S. Riddick, Duration, magnitude and frequency of subaerial volcano deformation events: New results from lattin america using insar and a global synthesis, *Geochem. Geophys. Geosyst.*, *11*(Q01003), doi: 10.1029/2009GC002558, 2010.

Froger, J.-L., Radar remote sensing, *Lecture notes, Clermont-Ferrand, France*, 2003.

Fukushima, Y., Transferts de magma au volcan du piton de la fournaise déterminées par la modélisation 3d de données d'interférométrie radar entre 1998 et 2000, Ph.D. thesis, Lab. Magmas et Volcans, Université Blaise Pascal, Clermont Ferrand, France, 2006.

Fukushima, Y., V. Cayol, and P. Durand, Finding realistic dike models from interferometric synthetic aperture radar data: The february 2000 eruption at piton de la fournaise, *Journal Geoph. Res.*, *110*(B03206), 15 pp., 2005.

Fukushima, Y., V. Cayol, P. Durant, and D. Massonet, Evolution of magma conduits during the 1998 - 2000 eruptions of piton de la fournaise volcano, réunion island, *J. Geophys. Res.*, *105*(B10204), 2010.

Gabriel, A. K., R. M. Goldstein, and H. A. Zebker, Mapping small elevation changes over large areas: differential radar interferometry., *J. Geophys. Res.*, *94*(B7), 9183 – 91, 1989.

Goldstein, R. M., and C. L. Werner, Radar interferogram filtering for geophysical applications, *Geophys. Res. Lett.*, *25*(21), 4035 – 8, 1998.

Green, W. V., U. Achauer, and R. P. Meyer, A three-dimensional seismic image of the crust and upper mantle beneath the kenya rift, *Nature*, *354*, 199 – 203, 1991.

Gudmundsson, A., and R. E. B. Andrew, Mechanical interaction between active volcanoes in iceland, *Geophys. Res. Let.*, *34*, 2007.

Guern, F. L., Mechanism of energy transfer in the lava lake of nyaragongo (zaire), 1959-1977, *J. of Volcanol. Geotherm. Res.*, *31*, 17 – 31, 1987.

Hagberg, J. O., L. M. H. Ulander, and J. Askne, Repeat-pass sar interferometry over forested terrain, *IEEE Trans. Geosci. Remote Sens.*, *33*, 331 – 340, 1995.

Hamaguchi, H., and N. Zana, *Introduction to Volcanoes Nyiragongo and Nyamuragira*, pp. 1 – 6, H. Hamaguchi (Ed.), Volcanoes Nyiragongo and Nyamuragira: Geophysical Aspects, The Faculty of Science, Tôhoku University, Sendai, Japan, 1983.

Hamling, I., A. Ayele, L. Bennati, E. Calais, C. Ebinger, D. Keir, E. Lewi, T. Wright, and G. Yirgu, Geodetic observations of the ongoing dabbahu rifting episode: new dyke intrusions in 2006 and 2007, *Geophysical Journal International*, *178*, 989–1003, 2009.

Hanssen, R. F., *Radar Interferometry Data Interpretation and Error Analysis*, 328 pp., Springer, 2001.

Hayward, N., and C. J. Ebinger, Variations in the along-axis segmentation of the afar rift system, *Tectonics*, *15*, 244 – 257, 1996.

Helffrich, G. R., How good are routinely determined focal mechanisms? empirical statistics based on a comparison of harvard, usg and eri moment tensors, *Geophys. J. Int.*, *131*, 741 – 750, 1997.

Hellfrich, G., How good are routinely determined focal mechanisms? empirical statistics based on a comparison of harvard, usgs and eri moment tensors, *Geophys. J. Int.*, *131*, 741 – 750, 1997.

Hooper, A., A multi-temporal InSAR method incorporating both persistent scatterer and small baseline approaches, *Geophys. Res. Lett.*, *35*, L16,302, doi: 10.1029/2008GL03465, 2008.

Hooper, A., H. Zebker, P. Segall, and B. Kampes, A new method for measuring deformation on volcanoes and other natural terrains using InSAR persistent scatterers, *Geophys. Res. Lett.*, *31*(23), doi: 10.1029/2004GL021737, 2004.

Hooper, A., P. Segall, and H. Zebker, Persistent scatterer InSAR for crustal deformation analysis, with application to Volcán Alcedo, Galápagos, *J. Geophys. Res.*, *112*(B07407), doi: 10.1029/2006JB004763, 2007.

Hooper, A. J., Persistent scatterer radar interferometry for crustal deformation studies and modeling of volcanic deformation, Ph.D. thesis, Stanford University, 2006.

Huppert, H., and A. W. Woods, The role of volatiles in magma chamber dynamics, *Nature*, *420*, 493 – 495, 2002.

Jaeger, J. C., N. G. W. Cook, and R. W. Zimmermann, *Fundamentals of rock mechanics*, 1 - 593 pp., 4th ed. New York, Chapman and Hall, 2007.

Johnson, D. J., Dynamics of magma storage in the summit reservoir of kilauea volcano, hawaii, *J. Geophys. Res.*, *97*, 1807 – 1820, 1992.

Johnson, D. J., F. Sigmundsson, and P. T. Delaney, Volume of magma accumulation or withdrawal estimated from surface uplift or subsidence, with application to the 1960 collapse of kilauea volcano, *Bull. Volcanol.*, *61*, 491 – 493, 2000.

Kampes, B., R. Hanssen, and Z. Perski, Radar interferometry with public domain tools, *Proceedings of FRINGE 2003, December 1-5, Frascati, Italy*, 2003.

Kampes, B. M., Displacement parameter estimation using permanent scatterers techniques interferometry, Ph.D. thesis, Delft University of Technology, Delft, Netherlands, 2010.

Kampunzu, M. M. A. B., M. N. Sebagenzi, J. P. H. Caron, and P. Vellutini, Comparaison pétrochimique entre les laves du champ sud-kivu (bukavu) et du nord-kivu (virunga), zaïre, *Annales de la Société Géologique de Belgique*, *105*, 25 – 29, 1982.

Kasahara, M., K. Tanaka, and N. Zana, A flank eruption of volcano nyamuragira in 1991 - mikombe, *Bull. Volcanol. Soc. Japan*, *39*, 29 – 50, 1991.

Kasahara, M., H. Hamaguchi, K. Tanaka, N. Zana, and M. K. M., Recent horizontal crustal movements in and around volcano nyamuragira, zaire, *Tectonophysics*, *209*, 267 – 272, 1992.

Kavotha, S., T. Mavonga, J. Durieux, and K. Mukambilwa, Towards a more detailed seismic picture of the january 17, 2002, nyiragongo eruption, *Acta Vulcanologica, The January 2002 eruption of Nyiragongo volcano and the socio-economical impact*, *Vol. 14 (1-2) and vol. 15 (1-2)*, 87 – 100, 2002/2003.

Keir, D., C. J. Ebinger, G. W. Stuart, E. Daly, and A. Ayele, Strain accommodation by magmatism and faulting as rifting proceeds to breakup: Seismicity of the northern ethiopian rift, *J. Geophys. Res.*, *111*, 17 pp., 2006.

Keir, D., C. Pagli, I. Bastow, and A.Ayele, The magma-assisted removal of arabia in afar: Evidence from dike injection in the ethiopian rift captured using insar and seismicity, *Tectonics*, *30*, 2011.

Kitagawa, S., K. Fukui, and A. Takagi, The december 1996 eruption at nyamuragira, africa, viewed from jers-1 insar, *Progress of Crustal and Deformation Research by Space Geodesy and Remote-sensing Techniques, Kyoto University, Japan, January 18-19, 2007*, 2007.

Komorowski, J.-C., et al., *The January 2002 flank eruption of Nyiragongo volcano (Democratic Republic of Congo) : Chronology, evidence for a tectonic trigger, and impact of lava flows on*

the city of Goma, vol. 14, pp. 27 – 61, Acta Vulcanologica - Istituti Editoriali e Poligrafici Internazionale, 2002-2003.

Kostrov, B., Seismic moment and energy of earthquakes, and seismic flow of rock, *Izvestiya Academy of Sciences of the USSR, Physics of Solid Earth*, *Vol. 14 (1-2) and vol. 15 (1-2)*, 87 – 100, 1974.

Lopez-Martinez, C., L. Ferro-Famil, and E. Pottier, Single vs multi-polarisation interferometry, *Polarimetry Tutorial, http://earth.eo.esa.int/polsarpro/tutorial.html*, 2005.

Lopez-Quiroz, P., M. P. Doin, F. Tupin, P. Briole, and J. M. Nicolas, Time series analysis of mexico city subsidence constrained by radar interferometry, *J. Appl. Geophys.*, *69*(1), 1 – 15, 2009.

Lu, Z., T. Masterlark, and D. Dzurisin, Interferometric synthetic aperture radar (insar) study of okmok volcano, alaska, 1992-2003: Magma supply dynamics and post-emplacement lava flow deformation, *J. Geophys. Res.*, *110*(B2, B02403), doi: 10.1029/2004JB003148, 2005.

Massonet, D., and K. L. Feigl, Radar interferometry and its application to changes in the earth's surface, *Reviews of Geophysics*, *36*(4), 441 – 500, 1998.

Massonnet, D., M. Rossi, C. Carmona, F. Adragna, G. Peltzer, K. Fiegl, and T. Rabaute, The displacement field of the Landers earthquake mapped by radar interferometry, *Nature*, *364*, 138 – 142, 1993.

Masterlark, T., Magma intrusion and deformation predictions: Sensitivities to the mogi assumptions, *J. Geophys. Res.*, *112*(B06419), doi: 10.1029/2006JB004860, 2007.

Mastin, L. G., and et al., Constraints on the size, overpressure, and volatile content of the mount st. helens magma system from geodetic and dome-growth measurements during the 2004-2006 eruption, *U.S. Geol. Surv. Prof. Pap.*, *1750*, 461 – 492, 2008.

Mastin, L. M., M. Lisowski, E. Roeloffs, and N. Beeler, Improved constraints on the estimated size and volatile content of the mount st. helens magma system from the 2004-2008 history of dome growth and deformation, *Geophys. Res. Lett.*, *36*(L20304), 2009.

Mavonga, T., Some characteristics of aftershock sequences of major earthquakes from 1994 to 2002 in the kivu province, western rift valley of africa, *Tectonophysics*, *439*, 1 – 12, 2007.

Mavonga, T., K. K. Sadaka, L. Nyombo, E. Osodundu, D. N. Jacques, R. Zana, and R. J. Durrheim, Seismic activity prior to the may 8, 2004 eruption of volcano nyamuragira, western rift valley of africa.studies of crustal structure, seismic precursors to volcanic eruptions and earthquake hazard in the eastern provinces of the democratic republic of congo, *Journal of Volcanology and Geothermal Research*, (158), 355 – 360, 2006.

Mavonga, T., N. Zana, and R. J. Durrheim, Studies of crustal structure, seismic precursors to volcanic eruptions and earthquake hazard in the eastern provinces of the democratic republic of congo, *Journal of African Earth Sciences*, p. 11 pp., 2010a.

Mavonga, T. G., Crustal stucture beneath two seismic broadband stations revealed from teleseismic p-wave receiver function analysis in the virunga volcanic area, western rift, *J. African Earth Sciences*, 2010.

Mavonga, T. G., S. K. Kavotha, N. Lukaya, O. Etoy, W. Mifundu, R. K. Bizimungu, and J. Durieux, Some aspect of seismicity prior to the 27 november 2006 eruption of nyamuragira volcano and its implication for volcano monitoring and risk mitigation in the virunga area, western rift valley of africa, *J. African Earth Sciences*, (58), 2010b.

McKenzie, D., Some remarks on the development of sedimentary basins, *Earth and Planetary Science Letters*, *40*, 25 – 32, 1978.

Meyer, A., Le volcan nyamuragira et son éruption de 1951-1952, *Bulletin de l'Institut Royal des Colonies Belges*, *24*, 233 – 287, 1953.

Miranda, and et al., Review of the impact of ers-2 piloting modes on the sar doppler stability, *Proc. of the 2004 Envisat and ERS Symposium, Austria 6-10 September 2004 (ESA SP-572, April 2005*, 2004.

Mishina, M., *Gravity survey in and around Volcanoes Nyamuragira and Nyiragongo*, pp. 69 – 74, H. Hamaguchi (Ed.), Volcanoes Nyiragongo and Nyamuragira: Geophysical Aspects, The Faculty of Science, Tôhoku University, Sendai, Japan, 1983.

Montelli, R., G. Nolet, F. Dahlen, G. Masters, E. Engdahl, and S. Hung, Finite-frequency tomography reveals a variety of plumes in the mantle, *Science*, *303*, 338 – 343, 2004.

Montgomery-Brown, E., P. Segall, and A. Miklius, Kilauea slow slip events: Identification, source inversions, and relation to seismicity, *J. Geophys. Res.*, *114*(B00A03), doi: 10.1029/2008JB006074, 2009.

Murray, J. B., The influence of loading by lavas on the siting of volcanic eruption vents, *J. Volcanol. Geotherm. Res.*, *35*, 121 – 139, 1988.

Newhall, C., and M. Tuttle, Volcanic, earthquake, and lake gas hazards of the lake kivu and virunga mountains area, rwanda-zairz-uganda rep., *Administrative report for USAID/OFDA*, 1988.

Noble, W. P., D. A. Foster, and A. J. W. Gleadow, The post-pan-african thermal and extensional history of crystalline basement rocks in eastern tanzania, *Tectonophysics*, *275*, 331 – 350, 1997.

Nyblade, A., and S. Robinson, The african superswell, *Geophys. Res. Letts.*, *21*, 765 – 768, 1994.

Nyblade, A. A., T. J. Owens, H. Gurrola, J. Ritsema, and C. A. Langston, Seismic evidence for a deep upper mantle thermal anomaly beneath east africa, *Geology*, *7*, 599 – 602, 2000.

Oyen, A. M., The unraveling of the 2007 continental rifting event in northern tanzania - towards a multi-acquisition insar approach, *MSc Thesis, TU Delft, Netherlands*, p. 124 pp., 2009.

Oyen, A. M., P. S. Marinkovic, C. Wauthier, N. d'Oreye, and R. F. Hanssen, A continental rifting event in tanzania revealed by envisat and alos insar observations, *Proc. of ALOS PI Symposium, Rhodes, Greece*, p. 8 pp., 2008.

Oyen, A. M., C. Wauthier, and N. d'Oreye, The 2007 rifting event in northern tanzania studied by c and l-band interferometry, *ECGS Blue Books*, p. 11 pp., 2010.

Parson, T., and G. Thompson, The role of magma overpressure in suppressing earthquekes and topography: worldwide examples, *Science*, *253*, 1399 – 1402, 1991.

Parsons, B. E., T. J. Wright, P. Rowe, J. Andrews, J. Jackson, R. Walker, M. Khatib, and M. Talebian, The 1994 sefidabeh (eastern iran) earthquakes revisited: new evidence from satellite radar interferometry and carbonate dating about the growth of an active fold above a blind thrust fault, *Geophys. J. Int.*,, *164*, 202 – 217, 2006.

Perlock, P., and et al., Time evolution of deformation using time series of differential interferograms: Application to la palma island (canary islands), *Pure and Applied Geophysics*, *165*(8), 1531 – 1554, 2008.

Pik, R., B. Marty, and J. Carignan, Stability of the upper nile drainage network (ethiopia) deduced from (u-th)/he thermochronometry: implications for uplift and erosion of the afar plume dome, *Earth Planet. Sci. Lett.*, *215*, 73 – 88, 2003.

Pinel, V., C. Jaupart, and F. Albino, On the relationship between cycles of eruptive activity and growth of a volcanic edifice, *Journal of Volcanology and Geothermal Research*, *194*(4), 150 – 164, 2010.

Platz, T., S. F. Foley, and L. Andre, Low-pressure fractionation of the nyiragongo volcanic rocks, virunga province, d.r. congo, *Journal of Volcanology and Geothermal Research*, *136*, 269 – 295, 2004.

Poland, M., Insar captures rifting and volcanism in east africa, *Alaska Satellite Facility News and Notes*, *Vol. 3:2*, 2006.

Pouclet, A., Contribution à l'étude structurale de l'aire volcanique des virungas, rift de l'afrique centrale, *Revues Géographie Physique et Géologie Dynamique*, *19*, 115 – 124, 1977.

Prati, C., and F. Rocca, Range resolution enhancement with multiple sar surveys combination, pp. 1576 – 1578, 1992.

Richard, J. J., *Nyamuragira - Nyiragongo*, pp. 91 – 112, Richard J.J. et Neumann Van Padang M. (eds), Part IV, Catalogue of the Active Volcanoes and Solfatara Fields of Africa and the Red Sea, International Volcanological Association, Napoli, Italy, 1957.

Rignot, E., Dual-frequency interferometric sar observations of a tropical rain fores, *Geophys. Res. Lett.*, *23*, 993 – 996, 1996.

Rivalta, E., and T. Dahm, Acceleration of buoyancy-driven fractures and magmatic dikes beneath the free surface, *Geophys. J. Int.*, *Vol. 166, Issue 3*, 1424 – 1439, 2006.

Rivalta, E., and P. Segall, Magma compressibility and the missing source for some dike intrusions, *Geophys. Res. Lett.*, *35*(L04306), doi: 10.1029/2007GL032521, 2008.

Rizzo, F. J., An integral equation approach to boundary value problems of classical elastostatics, *Quart. Appl. Math.*, *25*, 83 – 95, 1967.

Rogers, N. W., D. James, S. P. Kelley, and M. D. Mulder, The generation of potassic lavas from the eastern virunga province, rwanda, *J. Petrol.*, *39*, 1223 – 1247, 1998.

Rosen, P., S. Hensley, G. Peltzer, and M. Simons, Updated repeat orbit interferometry package released, *Eos Trans. AGU*, *85(5)*(47), doi: 10.1029/2004EO050004, 2004.

Rosen, P. A., Sar missions and new hardware developments, *InSAR Workshop, Oxnard, California, USA*, 2002.

Rowland, J., E. Baker, D. Keir, T. Kidane, J. Biggs, N. Hayward, T. Wright, and C. Ebinger, Fault growth at a nascent slow-spreading ridge: 2005 dabbahu rifting episode, afar, *Geophysical Journal International*, *171*, 1226–1246, 2007.

Rubin, A., A comparison of rift-zone tectonics in iceland and hawaii, *Bull. Volcanol.*, *52*, 302 – 319, 1990.

Rubin, A., Dike-induced faulting and graben subsidence in volcanic firt zones, *J. Geophys. Res.*, *97(B2)*, 1839 – 1858, 1992.

Rubin, A., Propagation of magma-filled cracks, *Annu. Rev. Earth Planet Sci.*, *23*, 287 – 336, 1995.

Rubin, A., and D. Pollard, Dike-induced faulting in rift zones of iceland and afar, *Geology*, *16*, 413 – 417, 1988.

Ruppel, C., Extensional processes in continental lithosphère, *Journal of Geophysical Research*, *100*(B12), 24,187 – 24,215, doi: 10.1029/95JB02955, 1995.

Sambridge, M., Geophysical inversion with a neighbourhood algorithm - i. searching a parameter space, *Geophys. J. Int.*, *138*, 479 – 494, 1999a.

Sambridge, M., Geophysical inversion with a neighbourhood algorithm - ii. appraising the ensemble, *Geophys. J. Int.*, *138*, 727 – 746, 1999b.

Samsonov, S., and K. Tiampo, Polarization phase difference analysis for selection of persistent scatterers in sar interferometry, *IEEE Geoscience and Remote Sensing Letters*, *8*(2), 331 – 335, 2011.

Sandwell, D. T., and E. J. Price, Phase gradient approach to stacking interferograms, *J. Geophys. Res.*, *103*(B12), 30,183 – 30,204, 1998.

Schmid, M., M. Halbwachs, and A. Wüest, Double diffusive convection in lake kivu, *Limnol. Oceanogr.*, *55(1)*, 225 – 238, 2010.

Seymour, M. S., and I. G. Cumming, Maxiumum likelihood estimation for sar interferometry, pp. 2272 – 2275, 1994.

Shanker, P. A., Persistent scatterer interferometry in natural terrain, Ph.D. thesis, University of Stanford, 2010.

Shirzaei, M., and T. R. Walter, Wavelet based insar (wabinsar): a new advanced time series approach for accurate spatiotemporal surface deformation monitoring, *IEEE Transactions on Geoscience and Remote Sensing*, in press.

Shudofsky, G. N., Source mechanisms and focal depths of east african earthquakes using rayleigh wave dispersion and body-wave modelling, *J. Geophys. Res.*, *89*, 5733 – 5762, 1985.

Simons, M., and P. Rosen, *Treatise on Geophysics, Interferometric Synthetic Aperture Radar Geodesy*, vol. Volume 3 - Geodesy, 391 - 446 pp., Elsevier Press, 2007.

Smets, B., and C. Wauthier, Tanzanie - octobre 2007 - rapport sur l'activité volcanique et sismique dans la région du lengai, *Rapport de mission MRAC*, p. 7 pp., 2007.

Smets, B., M. Kervyn, F. Kervyn, N. d'Oreye, and C. Wauthier, New insights into eruptive activity and lava flow hazard at nyamulagira volcano, d.r.c., from a new gis-based lava flow map, *Abstract V11C-2288, AGU13-17 December 2010, San Francisco, California, USA*, 2010a.

Smets, B., D. Tedesco, F. Kervyn, A. Kies, O. Vaselli, and M. M. Yalire, Dry vents ("'mazuku"') in goma region (north-kivu, democratic republic of congo): Formation and risk assesment, *Journal of African Earth Sciences*, *58*, 787 – 798, 2010b.

Smets, B., C. Wauthier, and N. d'Oreye, A new map of the lava flow field of nyamulagira (d.r. congo) from satellite imagery, *Journal of African Earth Sciences*, *58*, 778 – 786, 2010c.

Stamps, D. S., E. Calais, E. Saria, C. Hartnady, J.-M. Nocquet, C. J. Ebinger, and R. M. Fernandes, A kinematic model for the east african rift, *Geophys. Res. Letts.*, *35*, 6 p., 2008.

Stevens, N. F., G. Wadge, C. Williams, J. Morley, J.-P. Mauller, J. Murray, and M. Upton, Surface movements of emplaced lava flows measured by synthetic aperture radar interferometry, *J. Geophys. Res.*, *106*(B6), 11,293 – 11,313, 2001.

Tanaka, K., *Seismicity and focal mechanisms of the volcanic earthquakes in the Virunga Volcanic Region*, pp. 19 – 28, H. Hamaguchi (Ed.), Volcanoes Nyiragongo and Nyamuragira: Geophysical Aspects, The Faculty of Science, Tôhoku University, Sendai, Japan, 1983.

Tarantola, A., *Inverse Problem Theory: Methods for Data Fitting and Model Parameter Estimation*, Elsevier, 1987.

Tazieff, H., Première exploration du cratère du volcan nyiragongo, *Bull. Soc. Belge Géol.*, *58*, 165 – 172, 1949.

Tazieff, H., An exceptional eruption: Mt. nyiragongo, jan. 10th, 1977, *Bull. Volcanol.*, *40*, 189 – 200, 1977a.

Tazieff, H., An exceptional eruption : Mt. nyiragongo, january 10th. 1977, *Bull. Volcanol.*, *40-3*, 1 – 12, 1977b.

Tedesco, D., The january 2, 2010 eruption of mt. nyamulagira: Field observations, evolution and possible human and infrastructures impact, *UNOPS report - Prevention and Analysis of Volcanic Hazards in north Kivu, DRC*, p. 8 pp., 2010.

Tedesco, D., O. Vaselli, P. Papale, S. A. Carn, M. Voltaggio, G. M. Sawyer, J. Durieux, M. Kasereka, and F. Tassi, January 2002 volcano-tectonic eruption of nyiragongo volcano, democratic republic of congo, *J. Geophys. Res.*, *112*(B09202), 12 pp., 2007a.

Tedesco, D., F. Tassi, O. Vaselli, R. Poreda, T. Darrah, E. Cuoco, and M. Yalire, Gas isotropic signatures (he, c and ar) in the lake kivu region (western branch of the east african rift system): Geodynamix and volcanological implications, *J. Geophys. Res.*, *115*(B01205), doi: 10.1029, 2010.

Tedesco, D., et al., Cooperation on congo volcanic and environmental risks, *EOS, Transactions, American Geophysical Union*, *88*(16), 177 – 181, 2007b.

Townend, J., and M. Zoback, How faulting keeps the crust strong, *Geology*, *28(5)*, 399 – 402, 2000.

Traversa, P., V. Pinel, and J. Grasso, A constant influx model for dike propagation: Implactions for magma reservoir dynamics, *J. Geophys. Res.*, *115*(B01201), doi: 10.1029/2009JB006559, 2010.

van der Kooij, M., W. Hughes, S. Sato, and V. Poncos, Coherent target monitoring at high spatial density: Examples of validation results, *European Space Agency, (Special Publication) ESA SP-610*, 2006.

Villeneuve, M., La structure du rift africain dans la région du lac kivu (zaïre oriental), *Bull. Volc. Intern.*, *43*, 541 – 555, 1980.

Wauthier, C., Modélisation des déplacements insar survenus au nyiragongo en janvier 2002, *Master 2 Recherche, Université BLAISE-PASCAL, Lab. MAGMAS ET VOLCANS, Clermont-Ferrand, France*, p. 55 pp., 2007.

Wauthier, C., V. Cayol, A. Hooper, F. Kervyn, P. Marinkovic, N. D'Oreye, and M. P. Poland, Activity of Nyiragongo and Nyamulagira Volcanoes (Dem. Rep. of Congo) Revealed Using Geological, Geophysical and InSAR data, *AGU Fall Meeting Abstracts*, pp. D5+, 2010.

Wauthier, C., A. Hooper, E. Sansoti, G. Zeni, A. Pepe, and N. d'Oreye, Study of the nyiragongo - nyamulagira area (dem. rep. of congo) by means of multi-temporal insar approaches: Comparison of the stamps (tu delft) and sbas (irea) methods, *Abtract 1.4-P-06 in the Abstract Volume for the Cities on Volcanoes 6th, Puerto de la Cruz, Tenerife, Canary Island, Spain, May 31 - June 4*, 2010.

Wauthier, C., et al., L-band and c-band insar studies of african volcanic areas, *Geoscience and Remote Sensing Symposium, 2009 IEEE International, IGARSS 2009*, pp. II–210, 2009.

Weertman, J., Theory of water-filled crevasses in glaciers applied to vertical magma transport beneath oceanic ridges, *J. Geophys. Res.*, *76*, 1171 – 1183, 1971.

Wiedenmann, D., Petrologische und vulkanologische stellung von biotit-olivin-pyroxen-melilith-tuffen am oldoinyo lengai, tanzania, Ph.D. thesis, Albert-Ludwigs-Universität Freiburg, 2003.

Wolfenden, E., C. Ebinger, G. Yirgu, P. R. Renne, and S. P. Kelley, Evolution of a volcanic rifted margin: Southern red sea, ethiopia, *GSA Bulletin*, *117*, 846 – 864, 2005.

Wong, H. K., and R. P. V. Herzen, A geophysical study of lake kivu, east africa, *Geophys. J. R. Astron. Soc.*, *37*, 371 – 389, 1974.

Wright, T., B. Parsons, and Z. Lu, Towards mapping surface deformation in three dimensions using insar, *Geophys. Res. Lett.*, *31(1)*(L01607), doi: 10.1029/2003GL018827, 2004.

Wright, T., C. Ebinger, J. Biggs, A. Ayele, G. Yirgu, D. Keir, and A. Stork, Magma-maintained rift segmentation at contiental rupture in the 2005 afar dyking episode, *Nature*, *442 (7100)*(PMID 16855588), 291 – 294, doi: 10.1038/nature04978, 2006.

Yun, S., P. Segall, and H. Zebker, Constraints on magma chamber geometry at Sierra Negra Volcano, Galapagos islands, based on InSAR observations, *J. Volc. Geotherm. Res.*, *150*(1-3), 232 – 243, 2006.

Zana, N., and N. Hamagushi, Some characteristics of aftershock sequences in the western rift valley of africa, *Sci. Rep. Tôhoku Univ.*, *5*, 55 – 72, 1978.

Zebker, H., and R. Goldstein, Topographic mapping from interferometric sar observations, *J. Geophys. Res.*, *91*, 4993 – 5001, 1986.

Zebker, H. A., Imaging radar and applications, *Class notes*, p. EE355, 1996.

Zebker, H. A., and J. Villasenor, Decorrelation in interferometric radar echoes, *IEEE Trans. Geosci. Remote Sens.*, *30*(5), 950 – 9, 1992.

Zebker, H. A., P. A. Rosen, R. M. Goldstein, A. Gabriel, and C. L. Werner, On the derivation of coseismic displacement-fields using differential radar interferometry - the Landers earthquake, *J. Geophys. Res.*, *99*(B10), 19,617 – 19,634, 1994a.

Zebker, H. A., C. L. Werner, P. A. Rosen, and S. Henley, Accuracy of topographic maps derived from ers-1 interferometric data, *IEE Transactions on Geoscience and Remote Sensing*, *32*(4), 823 – 836, 1994b.

Zucca, J. J., D. P. Hill, and R. L. Kovach, Crustal structure of mauna loa volcano, hawaii, from seismic refraction and gravity data, *Bull. Seis. Soc. Am.*, *72*, 1535 – 1550, 1982.

Annexe 1

Nicolas d'Oreye, Pablo J. Gonzalez, Ashley Shuler, Adrien Oth, Louis Bagalwa, Göran Ekström, Déogratias Kavotha, François Kervyn, Celia Lucas, François Lukaya, Etoy Osodundu, Christelle Wauthier and José Fernandez (2010), Source parameters of the 2008 Bukavu-Cyangugu earthquake estimated from InSAR and teleseismic data, *Geophys. J. Int.*, **184**, 934-948

Annexe 2

Eric Calais, Nicolas d'Oreye, Julie Albaric, Anne Deschamps, Damien Delvaux, Jacques Déverchère, Cynthia Ebinger, Richard W. Ferdinand, François Kervyn, Athanas S. Macheyeki, Anneleen Oyen, Julie Perrot, Elifuraha Saria, Benoît Smets, D. Sarah Stamps and Christelle Wauthier (2008), Strain accomodation by slow slip and dyking in a youthful continental rift, East Africa, *Nature*, **456**, Macmillan Publishers Limited, 783-788

Annexe 3

A.M. Oyen, C. Wauthier and N. d'Oreye (2010), The 2007 rifting event in Northern Tanzania studied by C and L-band interferometry, *ECGS Blue Books*, 11 pp.